Investigation of the plasma electrolytic polishing process for metallic surface treatment

Dissertation

in fulfilment of the requirements for the degree of
Doctor of Natural Sciences (Dr. rer. nat.)
of the Faculty of Mathematics and Natural Sciences
at Kiel University

submitted by

Sehoon An

Greifswald, 2023

First examiner:	Prof. Dr. Holger Kersten
Second examiner:	Prof. Dr. Maik Fröhlich
Date of the oral examination:	13.10.2023

Abstract

Plasma electrolytic polishing (PEP) has recently attracted immense attention due to its ecological benefits and capability to considerably enhance surface properties for complex-shaped components (e.g., additive manufacturing (AM)) without complicated pre- and post-treatment steps. Although the PEP technique has great potential for direct application to various fields, a systematic investigation via surface characterization and appropriate process diagnostics is required to provide a fundamental understanding of the process. Furthermore, a feasibility test for its actual application must be provided to prove its industrial viability. Hence, this thesis focuses on surface characterization techniques and process diagnostics to better understand the PEP process and the fundamental mechanisms that govern the surfaces properties of metallic workpieces. Additionally, a feasibility study examining the actual uses of PEP-based surface treatment has been implemented to demonstrate its potential, thus broadening its application spectrum.

This thesis first demonstrates the PEP process for the surface pretreatment of cobalt-containing tungsten carbide (WC-Co) precision tools to achieve sufficient adhesion for the coating layers. The optimal operating conditions for a cleaning effect were identified depending on the electrolyte composition, temperature, and process voltage. Additionally, the PEP-treated workpiece surfaces were studied using diverse surface characterization techniques. The results confirm that after the PEP process, the elemental concentration of Co on the tool surface increases from 6.5 at% to 18.2 at% owing to selectively dissolved WC crystallites. In addition, the PEP process effectively reduced the surface contamination degree while maintaining cutting-edge sharpness. For a subsequent process step, two different types of hard coating layers (TiN and AlTiSiN) were deposited on the PEP-treated tool surface. From the tribological test, the PEP-pretreated tools exhibited superior machining performance for both types of coatings compared to the tools subjected to the conventional pretreatment process. This is attributed to the increased adhesion strength between the hard coating and the tool surface, facilitated by the thorough cleaning effect of the PEP process.

In a second part of this thesis, as an extensive study, the PEP process was diagnosed employing electrical and thermal measurements to characterize the temporal behavior of gaseous layer formation, and correlation with the resultant surface of the WC-Co workpiece was attempted. Based on the thermal measurement, the workpiece temperature during the PEP process reached around 150 °C from a starting temperature of 70 °C. A synchronous electrical measurement revealed that the current varied according to the workpiece temperature when the vapor-gaseous envelope (VGE) layer developed. The power transferred to the workpiece (P_{in}) was identified based on a calorimetric probe method using the time-derivative temperature data. Furthermore, the distinctive heating features could be identified depending on the workpiece temperature. In the low-temperature regime (T < 100 ºC), P_{in} was varied from ~105 W to ~363 W with the corresponding increase of workpiece immersion depth (d) from 5 mm to 20 mm, respectively. Meanwhile, in the high-temperature regime (T > 120 ºC), P_{in} remains constant at approximately 192 W regardless of the workpiece immersion depth. Furthermore, a liquid–gas mixture model was employed to simulate the temporal evolution of the electrolyte. In this model, the two-dimensional flow velocity was characterized, and the importance of the distance between

the workpiece (anode) and wall (cathode) was revealed, as the reverse stream of an electrolyte flow affect the electrolyte temperature near the workpiece. Furthermore, X-ray photoelectron spectroscopy (XPS) revealed a slight compositional gradient in vertical direction on the cylindrical workpiece after the PEP process. This could be attributed to varying current densities influencing the material removal rates. As a part of process diagnostics, synchronized high-speed camera and electrical measurements were employed to investigate the correlation between current waveform behavior and gas layer dynamics during the PEP process. Spectrogram analysis was applied to both the current waveform and high-speed images, revealing a correlation of oscillating behavior between the electrical current and bubble layer movement. Moreover, spatial analysis of the camera signal confirmed the presence of a vertical gradient on the workpiece surface as observed in the XPS line scan analysis. This is ascribed to variations in discharges generated at different vertical positions during the PEP process which can support the observation made from the XPS line scan analysis. This knowledge is essential for optimizing the PEP process, as it provides insights into the distribution of electrical discharges and their impact on surface quality, particularly for elongated workpieces.

Third part of this thesis is an exploration of the effects of PEP on 3D-printed metallic workpieces with complex geometries, with a goal to validate its practical feasibility. The specific focus of this study lies on the surface finishing of 3D-printed stainless-steel (SS) mist chambers for aerosol production in the process of thin film deposition through liquid precursor. Through surface finishing using the PEP process, the intent is to enhance the aerosol misting performance, consequently leading to the creation of uniform and consistent plasma-polymerized (pp) thin films. Surface analysis verified that the PEP process results in a smooth surface on a 3D-printed component. Additionally, the PEP-treated surface showed increased water contact angle compared to the untreated surface. The assessment of misting performance indicated that a 65% reduction in misting time was achieved when a 30-min PEP-treated mist chamber was used. This was attributed to the faster drainage of smaller droplets. The atmospheric-pressure plasma jet (APPJ) treatment was then performed on the mist generated by the mist chamber to obtain the pp-film. Notably, the pp-film analysis results showed that the surface-finishing of the PEP process is highly reproducible and time efficient for fabricating pp-films in a thickness range of 20 nm to 150 nm.

As an outlook, this thesis delivers substantial insight into PEP by establishing an understanding of the process encompassing process development, surface characterization, process diagnostics, and feasibility testing in case of actual application areas of precision tool and 3D-printing. The results of this work can serve as a benchmark to guide further investigations of different aspects of the PEP process in related fields.

Kurzfassung

Plasmaelektrolytisches Polieren (PEP) hat, aufgrund seiner ökologischen Vorteile sowie der Fähigkeit, die Oberflächeneigenschaften für komplex geformte Komponenten (z.B. additive Fertigung (AM)) ohne komplizierte Vor- und Nachbehandlungsschritte erheblich zu verbessern, in jüngster Zeit große Aufmerksamkeit erregt. Da die PEP-Technik großes Potenzial für die direkte Anwendung in verschiedenen Bereichen hat, ist eine systematische Untersuchung über die Oberflächencharakterisierung und geeignete Prozessdiagnostik erforderlich, um ein grundlegendes Verständnis des Prozesses zu erhalten. Aus diesem Grund konzentriert sich diese Arbeit auf die Prozessdiagnosik und die Charakterarisierung von Oberflächen, um den PEP-Prozess und die grundlegenden Mechanismen, welche die Oberflächeneigenschaften von metallischen Werkstücken bestimmen. Darüber hinaus wurde eine Machbarkeitsstudie zur Untersuchung PEP-basierter Oberflächenbehandlung durchgeführt. Zusätzlich wird dadurch das Potenzial von PEP-basierten Oberflächenbehandlungen aufgezeigt und deren Anwendungsspektrum erweitert.

Die vorliegende Arbeit legt den PEP-Prozesses zur Vorbehandlung von kobalthaltigen Wolframkarbid (WC-Co)-basierten Werkzeugen dar. Ziel ist es ausreichende Haftungswerte für die nachfolgenden Beschichtungen zu erreichen. Die optimalen Betriebsbedingungen für einen günstig Reinigungseffekt wurden in Abhängigkeit von der Elektrolytzusammensetzung, Elektrolyttemperatur und Prozessspannung identifiziert. Zusätzlich wurden die PEP-behandelten Werkzeugoberflächen mittels verschiedener Techniken zur Oberflächencharakterisierung untersucht. Die Ergebnisse bestätigten, dass nach dem PEP-Prozess die Elementkonzentration von Co aufgrund selektiv gelöster WC-Kristallite auf der Werkzeugoberfläche von 6,5 at% auf 18,2 at% ansteigt. Darüber hinaus reduzierte der PEP-Prozess den Verschmutzungsgrad der Oberfläche effektiv, während die Schneidkantenschärfe erhalten blieb. In einem nachfolgenden Prozessschritt wurden zwei verschiedene Arten von Hartbeschichtungen (TiN und AlTiSiN) auf der PEP-behandelten Werkzeugoberfläche abgeschieden. Aus dem tribologischen Test zeigten die PEP-vorbehandelten Werkzeuge zeigten eine deutlich bessere Zerspanungsleistung für beide Hartbeschichtungen, im Vergleich zu den Werkzeugen, die einem konventionellen Vorbehandlungsprozess unterzogen wurden. Grund dafür ist die erhöhte Haftfestigkeit zwischen der Hartbeschichtung und der Werkzeugoberfläche durch die Vorbehandlung mit der plasmaelektrolytischen Politur.

Im zweiten Teil der Arbeit, im Rahmen einer umfangreichen Studie wurde der PEP-Prozess mit elektrischen und thermischen Diagnostiken untersucht. Dabei wird das zeitliche Verhalten der Gasbildung charakterisiert und ein Zusammenhang mit der resultierenden Oberfläche des Werkstücks hergestellt. Die thermische Messung zeigte, dass die Temperatur des Werkstücks während des PEP-Prozesses von 70 °C auf etwa 150 °C anstieg. Eine synchrone elektrische Messung zeigte, dass der Strom in Abhängigkeit von der Werkstücktemperatur variierte, als die Dampf-Gas-Hülle sich entwickelte. Die auf das Werkstück übertragene Leistung (P_{in}) wurde auf Grundlage der zeitlich abgeleiteten Temperaturdaten ermittelt. Darüber hinaus konnten die charakteristischen Erwärmungsmerkmale in Abhängigkeit von der Werkstücktemperatur beobachtet werden. Im Niedertemperaturbereich (T < 100 °C) variierte die P_{in} von etwa 105 W bis etwa

363 W bei einer entsprechenden Zunahme der Werkstückeintauchtiefe (*d*) von 5 mm auf 20 mm. Im Hochtemperaturbereich (T > 120 °C) blieb die P_{in} unabhängig von der Eintauchtiefe des Werkstücks bei etwa 192 W konstant. Darüber hinaus wurde eine Flüssigkeits-Gas-Gemisch-Simulation verwendet, um die zeitliche Entwicklung des Elektrolyten zu modellieren. In dieser Simulation wurde die zweidimensionale Strömungsgeschwindigkeit charakterisiert. Die Bedeutung des Abstandes zwischen dem Werkstück (Anode) und der Wand (Kathode) wurde aufgezeigt, da der Rückfluss des Elektrolyten die Elektrolyttemperatur in der Nähe des Werkstücks beeinflusst. Zuletzt zeigte die Messung mittels Röntgenphotoelektronenspektroskopie (XPS) einen leichten Kompositionsgradienten des PEP-behandelten Werkstücks. Dieser Gradient ist auf unterschiedliche Stromdichten während des PEP-Prozesses zurückzuführen, welche die Materialabtragsraten beeinflussen. Als Teil der Prozessdiagnostik wurden Aufnahmen mit einer Hochgeschwindigkeitskamera synchronisiert mit elektrischen Messungen eingesetzt, um die Korrelation zwischen Stromwellenformverhalten und Gasdynamik während des PEP-Prozesses zu untersuchen. Eine Spektrogrammanalyse wurde sowohl auf die Stromwellenform als auch auf Hochgeschwindigkeitsbilder angewendet. Dabei wurde ein Zusammenhang des oszillierenden Verhaltens zwischen dem Strom und der Bewegung der Blasenschicht festgestellt. Die Analyse des Kamerasignals bestätigte die Existenz eines vertikalen Gradienten auf der Werkstückoberfläche, wie auch in der XPS Analyse beobachtet wurde. Dies wird Schwankungen in den Entladungen, welche an verschiedenen vertikalen Positionenen erzeugt werden, zugeschrieben. Insbesondere bei länglichen Werkstücken ist das Wissen über die Verteilung der elektrischen Entladungen während des PEP-Prozesses sowie deren Auswirkung auf die Oberflächenqualität unerlässlich.

Im dritten Teil dieser Arbeit wird die Wirkung von PEP auf 3D-gedruckte metallische Werkstücke mit komplexen Geometrien untersucht, mit dem Ziel, seine praktische Umsetzbarkeit zu bestätigen. Der besondere Fokus dieser Studie liegt auf der Oberflächenveredelung 3D-gedruckter Nebelkammern aus rostfreiem Edelstahl, welche für die Aerosol-Produktion im Prozess der Dünnschichtabscheidung mittels eines flüssigen Precursors genutzt werden. Durch die Oberflächenveredelung mit Hilfe des PEP-Prozesses soll die Nebelleistung versessert und damit zur Erzeugung einheitlicher und beständiger plasma-polymerizierter (pp) Dünnschichten erreicht werden. Anschließend wurde die Nebelleistung bewertet. Eine glattere Oberfläche konnte mit dem PEP-Prozess auf dem 3D-gedruckten metallischen Teil erzeugt werden, indem die Behandlungszeit verlängert wurde. In der PEP-behandelten Nebelkammer wurde die Nebelzeit um 65% verkürzt, weil ein schnellerer Abfluss der kleineren Tröpfchen erleichtert wurde. Um die pp-Schicht zu erhalten wurde eine atmospärische Plasmajetbehandlung (APPJ) auf den von der Nebelkammer erzeugten Neben angewendet. Bemerkenswerterweise zeigte die pp-Schicht-Analyse, dass die Oberflächenveredelung des PEP-Prozesses hoch reproduzierbar und zeiteffizient für die Herstellung von pp-Schichten einer Dicke von 20 nm bis 150 nm ist. Diese Arbeit gibt einen tiefen Einblick in das plasmaelektrolytische Polieren. Sie umfasst die Prozessentwicklung, Oberflächencharakterisierung, Prozessdiagnostik und Umsetzbarkeit realer Anwendungen 3D-gedruckter Werkstücke und zur Behandlung von Präzisionswerkzeugen. Die Ergebnisse dieser Arbeit können als Maßstab für weitere Untersuchungen verschiedener Aspekte des PEP-Prozesses in verwandten Bereichen diene.

Table of Contents

ABSTRACT I

KURZFASSUNG III

1 GENERAL INTRODUCTION 1

2 FUNDAMENTALS 5

2.1 General description of polishing 5

2.2 Plasma-liquid interactions 7
2.2.1 Discharges directly in the liquid 7
2.2.2 Externally-generated plasma with liquid 8
2.2.3 Plasma in multiphase systems 9

2.3 A comprehensive overview of plasma electrolytic polishing 10
2.3.1 Current-voltage characteristics of PEP 12
2.3.2 Discharge mechanism during the plasma electrolysis 13
2.3.3 Polishing mechanisms 17

3 EXPERIMENTAL DETAILS ON SURFACE AND PROCESS DIAGNOSTICS .. 23

3.1 X-ray photoelectron spectroscopy 23

3.2 White light interferometry 25

3.3 Scanning electron microscopy 29

3.4 Fourier transform infrared spectroscopy 29

3.5 Grazing incidence X-ray diffraction 31

3.6 Atomic force microscopy 31

4 INVESTIGATION OF THE PEP PROCESS FOR SURFACE PRETREATMENT OF CEMENTED TUNGSTEN CARBIDE 33

4.1 Introduction 33

4.2 Experimental details 35
4.2.1 Plasma electrolytic polishing for surface pretreatment 35
4.2.2 Deposition of hard coatings 36
4.2.2.1 TiN hard coating 37
4.2.2.2 AlTiSiN hard coating 39

4.2.3 Evaluation of the tribological performance of hard coatings 39
4.2.3.1 Scratch test 39
4.2.3.2 Machining tests 40

4.3 Results and discussion 40
4.3.1 Parameter study for optimization of PEP process 40
4.3.1.1 Selection of electrolyte 41
4.3.1.2 Voltage-current characteristics of the PEP process 43
4.3.1.3 Influence of the PEP process on the tool 46
4.3.1.4 Characterization of the surface cleaning effect 52
4.3.1.5 Effect on tool cutting edge 55
4.3.2 Assessment of the coated tools 57
4.3.2.1 Performance evaluation of TiN-coated cutting tool 57
4.3.2.2 Performance evaluation of AlTiSiN-coated cutting tool 60

4.4 Conclusions 62

5 PROCESS DIAGNOSTICS FOR PLASMA ELECTROLYTIC POLISHING (PEP) 63

5.1 Introduction 63

5.2 Experimental setup and model description 64
5.2.1 Plasma electrolytic polishing 64
5.2.2 Temperature measurement of workpiece and electrolyte 65
5.2.3 Evaluation of transferred power to the workpiece 66
5.2.3.1 Evaluating the low-temperature (LT) regime: challenges and calibration method 68
5.2.3.2 Determination of workpiece's heat capacity 70
5.2.4 Description of electrolyte temperature modeling 72
5.2.5 Synchronization of electrical and high-speed camera measurement 74

5.3 Results and discussion 75
5.3.1 Electrical and thermal characterization 75
5.3.2 Modeling of electrolyte temperature 81
5.3.3 Analysis of longitudinal surface composition via XPS line scans 84
5.3.4 Investigation of gaseous layer development via synchronized high-speed camera and electrical signal measurement 85
5.3.4.1 Temporal analysis of the PEP process via high-speed camera synchronized with electrical current measurements 85
5.3.4.2 Analysis of Current Waveforms and Frequency Components in the PEP Process 87
5.3.4.3 Correlation between camera signal intensity and electrical current waveform 93
5.3.4.4 Spatially-resolved camera signal analysis during PEP process 95

5.4 Conclusions 97

6 APPLICATION OF PEP IN SURFACE FINISHING OF 3D-PRINTED METALLIC PARTS 99

6.1 Introduction **99**
6.1.1 Surface-finishing of additive manufactured (AM) parts 99
6.1.2 The use of mist chambers for producing plasma-polymerized thin film 99

6.2 Experimental details **101**
6.2.1 Design and manufacturing of the mist chambers 101
6.2.2 Plasma electrolytic polishing process for 3D-printed parts 102
6.2.3 Fabrication of plasma polymerized thin films 104
6.2.4 Analysis of surface properties and misting effectiveness 105
6.2.4.1 Optical microscopy 105
6.2.4.2 Water contact angle 105
6.2.4.3 Ellipsometry 105
6.2.4.4 Quartz crystal microbalance 105

6.3 Results and discussion **106**
6.3.1 Influence of plasma electrolytic polishing on surface of 3D-printed part 106
6.3.2 Performance of the mist chamber 111

6.4 Conclusions **113**

7 SUMMARY AND OUTLOOK 115

8 REFERENCES 119

LIST OF FIGURES 133

LIST OF TABLES 139

LIST OF ABBREVIATION 140

LIST OF PUBLICATIONS & CONFERENCE CONTRIBUTIONS I

SWORN DECLARATION II

ACKNOWLEDGEMENT III

1 General introduction

In the course of history, metal manufacturing has played a vital role in the development of technology in a wide variety of fields, from industrial sectors including aerospace, automotive, construction, shipbuilding, and biomedical applications, as well as everyday items such as furniture, kitchenware, and home appliances. Consequently, there is a constant need to improve metal forming techniques in order to achieve optimal performance. While the characteristics of the bulk material hold great significance, surface properties crucially impact the material's durability, corrosion resistance, biocompatibility, adhesion properties, and even decorative effect. Thus, along with the advancement of metal forming techniques, surface engineering has also developed significantly. Surface engineering involves primarily two approaches: (1) modifying the structure or composition of the component's surface or (2) forming a suitable layer on the surface [1].

Among the various surface modification techniques, polishing involves smoothing a surface in order to improve its functionality. For example, polishing can improve the corrosion resistance of metal surfaces by removing rough spots or burrs that can trap moisture and corrode the surface over time. In addition, the smooth surface also reduces friction, which in turn extends the lifetime of moving components such as gears and bearings. Furthermore, polishing is often used as a surface preparation step for subsequent surface treatments, such as plating, painting, or coating, since a polished surface provides a smooth, uniform, and clean base for these treatments, which can improve their adhesion and durability. The numerous benefits associated with surface polishing have elevated its significance, leading to the development of various polishing techniques (mechanical polishing, chemical polishing, electrochemical polishing, laser polishing and so on) [2-5]. These techniques aim to meet the increasing demands for product surface quality and maintain competitiveness in industrial manufacturing processes [6]. In recent years, the fast-paced development of metallic 3D-printing technology has led to a greater demand for manufacturing more complex-shaped objects [6, 7]. However, the direct use of these parts is impeded by the need for post-surface finishing processes. Unfortunately, surface finishing of complex-shaped workpieces is difficult to achieve effectively using conventional polishing methods, such as mechanical polishing.

The complexity of workpiece geometries and the high demand for surface quality, combined with environmental concerns, has resulted in plasma electrolytic polishing (PEP) gaining significant attention due to its capability to produce the smoothed surface homogeneously on the entire workpiece while reducing the environmental impact associated with other electrochemical polishing methods [8, 9]. The basic configuration of the PEP process resembles the conventional electrochemical process; however, it operates under high voltage (several hundred volts), generating gaseous layers around the workpiece accompanied by electrical discharges, which results in material removal from the surface. Recently, there has been a growing interest in PEP processing, with significant efforts aimed at enhancing its efficiency and the broadening of its application to encompass a diverse range of materials. Additionally, significant effort has been directed towards understanding the surface-removing mechanism associated with electrical discharge and electrochemical reactions [9-16]. Nonetheless, the broad implementation of PEP as an industrial process remains constrained

by factors such as the limited range of treatable materials, excessive energy consumption, and incomplete comprehension of the interdependence between processing conditions, discharge features, and the resulting polished surface. Even though the PEP process is often lauded for its environmentally-friendly alternative to conventional polishing techniques due to its utilization of a mostly water-based electrolyte, its high electrical power consumption has raised doubts about its sustainability. Compared to conventional electropolishing, the PEP process requires nearly ten times the amount of electrical power, and its efficiency in anodic dissolution is disputed. Furthermore, while the PEP process has the potential to serve other functions, such as deburring or surface cleaning, it is predominantly employed for surface finishing purposes, specifically to decrease roughness. Moreover, the effectiveness of incorporating the PEP process with surface finishing in 3D-printing technology remains still unclear, as there is a lack of empirical examples demonstrating the correlation between the surface modification effect of the PEP process and the performance change of the final product for the specific application is yet to be established. Therefore, this thesis aims to address the present constraints of the PEP process by primarily pursuing the following objectives:

1. Develop the PEP process for surface pretreatment of WC-Co-based precision tool surface and demonstrate its feasibility for industrial applications.
2. Investigate the temporal behavior of the gaseous layer during the PEP process using electrical, thermal, and optical diagnostic techniques to enhance comprehension of the surface treatment effects on the anodic workpiece surface.
3. Investigate the surface treatment effect of PEP process in conjunction with metallic 3D-printing technology and provide proof of concept for its practical applicability as a final product.

The ultimate goal is to augment the understanding of the underlying mechanisms governing anodic surface dissolution, which will, in turn, aid in promoting the industrialization of PEP by improving the efficiency of the process. Therefore, the purpose of this thesis is to investigate the PEP process by leveraging a variety of surface characterization techniques and process diagnostics. Accordingly, this thesis is structured as subsequently outlined.

- **Chapter 2** establishes a fundamental basis for a comprehensive understanding of the PEP process by reviewing the state of the art covering a range of surface polishing techniques, plasma generation in liquid environments, the essential characteristics of PEP, and the suggested mechanisms that govern the surface polishing effect through the PEP process.
- **Chapter 3** provides an overview of the surface characterization techniques employed in this thesis, focusing on the investigating the influence of the PEP on the morphology and elemental composition of metallic surfaces in order to optimize the process for its intended applications. A brief explanation of the working principles of the related equipment is also included.
- **Chapter 4** examines the potential of the PEP process as a surface pretreatment process for WC-Co-based cutting tools, with the aim of expanding the scope of its application. A systematic experimental investigation, including various surface and geometrical analyses, has been performed simultaneously for process optimization to effectively remove grease contamination while maintaining cutting-edge definitions and minimizing surface compositional change. Subsequently, various hard coating layers were deposited on the tool surfaces and incorporated with a plasma fine-cleaning process through PVD

techniques. Finally, the coated tool performance was assessed through adhesion and machining tests. The coated tool lifetime with PEP treatment was benchmarked to the coated cutting tool with the conventional method to verify its possible direct application to the commercial tool production chain.

- **Chapter 5** presents a comprehensive study of the PEP process on WC-Co material, employing diagnostic methods. The thermal diagnostic approach employs calorimetric measurements to determine the energy aspect of the anodic workpiece, which is discussed in conjunction with the spatio-temporal gas layer development and supported by modeling. Moreover, synchronized high-speed camera and electrical measurements are applied as part of process diagnostics to explore the relationship between current oscillating behavior and gas layer dynamics during the PEP process. These diagnostic techniques are crucial for attaining a fundamental understanding of the PEP process and refining it to achieve the desired surface outcomes on the workpiece.
- **Chapter 6** highlights the potential of the PEP process as a viable method for surface finishing when integrated with metallic 3D-printing technology. This is particularly demonstrated through its application to a 3D-printed mist chamber, specially designed for the plasma polymerization (pp) process. To examine the impact of the PEP process on the surface of 3D-printed workpieces, various surface characterization techniques are employed, encompassing measurements of surface morphology, elemental composition, and wettability. Moreover, the performance of the mist chamber treated by the PEP process was assessed by measuring the mass transport rate. Subsequently, pp-films were fabricated using the mist provided by PEP-treated mist chamber. Their properties were contrasted with those from the untreated mist chamber, thus demonstrating the potential of the PEP process as a viable post-treatment for complex-shaped components produced by metallic 3D-printers.
- **Chapter 7** summarizes the results and provides a prospect for further development of the PEP process.

2 Fundamentals

This chapter offers an overview of PEP technology through a review of existing literature. First, it introduces conventional polishing techniques, and by systematically comparing their respective limitations in industrial applications, the rational for PEP technology is substantiated. The general concept of plasma in liquid environments is then presented, illustrating the diverse ways plasma interacts with liquid. The chapter then delivers an overview and in-depth description of the PEP technique, addressing its instrumental configuration and the current state of this technology. Finally, typical features of the PEP process are described including electrical characteristics and discharge phenomena, in the context of proposed mechanisms that integrate surface erosion effects with plasma generated within the liquid environment.

2.1 General description of polishing

Figure 2.1 Photograph of 3D-printed metallic parts (316L stainless steel): untreated (left) and polished (right)

Polishing refers to the process of obtaining a smooth and luster surface with a high specular reflection by removing surface protrusions through mechanical or chemical treatment. A representative example of a polished metallic surface can be seen in Figure 2.1. The surface polishing technique has been progressively refined along with the development of manufacturing industries such as automotive, aerospace, energy production, electronics, medical instruments, and even the production of luxurious goods [4, 17, 18]. The surface quality crucially determines the lifetime and performance of a product. Various polishing methods commonly adopted in the industries are presented in Figure 2.1. As Table 2-1 outlines, conventional polishing techniques offer both advantages and drawbacks in their industrial application. Mechanical polishing (MP) is performed using abrasive tools such as grinding rods, felt wheels, sandpapers, and abrasive pastes [4, 19, 20]. This technique can effectively cover pores and cracks, producing a smooth and lustrous surface. However, one of MP's significant disadvantages is that the precision tolerance is comparatively high as this technique often relies on manual skill. Additionally, surface deformation leading to decreased corrosion resistance has frequently been observed owing to the contact force between the polishing tool and the workpiece [21, 22].

Table 2-1 Comparison of various polishing techniques by their mechanisms and application concerns (adapted from [9])

	Mechanical polishing	**Chemical polishing**	**Electrochemical polishing**	**Abrasive jet polishing**	**Laser polishing**
Mechanism	Mechanical abrasion	Chemical corrosion	Electrochemical corrosion	Erosion and shear	Remelt regeneration
Restrictions on geometry	Simple profile	Complex profile	Complex profile (limited to metal)	Complex profile	Complex profile
Ecological impact	Low	Low	Low	Medium	High
Energy consumption	Medium	Low	High	Medium	High

Furthermore, the conventional MP technique can hardly achieve homogenous treatment of complex-shaped components, such as three-dimensional (3D) printed parts [23]. The surface uniformity could be improved by chemical or electrochemical polishing methods as the whole workpiece is processed in an aqueous solution. Chemical polishing (CP) employs a chemical dissolution reaction to reduce the surface roughness of the workpiece. It has been extensively used in semiconductor and modern additive manufacturing (AM) fields [2, 24-26]. Highly concentrated hydrofluoric acid (HF), nitric acid (HNO_3), or hydrogen peroxide (H_2O_2) is often utilized for the CP process.

Electrochemical polishing (EP), otherwise known as electropolishing, anodic polishing, or electrolytic polishing, also requires a chemical solution. However, the main feature that distinguishes EP from CP is that the surface-smoothing effect occurs via an electrochemical anodic dissolution process. The dissolution takes place when the metallic sample is anodically biased (typically $U < 50$) in a temperature-controlled electrolyte solution [5]. Typically, a highly concentrated acidic solution, such as sulphuric acid (H_2SO_4), phosphoric acid (H_3PO_4), or a mixture of those depending on the materials, is selected as electrolyte [27]. Owing to its capability in polishing complex-shaped workpieces, the EP method has been broadly used in surface finish industries ranging from kitchen utensils to laboratory equipment, such as ultra-high vacuum components [28, 29]. Even though CP and EP provide various advantages, a crucial drawback must be considered in terms of practical usage. Since both CP and EP processes involve highly concentrated hazardous chemicals, operators are inevitably exposed to poisonous fume released from the chemical substances, which can be fatal. In addition, the disposal of waste chemicals after these processes in industrial-scale facilities cause severe environmental pollution [21, 30].

Hence, alternative surface finish techniques have been extensively investigated along with improving conventional methods to meet ever-increasing industrial demands and ecological requirements. One of the alternative polishing methods is abrasive jet polishing (AJP) which can be applied to polish the surfaces of complex-shaped objects and small areas [31]. AJP uses the impact of abrasive particles on the surface of the workpiece under pneumatic pressure. The polishing rate is directly controlled by jet pressure and the hardness of the

abrasive granule in use [32]. However, the critical problem of the AJP process is embedding of the abrasive particle combined with ploughing grooves which results in fatigue cracks on the workpiece surface [33-35]. Another alternative polishing method is laser polishing, which is based on the melting and resolidification (remelting) of a thin layer on the substrate's surface [36]. Even though laser polishing has many advantages, numerous challenges exist for industrial application, such as high equipment costs and potential thermal damages [37, 38]. Therefore, there is still need to develop a cost-effective and sustainable pretreatment method. Thus, plasma electrolytic polishing (PEP) can be as a potential candidate, presenting itself as an effective alternative to conventional methods.

2.2 Plasma-liquid interactions

PEP process entails the direct generation of plasma around the surface of an anodically polarized workpiece in a liquid environment. Prior to a deeper exploration of the PEP process, an introduction to the concept of plasma in a liquid environment is initially provided in this section. Plasma-liquid interactions are becoming increasingly important due to their usefulness in various applications such as environmental and wastewater remediation, material processing, and healthcare [39-41]. There are numerous ways that plasma can interact with liquids for different purposes, usually falling into three main categories and each method is briefly described in the subsequent sections.

2.2.1 Discharges directly in the liquid

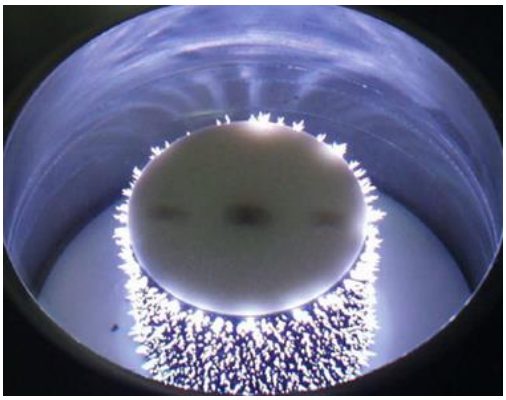

Figure 2.2 Visualization of direct water-based multichannel pulsed electrical discharges (source: [43]).

Similar to other plasmas, discharges produced directly in the liquid phase lead to numerous chemical and physical impacts. These include intense electrical fields, emission of UV radiation, high-pressure shock waves, and importantly, the creation of various chemically active species such as radicals (OH, H, and O) and molecular species (H_2O_2,H_2, and O_3) [42]. This process can be carried out using several different arrangements, such as point-plate, wire-cylinder, hole-plate, rod-rod, and ring-cylinder configurations. Discharges are generated directly in the liquid by applying high voltage pulses that range from a few to tens of kV, with pulse durations varying from nanoseconds to microseconds [43, 44]. Figure 2.2 presents an exemplary photograph of discharges occurring directly in the liquid, featuring multichannel discharges produced around a porous ceramic-coated electrode at an applied voltage of 28 kV in a NaCl water-based solution [43]. The generation of in-liquid plasma occurs directly in the liquid or within a transient gas phase, mainly consisting of the liquid with only slight contributions from dissolved gases such as nitrogen and oxygen [42, 45]. This leads to the production of reactive species interacting with the liquid medium that can be distinct from those in typical gaseous plasma. These reactive species interact with the medium on short

time-scales, giving rise to novel reaction mechanism. Presented below are some exemplary reactions that can occur during a direct electrical discharge in water [46]:

$$H_2O \rightarrow H^\bullet + HO^\bullet \quad 2.1$$

$$2H_2O \rightarrow H_3O^+ + e^- + OH^\bullet \quad 2.2$$

$$H^\bullet + O_2 \rightarrow HO_2^\bullet \quad 2.3$$

$$H^\bullet + H_2O_2 \rightarrow H_2O + OH^\bullet \quad 2.4$$

$$H^\bullet + HO_2^\bullet \rightarrow H_2O_2 \quad 2.5$$

$$e^- + HO^\bullet \rightarrow OH^- \quad 2.6$$

$$e^- + H + H_2O \rightarrow OH^- + H_2 \quad 2.7$$

$$e^- + H_2O_2 \rightarrow HO^\bullet + OH^- \quad 2.8$$

2.2.2 Externally-generated plasma with liquid

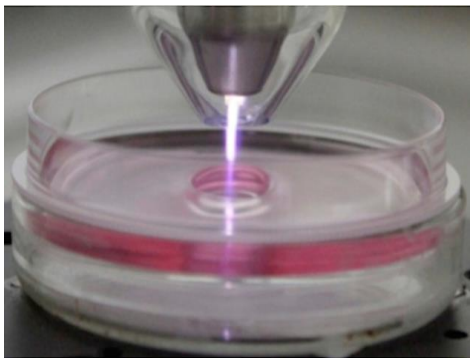

Figure 2.3 Application of liquid treatment using an argon plasma jet (kINPen) (adapted from [50])

Another approach to plasma-liquid interaction involves generating gas phase plasmas at atmospheric or even higher pressure in the presence of a liquid. There are two methods for achieving this. The first method utilizes a metal pin-to-liquid counter electrode configuration, which can function as either an anode or a cathode. Typical operating conditions include an electrode gap of a few mm, currents ranging from 5 to 50 mA, and voltages of approximately 1 kV [47]. A significant portion of the discharge power dissipates in the liquid, resulting in evaporation of the liquid [42]. The pin-water electrode process can generate corona or spark discharges in the gas phase, producing reactive species such as OH, NO, O, and HO_2 that interact with the liquid [48, 49]. A second method is to use an externally generated gas discharge commonly achieved by employing atmospheric pressure plasma jets (APPJs), which expose the liquid without direct electrical contact. A typical example of liquid treatment via an argon plasma jet (kINPen) is demonstrated in Figure 2.3. Depending on their configuration and the power source type, APPJs can be grouped into different categories. For instance, one type of APPJs operate as dielectric barrier discharges (DBD), using a pin electrode with power modulation between MHz to GHz, situated in a dielectric tube with an earthed outer ring configuration [50]. Another instance of APPJ operation is a radio-frequency (RF) type, operating within the frequency range of 1–100 MHz, with either inductive or capacitive coupled configuration [51, 52]. The reactive species produced by APPJs are convectively transported to the liquid by the gas flow through the jet [52]. This approach has been extensively studied in various fields such as medicine, wastewater purification, and plasma-polymerization [41, 53, 54].

2.2.3 Plasma in multiphase systems

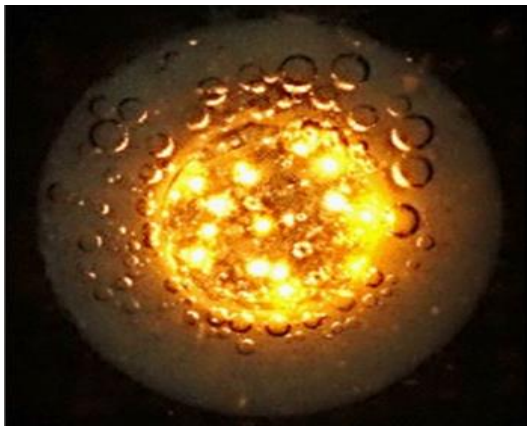

Figure 2.4 Visualization of discharges during the plasma electrolytic oxidation (PEO) process (taken from

One type of discharge in multiphase systems involves generating discharges in bubbles and foams, which are purposefully introduced into the liquid. When a sufficiently high voltage is applied, discharges can be created within the bubble prior to its detachment from the capillary [55]. The discharge typically presents as surface streamers progressing along the plasma-liquid interface [56]. The generation of plasma and the formation of reactive species predominantly takes place in the gas phase at the plasma-liquid interface, which can be utilized for water purification and medical treatment purposes [57, 58]. The gas temperatures and electron densities vary considerably, depending heavily on the gas composition within the bubble, liquid conductivity, discharge power, excitation voltage, and the size of the bubble [42]. Rather than intentionally injecting gas bubbles, discharges can be produced in the vapor phase through local heating of the electrolyte surrounding the active electrode. Intense local heating and electrolysis by pre-discharge currents can lead to the formation of a vapor phase within the liquid. Then, discharges are formed in the vapor phase with high voltage drop, leading to the surface treatment on metal electrodes [59, 60]. This type of discharge has a long-standing history in the development of current interrupters, where the current is obstructed due to the formation of the vapor bubbles around the active electrode [61]. The plasma electrolytic surface treatment process is widely utilized to enhance surface properties such as hardness, wear resistance, corrosion resistance, biocompatibility, and catalytic activity, overcoming limitations related to novel manufacturing techniques [40, 62-65]. In addition, the electrolytic plasma process has attracted considerable attention attributed to its environmentally friendly characteristics, ability to process materials of intricate shapes, and excellence in improving metallic surface properties. Figure 2.4 shows a photograph of the plasma electrolytic oxidation process, exemplifying plasma electrolytic surface treatment techniques. Although plasma electrolytic processes are similar to electrochemical ones, they require higher applied voltages (several hundred volts) and produce micro-discharges within the gaseous medium, facilitating the formation of intricate compounds on the metal electrode surface through plasma chemical reactions. These processes yield diverse surface modification effects, encompassing oxidation, dissolution, and saturation [66-68]. Plasma electrolytic polishing (PEP) is included in this category. Compared to other plasma electrolytic techniques, the PEP process is relatively novel, and its underlying mechanisms are not clearly understood. Hence, the subsequent sections will explore the current knowledge on the PEP process.

2.3 A comprehensive overview of plasma electrolytic polishing

PEP is a hybrid process of conventional electrolysis and the atmospheric plasma process, requiring a significantly higher electrical potential than conventional electrolysis [5, 69]. The PEP technology has gained significant attention, especially from surface-finishing industries, due to the considerable improvement of surface properties within a short time and its ecological benefits.

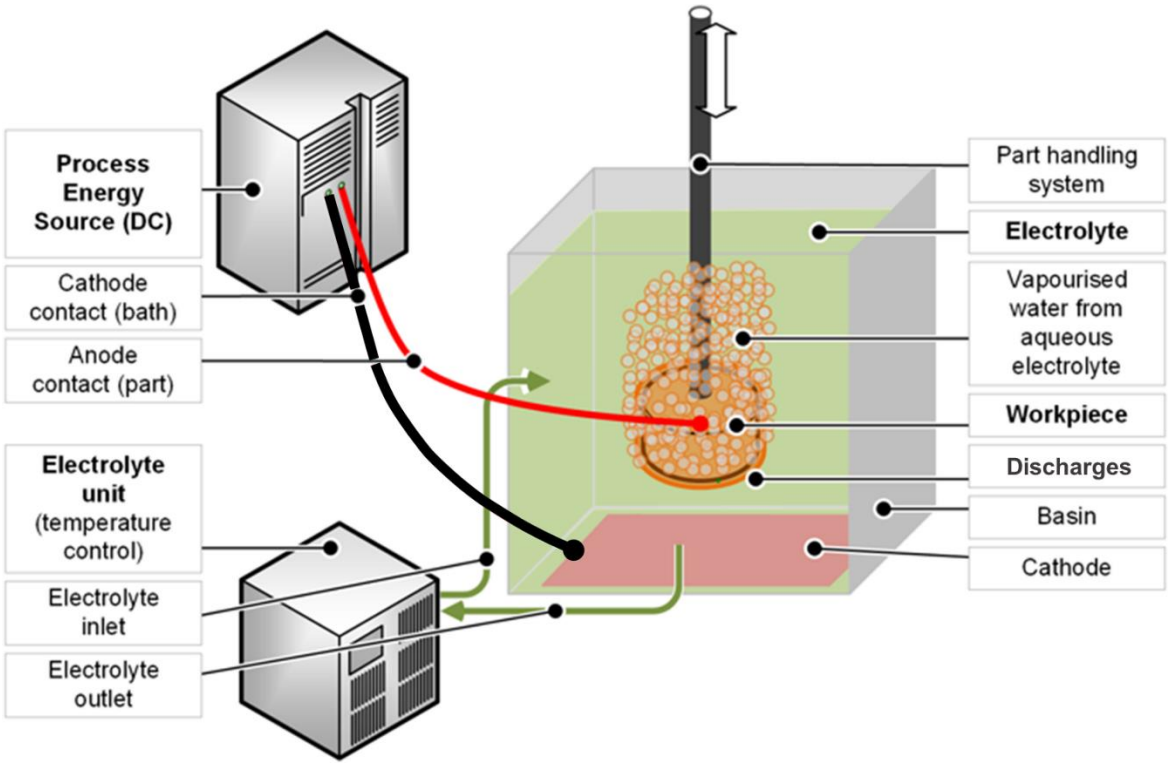

Figure 2.5 Schematic illustration of plasma electrolytic polishing apparatus (reprinted from [70]).

As presented in Figure 2.5, the basic configuration of the PEP process resembles conventional electropolishing; however, the PEP operates at a higher voltage regime (≥~100 V), which is required to build a gaseous layer accompanying the luminous discharges around the workpiece in an aqueous electrolyte solution comprised mainly of water. The physicochemical interaction on the anodic workpiece's surface leads to a surface-smoothing effect [69]. PEP was introduced in 1979 [71], and it has attracted significant and growing attention since it offers two major advantages compared with conventional polishing methods:

- Within a single-step process, a variety of modification functions can be accomplished in a short processing time, including deburring, surface smoothening, and surface cleaning.
- Environmental friendliness owing to its use of low-concentrated, non-toxic chemicals as electrolytes.

Furthermore, tools used in precision mechanics, particularly in the optical and medical technology industries, where no contamination is allowed, benefit from PEP because it

provides smooth and easy-to-clean surfaces while keeping high requirements on geometry definition and fitting accuracy [67]. Moreover, a crucial requirement for successful polishing results is to find material-specific process parameters such as process voltage, electrolyte composition, temperature, and process voltage. Hitherto, PEP's range of treatable materials has been ever growing to stainless-steel, copper, titanium, aluminum, and various types of alloys [8, 11, 72-74]. The PEP parameters for various materials are summarized in Table 2-2.

Table 2-2 Parameters of the PEP process for various materials

Materials	Electrolyte (wt%)	Temperature (°C)	Voltage (V)	Time (min)	[1]R_a (µm)	Ref.
Stainless-steel (1.4401)	$(NH_4)_2SO_4$	70	200 – 350	3	0.1	[72]
Stainless-steel (1.4021)	4 wt% $(NH_4)_2SO_4$	75	250	5	0.03	[11]
Al	10% NH_4Cl, 4% KCl, 3% $C_2H_2O_4$	60 – 80	300	0.5 – 4	0.02	[73]
Al alloy (EN AW 6082)	4% KCl, 2% $C_2H_2O_4$	80	320	1	0.25	[74]
CoCr alloy	4 wt% $(NH_4)_2SO_4$	75	450	8	0.02	[75]
WC-Co (10%)	10 wt% $(NH_4)_2SO_4$	70	350	0.25	0.13	[74]
Au	4% NH_4NO_3:NH_4Cl (1:3)	52 – 82	100	2	0.01	[76]
Pt	4% NH_4NO_3:NH_4Cl (1:3)	60	300	5 – 20	0.03	[76]
Cu alloy	10% NH_4Cl, 4% NH_4F, 1.5% $C_6H_{17}N_3O_7$	60 – 90	250 – 340	2		[77]

Despite the several benefits of the PEP process, many technical challenges exist, such as the limitations of bath size and electrical power proportional to the workpiece area. Thus, further modification of the PEP device is necessary. Accordingly, Cornelsen et al. [13] presented modified PEP equipment with a newly developed polishing head (cathode) to polish the inner pipe surface. In addition, Quitzke et al. [78] described a jet-based PEP device for localized surface treatment while overcoming the limited capability of the electrical power source as upscaling of the workpiece is constantly demanded. Besides these, various adaptations of the jet-PEP for difficult-to-treat workpiece shapes—too large, lengthy, or deep—are presented in Ref. [9]. In the subsequent sections, the typical features of the PEP process will be presented, encompassing electrical characteristics, discharge phenomena within the gaseous layer, and the suggested governing surface erosion mechanism.

[1] R_a is a value that represents the average roughness of a surface, defined as the arithmetical mean deviation of the assessed profile.

2.3.1 Current-voltage characteristics of PEP

A typical voltage-current characteristics of the PEP process are presented in Figure 2.6. Depending on the voltage, the PEP process encompasses several distinct regimes.

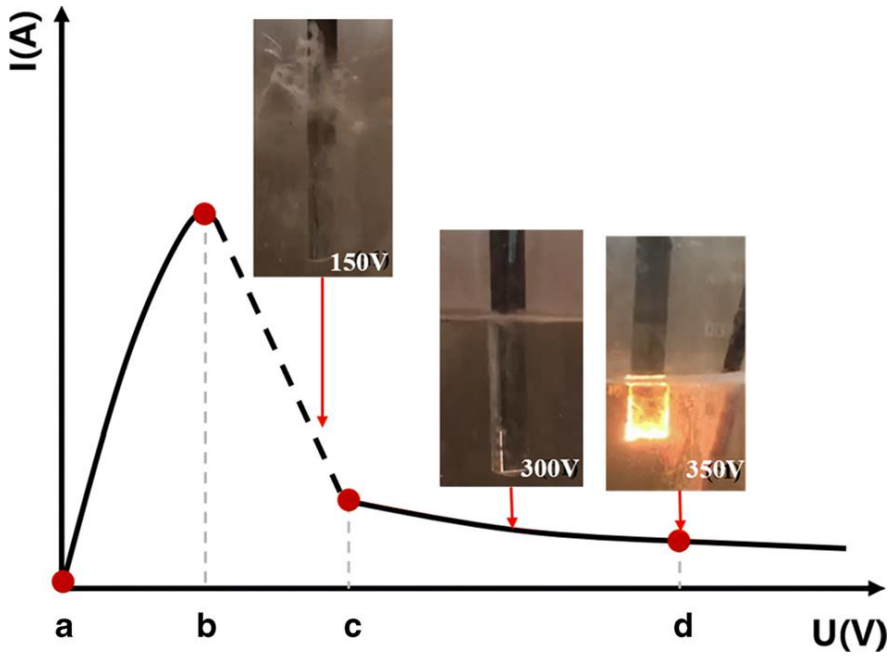

Figure 2.6 Voltage-current characteristics of the PEP process, accompanied by images representing each voltage regime (U_a to U_d), ranging from bubble formation to plasma development on the workpiece surface (taken from [9]).

- **Regime $U_a \rightarrow U_b$**

Initially, liquid electrolysis occurs with bubble generation at the workpiece as depicted in Figure 2.6. In this regime, the current density increases almost linearly, elevating the applied voltage, conforming to Ohm's law. When electrical power is supplied between the anode and cathode, hydrogen is generated at the cathode through the following reduction reaction [79]:

$$2H_2O + 2e^- \rightarrow H_2 + 2OH^- \qquad 2.9$$

Meanwhile, the electrolytic reactions, including the formation of oxygen gas and metal ions, take place near the anode [79]:

$$2H_2O \rightarrow O_2 + 4H^+ + 4e^- \qquad 2.10$$

$$M \rightarrow M^{2+} + 2e^- \qquad 2.11$$

"M" denotes a metal element

When the volume density of the bubble increases, the diameter of the oxygen gas bubble increases since they coalesce. According to Putra et al. [80], during the electro-flotation process, the diameter of the gas bubble formed on an anode increases from 33 µm to 46 µm when the voltage increases from 10 V to 30 V, respectively.

- **Regime $U_b \rightarrow U_c$**

At a critical voltage (V_2), a vapor gaseous envelope (VGE) is developed around the workpiece (anode) due to the evaporation of the electrolyte by Joule heating and accompanying electrical discharges as illustrated in Figure 2.6. The current density in this regime obtains a pulsed character due to the periodic creation and destruction of the VGE layer resulting in a current instability [15, 81, 82]. Further increasing the applied voltage to the second critical point (V_3) reduces oscillations of the current density. This is because a continuous VGE layer surrounds the workpiece, causing a significant current drop due to the VGE layer's low conductivity.

- **Regime $U_c \rightarrow U_d$**

During this regime, a stable VGE layer is formed over the workpiece due to augmented vaporization of the surrounding electrolyte involving intensified discharge emission. This regime is generally selected for plasma electrolytic surface treatment. Within this regime, several new species formed by collisions (e.g., ions and electrons collide with atoms/molecules) result in various surface modification effects, including oxidation or abrasion of the workpiece surface. During this stage, since the VGE attains the highest resistance, the majority of the electrical power is dissipated within the VGE layer. Thus, heat transfer occurs from the VGE to the anode and electrolyte. According to Belkin et al. [68], with the help of the stable VGE layer, the anode temperature can reach up to 1000 °C, which enables the saturation of metal surfaces with interstitial elements (e.g., nitrogen, carbon, and boron) for surface hardening.

2.3.2 Discharge mechanism during the plasma electrolysis

As mentioned in the preceding section, the PEP process involves the generation of electrical discharges in conjunction with the creation of the VGE layer. Thus, this section describes various discharge phenomena, including the principles of plasma generation, in order to discuss discharge mechanisms that occur during plasma electrolysis.

Generation of plasma

The electrical discharge denotes the passage of current through space. In order to ignite and sustain the discharge, it is imperative to generate enough charge carriers (electrons and ions). In neutral gases, free electrons are always available due to natural radiation, like cosmic radiation. By applying an electric field, those free electrons are accelerated. If the electrons possess kinetic energy greater than the ionization energy of the gas molecule, the neutral gas atoms or molecules, A, can be ionized by the collision of the electrons as follows:

$$e^- + A \rightarrow A^+ + 2e^- \qquad 2.12$$

By this process, two electrons are produced, which are accelerated by the electrical field, producing more electrons by ionizing the atoms, referred to as an "electron avalanche" [83] as schematically depicted in Figure 2.7. It is important to note that the electron avalanche cannot sustain the discharge solely. Therefore, another mechanism for generating electrons must be taken into account. The electrons produced during the avalanche process move toward the anode, while the ions move toward the cathode.

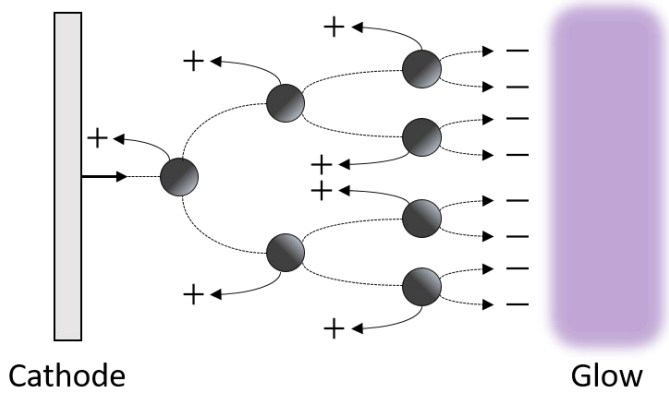

Figure 2.7 Schematic illustration of the electron avalanche effect (reproduced from [83]).

When an ion hits the cathode surface with enough energy to overcome the electrode material's workfunction, additional electrons are released from the cathode surface, a process known as a *secondary electron emission*. The efficiency of the secondary electron emission is denoted as *secondary electron yield*, γ which can be described as:

$$\gamma = \frac{number\ of\ released\ electrons}{number\ of\ incident\ ions} \qquad 2.13$$

The secondary electron yield, γ is typically between 0.01 and 0.1 [84]. The creation of the charge carriers through the avalanche process is limited by the loss processes, such as three-body recombination, radiative recombination, and wall recombination, which allows for maintaining the system in equilibrium. When sufficient electron-ion pairs are generated by secondary electron emission and avalanche processes, the discharge between the electrodes can be ignited. The condition for the ignition voltage (U_{bd}) can be described by Paschen's law [84]:

$$U_{bd} = \frac{Bpd}{ln(Apd) - ln(ln(1+\gamma^{-1}))} \qquad 2.14$$

A and B are coefficients that depend on the type of gas, p is the pressure within the discharge volume, and d is the electrode spacing. Figure 2.8 shows the Paschen curve for the breakdown voltage for water vapor as a function of pressure-distance (pd), which obtains a noticeable minimum breakdown voltage. The coefficients A and B are taken from Ref. [84]. On the left side of the minimum, the number of atoms is too low for the collisions. Meanwhile, on the right side of the minimum, the energy is not sufficiently gained for the ionization due to the shortened mean free path. This situation can be compensated by applying higher voltage [83]. Note that this law concerns the ignition of a DC discharge between two parallel electrodes with the inter-electrode distance, d. However, it might be differently applied in plasma electrolysis systems.

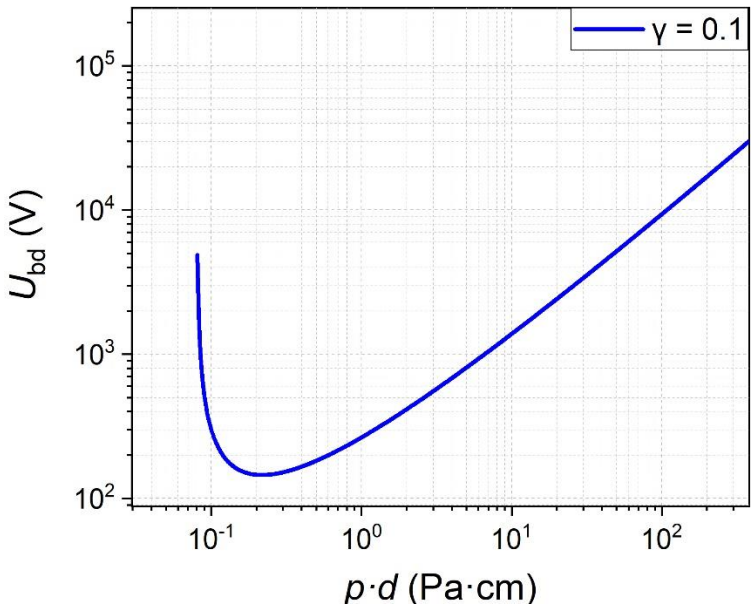

Figure 2.8 Paschen curve for water vapor. The calculation was performed according to Equation 2.14 using the constants A = 0.1 (Pa·cm)$^{-1}$, B = 2.2 V·(Pa·cm)$^{-1}$, and γ = 0.1.

When the PEP process begins, the workpiece is heated and the vapor layer surrounds it. Then, the interface between the liquid electrolyte and vapor layer acts as a virtual counter electrode during the PEP process. Accordingly, the inter-electrode distance, d, for the PEP process can be the thickness of the gaseous layer, usually a few tens of micrometers [15, 85]. With pressure (p) and distance (d) values, the electrical breakdown can be approximated to a few hundred volts according to the Paschen curve in Figure 2.8. Despite the fact that discharge can be ignited around the surface of the workpiece in pure water, the surface erosion effect does not usually occur for the PEP process. For a successful anodic dissolution, it is vital to select a suitable electrolyte composition, concentration as well as its temperature. Thus, the surface erosion induced by the PEP process cannot be solely explained by the generation of discharges, but it needs to be accompanied by electrochemical interactions as well.

Discharge phenomena during the PEP process

Visual representations in Figure 2.9(a) - (c) capture the anodic workpiece during the PEP process for diverse materials. A consistent observation in these images is the anodic workpiece being surrounded by a gaseous layer with visible luminous discharges. This luminous phenomenon was first described in 1844 by French scientists, Fizeau and Foucault from their experiment about the electrolytic decomposition of water with Pt wires [86]. Later, in the middle of the last century, Kellogg [87] investigated a phenomenon of a gaseous envelope surrounding the anode electrode at a critical voltage (45–50 V) during the electrolysis in molten salt, which was termed the *"aqueous anode effect"*.

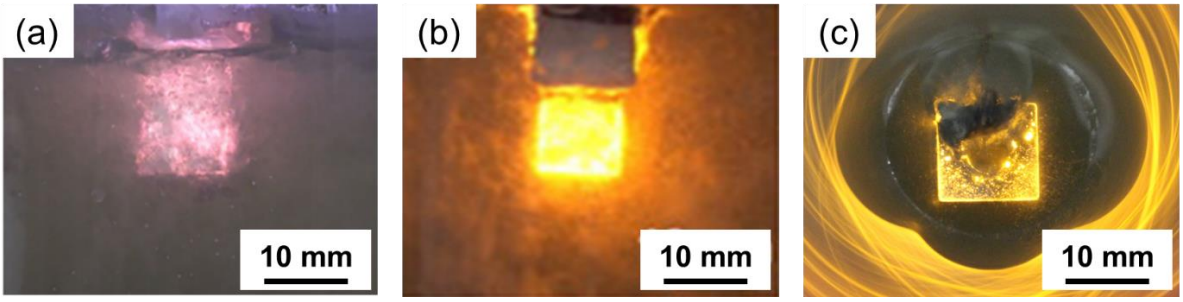

Figure 2.9 Photographs of the anode workpiece under the PEP process for varied materials including: (a) AISI 316 stainless steel [14]) , (b) Inconel 718 Ni-based superalloy [88], and (c) WC-Co-based cemented carbide [89].

In 1961, Hickling et al. [90] observed the glowing phenomenon through a vapor film on the Pt anode immersed in ammonia electrolyte. They termed the glowing phenomenon “contact glow discharge electrolysis (CDGE).” In addition, they suggested a mechanism to explain why a higher yield of hydrogen peroxide is obtained than the predicted amount by Faraday's law [90, 91].

However, as can be seen in Figure 2.9(c), the PEP does not appear to be a glow discharge, typically characterized by a uniformly glowing column. Figure 2.10 illustrates a typical relationship between the discharge voltage and discharge current across a low pressure DC discharge.

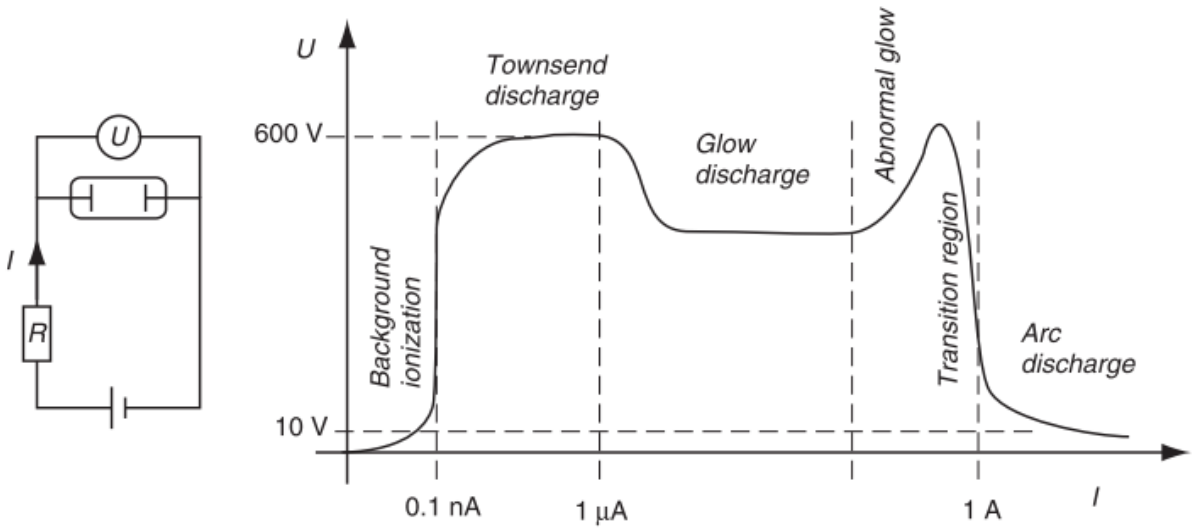

Figure 2.10 Gas discharge circuit (left) and its corresponding I-V characteristics (right) (reprinted from [92]).

Several discharge regimes can be identified depending on the (1) gas pressure, (2) nature of the working gas, (3) applied voltage, (4) electrode gap, and (5) electrode configuration. Even though discharges surrounding the workpiece are observed in the liquid electrolyte during the PEP process, they exhibit characteristics similar to those in typical low-pressure gas discharges, due to the presence of a gaseous envelope. The low-pressure gas discharges can be classified into four types and summarized as follows [92, 93]:

- **Townsend discharge** is characterized by fairly small currents (up to ~10^{-6} A), and it is not luminous due to the low electron density. Moreover, the discharge is not self-sustaining, as it does not entirely produce electrons on its own but requires external assistance to produce electrons, either from a negative electrode or from the gas itself.
- **Glow discharge** is a luminous low pressure discharge used in a wide range of practical applications such as analytical chemistry, microelectronic fabrication, lasers, and lamps. It is operated under low pressure (several mbar) at a relatively high voltage (~1 kV) and low current (~10^{-2} A). In this regime, the discharges become self-sustained due to the generation of secondary electrons, and the sustaining voltage is generally less than the breakdown voltage.
- **Spark discharge** is non-self-sustaining in the transient regime before the stable arc discharge. At atmospheric-pressure, the distance at which spark occurs is called the spark distance. A typical spark distance for air is approximately 200 mm at 100 kV.
- **Arc discharge** features intense light emission with low voltage (~50 V) and high current (~100 A), leading to thermionic emission owing to the heating of the cathode. Unlike the Townsend or glow discharges, the electrons produced by thermionic or field emission supply a sufficiently high electron current from the cathode approximately equal to the discharge current.

Concerning the various low-pressure gas discharges mentioned above, the PEP process could be within the spark discharge regime. The PEP process generally occurs within a voltage of ~100–400 V and a current of a few amperes involving short-lived individual discharges in the gaseous layer around the anodic workpiece. Even though the highly resistive gaseous layer separates the metallic surface from the liquid electrolyte, the electrical conductivity of the gaseous layer can be attributed to the ionized charged species resulting from the discharge activity under a sufficiently high electrical field. The surface flattening effect during the PEP process occurs through the combination of electrochemical and plasma–surface interaction with the ionized species; however, the exact mechanism of the role of discharge is still unclear. The next section describes the suggested mechanisms for the PEP process.

2.3.3 Polishing mechanisms

Figure 2.11 shows the surface roughness (R_a) of stainless-steel (AISI 304) from Danilov et al. [11]. The PEP was performed on these workpieces from 1 min to 5 min with an electrolyte of 5 wt% ammonium sulfate ($(NH_4)_2SO_4$). The surface roughness of the workpieces is gradually reduced from 0.14 µm to 0.05 µm as the treatment duration is prolonged from 1 min to 5 min, respectively. A rapid reduction in roughness value is observed at the beginning of the process, and then the reduction becomes less significant over time. Others have also observed a non-linear relationship between roughness (R_a) and PEP treatment time (t), which can be described as follows [10, 11]:

$$R_a = R_{a0} \cdot exp(-k \cdot t) + R_{a,min} \qquad 2.15$$

where R_{a0} is an initial roughness, k is a constant depending on the material properties and the polishing condition, and $R_{a,min}$ is the minimal achievable surface roughness. As the treatment

time is prolonged, the roughness value decays exponentially, which can be attributed to two factors.

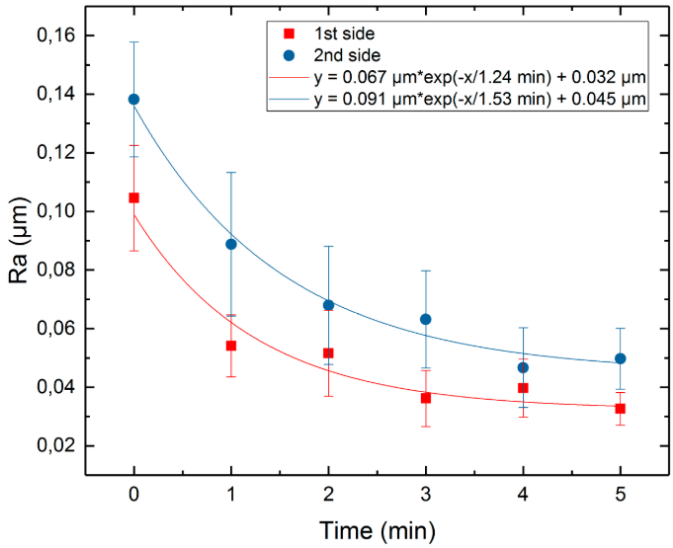

Figure 2.11 Surface roughness values of stainless-steel (AISI 304) workpieces before and after the PEP process measured by AFM (reprinted from [11]).

First, the polishing rate is higher at surface protrusions, so these are rapidly removed in the beginning. Consequently, the surface becomes progressively flatter, and the polishing rate reduces [15, 94]. Secondly, as the PEP process progresses, the gas layer thickness expands around the workpiece since the surrounding electrolyte temperature rises, reducing current density with a diminished polishing rate as a result of reduced electrochemical dissolution [11]. Including treatment time, the following factors influence material removal rate and surface properties: applied voltage, electrode distance, and electrolyte properties, such as concentration, temperature, and composition [9, 15]. Although various factors mentioned above affect the surface of the material during the PEP treatment, the exact mechanism on the surface of the anodic workpiece and the discharges during the PEP process remains unclear. Therefore, many research groups have devoted themselves to describing the surface-smoothing effect mechanism during the PEP process. The mechanisms of the PEP process are mainly explained by two factors (main influencing factors): material melting by the high-temperature involving discharges or electrochemical dissolution. Vaňa et al. [95] investigated PEP's effects on stainless-steel surfaces. They explained that the reduction of the surface roughness occurs as discharges melt initially where the thickness of the ionized water-steam film is thin, as depicted in Figure 2.12. The protrusion marked as h_1 is eroded more rapidly than h_2 since each discharge removes an equal amount of material ($S_1 = S_2$). Therefore, the surface roughness removal rate gradually decreases as surface peaks are removed.

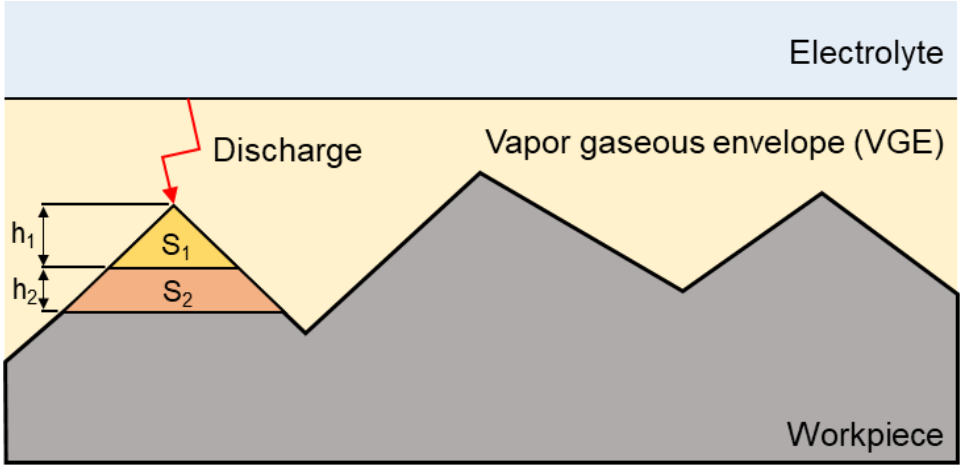

Figure 2.12 Schematic diagram of the PEP process by Vaňa et al. (adapted from [95]).

Wang et al. [96] and Cornelsen et al. [13] adopted a streamer to elucidate the polishing mechanism on the stainless-steel workpieces, as illustrated in Figure 2.13. The steps preceding the occurrence of streamer discharges, which lead to material removal, are outlined as follows:

(1) Primary electron avalanche:

Under the high electric field, an initial electron avalanche takes place as detailed in Section 2.3.2. As illustrated in Figure 2.13(a), the avalanche head is formed by electrons that move quickly, while the avalanche tail is formed by ions that remain nearly stationary owing to the lower mass of the electron compared to the ion.

(2) Secondary electron avalanche:

During the primary electron avalanche, a large number of photons are also emitted due to the recombination process, which induces a second electron avalanche near the primary one, as shown in Figure 2.13(b) and (c).

(3) Streamer formation:

Electrons of the secondary avalanches are attracted to the trail of the primary avalanche owing to the electric field distortions; thus, a streamer is created, as illustrated in Figure 2.13(d).

(4) Formation of plasma channel and material removal:

Subsequently, a plasma channel is formed between electrodes as depicted in Figure 2.13(e), a result of the streamer propagation accompanied by significantly increased current flow. Finally, material removal occurs, involving a gas explosion, and the plasma channel collapses.

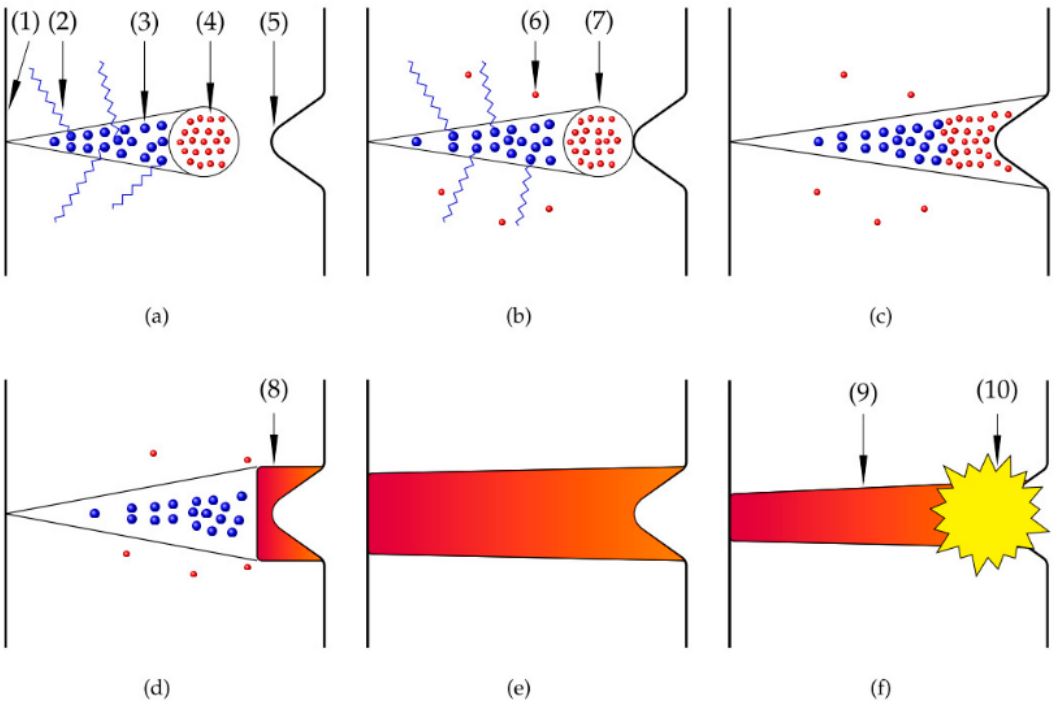

Figure 2.13 Schematic illustration of the formation of a streamer discharge. (1) Electrolyte, (2) photoionization, (3) ions, (4) electrons, (5) workpiece surface, (6) secondary electrons, (7) avalanche head, (8) the streamer, (9) plasma channel, and (10) a gas explosion (reprinted from [13])

Conversely, Kalenchukova et al. [97] suggested that the polishing effect is derived from electrochemical dissolution instead of surface melting. According to them, the protruded part on the anode surface has a higher current density than the concaved part since it has a shorter distance to the steam-gas shell. Therefore, the electrochemical dissolution removes the protruded peak quicker so that surface flattens. Meanwhile, Yerokhin et al. [12] investigated the transition from normal electrolysis to plasma electrolysis on the anodic stainless-steel surface. They elucidated that the mass and charge transfer during PEP is mainly governed by the electrochemical reactions rather than the electrolyte evaporation and associated boiling. Recently, Zhou et al. [72] described the surface-smoothing mechanism of the PEP with a repetitively occurring 2-step process of electrochemical reaction and electrical discharge, correlated to the fluctuation of the VGE layer. They conclude that the VGE instability accompanying the current oscillation fundamentally affects the PEP process, producing constant contact between the electrolyte and the workpiece. The electrochemical dissolution and adsorption occur when the electrolyte directly contacts the workpiece surface. Subsequently, when the VGE layer formed, separating the contact between the workpiece and electrolyte, the high-temperature melting and shock waves generated from collapsing bubbles might play a role in the removal of products adsorbed on the workpiece surface. The new surface is then exposed, and these processes are repeated, gradually reducing the surface roughness. In addition, they found that applying a high voltage (exceeding 400 V) facilitates generating a thick and continuous VGE layer; however, it deteriorates the polishing effect owing to the lack of an electrochemical reaction that reduces the contact between the electrolyte and the workpiece surface. Based on their findings, the crucial function of the VGE layer regarding the surface polishing effect is to generate a shock wave upon its collapse,

thereby aiding the removal of the adsorbed layer, revealing a fresh surface, and enhancing subsequent polishing reactions rather than inducing melting due to high temperatures.

The mechanisms behind the polishing effect on material surfaces during PEP, as proposed by various researchers, have been discussed above and it is still a subject of intense research. In light of this, this thesis aims to delve deeper into the polishing mechanism, employing various surface characterization techniques and process diagnostic methods. Additionally, a secondary objective of this research is to demonstrate the adaptability of PEP technology to expand the horizons of PEP technology. This includes exploring its potential in novel applications such as surface cleaning of WC-Co based cemented carbide and the surface finishing of 3D-printed components, underscoring its technical versatility.

3 Experimental details on surface and process diagnostics

In this thesis, a variety of surface characterization and process diagnostic techniques are employed to assess the influence of the PEP process on workpiece surfaces and to understand the underlying mechanisms during the PEP process. Further experimental specifics, related to each chapter such as PEP parameters, evaluations for distinct applications, and diagnostic methods, are entailed in the respective sections of subsequent chapters as follows:

Section 4.2 presents methods for hard coating deposition and tribological evaluation techniques used to validate the practical viability of the PEP process.

Section 5.2 details the experimental setup, including temperature measurement, calorimetric method for power evaluation, and synchronized electrical and high-speed camera measurements, as well as an overview of the modeling.

Section 6.2 outlines the methods for the metallic 3D printing, the process for pp thin films, and the characterization of the mist chamber, thereby demonstrating the potential applications of the PEP process.

The subsequent sections of this chapter aim to outline the primary surface characterization techniques consistently utilized throughout this thesis, thereby preventing repetitive descriptions in each chapter. Brief explanations of the operating principles of the relevant equipment are also provided. The primary objective of these surface characterization techniques is to investigate the influence of the PEP process on the morphology and elemental composition of metallic surfaces, thereby optimizing the process for specific applications.

3.1 X-ray photoelectron spectroscopy

X-ray photoelectron spectroscopy (XPS), also known as electron spectroscopy for chemical analysis (ESCA) is a surface-sensitive analytical technique used to study the elemental composition, chemical states, and electronic structure of materials. It is particularly useful for characterizing the surface chemistry of solid materials, as it provides information about the elements present, their oxidation states, and the nature of chemical bonds within a depth of few nanometers from the surface [98]. In XPS, the sample is irradiated with monochromatized X-rays, which cause the ejection of electrons from the inner shell orbitals of surface-adjacent atoms. Figure 3.1 depicts a schematic illustration of the photoelectron generation process. These ejected electrons, known as photoelectrons, are then detected and analyzed in terms of their kinetic energy, E_{k}. The kinetic energy of the photoelectrons can be used to determine the binding energy, E_{B} of the electrons in their original atomic orbitals, which is characteristic of the elements and their chemical states.

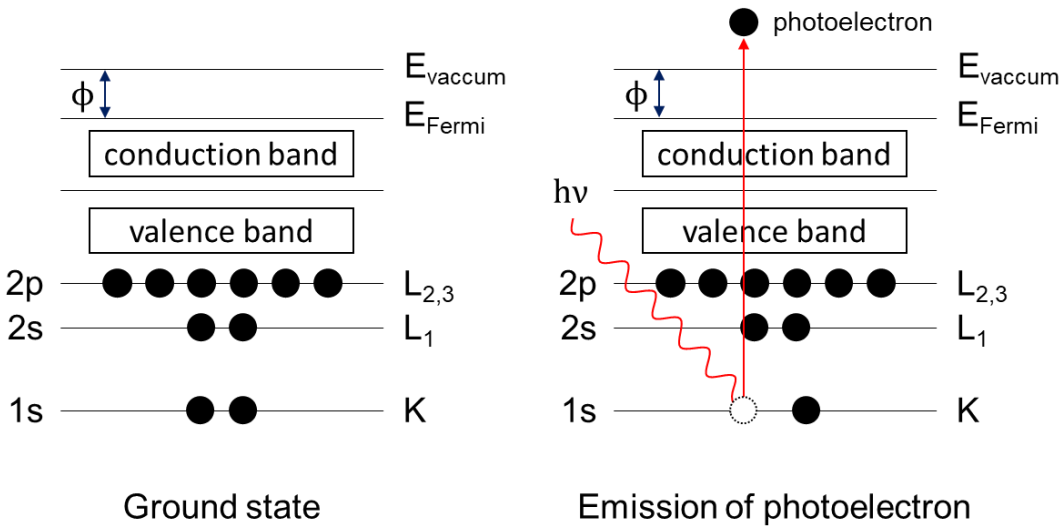

Figure 3.1 A schematic diagram of an undisturbed (left) and the shell electron energy of an atom subjected to XPS (right). The core electrons, bound to the atom, occupy the lowest energy states 1s, 2s, and 2p. Incident X-rays excite to an unbound state above the surface workfunction, ϕ (adapted from [98]).

The relationship between kinetic energy and binding energy can be given by:

$$E_k = h\nu - E_B - \phi \qquad 3.1$$

where E_k is measured kinetic energy of the emitted electron, $h\nu$ energy of the X-ray photon, E_B is electron binding energy of the atomic orbit, and ϕ is work function of the spectrometer. Given that $h\nu$ and ϕ are known values and E_k is measured, the E_B can be determined accordingly. This creates a spectrum which is represented as the intensity of the signal, *i.e.* the count rate, over the binding energy of the photoelectrons [98]. Each element or each atomic orbital from which the core electron has been removed can be assigned characteristic binding energies; therefore, XPS can be used to identify the binding state and to determine the concentration of the elements on the surface [99].

In this study, the surface elemental composition was examined using XPS (Axis Ultra, Kratos) with an Al Kα X-ray source at 1486.6 eV (*P* = 225 W) before and after surface cleaning by an Ar ion source (Minibeam 2, Kratos) at an energy of 4.5 keV. The aliphatic component of the C1s peak (285.0 eV) was used to calibrate the energy scale. Surface depth profiling was conducted by other XPS equipment (Axis Supra, Kratos) with an Al Kα X-ray source at 1486.6 eV (*P* = 150 W). The depth profiling spectra were obtained by alternating cycles of spectral acquisition of the sample surface followed by Ar_{500}^{+} cluster source (Gas Cluster Ion Source (GCIS) Minibeam 6, Kratos) set an energy of 20 keV, an etched area of 1.9 × 1.9 mm^2, 30 s etch time for 20 cycles. Finally, data acquisition and processing were performed using ESCApe™ software version 1.2.0.1325 (Kratos) and CasaXPS 2.3.15 software (Casa Software, Ltd), respectively.

3.2 White light interferometry

Measurement principle

White light interferometry (WLI), a form of optical profilometry, is a non-contact measurement technique commonly employed for topographical observations due to its rapid measurements without causing damage or contamination [100, 101]. WLI works by using the interference patterns created by the superposition of light waves to measure the topography of a surface.

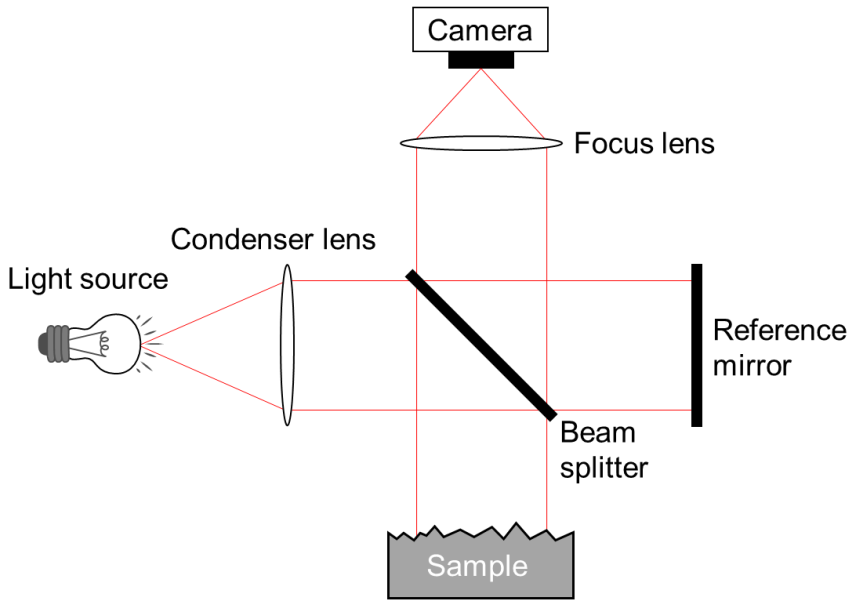

Figure 3.2 Schematic diagram of white light interferometer (adapted from [102]).

Figure 3.2 presents a schematic diagram illustrating the components and setup of a WLI. In principle, a WLI is a Michelson interferometer that employs a broadband light source. Common light sources used in WLIs include light-emitting diodes (LEDs), incandescent lamps, and superluminescent diodes (SLDs) [102]. The white light is directed towards a beam splitter, which divides the light into two separate beams. One beam, called the reference beam, reflects off a reference mirror with a known position. The other beam, called the sample beam, reflects off the surface being measured. Constructive interference occurs when the waves are in phase, while destructive interference emerges when they are out of phase. Utilizing the low coherence property of a white light source enables the acquisition of diffraction patterns with reduced noise in comparison to monochromatic light. Typically, a CCD camera is used at the interferometer's output, and the light intensity for each pixel on the camera provides information about the geometric shape of the measured surface or object.

In this study, WLI (Profilm 3D, FILMETRICS) is employed to measure the surface roughness of the probe samples. The 3D-surface profile was obtained using a X20 interferometry objective (MUL40201, Nikon) in a vertical scanning interferometry (VSI) mode (back scan = 20 µm and scan length = 90 µm). The obtained data was processed and evaluated by a Profilm 3D Image Acquisition, Visualization, and Analysis Software, version 3.2.3.1 (FILMETRICS), from 4 measurement points (n = 4) for each sample.

Surface roughness parameters

A suitable representation of measured surface topographies requires the careful selection of roughness parameters. Over time, the development of roughness measurement techniques has given rise to numerous parameters aimed at describing different aspects of surface topographies. This study employs $R_a$value, arithmetical mean height, a parameter commonly adopted in industrial applications. R_a is calculated from the sum of all measured height values $Z(x)$ within a defined individual measuring length (l), as depicted in the Figure 3.2. The mathematical formula for determining R_a is provided in Equation 3.2:

$$R_a = \frac{1}{l}\int_0^l |Z(x)|dx \qquad 3.2$$

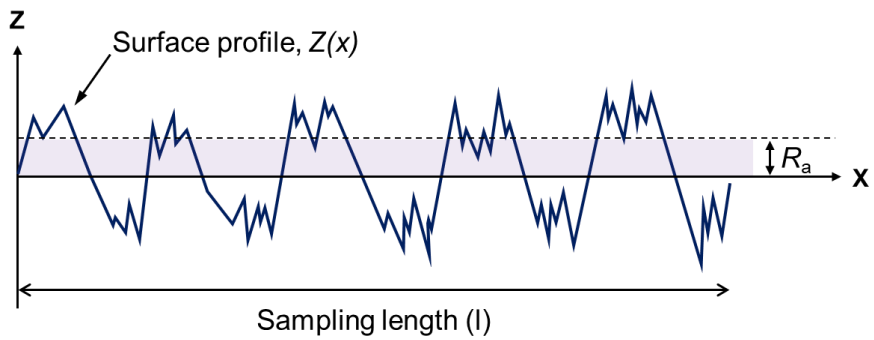

Figure 3.3 Visual depiction of the arithmetic mean height of a line, R_a.

The R_a value is usually expressed in micrometers (µm) and a smaller R_a value signifies a smoother surface. It should be noted that R_a, a single-value average measure, does not convey information about the distribution of surface peaks and valleys. Depending on the application, other parameters such as R_z (Maximum height of assessed profile), R_q (root mean square deviation of the assessed profile), and R_t (total height of the assessed profile) can be alternatively employed. Detailed description of these parameters can be found in Ref. [103, 104]. In addition, surface roughness can also be expressed as an areal roughness parameter, S_a, which denotes the mean arithmetic height in a 3D space and is calculated by Equation 3.3. S_a can be perceived as an expansion of R_a (line roughness parameter) to an area A, as depicted in Figure 3.4.

$$S_a = \frac{1}{A}\int_0^{l_x}\int_0^{l_y} |Z(x,y)|dxdy \qquad 3.3$$

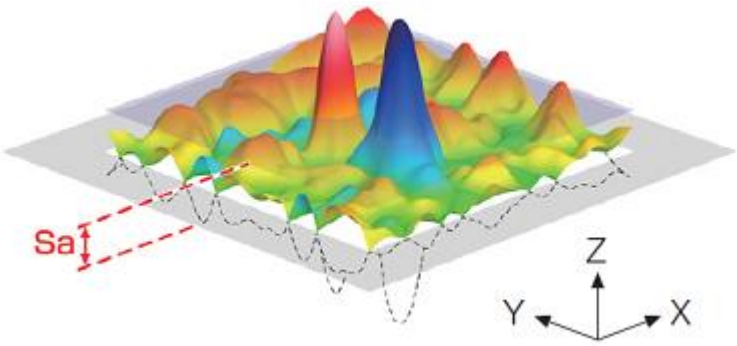

Figure 3.4 Visual representation of areal arithmetical mean height, S_a (reprinted from [105].

The S_a parameter addresses some of the shortcomings of R_a, which does not sensitively represent the surface texture or the dispersion of peaks and valleys. By considering the entire measured area rather than just a single profile line, S_a is able to accurately represent the overall surface characteristics, including variations in texture across the entire measured area. Consequently, S_a provides a more robust and representative analysis when examining surfaces with intricate textures or surfaces where the directionality of the features is of importance.

Characterization of the cutting edge using WLI

WLI serves as a useful instrument in evaluating not only surface roughness but also edge sharpness. The sharpness of tools, encompassing drills and endmills, within the machining sector holds considerable significance as it directly influences work efficiency and the service life of the tools. In the present study, the PEP is employed for the tool pretreatment stage, necessitating the effective removal of surface contaminants while preserving the tool's geometric definition. However, given that the PEP functions as a material erosion process, the cutting edge exhibits noticeable rounding subsequent to the PEP procedure. To address this issue, the determination of edge sharpness ought to proceed concurrently with the modification of the PEP experimental parameters in order to minimize edge radius erosion. Consequently, the WLI was employed to obtain a three-dimensional profile of the tool edge, after which the data was analyzed using a Gaussian-fitted circle method proposed by Wyen et al. [106] to quantify the edge radius. As shown in Figure 3.5(a), the wedged tool's cutting-edge profile was first characterized by using WLI (Profilm 3D, FILMETRICS), using an X20 interferometry objective (MUL40201, Nikon) in a VSI mode (back scan = 100 µm and scan length = 110 µm).

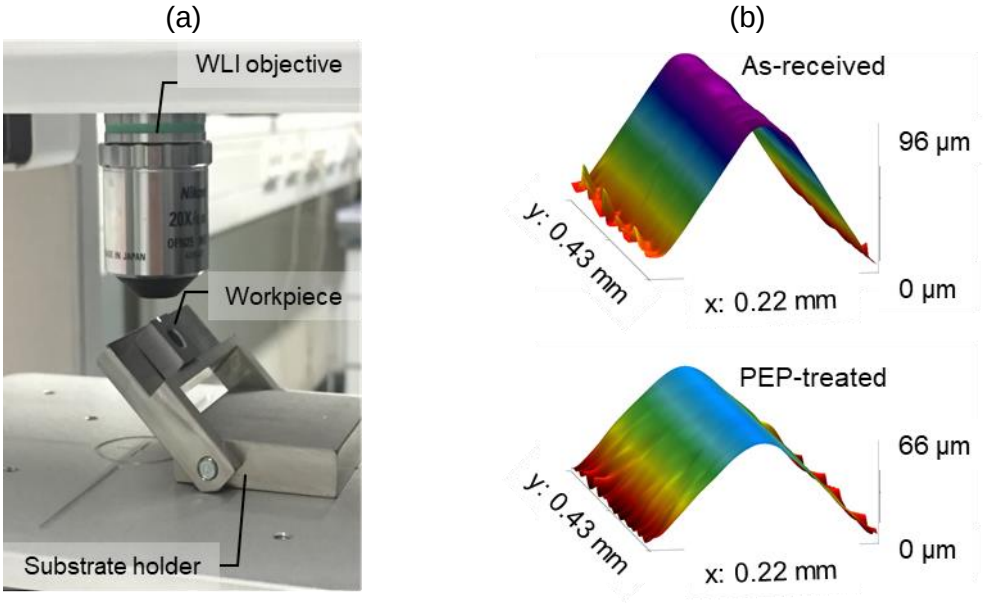

Figure 3.5 (a) photograph of WLI equipment for the tool cutting edge measurement. (b) 3D profiles of cutting edge on as-received (upper) and PEP-treated inserts (bottom) measured by WLI.

Figure 3.5(b) illustrates typical cutting-edge profiles before and after a PEP treatment. After a PEP treatment, the cutting edge was noticeably rounded. A fitting procedure based on fitting a circle to the tool flanks as described in Ref. [106] was applied to the 3D edge profile data acquired from WLI to define the edge sharpness.

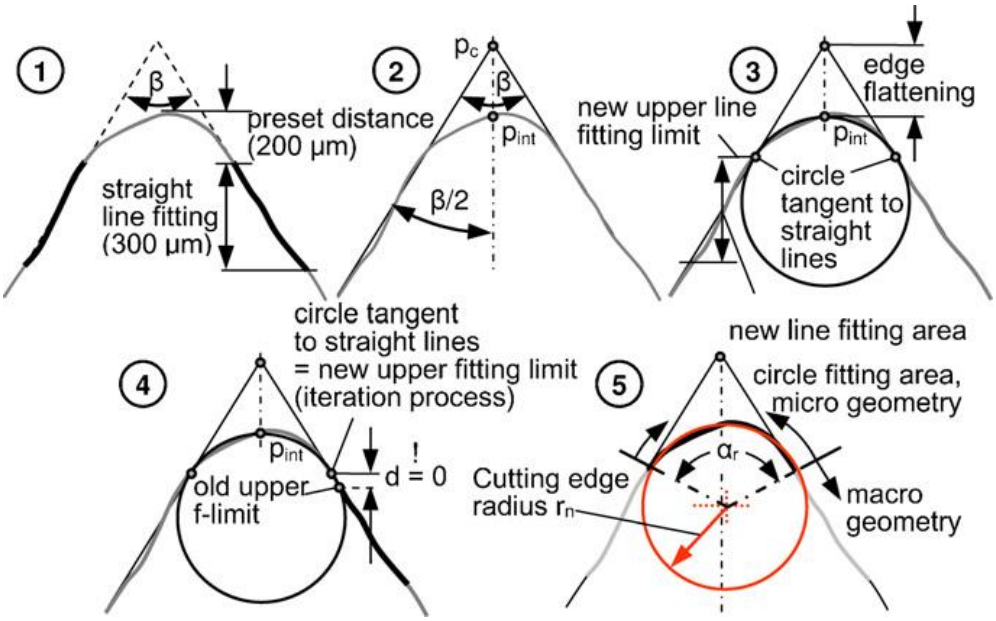

Figure 3.6 Gaussian fitted circle process to define a cutting-edge radius (Reprinted from Wyen et al. [106]).

The edge radius value is obtained through the following procedure described in Figure 3.6: (1) a least squares straight line is fitted through the tool's flank and clearance face. (2) The least

squares straight lines intersect in point p_c, and the angle inscribed by the straight lines is defined as wedge angle β. The bisector of the wedged angle determines the intersection with the cutting-edge profile point p_{int}. (3) A circle tangent to both straight lines and intersects P_{int} is drawn. (4) Procedures (2) and (3) are repeated to determine the optimum fit. (5) The fitted edge radius indicates the cutting-edge sharpness. The obtained data were processed and evaluated by Gwyddion software (ver. 2.56) and MATLAB 2019.

3.3 Scanning electron microscopy

Morphological analysis

Scanning electron microscopy (SEM) is one of the most widely used imaging technique for analyzing the surface structure and composition of various materials at the micro- and nanometer scales [107]. SEM uses a focused beam of electrons instead of light, as in conventional optical microscopy, to interact with the sample and generate high-resolution images. In SEM, an electron beam is generated in an electron gun and then focused onto the sample using electromagnetic lenses. As the electrons interact with the sample, they generate various signals such as secondary electrons, backscattered electrons, and characteristic X-rays. These signals are collected and processed by detectors within the SEM to create detailed images of the sample surface.

In this study, the surface morphology of samples before and after the PEP process was examined using a SEM (JEOL JSM 7500F) at an acceleration voltage of 5 kV and a working distance between 6 and 8 mm. To enhance contrast, a low-angle backscattered electron (LABE) detector was utilized, which provided more element-sensitive surface data in comparison to the analysis of secondary electrons. It is important to note that factors such as sample topography, inclination, potential charging effects, or shadowing may also affect the intensity of the signal from the electrons when evaluating these images.

Elemental analysis

To investigate the elemental properties of the surface, energy dispersive X-ray (EDX) analysis was conducted. EDX is typically equipped to SEM instrument, operates by detecting and quantifying energies of emitted X-rays, which are unique to each element in a sample surface. The EDX detector gathers these X-rays, creating an energy spectrum with peaks representing each element's X-ray energies. Examining this spectrum allows for the determination and quantification of elements in the sample [108]. Here, surface composition of the specimens was assessed using an EDX system (Quantax 200, Bruker), using both point analysis and area mapping modes, with an applied acceleration voltage of 15 kV.

3.4 Fourier transform infrared spectroscopy

To ascertain whether the PEP process can serve as a pretreatment step for surface cleaning, it is imperative to develop a method for characterizing surface contamination. Considering that the majority of contamination from tool manufacturing comprises grinding oil and fine metallic powders, Fourier transform infrared spectroscopy (FTIR) presents a suitable analytical method for evaluating the remaining surface contamination on cemented carbide tools.

FTIR is a versatile material analytical technique, providing qualitative as well as quantitative information on the molecular structure of organic and inorganic compounds. This technique relies on the resonant interaction between infrared (IR) radiation and molecular vibrational states [109]. When IR radiation is applied to a sample, molecules selectively absorb specific wavelengths, altering the bond's vibrational energy. If the energy of the IR light matches with the energy needed for a molecular vibration, photons are absorbed. This produces an IR spectrum with distinct absorption bands, representing a molecular "fingerprint" that can be utilized to determine the sample's chemical structure. In the implementation of FTIR analysis, sample preparation stages are requisite. This typically involves: (1) mixing the pulverized sample homogeneously with potassium bromide (KBr) which is a background matrix, and then (2) applying high pressure to create a transparent pellet [110]. In this study, however, the sample preparation stage faces significant challenges due to the difficulty in pulverizing cemented carbide.

Hence, the attenuated total reflection (ATR)-FTIR technique is adopted to assess the residual contamination on the workpiece, as it circumvents the requirement for pellet preparation, thereby facilitating direct examination of the surface. The principle of ATR-FTIR is based on the measurement of changes in an internally reflected infrared (IR) beam as it interacts with a sample [111].

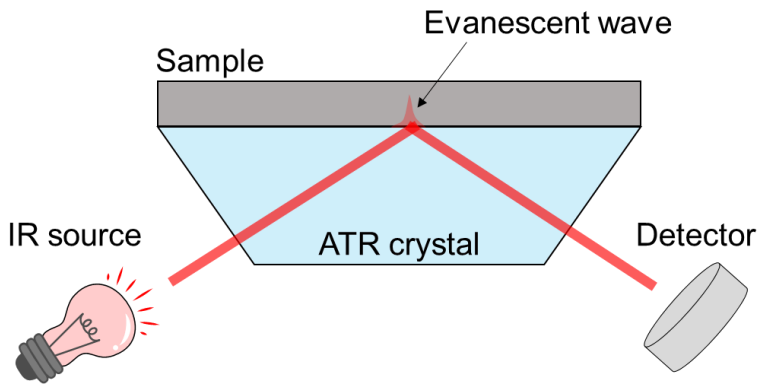

Figure 3.7 Schematic diagram of attenuated total reflectance Fourier transform infrared spectroscopy (ATR-FTIR) (adapted from [111]).

As depicted in Figure 3.7, the IR beam is directed onto an ATR crystal, such as diamond or Germanium that has a high refractive index (ranging from 2.4 to 4.0). This generates an internal reflection that produces evanescent waves, which penetrate a few µm into the sample. The evanescent waves interact with the sample, which is in contact with the crystal, across the crystal's surface. The reflected IR beam is then measured and analyzed to determine the composition of the sample. Therefore, the degree of contamination on the tool surface was analyzed by ATR-FTIR (Spectrum One, Perkin Elmer). The range of 4000 to 650 cm^{-1} was used to record the spectra, with a scanning resolution of 4 cm^{-1} and a number of 16 scans, employing a diamond attenuated total reflection (ATR) crystal.

3.5 Grazing incidence X-ray diffraction

The surface microstructure alterations caused by the PEP process were investigated using X-ray diffraction (XRD). The XRD is based on the interaction of X-rays with the atoms in a crystalline material and the constructive interference of scattered X-rays which generates a diffraction pattern. In a crystal lattice, X-rays are reflected by parallel lattice planes composed of periodically arranged atoms. The relationship between the crystal lattice plane spacing (d), the wavelength of the incident X-ray (λ), and the incident angle (θ) can be described by Bragg's law:

$$2d\,sin\,\theta = n\lambda \qquad 3.4$$

When the path difference between scattered X-rays is an integer multiple of the wavelength (λ), constructive interference occurs, and a diffraction peak is observed. By varying the angle (θ) and measuring the intensity of the scattered X-rays, a diffraction pattern can be obtained. The diffraction pattern (the positions and intensities of the peaks) serves as a "fingerprint" of the crystal structure of materials.

In this investigation, the specimen's crystalline structure was identified using grazing incidence X-ray diffraction (GIXRD; D8 Advance Diffractometer, Bruker) with a 1° grazing incident angle, allowing to obtain more surface-sensitive information than normal XRD mode. The scanning step was set as 0.02° with a 2θ scan between 20° and 80°. The crystallite size was determined by the TOPAS software (v5.0, Bruker). The software employs a model of the Double-Voigt approach to determine crystallite size [112, 113]. The crystallite size comprises Lorentzian and Gaussian component convolutions varying in *2θ* as a function of *1/cos(θ)* and *tan(θ)*, respectively. The crystallite size (ε) is estimated from the Scherrer equation:

$$\varepsilon = \frac{\lambda}{\beta_{FWHM}\,cos\,(\theta)} \qquad 3.5$$

where λ is the wavelength, θ the Bragg angle and β_{FWHM} is the full width at half maximum of the profile component related to size broadening.

3.6 Atomic force microscopy

The atomic force microscope (AFM), a high-resolution scanning probe microscopy technique, was used to examine the surface morphological changes resulting from the PEP process. This method provides comprehensive three-dimensional topographical information on a wide range of surfaces [114]. The basic principle of AFM is the detection of the bending of a cantilever as a response to external forces. As illustrated in Figure 3.6, an AFM equipment is mainly consisted of a sharp tip attached to a flexible cantilever, a laser and a photodetector. The AFM technique operates by scanning the sample's surface using the tip while maintaining the force between the tip and the surface at a constant level, regulated by a piezoelectric scanner. The probe tip is typically composed of Si or Si_3N_4 and has a curvature radius of only a few tens of nm. [115]. The laser focuses on the backside of the cantilever and reflects onto the position-sensitive photodetector.

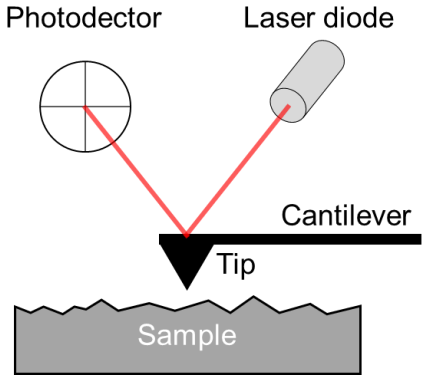

Figure 3.8 Schematic representation of the atomic force microscope (AFM) apparatus (adapted from [116]).

As the cantilever deflects, the position of the reflected beam shifts, and the photodetector transforms this change into an electrical signal which is used for surface imaging. The resolution of AFM is primarily determined by the sharpness of the probe tip, the mechanical properties of the sample, and the noise level of the instrument. For the lateral resolution, it is generally feasible to achieve values between 2 and 10 nm. With exceptionally sharp tips, these values can approach sub-nm dimensions. For vertical resolution, achieving sub-angstrom resolution is feasible, primarily influenced by the accuracy of the vertical scanner. The AFM can function in various modes, based on the particular application needs, with imaging modes generally classified into static (contact) and dynamic (non-contact) categories. The following are some notable AFM modes:

Contact mode

The contact mode of AFM involves mechanically bringing the probe into contact with the sample surface and maintaining a constant force. The probe is then scanned across the surface in a raster pattern, and an electronic feedback control is used to keep the resulting deflection constant by adjusting the z position. The force required to maintain the constant contact is measured, and this information is used to generate an image of the surface. However, this method can cause damage to soft surfaces due to the applied force.

Non-contact mode

In non-contact mode, the cantilever is oscillated (~400 kHz) near the surface of the sample without touching it. During the scanning process, the variation of interaction forces between the tip and sample cause changes in the resonance frequency and amplitude of oscillation of the cantilever. These changes in oscillation provide information about the topological information on the sample's surface. Non-contact AFM is particularly useful for measuring soft samples, as it avoids the tip or sample degradation effects that can occur when using contact AFM for numerous scans.

In this investigation, residual contamination on the samples may adhere to the AFM tip during scanning, potentially shortening its lifetime. To prevent this issue, non-contact mode AFM was employed using a diCP-II scanning probe microscope from Veeco Instruments to analyze the morphology of the PEP treated surfaces. Each tool sample was measured five times in different spots within a scanned area of 20 × 20 μm^2, and the obtained data were evaluated using the Gwyddion software (ver. 2.56).

4 Investigation of the PEP process for surface pretreatment of cemented tungsten carbide

In this chapter, the potential of the plasma electrolytic polishing (PEP) process as a surface pretreatment technique for cemented tungsten carbide with cobalt matrix (WC-Co) based cutting tools is explored, with the aim to broaden its range of applications. A comprehensive experimental investigation is presented, including a parameter study of the PEP process on WC-Co materials, supplemented by various surface and geometrical analyses, to assess the practicality of using PEP as a pretreatment process step. Furthermore, the applicability of the PEP process is demonstrated through industrial-level machining tests, where it is benchmarked against coated cutting tools produced using conventional methods, in order to verify its potential for direct integration into the commercial tool production chain. This research is part of the project "Ecological and Functional Optimized Pretreatment Chain for Plasma Coating of Complexly Shaped Cutting Tools (contract No. 33033/01) [117]", funded by the German Federal Environmental Foundation (Deutsche Bundesstiftung Umwelt).

4.1 Introduction

Throughout history, machining has been considered a vital shape-forming process in various industrial areas such as automotive, aerospace, energy production, and electronics. Consequently, the precision tool industry has extensively grown owing to the usage of difficult-to-cut materials and the enhancement of manufacturing productivity. According to a market report in 2022 from the German Machine Tool Builders Association (VDW - Verein Deutscher Werkzeugmaschinenfabriken e.V) [118], the world machine tool production from the year of 2003 to 2022 almost doubled from EUR 33.2 to 80.3 billion, as shown in Figure 4.1.

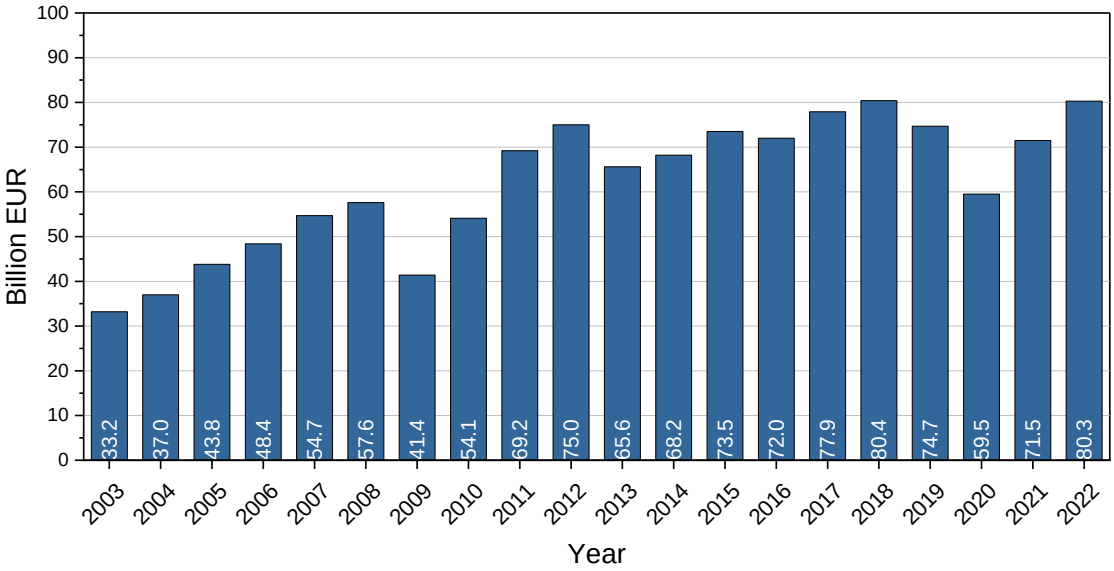

Figure 4.1 Trend in global machine tool production over the last 20 years sourced from the VDW Market Report 2022 ([118]).

Figure 4.2 Photographic illustration of the variety of scale, surface coatings, and geometric complexity of precision tools (Source: GÜHRING KG).

In addition, German domestic tool production occupies 13% of the world share, which is third place in 2022. Prerequisites for advanced machining tools are long service life, high-feed rate, and reduced lubricant consumption. Additionally, increased productivity, followed by improved product quality and process reliability to reduce manufacturing costs, has to be considered. It is essential to produce tools that can endure extreme machining circumstances to meet all the aforementioned demands. Among the various tool materials, cemented carbide is preferred by machining manufacturers and occupies more than half of the global market share owing to its outstanding toughness [119-121]. However, a significant vulnerability of cemented carbide tools is poor wear resistance against high mechanical and thermal loads, especially on cutting-edge surfaces. A hard coating is commonly deposited on the tool's surface to overcome this weakness. Notably, ~85% of the hard-cutting materials on the global market are coated with a hard coating layers [119]. In Figure 4.2, photographs of precision tools with varying scales, surface coatings, and geometric complexities currently available in the market are displayed. Since the appearance of hard refractory metal carbide and aluminum oxide coatings in the 1970s, the performance of cutting tools has been significantly improved in terms of wear resistance at high temperatures [122, 123]. Moreover, cemented carbide coatings are responsible for chemical inertness, oxidation stability, and, eventually, longer tool service life [124]. Transition metal-based nitride, oxide, or carbide is commonly adopted as the hard coating layer and deposited physical vapor deposition (PVD) method [119]. As one of the PVD techniques, DC magnetron sputtering (DCMS), a plasma-based coating technique, has been widely used in industrial hard coatings since it is capable of creating coatings with excellent adhesion, hardness, and corrosion resistance properties. Recently, TiAlSiN coating fabricated by the PVD has gained much attention for high-speed and dry-cutting applications because it obtains high hardness (~54 GPa) and superior thermal stability even at 900 °C [125-127]. Furthermore, in recent years, high power impulse magnetron sputtering (HiPIMS) has attracted attention for its capability to fabricate Ti-based hard coatings for commercial cutting tools, offering superior layer properties and extended tool service life [128-130]. Further details on the PVD method can be found in Section 4.2.2 Deposition of hard coatings. However, without a suitable tool surface cleaning process, the coated film cannot exhibit peak performance since the film might peel off during the machining process. In particular, residual contamination (e.g., grinding oil, polishing agent, and metallic particles) from tool production decreases adhesion between the hard coating layer and tool surface. Therefore, a coordinated and efficient cleaning technology is required before the coating process. Several pretreatment methods have been used for adhesion enhancement and surface texturing purposes, for example, water jets, chemical etching, ultrasonication, ion etching, and laser texturing [131-135]. In particular, tool manufacturers have frequently employed multi-chamber cleaning systems with proper washing agents. Nevertheless, the above methods have several disadvantages, such as poor

reproducibility, time-consuming, insufficient cleaning effect, and environmentally harmful substance emission.

Thus, the PEP process has the potential to fulfill all requirements; however, PEP treatment for carbide materials remains underexplored as a practical method. Most PEP research concentrates on surface smoothing applications, even though PEP technology is considered a promising eco-friendly and cost-effective alternative to conventional surface pretreatment methods. Consequently, this chapter is committed to presenting the development of the PEP process for surface pretreatment of WC-Co material, with a focus on its practical applicability.

4.2 Experimental details

This section contains the details of the experiments particular to this chapter, which include the PEP process as the surface pretreatment step, the method of hard coating deposition, and the assessment of the tribological performance of the coated tools.

4.2.1 Plasma electrolytic polishing for surface pretreatment

The PEP experimental configuration is represented by a photograph in Figure 4.3(a) and a schematic illustration in Figure 4.3(b).

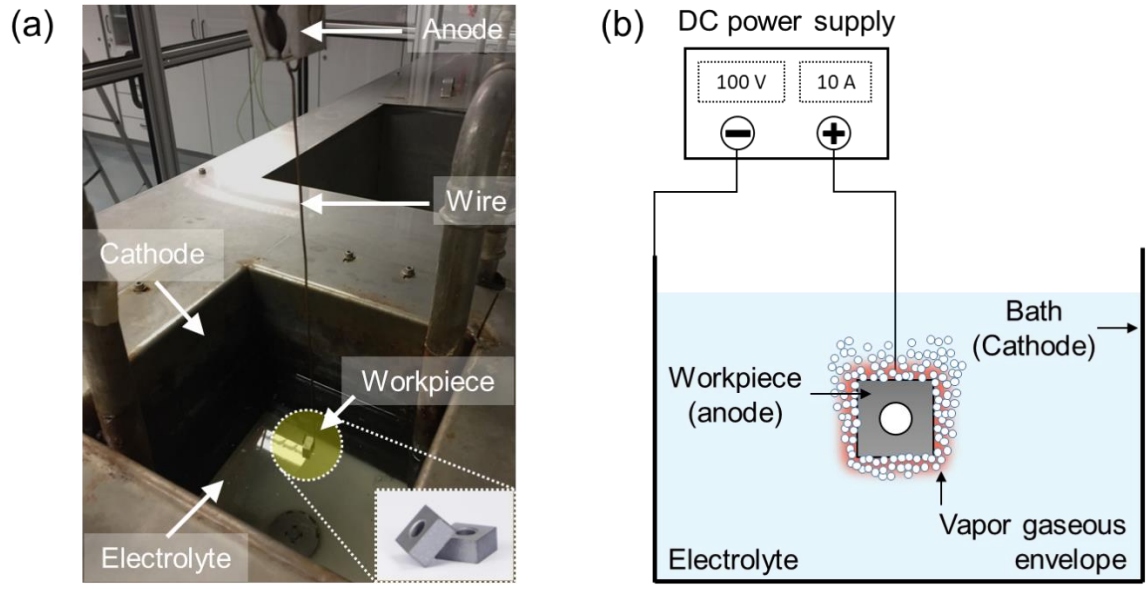

Figure 4.3(a) Photograph and (b) schematic illustration of PEP equipment.

The tool workpiece used in this study is cemented carbide indexable insert from BOEHLERIT GMBH & CO KG, geometry SNMA120604 (ISO 1832), which has dimensions of 12.7 mm width and 6.35 mm thickness. The insert consists of WC (88.4 wt%), Co (10 wt%), and TaC (1.6 wt%). The tool workpiece is connected to the anode part of the power supply and placed in the electrolyte heated to a temperature ranging between 40 °C - 90 °C, which is contained by a bath surrounded by a metallic wall connected to the cathode. The electrolyte solution was prepared by mixing electrolyte powders with deionized water and was changed regularly to

avoid contamination by eroding material from the workpiece. Upon completion of the PEP treatment process, the workpiece was ultrasonically cleaned in distilled water for 15 min, and it was subsequently dried by blowing N_2 gas to remove the remaining electrolyte.

4.2.2 Deposition of hard coatings

Hard coatings are typically deposited on tool surfaces using physical vapor deposition (PVD) methods, characterized as thin film deposition techniques that entail the condensation of a material in its vapor phase onto a substrate [136, 137]. Figure 4.4 depicts the schematic illustration of DC magnetron sputtering (DCMS) equipment.

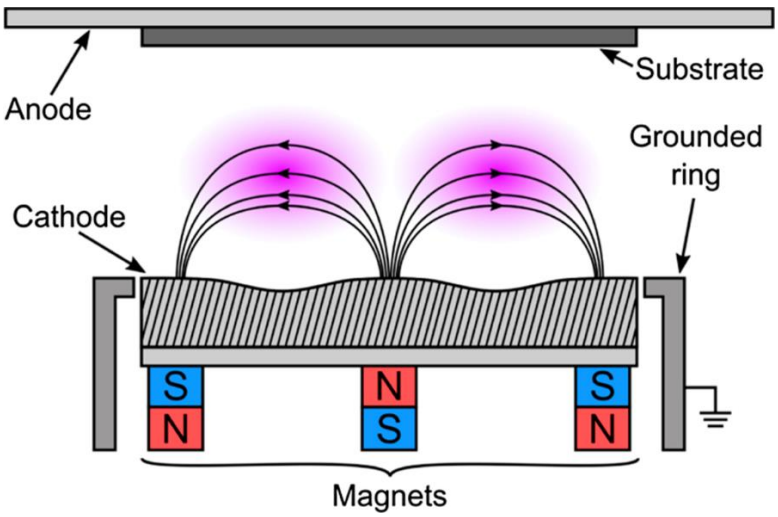

Figure 4.4 A schematic diagram of a magnetron sputtering system (reprinted from [138]).

Using the DCMS, the thin film is created on a substrate by condensation of the sputtered materials, which are ejected by the bombardment of energetic ions in the plasma generated near a cathode target surface. In the last few decades, pulsed magnetron sputtering techniques have gained a lot of popularity due to the ever-increasing requirements of film properties along with the availability of more sophisticated power sources. High-power impulse magnetron sputtering (HiPIMS) is one of the pulsed magnetron sputtering techniques which is typically operated under a low-duty cycle (<10%) with a high peak power density (~1 kW/cm^2), leading to high plasma density (>10^{19} m^{-3}) in the vicinity of the cathode target [139]. The HiPIMS allows control of ion-to-neutral ratio within a broader range than conventional DC magnetron sputtering. The generation of a sufficient ion-to-neutral ratio of the sputtered species benefits the film texture and density during the film growth since the ion-bombardment increases adatom motilities [140, 141]. Thus, in this study, the potential benefits of the PEP pretreatment process to the tribological properties of the hard coating were investigated by depositing the TiN layer using HiPIMS. Moreover, given that most conventional PVD coated tools in the market are coated with the DCMS technique, a commercial DCMS from company A+S (Albrecht + Schumacher Oberflächentechnik GmbH, Bassum, Germany) was applied to deposit AlTiSiN hard coating to examine its industrial applicability.

4.2.2.1 TiN hard coating

The TiN hard coating layer was deposited using reactive high-power impulse magnetron sputtering (R-HiPIMS). Before the TiN layer deposition, a plasma fine-cleaning step was employed to achieve the further removal of remaining residues and enhanced adhesion between coated layer and substrate. This was achieved using the synchronized HiPIMS and plasma-based ion implantation (HiPIMS/PBII) process with the apparatus depicted in Figure 4.5.

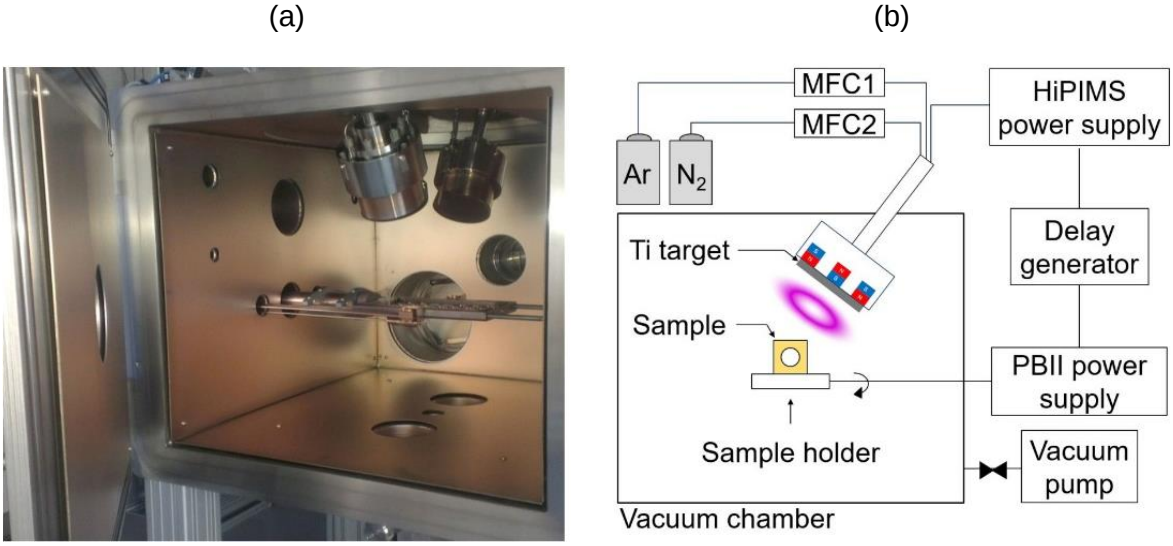

Figure 4.5 (a) HiPIMS/PBII apparatus. (b) Schematic diagram of HiPIMS/PBII system.

Before initiating any processes, the HiPIMS/PBII chamber was firstly evacuated by the turbomolecular pump (Turbovac MAG W 700 iP, Leybold) backed by a rotary pump (TRIVAC D 65 BCS, Leybold) to achieve base pressure of 1.0×10^{-6} mbar measured by a full-range pressure gauge (PKR 251, Pfeiffer). Following the chamber evacuation, gases of Ar (60 sccm) and N_2 (10 sccm) gas were introduced into the chamber, regulated by mass flow controllers (MF-1, MKS). The working pressure was maintained at 0.005 mbar through a gate valve (HV Control Gate Valve, VAT). For the plasma fine-cleaning process on a 4-inch Ti target (purity: 99.999%, Sindlhauser Materials GmbH), pulsed bias of −700 V is applied by a HiPIMS pulse unit (SPIK 2000USB, Melec GmbH). Meanwhile, a bias voltage of −10 kV is applied to the sample using a pulsed power supply (RUP6-35, GBS Elektronik GmbH). A mixture of Ar (60 sccm) and N_2 (10 sccm) gas were introduced into the chamber controlled by mass flow controllers (MF-1, MKS) and the working pressure was measured maintained at 0.005 mbar controlled by gate valve (HV Control Gate Valve, VAT). The high voltage pulsed bias on the substrate and HiPIMS pulse on the Ti target were synchronized at 500 Hz, but the bias on the substrate was 35 µs delayed by a delay generator (DG 535, SRS) for efficient ion implantation effect [142, 143]. The plasma fine-cleaning process was conducted for 20 min. Figure 4.6 depicts typical voltage and current waveforms recorded using a digital oscilloscope (TDS2024B, Tektronix) during the synchronized HiPIMS/PBII process.

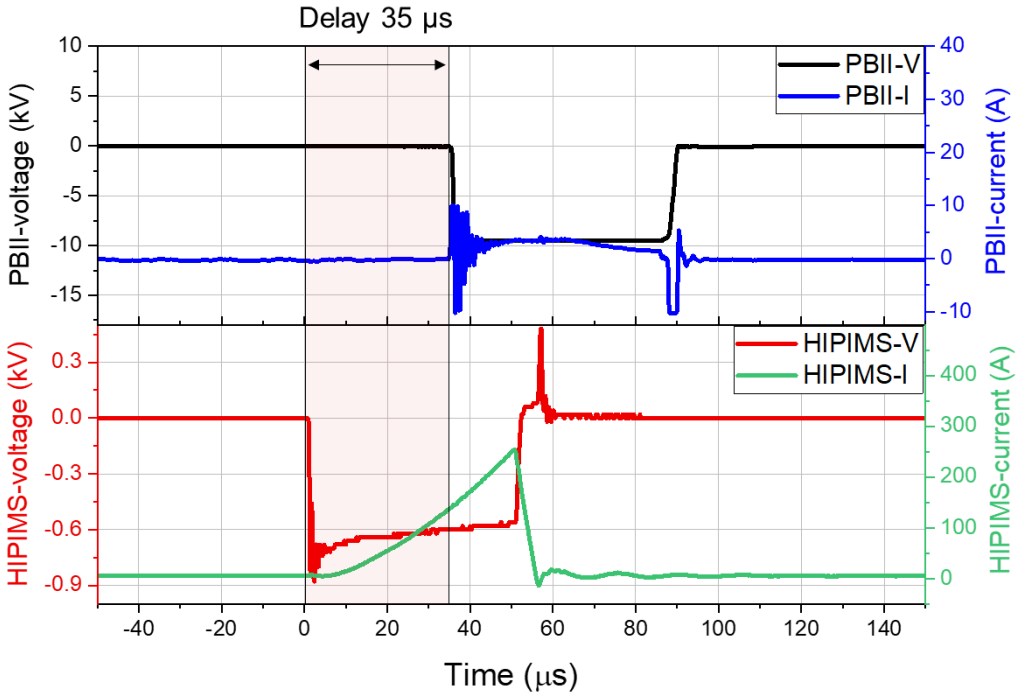

Figure 4.6 Voltage and current waveforms of synchronized HiPIMS (bottom) and PBII (upper) process with delay of 35 µs.

The R-HiPIMS process was subsequently followed to deposit the TiN layer for 10 hours after the plasma fine-cleaning process. During the fine-cleaning and TiN-deposition processes, samples were rotated axially at 3 rpm in one direction to achieve geometrical homogeneity. Table 4-1 presents detailed process parameters for plasma fine-cleaning and TiN deposition.

Table 4-1 Process parameters for plasma fine-cleaning and TiN deposition

Condition		Plasma fine-cleaning	TiN deposition
Base pressure		1.0 x 10^{-6} mbar	
Working pressure		0.005 mbar	
Gas flow	**Ar**	60 sccm	
	N_2	10 sccm	
HiPIMS	**Pulse width**	50 µsec	200 µsec
	Frequency	500 Hz	250 Hz
	Duty cycle	2.5%	5%
	Voltage	700 V	670 V
Substrate bias	**Voltage**	−10 kV	−50 V DC
	Pulse width	50 µsec	
	Frequency	500 Hz	
	Duty cycle	2.5%	
	Delay	35 µsec	
Substrate rotation		3 rpm	
Time		20 min	10 h

4.2.2.2 AlTiSiN hard coating

Figure 4.7 Magnetron sputtering system from a company, A+S.

The primary aim of this study was to assess the efficacy of the PEP technique as a pretreatment method in compare to conventional cleaning processes for the preparation of tools for hard coating deposition. For comparison purposes, contaminated tools were subjected to the industry-standard wet-chemical cleaning procedures by a company A+S. This conventional approach involved the application of commercial standard cleaning agents, employing a combination of ultrasonic and rinse baths before the deposition of the hard coating. After being subjected to wet-chemical cleaning, compressed air was blown on the tools, and the tools were stored in a heating furnace. The tools were then loaded into magnetron sputtering equipment, as shown in Figure 4.7. Before the hard coating layer is deposited, a multistep plasma fine-cleaning procedure is performed in a vacuum atmosphere to completely remove contamination residues. Multiple steps of plasma fine-cleaning were performed on the tool surface by applying a pulsed biased voltage (200–500 V) to the tool workpiece while flowing the Ar-H_2 gas mixture. The deposition of an AlTiSiN monolayer with a metallic adhesive layer was subsequently performed without interrupting the vacuum after the plasma fine-cleaning procedure. The thickness of the AlTiSiN layer is approximately 2 µm, based on which the adhesive strength of HF2 (VDI 3198, "Beschichten von Werkzeugen der Kaltmassivumformung CVD- und PVD-Verfahren") can be obtained on the test disk. More detailed information of the processes from A+S are documented in Ref. [117].

4.2.3 Evaluation of the tribological performance of hard coatings

4.2.3.1 Scratch test

The adhesive strength of the hard coating was determined using a scratch tester (CSM Revestester, CSM INSTRUMENTS SA) according to DIN EN ISO 20502 at the Technical university of Berlin. This method uses a Rockwell C diamond indenter, which is transferred to the specimen with increasing normal force to F_{N} = 100 N over a travel distance of s = 10 mm. The normal and tangential force and the acoustic emission signal are recorded during the scratch test. These data enable the detection of a layer defect. The critical load is used to evaluate the adhesive strength. DIN EN ISO 20502 differentiates the values L_{C1}, $L_{C2,}$ and L_{C3}, where L_{C1} corresponds to the load under which the first cracks appear. Conversely, L_{C2} corresponds to the load under which the first spalling of the coating occurs, and L_{C3} describes the load when the coating is completely delaminated. In practice, the L_{C2} value is used to

describe the coating adhesion, as in the following. The test was performed using a diamond tip with a radius of r_β = 20 µm and a speed of v_s = 0.01 m/min.

4.2.3.2 Machining tests

Figure 4.8 Universal lathe DMG MORI CTX gamma 1250 TC.

To assess coated tools' service life, carbon steel C45E (1.1191) was machined using a universal lathe (CTX gamma 1250 TC, DMG MORI AG) as shown in Figure 4.8 at the Technical University of Berlin. The evaluations were carried out at a cutting speed of 250 m/min, a feed of f = 0.1 mm, and a cutting depth of a_p = 0.25 mm under dry conditions. The width of the flank wear land (VB) was measured during the machining process using a stereomicroscope (M3Z, LEICA MICROSYSTEMS). A tool life $t_{VB0.3}$ is determined by measuring the flank wear VB until it reaches the $VB_{\max}$ = 0.3 mm, which is a criterion for tool life. Further details on the tribological tests is provided in Ref. [117, 144].

4.3 Results and discussion

4.3.1 Parameter study for optimization of PEP process

In this section, the document outlines numerous approaches undertaken to optimize the PEP process specifically for the pretreatment of WC-Co materials. This encompasses aspects such as selecting the appropriate electrolyte and its parameters, identifying the optimal voltage regime, and strategies to reduce variations in surface elemental composition and tool cutting edge definition.

4.3.1.1 Selection of electrolyte

For the surface erosion by the PEP process, it is crucial to choose material-specific electrolytes because the electrolyte composition significantly affects the resultant surfaces. Therefore, this section is aimed to describe how the WC-Co surface is influenced after the PEP process using different kinds of electrolytic solutions. Ammonium sulfate ($(NH_4)_2SO_4$) and sodium carbonate (Na_2CO_3) were tested to use as an electrolyte in the PEP process to treat the surface of WC-Co-based cemented carbide insert. The detailed PEP process parameters are presented in Table 4-2.

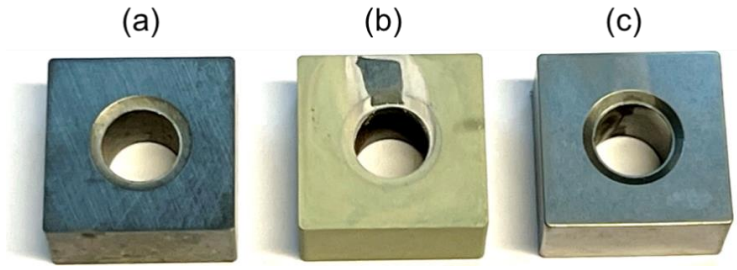

Figure 4.9 Photographs of WC-Co-based tools: (a) untreated and PEP-treated with (b) $(NH_4)_2SO_4$ and (c) Na_2CO_3

As seen in Figure 4.9(a) – (c), the insert treated in $(NH_4)_2SO_4$ appears greenish, whereas the untreated and PEP-treated in Na_2CO_3 inserts appear metallic gray. On the upper part of both PEP-treated workpieces, a masking effect from the clamp is visible.

Table 4-2. Process parameters for PEP pretreatment

Condition	Value	
Electrolyte	$(NH_4)_2SO_4$	Na_2CO_3
Electrolyte concentration	4 wt%	10 wt%
Electrolyte temperature	70 °C	70 °C
pH	6	11
Process voltage	100 V	110 V
Treatment time	60 s	80 s

Figure 4.10(a) depicts the elemental composition of untreated and PEP-treated inserts analyzed by XPS. The untreated tool surface primarily contains W, C, O, and Co. After the PEP process with the electrolyte of $(NH_4)_2SO_4$, the fraction of C decreased from 52.5% to 24.7%, while the fraction of O increased from 8.3% to 47.8%. The surface of the PEP-treated workpiece with Na_2CO_3 has also indicated increased oxygen atomic content (23.9%) compared to untreated inserts, though this is still lower than inserts treated with $(NH_4)_2SO_4$. As shown in Figure 4.10(b), the shape of the W 4f peak was analyzed to determine the chemical state of the W. The shape of the W 4f peak changed after the PEP process due to the formation of the tungsten oxide (60% WO_3), when exposed to water or oxygen, WC readily oxidizes through the following reaction path [145].

$$WC(s) + 3H_2O(l) \leftrightarrow WO_3(s) + CH_4 + H_2(g) \qquad 4.1$$

WO_3 can be electrochemically dissolved as a result of Reaction 4.2 in a strongly acidic atmosphere (pH < 1) [146]. However, when a weak acid (4.5 < pH < 6) is present, the WO_3 remains on the surface of the WC workpiece [147, 148].

$$WO_3(s) + 2H^+ \leftrightarrow WO_2^{2+} + H_2O \qquad 4.2$$

Meanwhile, as depicted in Figure 4.10(b), the W 4f peak of the insert workpiece treated in Na_2CO_3 primarily comprises WC binding (81.2%) with WO_3 (18.8%) which is comparable to the untreated insert surface. In an alkaline environment, W is favorably dissolved as a form of tungstate ions by the following Reaction 4.3 instead of remaining as oxidized W; therefore, WC binding is dominantly detected by XPS analysis [145, 146].

$$W + 8OH^- \leftrightarrow WO_4^{2-} + 4H_2O + 2e^- \qquad 4.3$$

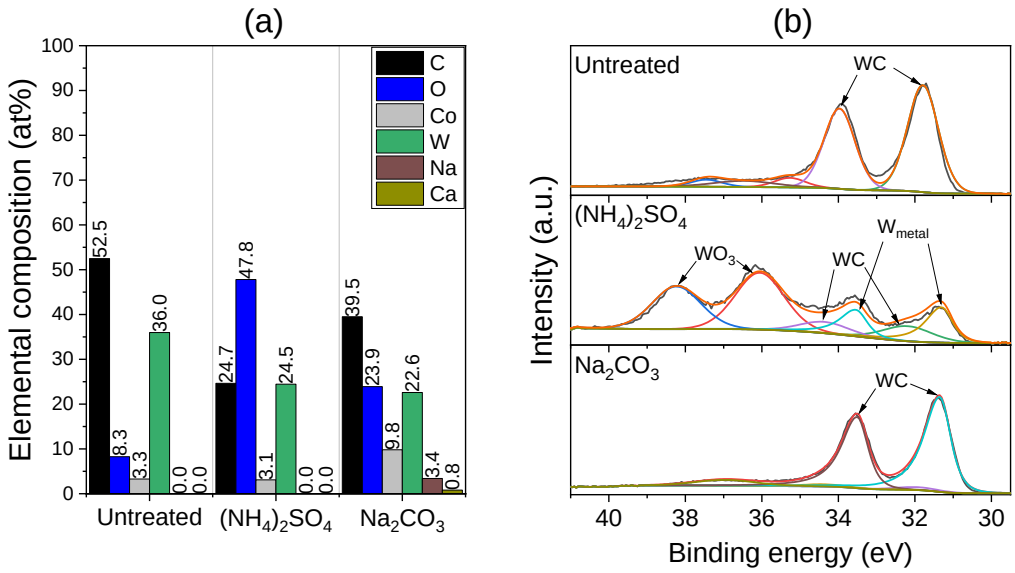

Figure 4.10 XPS analysis of untreated and PEP-treated sample: (a) elemental composition and (b) W 4f spectra of the tool surface.

To apply PEP technology effectively for the tool surface pretreatment, besides the dissolution of W, it is also necessary to consider suppressing Co leaching. Consequently, meticulous attention is required when pretreating the tool surface because cobalt leaching from the tool surface leads to a mechanically weak surface, ultimately resulting in hard coating adhesion failure [149, 150]. The following methods have been proposed to mitigate this problem: (1) replacing Co with an alternative element, in particular, Cu, or (2) forming a stable compound on the tool surface containing Co, such as Co_3W_3C [150-152]. After the PEP treatment with Na_2CO_3 electrolyte, the elemental fraction of Co noticeably increased to 9.8% from 3.3%, as shown in Figure 4.10(a). This can be attributed to the surface precipitation of Co in the form of $Co(OH)_2$ and/or $CoWO_4$ instead of Co leaching [145]. The detailed elemental and structural

surface analysis on the workpiece surface after the PEP process with Na_2CO_3 electrolyte in various process parameters will be provided in the next section.

The following conclusions can be drawn from this preliminary result using two different types of electrolytes for WC-Co materials:

- W on the tool surface can be dissolved in an alkaline environment instead of forming WO_3.
- Co can remain after the PEP process with the electrolyte of Na_2CO_3.

Therefore, Na_2CO_3 is selected as a default electrolyte in this study due to its surface compositional advantage, despite $(NH_4)_2SO_4$ being widely used to treat various materials. The following chapters provide an investigation into further optimization of the process in terms of its practical application by changing various process parameters accompanying the surface and geometrical characterizations.

4.3.1.2 Voltage-current characteristics of the PEP process

This section demonstrates the electrical characteristics of the PEP process, featuring voltage-current measurements taken during the PEP process at varying electrolyte concentrations and temperatures.

4.3.1.2.1 Influence of electrolyte concentration

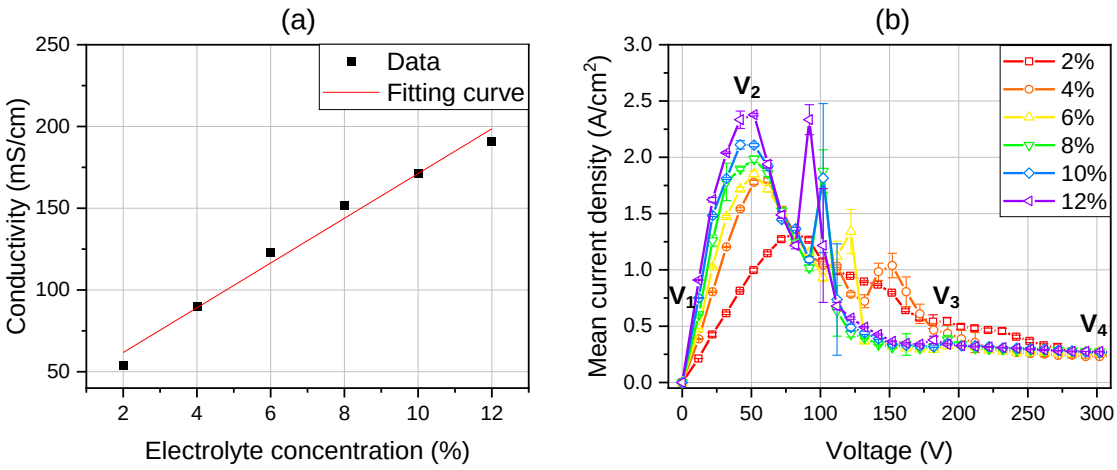

Figure 4.11 (a) Electrical conductivity of Na_2CO_3 electrolytes and (b) current-voltage characteristics at varying electrolyte concentrations (ranging from 2 wt% to 12 wt%) at consistent temperature of 70 °C (adapted from [89]).

Figure 4.11(a) illustrates the electrical conductivity of Na_2CO_3 over its concentration, measured by a conductometer (Cond 3210, WTW). The electrical conductivity of the electrolyte continuously increases from 52 to 191 mS/cm as the concentration rises since more ions, including Na^+ or CO_3^{2-}, dissolve in water. In Figure 4.11(b), the voltage-current characteristics were observed for different electrolyte concentrations (ranging from 2 wt% to 12 wt%) when the electrolyte temperature was maintained at 70 °C during the PEP process. At all electrolyte

concentrations, distinct characteristics are observed at voltage regimes, marked V_1 to V_4. A description of this typical voltage-current behavior during the PEP process has already been provided in Section 2.3.1. As shown in Figure 4.11(b), the critical voltage (V_2) tends to be lower when the concentration is increased since a lower electrical field is required for charge extraction from the electrolyte [153]. In the voltage and current characteristics, there is a noticeable peak of current density between V_2 and V_3; however, the peak is obscured to some extent with the relatively large error bars in that range but is still prominent at all concentrations. In addition, the peak position shifts to lower voltages with increasing electrolyte concentration. The occurrence of the current peak can be attributed to the electrical breakdown of the dielectric layer. Insulating layers initially passivate the workpiece surface at low voltages (around V_2). However, when the voltage reaches a particular threshold point, the dielectric layer breaks down, resulting in excessive current flowing through the layer, effectively removing insulating material, partially exposing the metal surface, and causing a sharp current peak. A similar phenomenon has also been observed during a plasma electrolytic oxidation (PEO) process as a sparking regime [154, 155].

4.3.1.2.2 Influence of electrolyte temperature

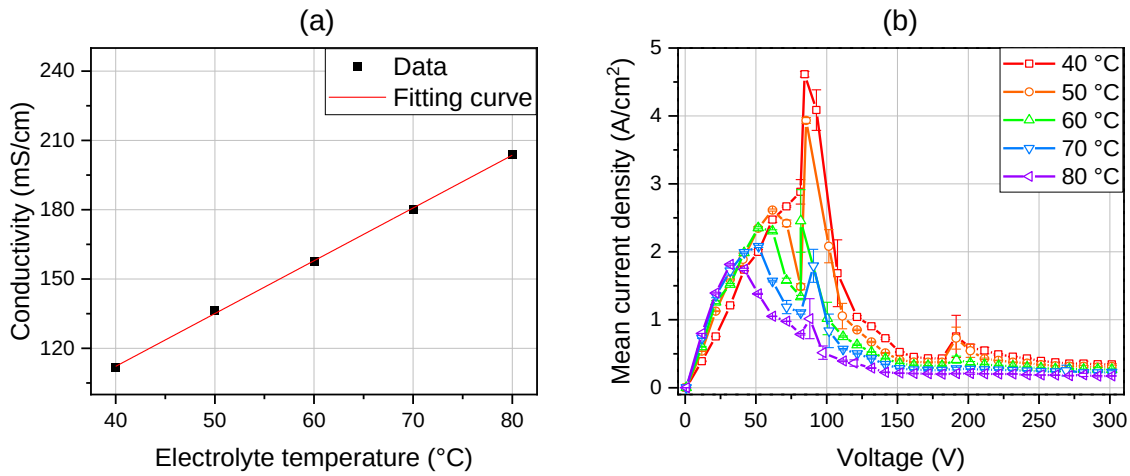

Figure 4.12 (a) Electrical conductivity of Na_2CO_3 electrolyte and (b) current-voltage characteristics at varying electrolyte temperatures (ranging from 40 °C to 80 °C) at fixed concentration of 10 wt%. (adapted from [89]).

Furthermore, as shown in Figure 4.12(b), voltage and current characteristics have been studied in a range of electrolyte temperatures (40 °C–80 °C) at a concentration of 10 wt% electrolyte. As shown by Figure 4.12(a), the electrolyte conductivity increases linearly with increasing temperature of the liquid, as both ionic mobility and degree of dissociation increase as the temperature increases. In Figure 4.12(b), as electrolyte temperatures increase, the critical voltage decreases, possibly due to heat transfer phenomena. During the PEP process, the majority of the electrical power is dissipated within the VGE. This power is then partially transferred to the bulk electrolyte to maintain a stabilized interface between the electrolyte and the VGE (heating and evaporating electrolyte). The establishment of an energy balance includes the following contributions: heating of the workpiece, generation of plasma, and electrochemical reactions (exothermic and endothermic) [156]. The higher the electrolyte

temperature, the easier it is to sustain a steady VGE layer around the workpiece surface with a lower critical voltage [157]. In addition, the mean current density is generally low at higher electrolyte temperatures due to the formation of thicker VGE at higher electrolyte temperatures, which suppresses the flow of electrical current. Furthermore, as depicted in Figure 4.12(b), there is no change in the position of the sharp secondary peak (~90 V), but its intensity decreases with increasing electrolyte temperature. The polishing process is terminated by increasing the voltage above 180 V, which results in another current peak, however smaller in size. The partial removal of an insulating layer may also be responsible for this.

Photographs of the tool workpiece during the PEP process at varying voltages at fixed electrolyte temperature and concentration (70 °C and 10 wt%, respectively) was taken by a digital camera to observe gas layer development and discharge phenomena during the PEP process, as shown in Figure 4.13(a). Besides, the current density was synchronously recorded, as shown in Figure 4.13(b).

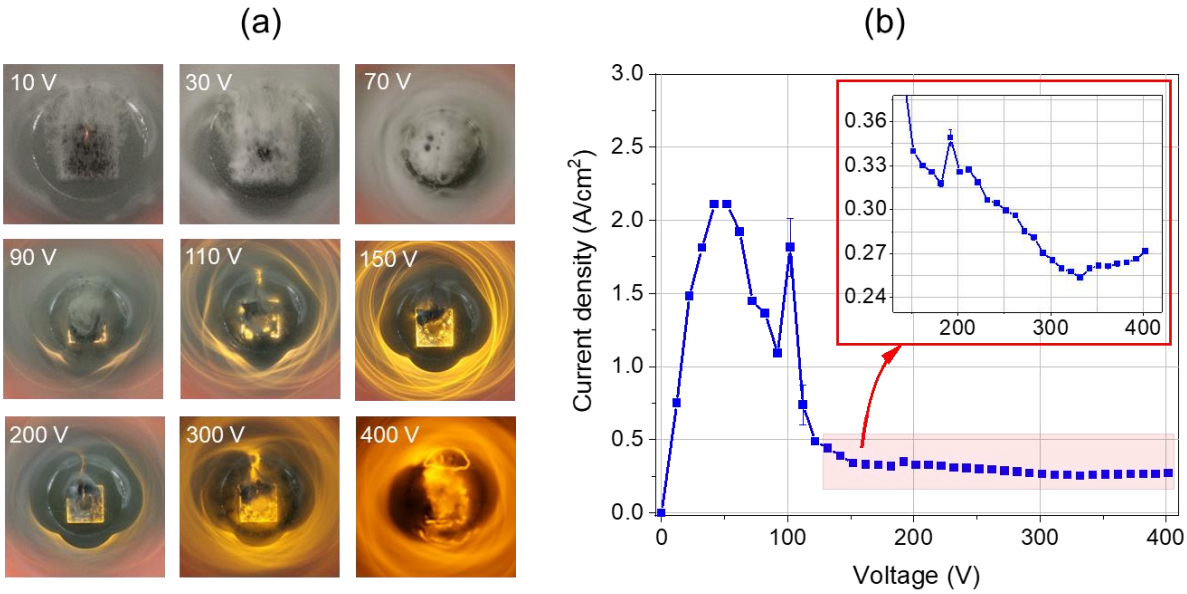

Figure 4.13 (a) A series of photographs illustrating stages of the PEP process at distinct voltages. (b) Evolution of current density over the process voltage from 0 V to 400 V. The segment highlighted in red is detailed further in the inset.

For this investigation, the process voltage was raised gradually from 10 to 400 V, increasing in 10 V steps, and maintained for 10 s at each voltage to stabilize the process. At low voltages (up to 30 V), bubbles are generated around the workpiece, and the amount of gas increases with increasing the voltage to 70 V. As the voltage further rises, discharges are observed starting from the lower corners of the sample owing to the high electric field [16, 158]. As the voltage increases, short-lived discharges appear sporadically all over the workpiece. An increase in the number of discharges on the surface of the workpiece is observed when the voltage is elevated to 150 V. However, the discharge intensity is reduced at 200 V with a reduction of the current density, as shown in Figure 4.13(b). This reduction of the discharge intensity can be speculated by the formation of an excessive oxide layer on the tool surface rather than surface dissolution. There is a similar phenomenon in the soft sparking regime of the PEO process occurring due to the formation of a densified oxidized layer that facilitates the extinguishing of micro-discharges and reduction of power consumption [63, 159]. The next

section will present a surface analytical result on the tool after the PEP process at 30 V, 110 V, and 200 V. Above 300V, it is observed that emission is also formed in the surrounding electrolyte, and the current rises as charged species are formed accordingly.

4.3.1.3 Influence of the PEP process on the tool

In this section, the impact of the PEP process on the tool surface is elucidated using various surface analysis techniques, aiming to identify structural, morphological, and elemental characteristics. To investigate the surface compositional status of the tool, XPS analysis was performed on the PEP-treated tool surfaces at 30 V, 110 V, and 200 V which represent voltage regimes of V_1-V_2, V_2-V_3, and V_3-V_4 respectively. Table 1 summarizes the detailed PEP process parameters employed for this investigation. The photographs of the tools before and after the PEP process are exhibited in Figure 4.14.

Table 4-3. Process parameters for PEP pretreatment

Condition	Value
Electrolyte	Na_2CO_3
Electrolyte concentration	10 wt%
Electrolyte temperature	70 °C
pH	11
Treatment time	1 min

As shown in Figure 4.14, as a result of the PEP process at voltage ranges of V_1-V_2 and V_3-V_4, the surfaces of inserts treated exhibited a noticeably black appearance, whereas the surfaces of inserts treated at voltage ranges of V_2-V_3 remained metallic gray, similar to the untreated workpiece.

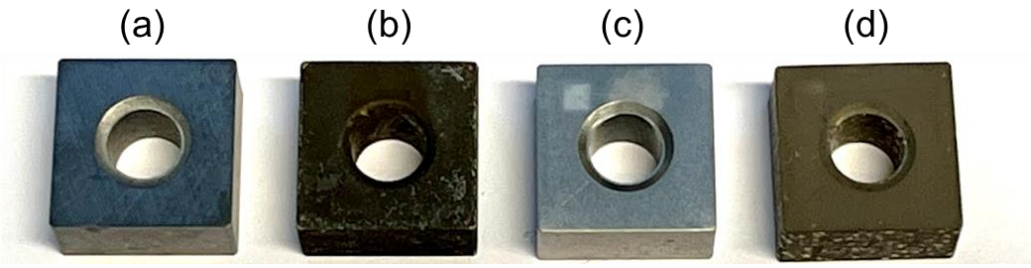

Figure 4.14 Photographs of tool workpiece (a) before and after the PEP process at varied voltages: (b) 30 V (V_1-V_2), (c) 110 V (V_2-V_3), and (d) 200 V (V_3-V_4).

Figure 4.15(a) illustrates representative XPS survey spectra of untreated and PEP-treated inserts, showing the presence of Co, O, W, and C on the tool surfaces. The XPS depth profiles of untreated and PEP-treated inserts at various voltages are shown in Figure 4.15(b)–(e). As depicted in Figure 4.15(c), a PEP treatment at 30 V increased oxygen atomic content from 8 at% to 33 at%, indicating that the insert surface had been oxidized.

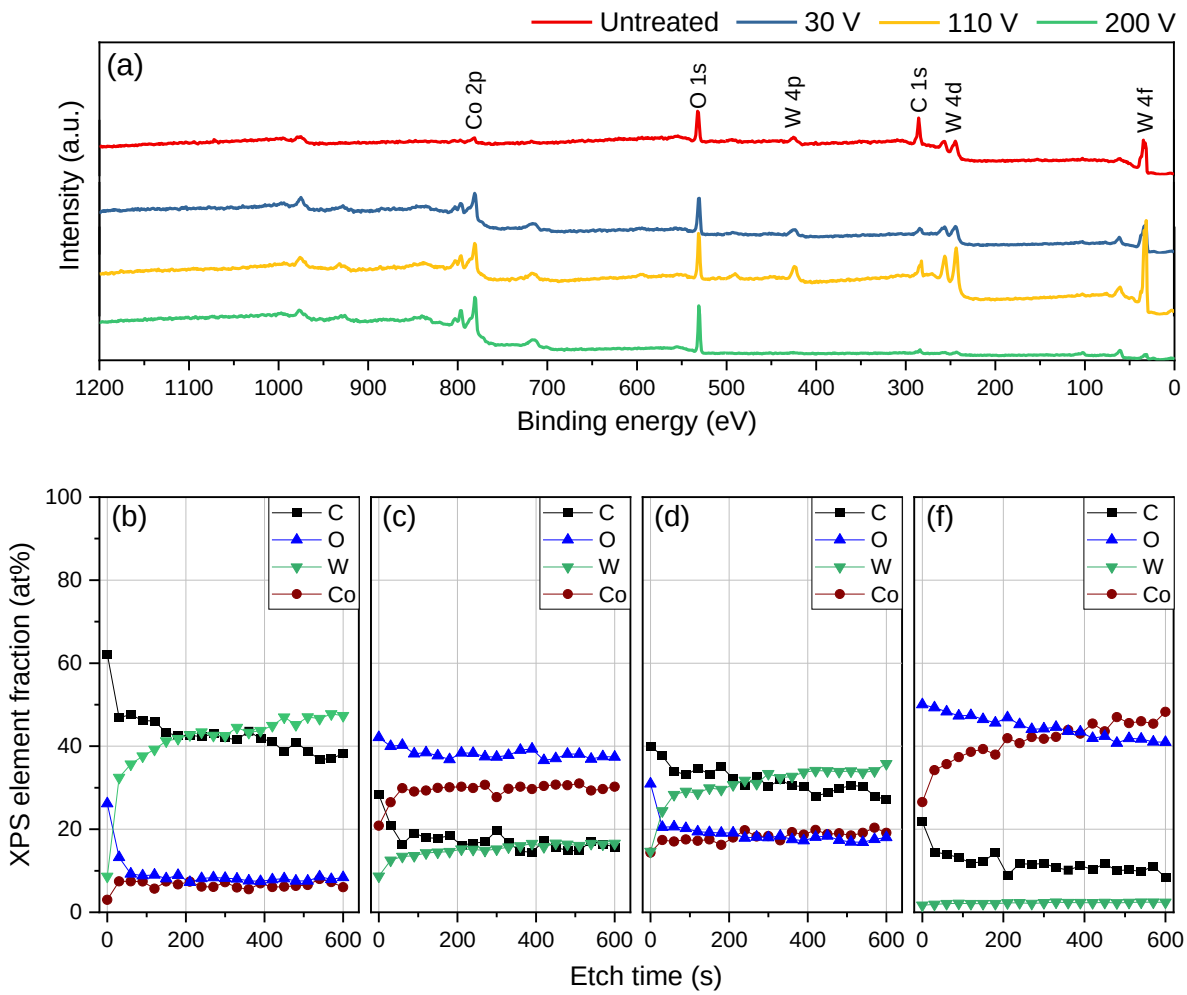

Figure 4.15 (a) XPS survey spectra of untreated and PEP-treated workpieces. XPS depth profile data of (b) untreated and (b–d) PEP-treated inserts at different voltages (30, 110, and 200 V).

The chemical state of W was ascertained by a curve fitting process from the W 4f spectrum, which exhibited four distinct components with binding energies at 37.7 eV, 35.6 eV, 34.1 eV, and 31.9 eV. The two peaks at 37.7 eV and 35.6 eV are associated with oxidic components of W $4f_{7/2}$ and W $4f_{5/2}$, whereas the other two peaks at 34.1 eV and 31.9 eV are assigned to metallic components, as shown in Figure 4.16(a)–(d) [98, 145, 160, 161]. In addition, highly-resolved Co 2p peaks are fitted with peaks at 787.4 eV, 784.1 eV, 781.8 eV, 780.5 eV, and 778.5 eV. The peak of 778.8 eV is attributed to the metallic Co, and the other peaks are assigned to oxidized/hydroxide Co components, as shown in Figure 4.16(e)–(h) [98, 145, 162]. PEP treatment of a workpiece at different process voltages results in different peak shapes of both W 4f and Co 2p peaks compared with an untreated surface. Table 4-4 summarizes the fractions of relative peak areas between WC and WO_3. The treated tool workpiece has a higher percentage of oxidized W binding (30%) than the untreated workpiece since W is readily oxidized by Reaction 4.1 in water or an oxygen atmosphere, owing to its thermodynamic instability. Meanwhile, after the PEP process at 30 V, a significant increase in metallic Co was observed from 20% to 79%. Compared to the workpiece treated at 30 V and 200 V, the workpiece treated at 110 V exhibits less oxidation, as depicted in Figure 4.15(d).

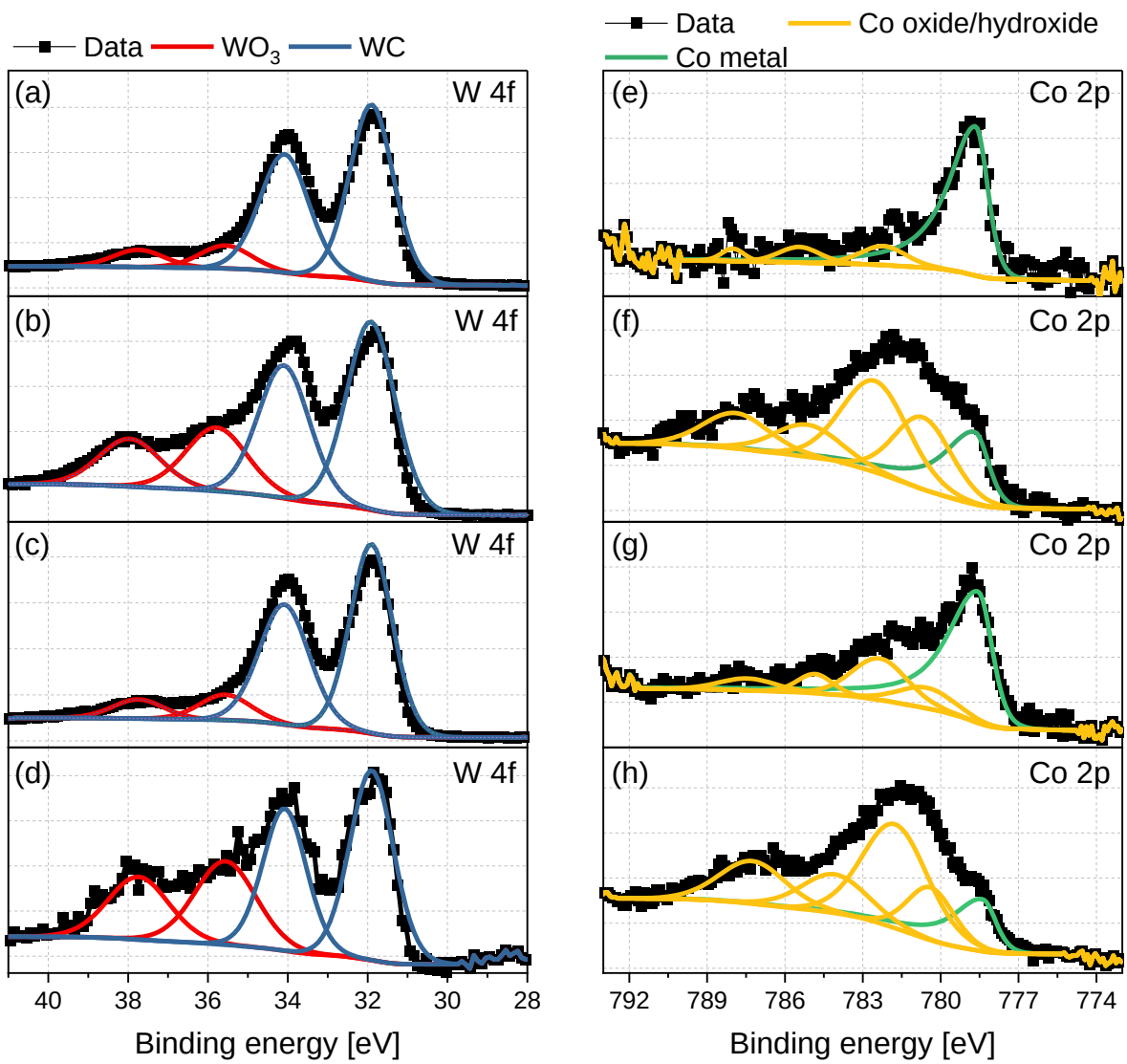

Figure 4.16 XPS spectra of highly-resolved W 4f (left side) and Co 2p (right side) peaks of (a), (e)untreated, and PEP-treated at (b), (f) 30 V, (c), (g)110 V, and (d), (h)200 V insert surfaces.

In addition, the workpiece surface with 110 V occupies the highest binding fractions of WC (86%) and metallic Co (60%) in the W 4f and Co 2p peaks, respectively, as indicated in Table 4-4. As described by Andersson et al. [145] and Hochstrasser-Kurz et al. [163], the polishing of cemented carbide surfaces at 110 V can be attributed to a two-step process. This process involves an initial stage of tungsten oxidation, followed by a subsequent dissolution stage, which is favored in alkaline environments. The Co fraction increases after the PEP process at 110 V from 6.5 at% to 18.2 at%, owing to the dissolution of WC on the surface, as illustrated in Figure 4.15(d). According to Figure 4.15(e), the elemental fractions of Co and O on the workpiece surface crucially rise to 42 at% and 43 at%, respectively, after the PEP process at 200 V.

After the PEP treatment at 200 V, the binding fractions of W and Co on the insert surface are generally very similar to the binding fraction at 30 V as indicated in Table 4-4. However, a significant difference in surface compositional characteristics is that the workpiece surface treated at 30 V contains 17% of the elemental fraction of W. However, after PEP treatment at 200 V, only 2% of W remains due to Co species passivating the surface. It can be speculated that when PEP is conducted at a higher voltage, there is an excessive generation of tungstate ions (WO_4^{2-}) accompanied by the release of protons. This reduces the pH value around the workpiece surface, promoting Co dissolution to the detriment of the WC dissolution. The dissolved Co species can be precipitated on the surface of oxidized WC in the form of $Co(OH)_2$ or $CoWO_4$ [145, 163].

Table 4-4 Binding fraction of the W 4f and Co $2p_{3/2}$ peaks

	W 4f		**Co 2p**	
	WC (%)	WO_3 (%)	Co-metal (%)	Co-oxide/hydroxide (%)
Untreated	87	13	80	20
30 V	70	30	21	79
110 V	86	14	60	40
200 V	62	38	16	84

As illustrated in Figure 4.17, the GIXRD was performed on the untreated and PEP-treated tool workpiece to discern the influence of the PEP process on the crystal structure of the WC-Co workpiece. On all workpiece surfaces, WC phases are the predominant crystalline structures. After the PEP process at 110 V, the crystallite size of WC increases to 45.1 nm from 7.8 nm, determined, as described in Section 3.5. A plausible explanation for this is that smaller crystallites of WC tend to dissolve preferably during the PEP process, while relatively larger crystallites remain on top of the surface of the workpiece. The Co phases (e.g., at 44.10°) are noticeably observed on the workpiece surface treated at higher process voltages, which is associated with the selective dissolution of WC during PEP. TaC crystalline phases can only be detected at surfaces after processes have been conducted at 30 V or 200 V. As a result of the dissolution-dominated reaction associated with PEP treatment at 110 V, the modified surface layer is assumed to be deeper than the surface layer resulting from other voltage treatments, resulting in fewer TaC crystallites remaining.

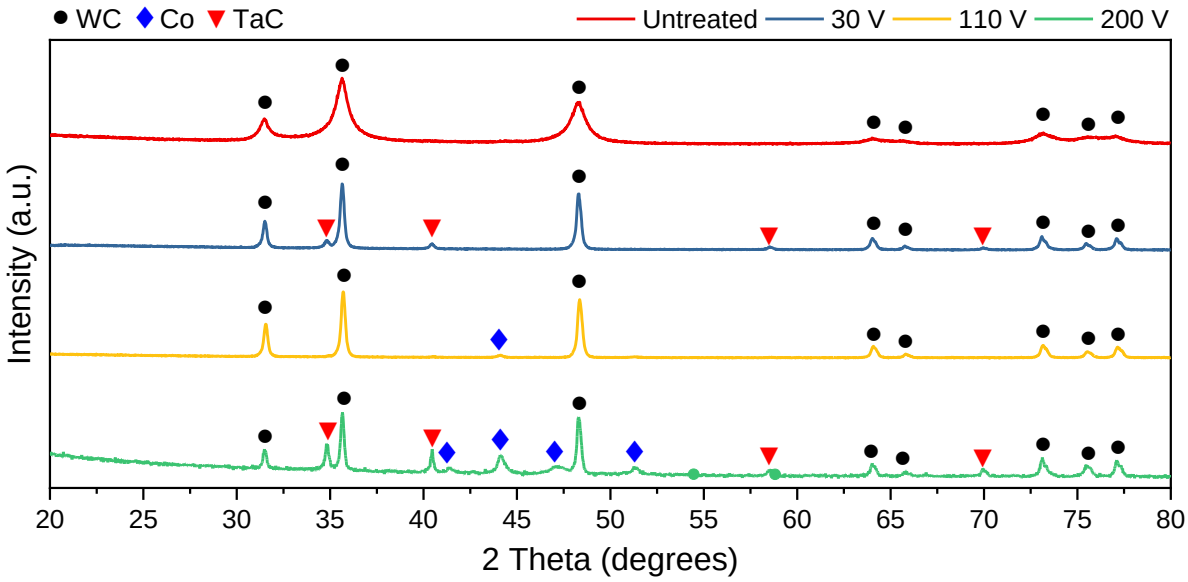

Figure 4.17 XRD patterns of untreated and PEP-treated inserts at different process voltages of 30 V, 110 V, and 200 V (adapted from [89]).

The surface morphology and elemental composition were examined further using SEM/EDX. Table 4-5 summarizes the elemental fractions of the tool surfaces. A detailed overview of the SEM/EDX analysis is presented in Section 3.3. From an untreated cemented carbide workpiece depicted in Figure 4.18(a), a distinct mechanically ground surface with striped abrasion can be observed, created by a grinding process from the tool manufacturer to improve the surface wear property [164, 165]. The EDX mapping indicates that the untreated tool's surface is composed of W (85.6 at%), O (12.8 at%), and Co (1.7 at%). After the PEP process at 110 V, a pulverized WC grain and cobalt matrix subsurface are observed, as shown in Figure 4.18(c). After the PEP treatment at 30 V, the elemental fraction of O significantly increases to 83 at% from 12.8 at% due to surface oxidation. However, for the tool surface treated by the PEP at 110 V, the elemental fraction of O decreases to 5.7 at%, while Co rises to 3.9 at% from 1.7 at% owing to the dissolution of the oxidized W. In the case of the surface of the PEP-treated tool at 200 V, the tool surface is predominantly covered with Co rather than W, as shown in Figure 4.18(h). In this case, the elemental fraction of Co has increased steeply from 1.7 at% to 38 at%, as well as the elemental fraction of O has risen to 51.3 at% from 12.8 at%. This can be attributed to oxidized Co-containing compounds forming on the tool surface due to the electrolytic anodic reaction.

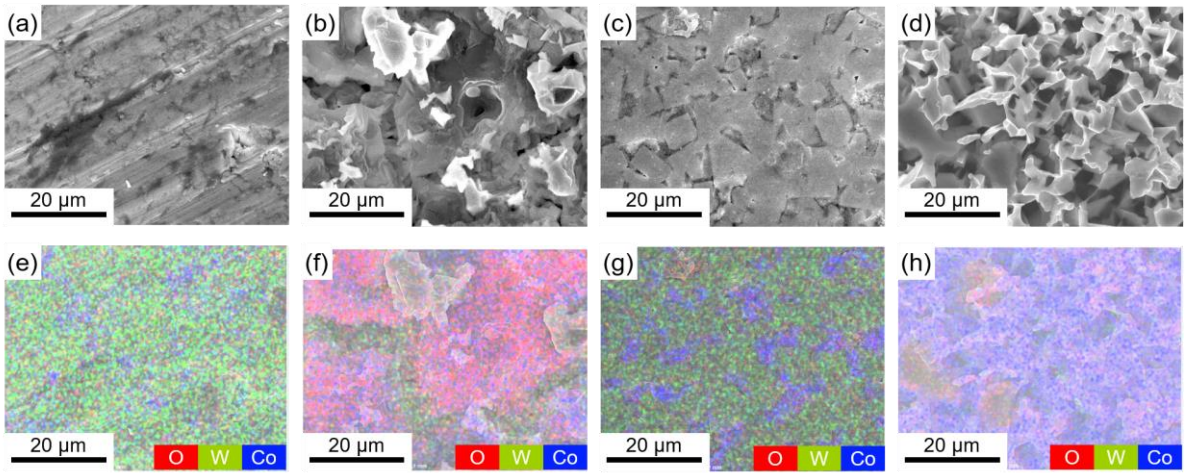

Figure 4.18 SEM images of the (a) untreated and PEP-treated inserts at different process voltages: (b) 30 V, (c) 110 V, and (d) 200 V. EDX mapping images of the (e) untreated and PEP-treated inserts at different process voltages: (f) 30 V, (g) 110 V, and (h) 200 V.

Table 4-5 Elemental fractions of tool surfaces measured by EDX

Elements (at%)	Treatment voltage			
	Untreated	**30 V**	**110 V**	**200 V**
W	85.6	15.5	90.4	10.3
O	12.8	83.0	5.7	51.3
Co	1.7	1.5	3.9	38.4

Coating adhesion can be crucially influenced by surface roughness. However, this study aims to evaluate the decontamination effect of the PEP process while minimizing the changes to the tool's intrinsic surface composition and morphology. The roughness value must remain the same before and after the process to observe only the cleaning effect of the PEP. Therefore, to ensure comparable conditions, the surface roughness was evaluated on the tool surfaces over a 0.34 × 0.4 mm^2 area using WLI analysis, as shown in Figure 4.19(a). The WLI analysis details have been documented in Section 3.2. Surface roughness values of PEP-treated tools at various voltages are shown in Figure 4.19(b). After the PEP process at 30 V and 200 V, the surface roughness (R_a) increased from 0.13 µm to 0.61 µm and 0.88 µm, respectively. It can be speculated that the reduced rate of dissolution of the oxidized surface at 30 V and 200 V is due to dominant passivation by the oxidized components, even though different types of components are formed at these voltages. On the other hand, anodic dissolution primarily occurs at 110 V. As a result, surfaces covered by oxidized components at 30 V and 200 V exhibit relatively low dissolution rates; meanwhile, dissolution still occurs at the surface region, which is not passivated by the oxidized component. Consequently, an uneven surface can be generated on the tool surface after the PEP process. It has been observed in various studies

that roughness increases after the PEP process on various materials emphasizing the necessity of selecting the voltage regime for efficient polishing [72, 75].

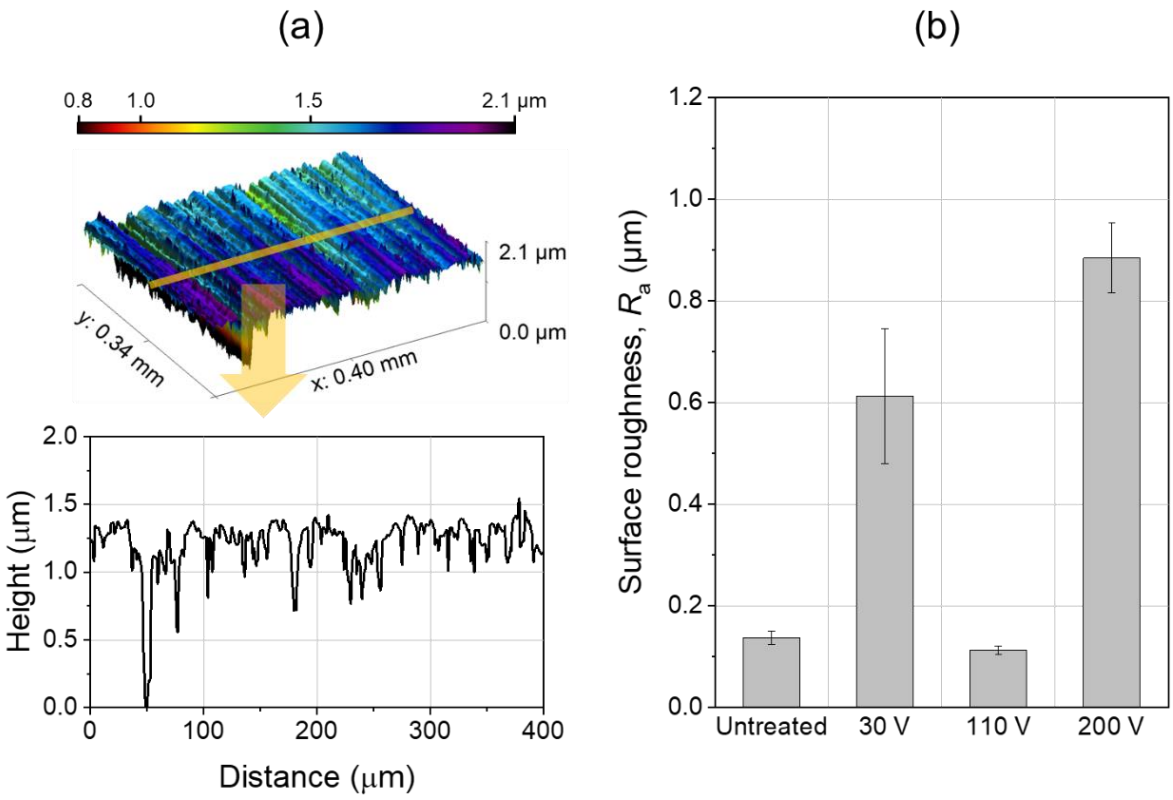

Figure 4.19 (a) 3D surface profile on the untreated tool surface measured by WLI. (upper) and line profile corresponding to the specified line (below). (b) Comparative average roughness (R_a) values for untreated and PEP-treated tool surfaces across voltages ranging from 30 V to 200 V.

4.3.1.4 Characterization of the surface cleaning effect

In this section, to determine whether the PEP process can effectively remove surface contamination, the contaminated tools were treated using the PEP process. Subsequently, this method was compared with other cleaning processes. Firstly, the contamination, which resembles the contamination smudging during tool manufacturing, has to be defined to evaluate the cleaning effect of the PEP process. In cooperation with industrial tool manufacturers, a reference contamination has been synthesized, containing grinding oil, washing solution, and abrasive agents. Upon application, the synthesized contamination is applied to the insert tools, and they are then heated in a furnace for 1 min at 700 °C, as shown in Figure 4.20.

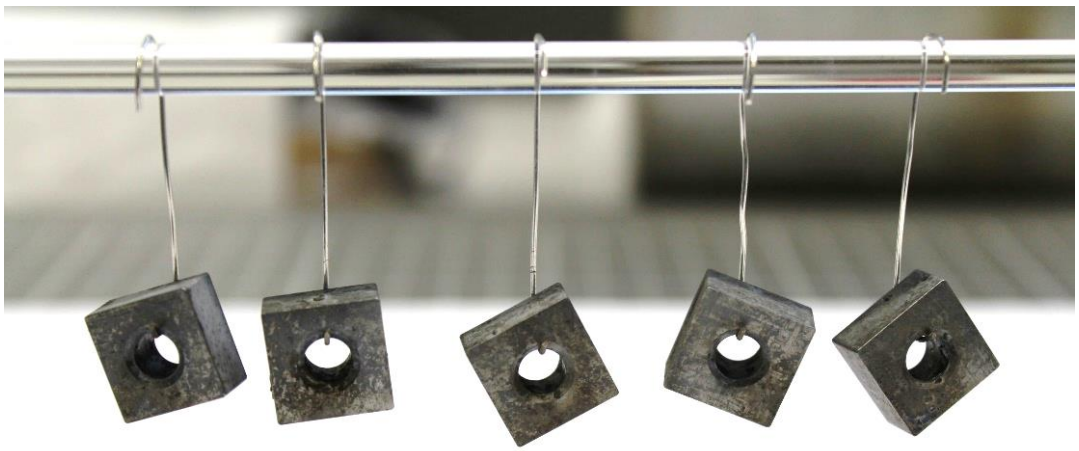

Figure 4.20 Photographs of contaminated insert tools.

The tool surface was then cleaned using various pretreatment methods, as summarized in Table 4-6. Then, ATR FTIR was utilized to assess the cleaning results by characterizing the remaining contamination on the tool surface. The contaminated tool underwent treatment through the PEP process (process 3) at 110 V for 1 min in a Na_2CO_3 electrolyte (10 wt%) since this parameter was identified in the earlier section as beneficial for achieving surface erosion with minimal oxidation on the tool surface. After the PEP process, the workpiece surface underwent ultrasonication for 15 min with deionized water to facilitate the removal of electrolyte residue. For comparison, the contaminated tools underwent treatment with ultrasonication for 15 min in the 10 wt% Na_2CO_3 electrolyte (process 2) – the same electrolyte used in the PEP process. Subsequently, these tools were also subjected to treatment with deionized water to facilitate the removal of electrolyte residue. In process 3, tools were subjected to ultrasonication using only deionized water for cleaning.

Table 4-6 Overview of pretreatment methods for cleaning tools

Process no.	**Pretreatment methods**		
	PEP	**Ultrasonication**	
	Na_2CO_3	**Na_2CO_3**	**Water**
1	O	O	O
2		O	O
3			O

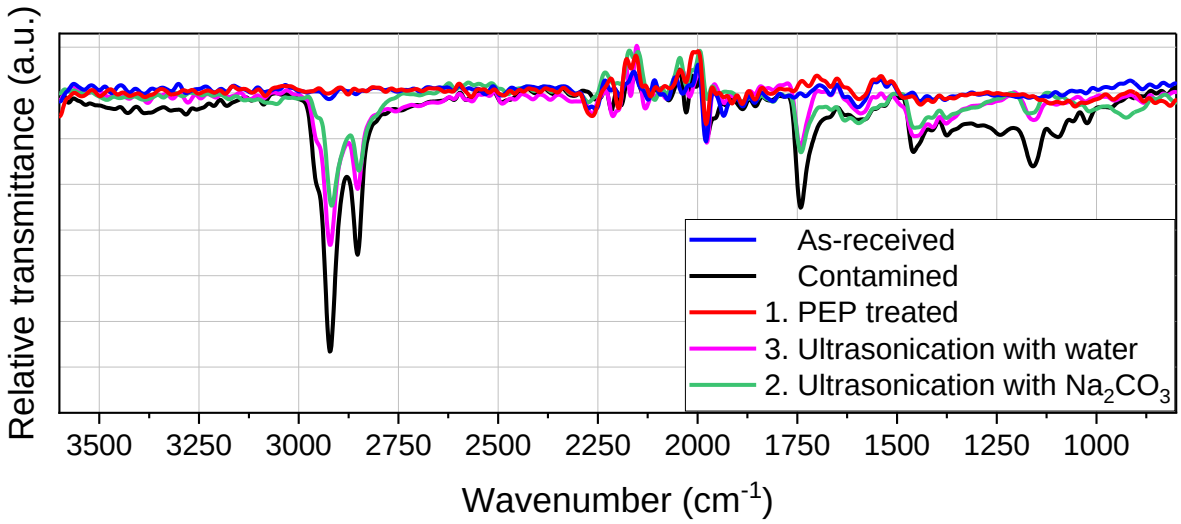

Figure 4.21 (a) ATR-FTIR spectra of as-received, contaminated, and cleaned inserts' surfaces.

The contamination remaining on the tool surface after various pretreatments was characterized by ATR-FTIR. This was then compared to both a contaminated tool without any cleaning and an as-received tool that underwent the standard cleaning procedure at the manufacturer, as depicted in Figure 4.21. In the contaminated tool without any cleaning procedure (black curve), several peaks have been identified that can be attributed to organic groups, summarized in Table 4-7.

Table 4-7 FTIR band assignment of insert surface

Wavenumber (cm^{-1})	Band assignment	Ref.
2955	Asymmetric CH_3 stretching	[166]
2923	Asymmetric CH_2 stretching	
2853	Symmetric –C–O stretching	
1744	C=O stretching from ester	[167]
1459	Symmetrical CH_3 bending	[168]
1104	C–O stretching	[169, 170]
1030	C–O stretching	

Three peaks at 1030, 1104, and 1744 cm^{-1} indicate the formation of oxidized hydrocarbon compounds from thermally aged grease from the reference contamination. After both ultrasonication processes (2 and 3), there was no chemical change in the spectra; however, the signal intensity decreased due to a reduction in contamination. The spectrum of the PEP-treated tool (red curve) did not exhibit peaks associated with contamination, similar to the spectrum of the as-received tool surface. For a more refined detection of residual surface contaminants, XPS analysis was employed on both the as-received and PEP-treated tool surfaces.

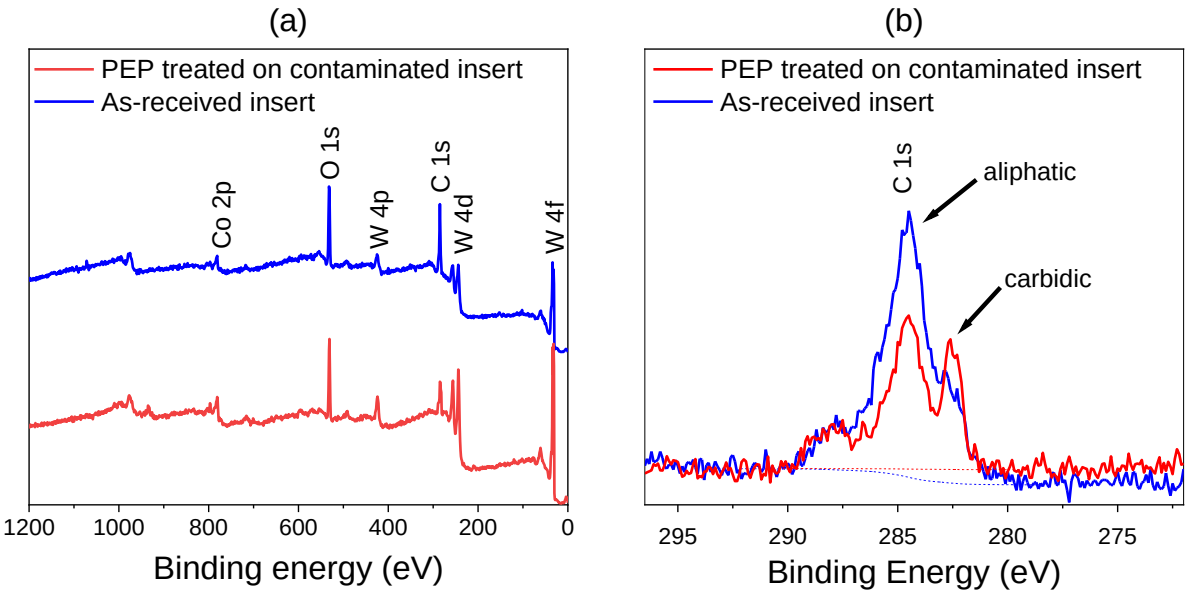

Figure 4.22 (a) XPS survey spectra of as-received and PEP-treated inserts. (b) High-resolution XPS spectra of carbon (C 1s) (Adapted from Ref. [89]).

XPS survey spectra of PEP-treated and as-received insert tools are shown in Figure 4.22(a), demonstrating the presence of several elements, including Co, O, W, and C, on both surfaces. Figure 4.22(b) shows that the C 1s peak obtained from the as-received tool surface primarily contains aliphatic carbon from contamination. On the other hand, after the PEP treatment, the aliphatic peak is effectively reduced, and the carbide peak from WC at 282.8 eV becomes more pronounced. The results from XPS analysis confirm that the PEP pretreatment effectively removes contamination from WC-Co tool surfaces.

4.3.1.5 Effect on tool cutting edge

A cutting tool's edge radius is one of the most significant parameters for the machining process since it affects chip formation, minimum chip thickness, cutting forces, tool wear, and, eventually tool's service life [171]. Commercial tools are manufactured with finely tuned cutting edge in the micrometer range to ensure optimum performance. The PEP process in the commercial tool manufacturing process will be applied after the micro-geometry configuration step. Thus, after the PEP process, it is crucial to maintain the micro definition of sharp edge and effectively remove the surface contamination. Consequently, this section first provides a quantitative evaluation method for the cutting-edge radius. Then, the result of the parameter study will be provided to optimize its micro-geometry as a cutting tool. The edge radius in Figure 4.23(a) is determined by the method described in the previous section at varied process parameters, as listed in Table 4-8.

Table 4-8 PEP process parameters

Process no.	Voltage (V)	Time (s)
1	90	100
2	95	100
3	100	100
4	105	100
5	110	100
6	110	40 s (3 times rotation)

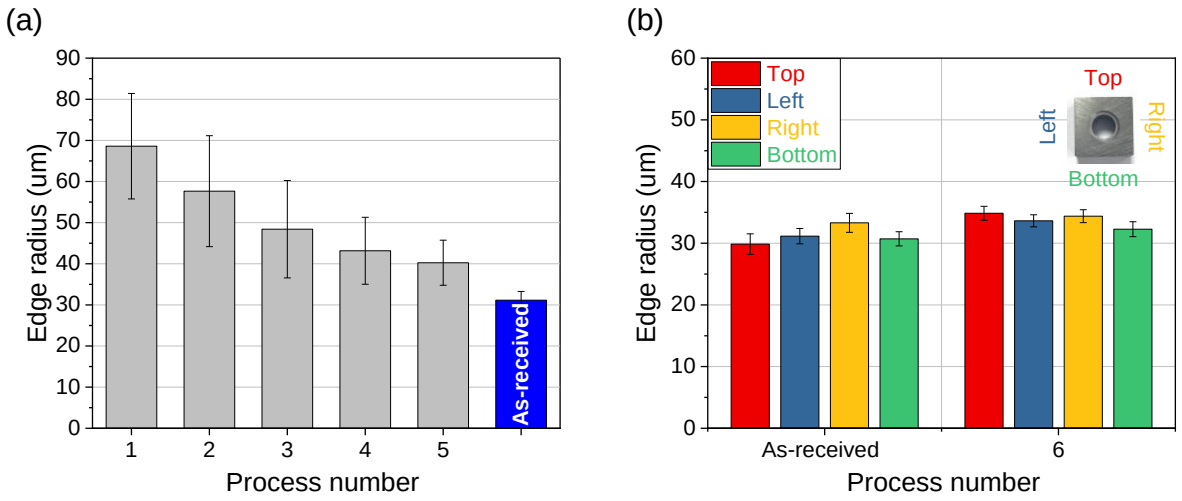

Figure 4.23 (a) Comparative cutting-edge radius for as-received inserts and PEP-treated inserts under Processes 1-5 (voltage variations between 90 V and 110 V). (b) Comparison of cutting-edge radius on all four orientations of the tools before and after the PEP Process 6.

As depicted in Figure 4.23(a), all tools subjected to the PEP treatment (Processes 1 – 5) display an increased edge radius in comparison to the as-received tool. This change can be attributed to material dissolution during the PEP process. Additionally, this edge smoothing effect diminishes as the process voltage rises from 90 V to 110 V, suggesting a decreased material dissolution rate at elevated process voltages. Vopat et al. [172] and Danilov et al. [74] also observed the same phenomena occurring on sharp edges of cemented carbide cutting tools when applying a plasma electrolytic process in the ammonium sulfate electrolyte. In addition, Parfenov et al. found that stainless-steel corners dissolved more rapidly than flat surfaces after PEP [16]. They also observed a decrease in the dissolution rate with an increase in applied voltage. The phenomenon can be explained by the development of thicker VGE layers around the workpiece at increased voltages, which in turn suppress current flow at its edge and causes a reduction in material removal rate. Eventually, with increased process voltage after the PEP process, the edge smoothing effect becomes less pronounced. Figure 4.23(a) shows relatively wide error bars. This is primarily due to the varying dissolution with a vertical orientation of the tool workpiece. Lower dissolution is observed on the upper part of

the carbide insert. Gaseous films are formed around the workpiece surface by the coalescence of bubbles resulting from electrochemical reactions and vapor bubbles created by evaporating electrolytes. Because the bubbles in the VGE are forced to move upward due to buoyancy force, the dissolution rate is expected to vary with the orientation of the tool's surface owing to the inhomogeneity of VGE thickness over the tool geometry. Therefore, with the increasing PEP process time, the geometrical inhomogeneity in the vertical direction becomes more pronounced [16, 173]. To compensate for the inhomogeneity and reduce the PEP process time, insert tools were successively turned thrice by an angle of 90 º after every 10 s of treatment time. Figure 4.23(b) shows the resulting edge radius of four sides of the tool before and after PEP treatments with three rotations at 110 V. As a result of the significant reduction in error bars, the tool rotating procedure proved successful. Furthermore, the reduction in the process time from 100 s to 40 s is clearly beneficial for minimizing the deformation of the tool shape because the edge radius of the insert only slightly increased from 32 µm to 34 µm after the PEP process. As a pretreatment step before coating, these optimized process parameters are applied to the contaminated inserts.

4.3.2 Assessment of the coated tools

This section presents tribological analysis on the coated tools to examine the influence of the PEP process on the adhesion between the tool surface and the hard coating, and its consequent impact on the tool's lifetime. At first, tribological evaluations were performed with a lab-manufactured TiN layer deposited on the PEP-treated tool surface. Subsequently, in the following section, the PEP-treated tools were coated with an AlTiSiN layer by industrial equipment, with the aim of evaluating its industrial feasibility.

4.3.2.1 Performance evaluation of TiN-coated cutting tool

A TiN layer was deposited on the PEP-treated tool surface, and then a machining test was performed to determine whether the PEP process increases tool life by improving adhesion. Table 4-9 summarizes the variation in cleaning and coating processes. For each process combination, two inserts were utilized. Furthermore, every insert was evaluated thrice for the tool assessment to verify reproducibility and obtain the mean value. To prepare the tool for Process 1, ultrasonically cleaning with acetone and isopropyl alcohol was used as a conventional atmospheric pretreatment. Meanwhile, for Processes 2 and 3, PEP was conducted to pretreat the grease-contaminated tools. The plasma fine-cleaning followed by TiN deposition was then performed using the same process parameters listed in Table 4-1. For Process 3, plasma fine-cleaning was not performed before the deposition of TiN layers.

Table 4-9 Overview of cleaning and coating processes on the tools

Process No.	Reference contamination	Atmospheric pretreatment process		Vacuum process	
		Ultrasonic cleaning	PEP	Plasma fine-cleaning	TiN deposition
1		O		O	O
2	O		O	O	O
3	O		O		O

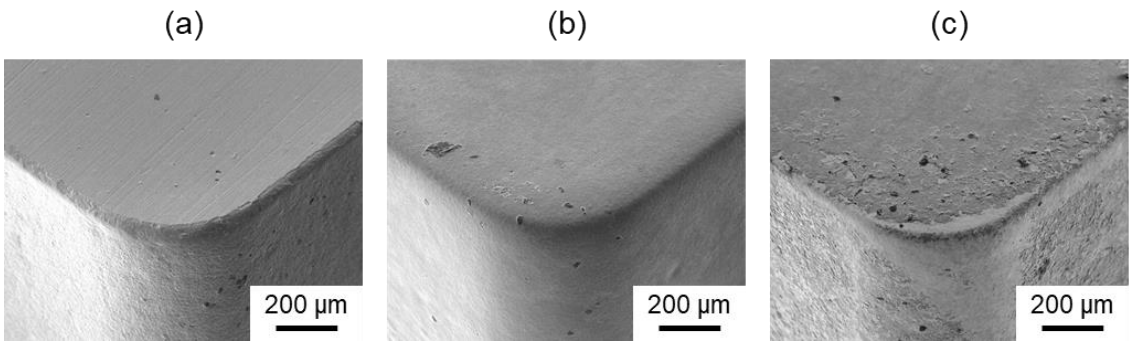

Figure 4.24 SEM images of the insert tools; (a) Process 1, (b) Process 2, and (c) Process 3.

As shown in Figure 4.24, the SEM analysis was performed on TiN-coated tools with various parameters listed in Table 4-9. Without the plasma fine-cleaning process, the TiN layer was significantly delaminated from the tool surface due to remaining contamination, as depicted in Figure 4.24(c). Conversely, as shown in Figure 4.24(a) and (b), no noticeable peeling was observed from the TiN-coated tools since the plasma fine-cleaning process is beneficial for adhesion between the TiN layer and tool surface by removing residual contamination.

Figure 4.25 shows the results of the scratch tests with Processes 1–3. This method uses a Rockwell C diamond indenter to indent the specimen over a distance of s = 10 mm with increasing normal force F_{N} = 100 N. The scratch test records normal and tangential forces and acoustic emission signals, allowing for the detection of layer defects. The adhesive strength is assessed by employing the critical load values: L_{C1}, L_{C2}, and L_{C3} as described in section 4.2.3.1. Coating adhesion is typically described by the L_{C2} value. In the case of the tool with Processes 1 and 2, further analysis by light microscopic images was required due to the small deflections of the signals. Thus, the signals from the scratch test could be compared using the images shown in Figure 4.25(d)–(f). These results allowed the first spalling points of the coating to be determined, which are indicated by green circles. As a result of these investigations, the PEP-treated tool (Process 2) showed slightly higher adhesive strengths than the tool treated with the conventional cleaning method (Process 1). However, the coated tool without the plasma fine-cleaning step (Process 3) shows significantly lower adhesive strength than the other coated tools, which were fine-cleaned.

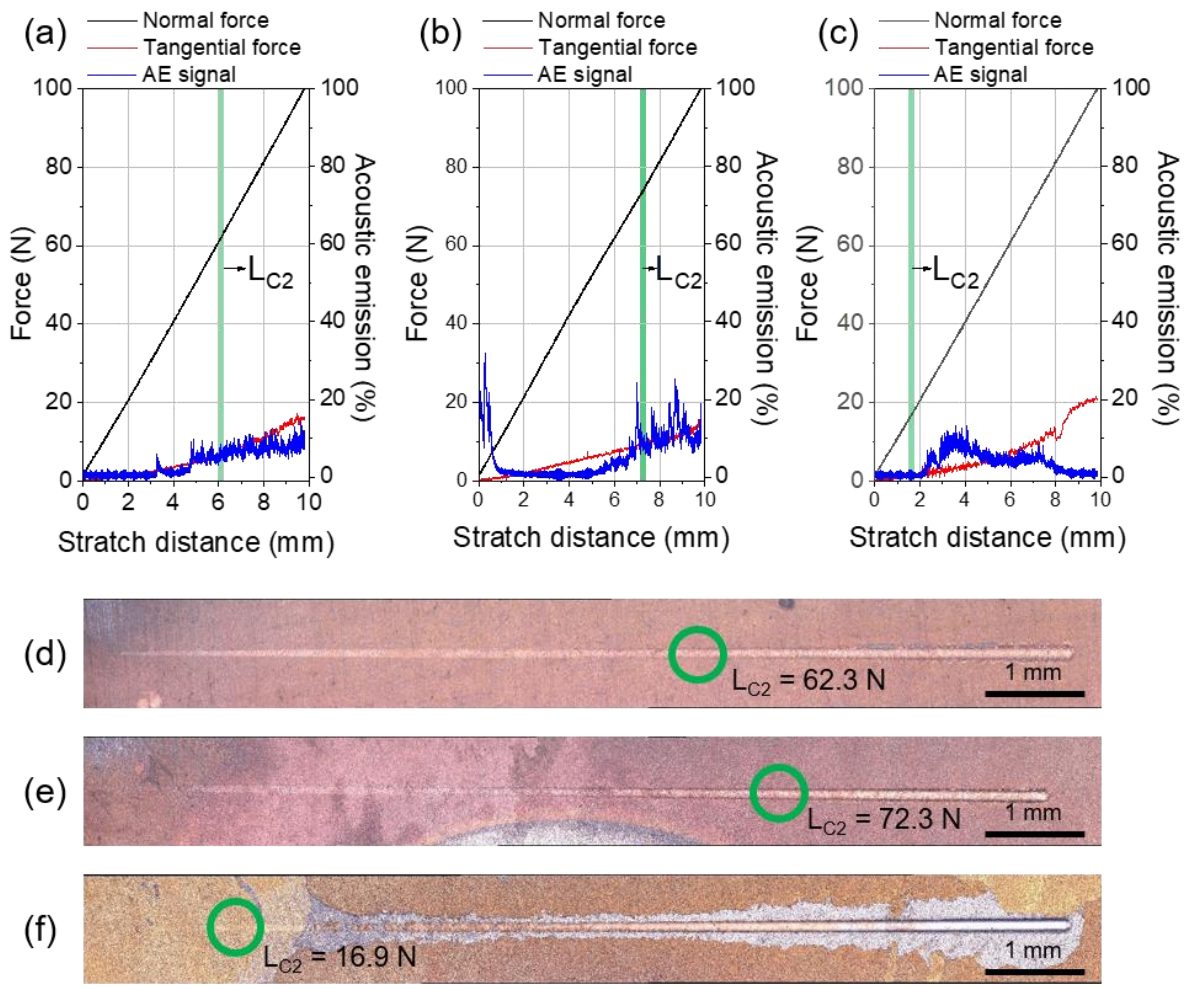

Figure 4.25 Scratch test results for coated turning tools with each Process - Process 1: (a), Process 2: (b), and Process 3: (c). Green lines in the graphs represent L_{C2}. Images of the scratched areas corresponding to each process - Process 1: (d), Process 2: (e), and Process 3: (f). Green circles in the images mark the L_{C2} point.

Figure 4.26 shows the results of the machining tests of the tools and the scratch test results on layer adhesion. Lower values are obtained for the average tool life of the tools with the conventional pretreatment method (Process 1): $t_{VB0.3}$ = 44 min and adhesive strength of L_{C2} = 58 N. The coated tool with PEP pretreatment (Process 2) achieved an average tool life of $t_{VB0.3}$ = 58 min, which is longer than the tool with Process 1 since the PEP process led to a higher layer adhesive strength L_{C2} = 65 N than the coated tool with the conventional cleaning process, despite the coated tool being heavily contaminated at first. Conversely, the coated tool without the fine-cleaning step (Process 3) has an almost identical tool lifetime as the uncoated tool due to its deteriorated adhesive strength.

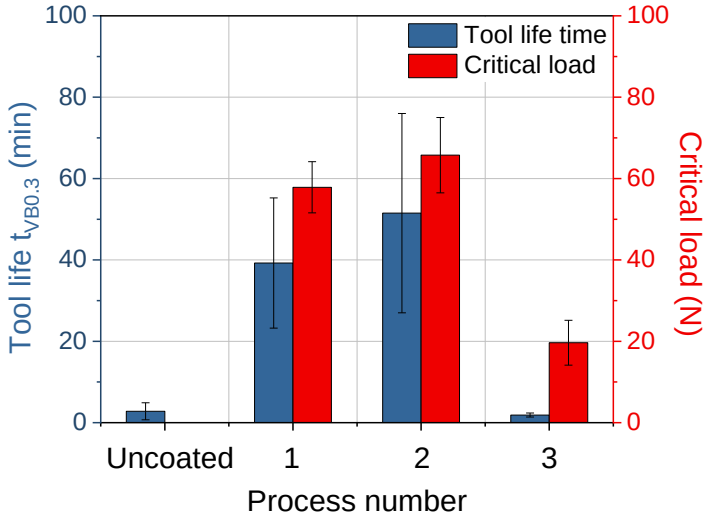

Figure 4.26 Comparison of tool life time ($t_{VB0.3}$) and critical load.

4.3.2.2 Performance evaluation of AlTiSiN-coated cutting tool

The tools were coated with the AlTiSiN layer employing a commercial magnetron sputtering system from the company A+S (see Figure 4.7) to verify the pretreatment effect of the PEP process and determine whether it could be feasible for commercial applications. Table 4-10 summarizes the variation in the cleaning and coating processes.

Table 4-10 Overview of cleaning and coating processes on the tools

Process No.	Reference contamination	Atmospheric pretreatment process		Vacuum process
		Commercial wet-chemical process	PEP	Plasma fine-cleaning and AlTiSiN deposition
1		O		O
2	O	O		O
3	O		O	O

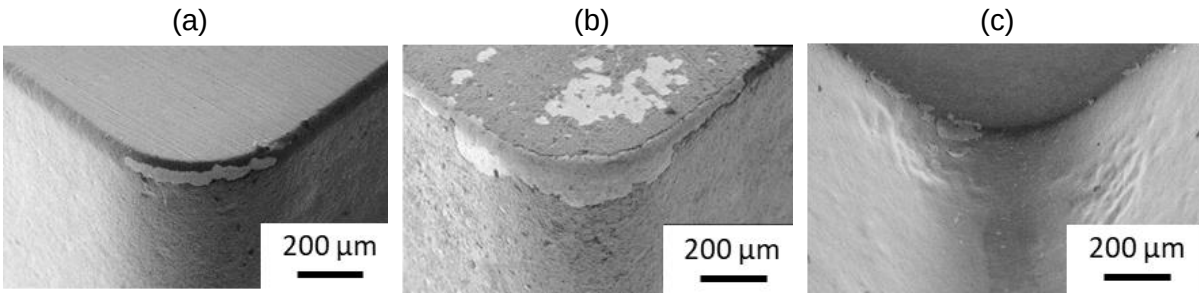

Figure 4.27 SEM images of the insert tools; (a) Process 1, (b) Process 2, and (c) Process 3

After the cleaning and coating processes described in Section 4.2.2.2, the coated tools were examined by SEM, as depicted in Figure 4.27(a)–(c). As shown in Figure 4.27(b), significant

delamination of the coating layer from Process 2 is observed in the cutting edge and rake face area since the contamination could not be thoroughly removed by the wet-chemical-based industrial standard cleaning process. It is also observed that the coated tools with Processes 2 and 3 have coating delamination to some extent due to minor residual contamination, as depicted in Figure 4.27(a) and (c), respectively.

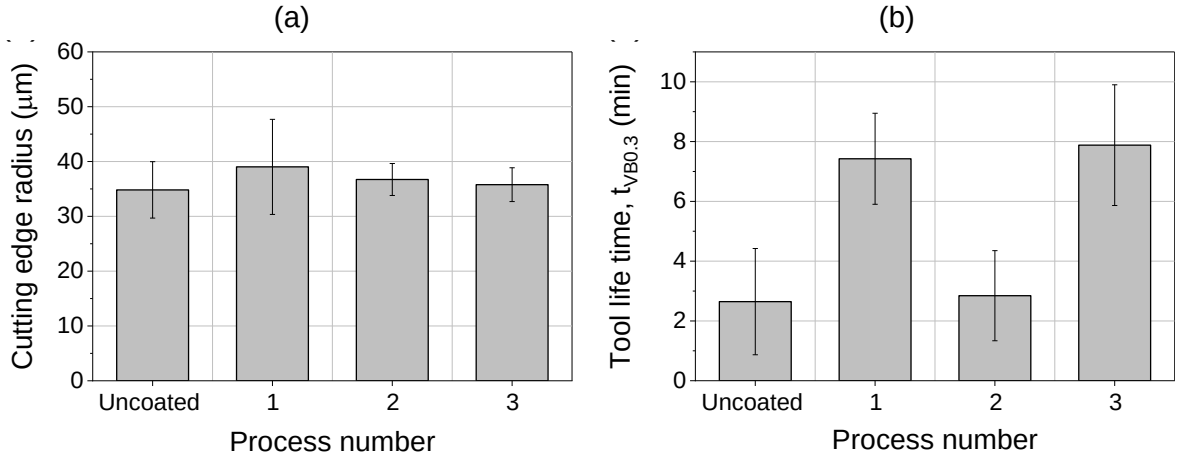

Figure 4.28 Comparison of (a) cutting-edge radius and (b) tool life $t_{VB0.3}$ and critical load.

The previous section has already demonstrated that the PEP process considerably alters the tool's cutting edge, affecting the tool's service life. Therefore, it is necessary to measure the cutting-edge radius of the coated tools prior to investigating the tool lifetime to ensure that it is within the appropriate range. Under each set of process conditions, two inserts were employed. Additionally, to ensure reproducibility and obtain the average value, all four edges of each insert were examined. As depicted in Figure 4.28(a), the cutting-edge radius of the uncoated tool is ~34.8±5.1 µm. The cutting-edge radius of coated tools with varying cleaning procedures (Processes 1–3) does not significantly differ from the cutting-edge radius of uncoated tools. Particularly, PEP treatment did not appear to have affected its micro-geometry significantly. The machining process was then conducted to ensure how long the tool would last. The same parameters were used for the machining test, as described in the previous section. Figure 4.28(b) shows the lifetime of the tools after reaching the wear mark width of VB = 0.3 mm. The uncoated tool has the shortest service life at $t_{VB0.3}$ ≈ 2.8 min. The coated tool with Process 2 showed $t_{VB0.3}$ ≈ 3 min, similar to the uncoated tool, since the hard coating barely adheres to its surface, as shown by SEM analysis. Meanwhile, the tool lifetime with Process 3 is approximately 8 min, comparable to that of a coated tool treated only with conventional cleaning (Process 1) since the adhered hard coating layer reduces tool erosion. Accordingly, the PEP process can enhance layer adhesion and provide a good cleaning performance. Furthermore, even though the coated tool lifetime with the PEP process is similar to that of the industry standard cleaning method, PEP has the advantage of being an environmentally friendly and highly effective cleaning method since it enables the removal of substantial amounts of contamination that a commercial cleaning method cannot.

4.4 Conclusions

The investigation has been carried out to test whether the PEP process can be used as a pretreatment step for cleaning WC-Co-based tool surfaces employing surface characterization and mechanical performance assessment with hard coating application. Various parameters, including voltage, process duration, electrolyte type, concentration, and temperature, have been examined for further process optimization aimed at selective elemental dissolution and minimizing shape deformation at the cutting edge by controlling the material dissolution rate. A preliminary investigation has been conducted using two different electrolytes ($(NH_4)_2SO_4$ and Na_2CO_3) and has shown that W on the tool surface can readily be dissolved in Na_2CO_3, owing to the alkaline environment facilitating the dissolution of WO_3. Thus, Na_2CO_3 has been chosen as the electrolyte for further investigation. Regarding the voltage variation, the PEP treatment at 110 V is associated with a dissolution of WC rather than surface oxidation, which favorably occurred at the voltage of 30 V and 200 V. As a result of the selective dissolution of WC, the relative Co atomic content on the tool surface measured by XPS increased from 6.5 at% to 18.2 at% after the PEP process. Furthermore, excessive material dissolution on the cutting edge of tools can be prevented by controlling the process parameters. Additionally, by varying the workpiece orientation during treatment, the uniformity of the tool edge radius can be significantly improved. Defined contamination was applied to the tool surfaces and then treated using the optimized PEP process to investigate the surface decontamination effect of the PEP process. ATR-FTIR and XPS analyses indicated an efficient removal of the contaminants as less contamination remained on the surface than on the as-received insert.

In order to verify whether the PEP pretreatment process could benefit the coated tools' performance, two different types of hard coatings were deposited on the PEP-treated tools, and then machining tests were performed: a TiN layer was deposited using R-HiPIMS in combination with PBII for a surface preconditioning process. The machining test results showed that coating adhesion could be increased in addition to enhanced cleaning performance, resulting in improved cutting performance. With a conventional cleaning method, the coated tool had an adhesive strength of 58 N and a tool life of 44 min, whereas coating the tool with PEP improved its adhesive strength and tool life to 65 N and 58 min, respectively. To evaluate the PEP process for industrial relevance, the AlTiSiN layer was commissionally applied using a commercial standard method. To determine the tool service life ($t_{VB0.3}$), a machining test was carried out based on the wear mark width criterion of *VB* = 0.3 mm. The coated tool, when inadequately cleaned, showed a service life ($t_{VB0.3}$) of roughly 3 min, similar to its uncoated insert tools. However, PEP-treated coated tools exhibited a lifespan of about 8 min, comparable to tools processed through industry-standard methods. This underscores the efficacy of the PEP process in eliminating contamination from the tool's surface before coating.

The results of this research provide fundamental insight into the PEP process, particularly influence on the surface of WC-Co based cemented carbide materials. PEP can be an innovative and highly efficient pretreatment method for a sustainable tool production chain. Nevertheless, this chapter focuses primarily on material characterization prior to and after PEP. Thus, the following chapters describe an investigation of synchronous electrical and thermal diagnostics methods integrating material analysis to characterize the PEP process.

5 Process diagnostics for plasma electrolytic polishing (PEP)

In the previous chapter, the plasma electrolytic polishing (PEP) has been demonstrated as a practical method for surface pretreatment on cemented carbide, with various surface characterizations performed before and after the process. As an extension of the previous chapter, the underlying mechanisms of the PEP process are examined more closely in this chapter. Various diagnostic methods, such as thermal, optical, and electrical analyses, are employed to characterize the dynamics of the gaseous layer associated with discharge behavior.

5.1 Introduction

As it was shown in previous section 4.3.1.2, when the process voltage exceeds a critical voltage during the PEP process, the workpiece is covered by a vapor gaseous envelope (VGE) layer owing to evaporation of the surrounding electrolyte accompanying intensified discharge emission. When the VGE is formed around the anodic workpiece surface, the system consists of three phases: metallic anode, vapor layer, and liquid electrolyte. As a consequence of the low conductivity of the continuous VGE layer, the electrical current drops significantly. This voltage regime is typically chosen for the plasma electrolytic surface treatment [16, 40, 174]. When the VGE layer is present, the input electrical power mostly dissipates in the VGE layer. The following contributions balance this dissipated power: heating the workpiece, generation of plasma, and (electro)chemical reactions (exothermic and endothermic). The dissipated power is partially transferred to the bulk electrolyte maintaining stable interface between the bulk electrolyte and the VGE. The VGE layer separates the anodic workpiece from the aqueous electrolyte, allowing the workpiece to be heated. To our knowledge, only a few studies [153, 175] have been published regarding plasma electrolysis that measures the temperature during the process. These publications focus on a high-temperature treatment for surface carburizing, nitriding, or oxidizing applications, with temperatures reaching 1000 °C at the voltage and current density of 250 V and 0.015 A/mm^2. During anodic plasma electrolysis, the uniform distribution of the VGE layer along the workpiece in the longitudinal direction is essential since it directly affects the dimensional homogeneity of the workpiece, which is particularly important for precision tool applications. The previous chapter demonstrated the PEP process's feasibility for WC-Co-based cemented carbide pretreatment. In the PEP process, the stability of the gaseous layer influences the material removal rate, geometrical homogeneity, and surface composition. It is essential to comprehend the energetic aspects of the process attributed to gaseous layer evolution to obtain the desired results on the surface of the workpiece using the PEP process.

Thus, this chapter offers a comprehensive investigation of various aspects of the PEP process. Synchronous electrical and thermal measurements are used to characterize the temporal evolution of the VGE layer during the PEP process of WC-Co based material. The variation of power towards a cylindrical workpiece surface at different electrolyte immersion depths (5 mm – 20 mm) is investigated using a calorimetric probe method, which employs the time

derivative of the temperature curve measured both during and after the PEP process. Additionally, the efficiency of power consumption at different workpiece treatment areas was evaluated, and it was related to the evolution of the surrounding electrolyte temperature. As a complementary approach, the temperature of the surrounding electrolyte is measured and a hydrodynamic model, developed with the help of COMSOL Multiphysics® software, is employed to ascertain the heat transfer to the electrolyte based on the measured temperature of the surrounding electrolyte. Furthermore, an XPS line scan analysis is carried out to investigate the PEP process's influence on the consistency of the workpiece's elemental composition along the vertical axis. In the later sections of this chapter, the intricate interplay between electrical and gas layer dynamics during the PEP process is explored. Synchronized electrical and high-speed camera measurements are employed to examine the correlation between the temporal behavior of the non-linear load character of the current waveform and the gas layer dynamics captured by the high-speed camera. Additionally, a spatially resolved analysis of the high-speed camera signal is conducted, and its significance for the longitudinal compositional gradient in relation to the spatial discharge emergence associated with the VGE development.

5.2 Experimental setup and model description

This section provides an experimental setup for the PEP process, accompanied by a description of various diagnostic techniques, encompassing thermal, optical, and electrical measurements. Additionally, this section incorporates the calorimetric method employed for determining power transferred to the workpiece and also offers a description of two dimensional hydrodynamic modeling.

5.2.1 Plasma electrolytic polishing

A schematic illustration of the PEP experiment setup is shown in Figure 5.1(a). Even though the experimental parameters resemble those used in the previous section, the PEP equipment has been modified to better accommodate process diagnostics, facilitating easier process monitoring and the integration of diagnostic instruments. The workpiece is a cylindrical cemented carbide rod (DK460UF, Gühring KG) with a central, axially symmetric hole (coolant duct). The diameter and height of the rod are 16 mm and 20 mm, respectively, and it is primarily composed of WC (~90 wt%) and Co (~10 wt%). A stainless-steel rod (Ø5 mm) is welded to the upper part of the workpiece for fixation with sufficient electrical conduction. This rod is connected to the positive output voltage of a DC power supply. The power supply employed here (PowerRack, MUNK GmbH) can deliver 500 V and 200 A. The workpiece is immersed in a glass beaker of 3 l volume filled with 2.5 l of a 10 wt% Na_2CO_3 electrolyte. A heating plate (C-Mag HS 7, IKA) is employed to heat the electrolyte solution to 70 °C. The electrolyte was not stirred or mixed in any other way, except for the partial mixing that occurred due to boiling. A perforated steel cylinder next to the inner wall of the beaker serves as a cathode, and a 40 mm axial gap is left in the cylinder to facilitate visual inspection of the anode region. Workpiece immersion depths (*d*) were varied from 5 mm to 20 mm, thus effectively increasing the active workpiece surface area, as specified in Figure 5.1(b). A voltage of 120 V

was applied for 30 s during the PEP process, leading to discharge currents between 2 A and 20 A, depending on the value of immersion depth, *d*.

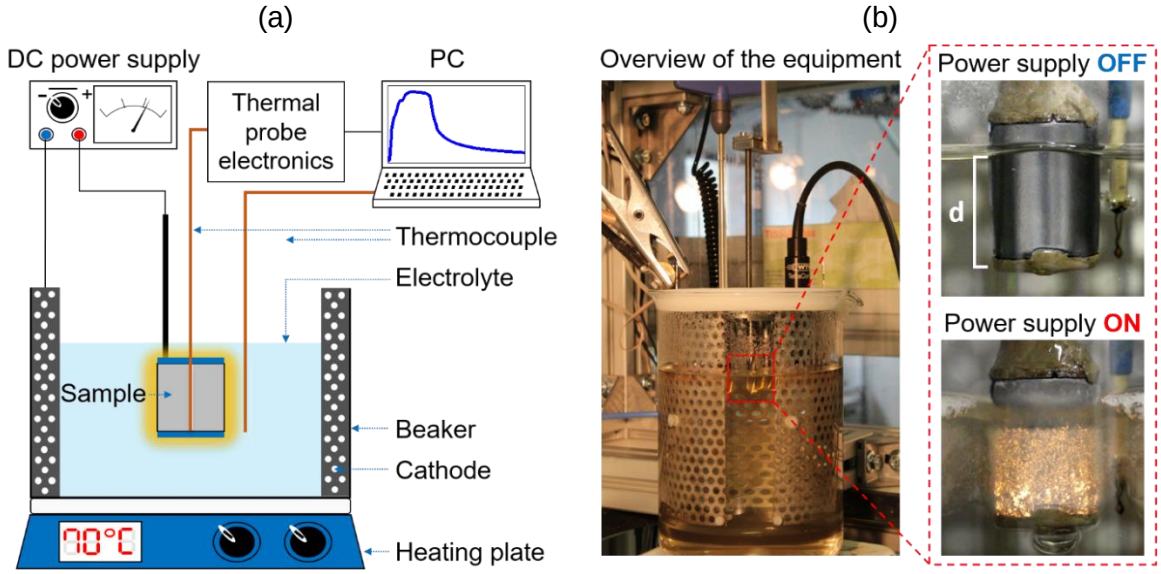

Figure 5.1 (a) Schematic illustration of the experimental setup. (b) Photograph of PEP apparatus (left) and enlarged photographs of the workpiece in the electrolyte without PEP and during PEP (right) with indicated immersion depth, d (reprinted from [176]).

5.2.2 Temperature measurement of workpiece and electrolyte

A type K thermocouple, positioned in the workpiece's central hole, was used to measure the bulk temperature during the PEP process. This thermocouple is connected to data acquisition electronics that have a galvanic insulation of up to 5 kV, enabling to record the temperature at a frequency of 90 Hz with a biased anodic workpiece. In Ref. [177], the data acquisition process is described in detail. The top side of the central hole was sealed to prevent direct contact with the electrolyte for measuring the temperature of the workpiece, while an epoxy sealant (MD MIX METALL, Marston-Domsel GmbH) was used on the other side to block the hole. During the PEP process, the plasma generated in the vapor phase near the workpiece interacts with its outer surface, while the workpiece temperature is measured on the inside. This can result in a temperature variation between the inside and outside of the workpiece. To discern this discrepancy, the temperature evolution within the workpiece was simulated using COMSOL Multiphysics® software, which solved the heat transfer equation in cylindrical coordinates. All values for the workpiece properties, specific to tungsten, were sourced from the COMSOL Multiphysics® database. As depicted in the schematic representation of the modeling domain for the workpiece in Figure 5.2(a), the bottom surface of the workpiece is insulated in the experiment; therefore, a no heat flux boundary condition is applied in the model. The sidewall temperature is predefined using a time-dependent function that is similar to the shape of the measured temperatures. A comparison between the wall temperature and the modeled temperature at the measurement position can be seen in Figure 5.2(b). It is evident that both temperatures follow almost identical profiles.

The only notable difference is the duration it takes for the inner point to match the temperature of the workpiece wall. This disparity is a maximum 0.2 s, which is practically negligible when compared to the total time interval.

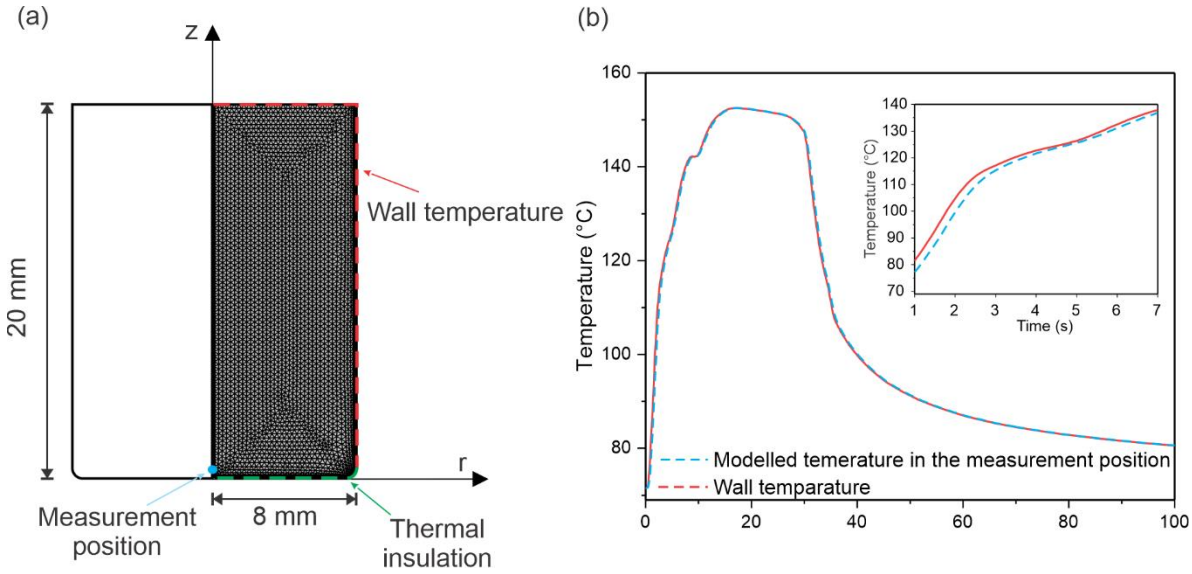

Figure 5.2 (a) A schematic representation of the modeling domain for the workpiece, including the computational mesh. (b) A comparison is presented between the wall temperature and the temperature simulated by the model at the measurement location.

Therefore, the internal temperature measurements remain viable for subsequent thermal evaluation on the workpiece surface incorporating the development of the plasma-vapor layer during the PEP process. For temperature monitoring of the electrolyte in the vicinity of the workpiece, a type K thermocouple was deployed at a 15 mm distance from the bottom end of the workpiece. The temperature data was then acquired utilizing a digital multimeter (VOLTCRAFT VC 960).

5.2.3 Evaluation of transferred power to the workpiece

Using the calorimetric probe, various methods have been developed for evaluating the energy flux towards a substrate and adapted successfully to low pressure and atmospheric-pressure plasmas [143, 177-180]. Here the evaluation procedure for the power transferred to the anodic workpiece in the liquid environment during the PEP process will be described. During the heating ($\dot{T}_s$, power supply on) and cooling ($\dot{T}_c$, power supply off) phases, the power toward a workpiece is determined by the relation between the time-derivative of the substrate's enthalpy ($\dot{H}$) and the time-derivative of its temperature ($\dot{T}$).

Heating $$\dot{H}_h = C_s\dot{T}_h = P_{in} - P_{out,h} \quad 5.1$$

Cooling $$\dot{H}_c = C_s\dot{T}_c = -P'_{out,c} \quad 5.2$$

The heat capacity (C_s.) of the cemented carbide cylinder was investigated through a calibration procedure utilizing a Dewar flask. Further details on this method will be presented later. $P_{\mathrm{out,h}}$ and $P'_{\mathrm{out,c}}$ represent the power dissipated from the substrate during the heating and cooling processes, respectively. P_{in} represents the power transferred to the substrate during PEP. Assuming both loss terms during the heating and cooling phases are equal ($P_{\mathrm{out,h}}$ and $P'_{\mathrm{out,c}}$), Equations 5.1 and 5.2 can be expressed as:

$$P_{in} = C_s(\dot{T}_h - \dot{T}_c) \qquad 5.3$$

Therefore, according to Equation *5.3*, the mean power values resolved by temperature can be obtained using the time derivative of the temperature curve (*dT-depiction,* [181]).

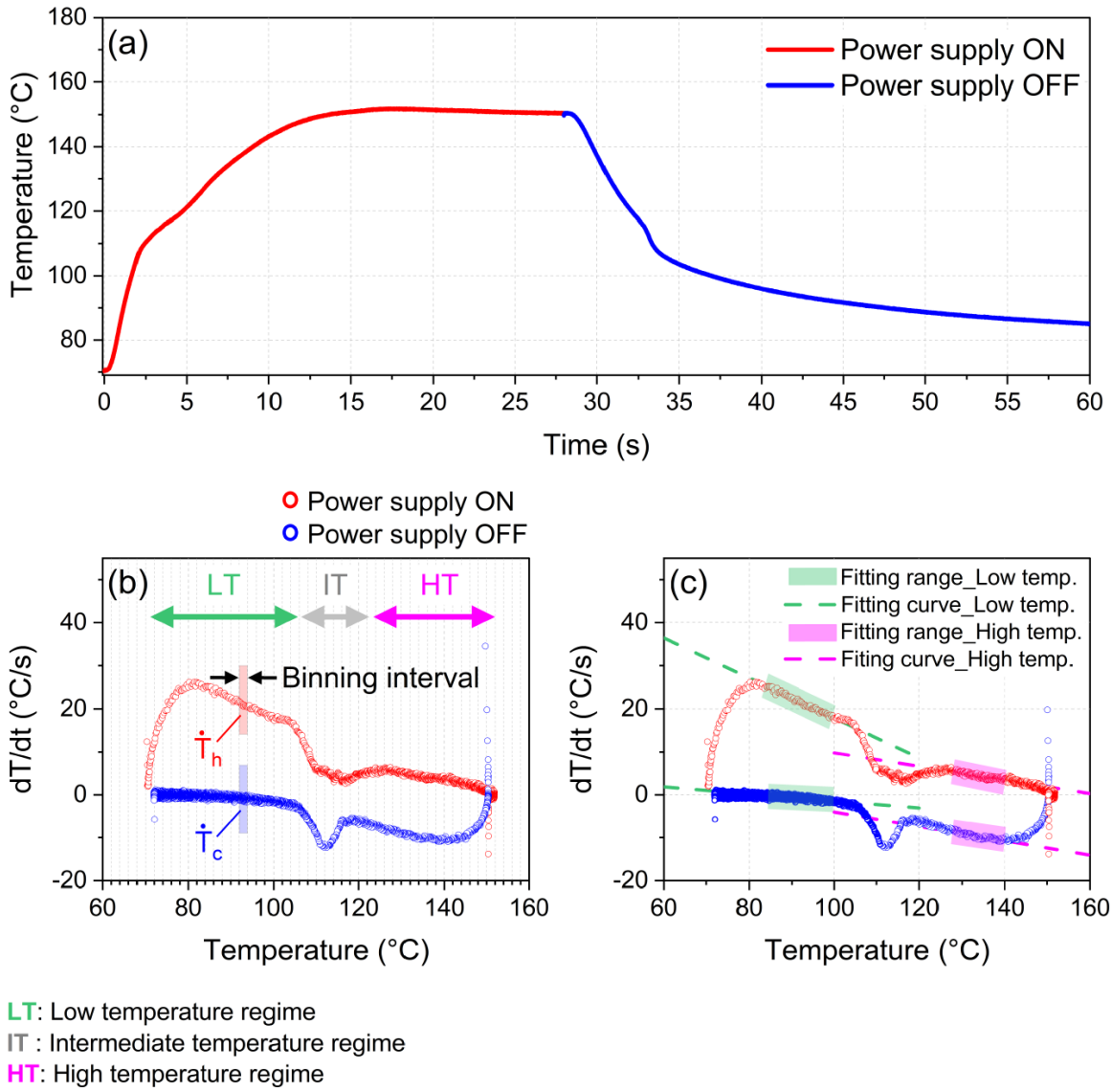

Figure 5.3 An example of assessing the power transfer to a workpiece: (a) measured workpiece temperature over time. The time-derivative of the temperature curve over time (dT-curve) for two methods: (b) binning and (c) linear interpolation (reprinted from [176]).

Figure 5.3(a) displays the change in anodic workpiece temperatures over time and when the power supply is on (red) and off (blue). To determine the incoming power to the anodic workpiece (P_{in}), two different analysis methods: binning and interpolation have been employed on the *dT-depiction* as displayed in Figure 5.3(b) and (c), respectively. Figure 5.3(b) illustrates the division of temperature regions for the *dT-curve* into three distinct areas: the low temperature region (LT), the intermediate temperature region (IT), and the high temperature region (HT). The LT region is below the onset of the VGE generation, while the IT region is associated with the boiling point of the electrolyte and the formation of the VGE. The HT region is characterized by the presence of a relatively stabilized VGE. Using the *dT-depiction*, the mean power values resolved by temperature can be obtained through the binning method, as shown in Figure 5.3(b), employing the time-derivative of temperature curves during heating ($\dot{T}_{\mathrm{h}}$, marked red) and cooling ($\dot{T}_{\mathrm{c}}$, marked blue) within bins with 2 °C intervals as shown in Figure 5.3(b). Temperature binning allows temperature and time-resolved evaluations, minimizing systematic errors caused by the temperature-depending cooling process. A bin width of 2 °C was chosen to minimize systematic errors while maintaining enough data points to compute mean values and standard deviations meaningfully. A linear interpolation fitting can also be used to evaluate power values, as illustrated in Figure 5.3(c). The linear fits are carried out separately within the selected linear region of the curves for the low-temperature (LT, marked in green) and high-temperature regimes (HT, marked in magenta). The limits of the linear portion are identified as the points where the linear extrapolation curve begins to deviate substantially from the measurement curve. A marked decrease in the R-square value from the fitting process signals that the acceptable data range might be surpassed. Consequently, this decrease is used as a criterion to delineate the limits of the fitting range. A range was deliberately selected to maximize the valid data range while maintaining the adjusted R-square value at an optimal level. This is done for heating and cooling curves separately and in both regions of LT and HT. The intermediate temperature regime (~100 °C ≤ T ≤ 120 °C) was not taken into account for the power transfer evaluation since reproducibility can hardly be achieved within this transient regime owing to the instability of the gaseous layer.

5.2.3.1 Evaluating the low-temperature (LT) regime: challenges and calibration method

When examining the LT regime, meticulous attention is essential due to the following reasons. During the process, the electrolyte's temperature increases, particularly near the anodic workpiece, as detailed in the results and discussion section 5.3.1. This causes the workpiece in the LT region to reach thermal equilibrium with its surroundings at a considerably higher temperature than the initial 70 °C. The workpiece and surrounding electrolyte then cool down together, forming a distinctly different physical system compared to the initial heating (LT) with different loss terms. Consequently, Equation 5.3 is not applicable. However, an additional calibration procedure can provide the appropriate cooling curve for the LT regime. An additional calibration procedure can yield the correct cooling curve pertaining to the LT regime. The following steps describe this supplementary experiment, as demonstrated schematically in the Figure 5.4.

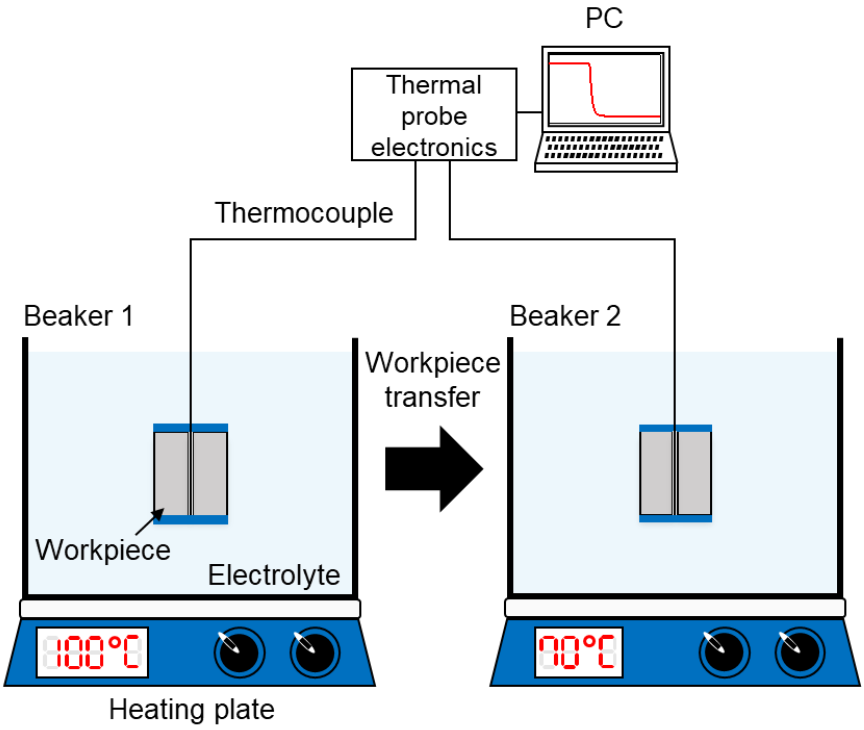

Figure 5.4 A schematic representation of the calibration process for acquiring the cooling calibration curve in the LT regime.

i. Initially, the workpiece is immersed in the electrolyte at 100 °C to raise its temperature to 100 °C, as illustrated in Beaker 1 (left side) of Figure 5.4.
ii. Subsequently, the workpiece is transferred to the 70 °C electrolyte in Beaker 2 (right side) while recording its temperature drop.

In Figure 5.5(a), the monitored temperature decrease from 100 °C to 70 °C is displayed. The temperature data is subsequently converted into a *dT-curve* and contrasted with the *dT-curve* obtained during the cooling stage in the LT regime of the PEP process, as depicted in Figure 5.5(b). The slope of the calibrated curve (red) is steeper and obtains better parallelity with the heating curve (black) in comparison to the uncalibrated curve (blue). The presence of parallel curves indicates that the assumption of similar loss terms for the cooling and heating processes has been fulfilled to a greater extent, establishing it as a necessary precondition. This calibration method ensures similar loss terms for the cooling and heating phases within the LT region. Calibration can be executed just before the plasma process is started and incorporated into the same measurement. Nonetheless, in the HT region, when the VGE becomes stable, the cooling terms during heating and cooling turn out to be analogous, eliminating the need for obtaining a calibration curve.

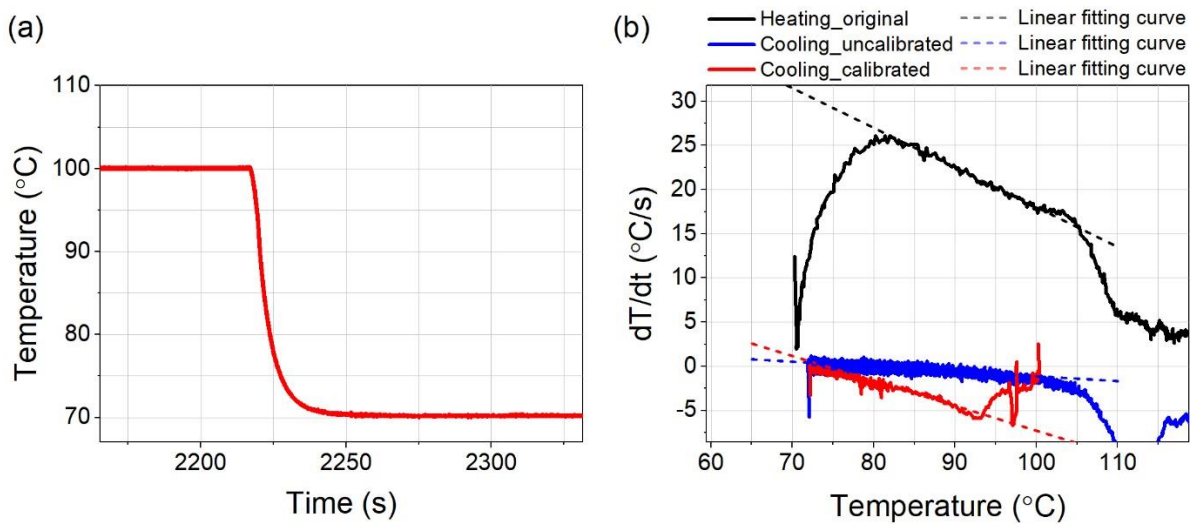

Figure 5.5 Representative curve of the calibration procedure: (a) Recorded temperature as a function of time during the calibration procedure (b) comparison of the dT-depiction between the original cooling curve (blue) and the calibrated cooling curve (red).

5.2.3.2 Determination of workpiece's heat capacity

To evaluate the power transferred to the workpiece (P_{in}), the heat capacity of the workpiece has to be obtained. This section describes the method for obtaining the heat capacity of the workpiece using the given steps.

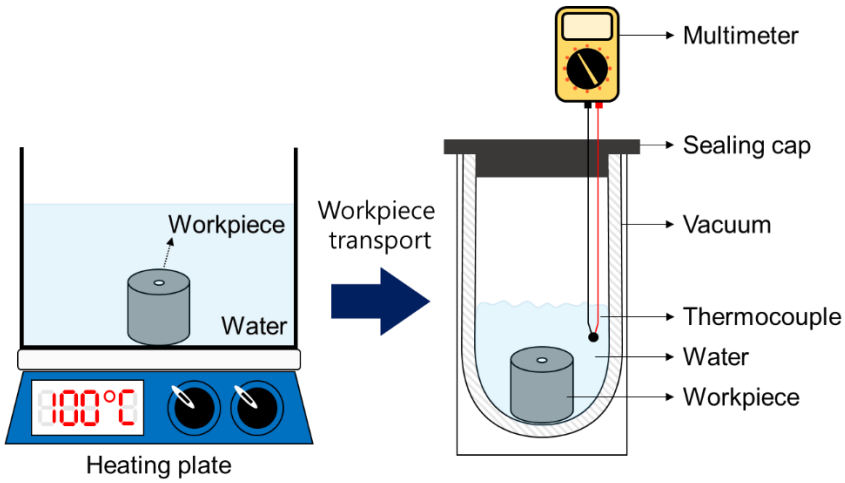

Figure 5.6 Schematic representation of the method used to determine the heat capacity of the workpiece.

Figure 5.6 demonstrates the process for determining the heat capacity of the workpiece. First, the cylindrical cemented carbide workpiece is immersed in boiling water ($T_{\mathrm{w,sat}}$ = 100 °C). When the workpiece temperature reaches the $T_{\mathrm{w,sat}}$, referred to as $T_{\mathrm{s,sat}}$, the workpiece is relocated to a 200 ml double-walled vacuum-insulated container (Dewar flask F 0 C,

KGW-ISOTHERM) filled with 50 g (m_{w}) of room temperature ($T_{\mathrm{w,RT}}$) water, as depicted in the right side of Figure 5.6. Then the water temperature is monitored until it reaches an equilibrium temperature ($T_{\mathrm{w,eq}}$) in the isothermal container by a type K thermocouple connected to a digital multimeter (VC 960, VOLTCRAFT).

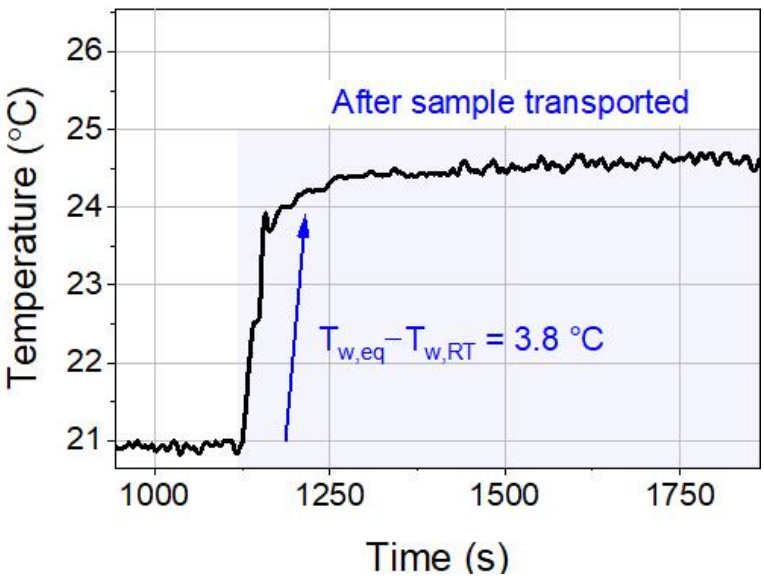

Figure 5.7 Change in the temperature of water in the isothermal container after the heated workpiece has been transferred.

Figure 5.7 presents the monitored water temperature in the isothermal container after moving the workpiece. After transferring the workpiece to the isothermal container, the water temperature increases by 3.8 °C. With the known specific heat capacity of water ($C_{\mathrm{w}} = 4.2$ kJ/kg), the heat absorbed by the water (Q_{w}) is calculated by:

$$Q_w = c_w \cdot m_w \cdot \left(T_{w,eq} - T_{w,RT}\right) \qquad 5.4$$

The heat from the workpiece (Q_{wp}) is released to water in the container, and it results in the workpiece temperature difference ($\Delta T_{\mathrm{s}} = T_{\mathrm{s,sat}} - T_{\mathrm{w,eq}}$). With the assumption $Q_{\mathrm{w}} = Q_{\mathrm{wp}}$, the heat capacity of the workpiece (C_{wp}) is given as:

$$C_{wp} = \frac{Q_{wp}}{\Delta T_{wp}} \qquad 5.5$$

The heat capacity of the workpiece (C_{wp}) is determined to 10.4±0.2 J/K. However, this experimentally derived value is approximately 18% lower than the heat capacity value calculated based on material constants and workpiece dimensions. The reason for the consistently lower measured values in comparison to the calculated value could be the apparent temperature loss during the workpiece's relocation to the Dewar flask. As a result, the heat capacity of the workpiece (C_{wp}) is always underestimated. Thus, for the calculation of P_{in}, the calculated value of the heat capacity (13 J/K) is employed in this study.

5.2.4 Description of electrolyte temperature modeling

Through a collaborative effort, the temperature evolution of an electrolyte in two dimensions was modeled using the mixture of liquid and gas phases, as boiling was observed at temperatures above the saturation temperature of the electrolyte, leading to bubble generation. It solves the following system of equations by assuming two phases with constant densities are equal to one phase characterized by the properties of a mixture [182, 183].

$$\nabla \cdot \boldsymbol{j} = m_{gl}\left(\frac{1}{\rho_l} - \frac{1}{\rho_g}\right) \tag{5.6}$$

$$\begin{aligned}\rho\frac{\partial \boldsymbol{j}}{\partial t} + \rho(\boldsymbol{j}\cdot\nabla)\boldsymbol{j} + \rho_l\varepsilon(\boldsymbol{j}_{slip}\cdot\nabla)\boldsymbol{j} = \nabla[-p\boldsymbol{I} + \boldsymbol{K}] + \rho\boldsymbol{g} - \nabla\cdot\left[\rho_l(1+\phi_l\varepsilon)\boldsymbol{u}_{slip}\boldsymbol{j}_{slip}^T\right] \\ -\rho_l\varepsilon\left[(\boldsymbol{j}\cdot\nabla)\boldsymbol{j}_{slip} + \left(\nabla\left(D_{md}\nabla\phi_g\right)\right)\boldsymbol{j} + \boldsymbol{j}_{slip}m_{gl}\left(\frac{1}{\rho_l} - \frac{1}{\rho_g}\right)\right]\end{aligned} \tag{5.7}$$

$$\frac{\partial \phi_g}{\partial t} + \boldsymbol{j}\cdot\nabla\phi_g + \nabla\cdot\boldsymbol{j}_{slip} = \nabla\cdot\left(D_{md}\nabla\phi_g\right) - m_{gl}\frac{\rho}{\rho_g\rho_l} \tag{5.8}$$

$$\rho C_p\frac{\partial T}{\partial t} + \rho C_p\boldsymbol{u}\cdot\nabla T + \nabla\boldsymbol{q} = Q \tag{5.9}$$

Equation 5.6 is the mixture continuity equation, while Equation 5.7 represents the mixture momentum equation. In the given equations, $\boldsymbol{j}$ represents the volume-averaged mixture velocity, m_{gl} stands for the mass transfer rate between the gas and liquid phases, ρ_{l} and ρ_{g} are the densities of the liquid and gas phases respectively, while ρ signifies the mixture density. Moreover, $\boldsymbol{j}_{\mathrm{slip}}$ is the slip velocity, p denotes pressure, $\boldsymbol{I}$ corresponds to the unit tensor, and $\boldsymbol{K}$ is the combined viscous and turbulent stress tensors. Additionally, $\boldsymbol{g}$ symbolizes the gravity acceleration vector, ε refers to the reduced density, and D_{md} is the turbulent dispersion coefficient. The relations $\phi_{\mathrm{l}}\rho_{\mathrm{l}} + \phi_{\mathrm{g}}\rho_{\mathrm{g}}$ and $(\rho_{\mathrm{g}} - \rho_{\mathrm{l}})/\rho_{\mathrm{l}}$ are used to express the mixture density ρ and reduced density ε, respectively. Considering evaporation and condensation based on Ref. [182], the mass transfer rate from the gas to liquid phase m_{gl} was determined. An equation for determination of the gas phase volume fraction, ϕ_{g} is given by relation 5.8. As the sum of the volume fractions of the liquid (ϕ_{l}) and gas phases (ϕ_{g}) is 1, ϕ_{l} can be expressed as $1 - \phi_{\mathrm{g}}$. The heat transfer in the mixture is described by Equation 5.9, which pertains to heat transfer, where T symbolizes the mixture temperature, C_{p} represents the mixture heat capacity, and $\boldsymbol{u}$ denotes the mass-averaged velocity of the mixture. A vector $\boldsymbol{q}$ represents the heat flux determined by the relation $\boldsymbol{q} = -k\nabla T$, where k denotes the thermal conductivity. A heat source, Q is determined by the equation $Q = -m_{\mathrm{gl}}h_{\mathrm{gl}}$, where h_{gl} represents the latent heat of vaporization. Similarly to the mixture density ρ, the values of the mixture parameters for the calculations were derived based on the volume fractions of two phases. All equations were solved in cylindrical geometry. As illustrated in Figure 5.8(a), the modelling domain consists of fluid region, cathode and beaker wall. Equations 5.6 – 5.8 were solved only in fluid domain, while Equation 5.9 was defined in whole modelling domain.

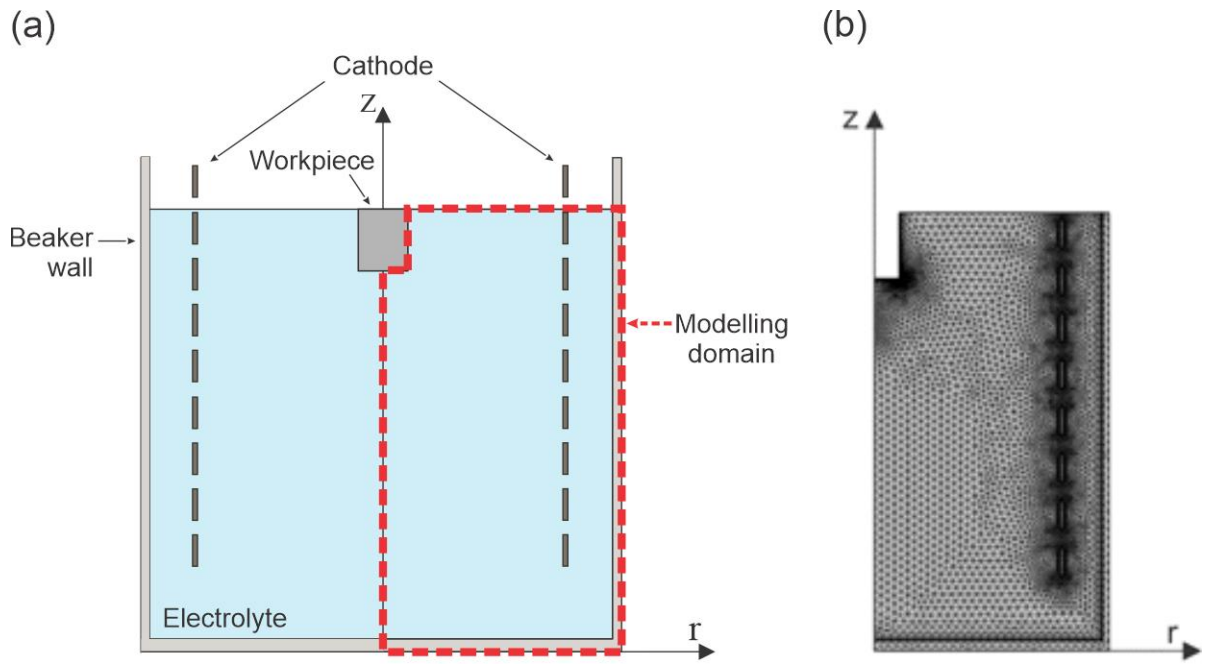

Figure 5.8 (a) Schematic description of the modeling domain and (b) illustration of the computational mesh.

Appropriate boundaries and initial conditions are required for the system of Equations 5.6 – 5.9 to be solvable. A no-slip boundary condition was employed for the flow velocity on the beaker wall facing the fluid, cathode, and anode surfaces. It was assumed that there is no gas flux on the same boundaries. However, the slip boundary condition was applied for flow velocity and gas phase outlet at the fluid-air boundary. In order to solve the heat transfer equation, temperature values measured experimentally in the previous section were employed on the workpiece surface and bottom of the beaker. Moreover, the convective heat flux serves as a boundary condition between the beaker wall and ambient air, as well as the fluid and ambient air. It was assumed that there was no electrolyte flow at the beginning of the calculation. Additionally, a constant temperature of 70 °C was set as the initial temperature of workpiece, electrolyte and beaker. Modeling was carried out by COMSOL Multiphysics® software, using the coupling between heat transfer and mixture flow modules. Equations 5.6 – 5.9 represent the system of partial differential equations solved by time-dependent solver using the finite element method with linear Lagrange elements. The computational domain was meshed with triangle elements whose size decreases from the middle of the domain towards the domain boundaries as illustrated in Figure 5.8(b). The appearance of darker areas in the mesh is attributed to the increased mesh density (smaller size of the elements) observed near the boundaries. For all calculations, the tolerance of the maximum relative error was set to be 10^{-3}.

5.2.5 Synchronization of electrical and high-speed camera measurement

The synchronous recording of electrical signals and high-speed images was conducted, with the experimental configuration illustrated in Figure 5.9.

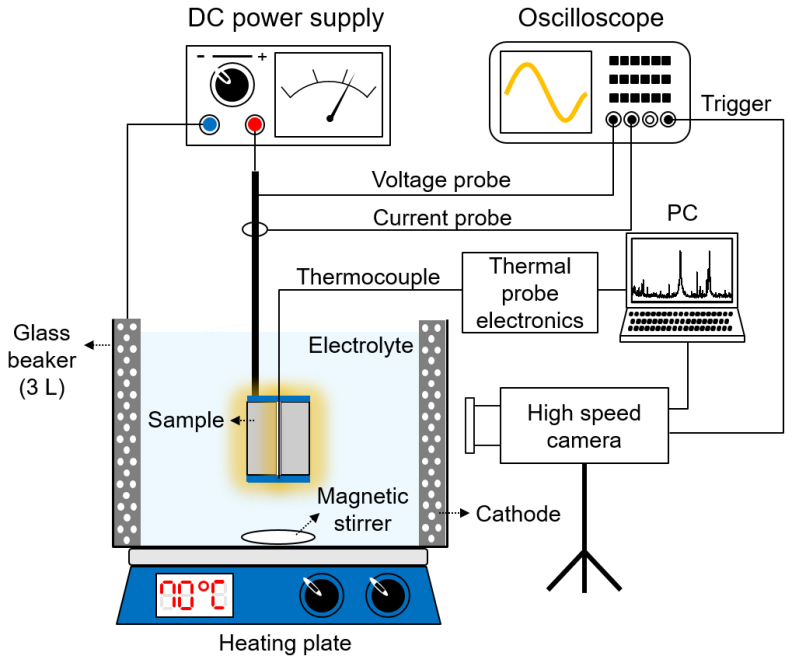

Figure 5.9 Schematic illustration of a synchronized high-speed camera and electrical measurement.

During the PEP process, the electrical signals (voltage and current) were recorded using a 1 GHz digital oscilloscope (MDO 34, Tektronix) for 40 s with a temporal resolution of 0.4 µs. Process voltage and current were measured with a passive voltage probe (TPP0500B, Tektronix) and a current transducer (HAL 200-S, LEM), respectively. The generation of the vapor and the appearance of luminous events from the discharges during PEP was monitored by a high-speed camera (FASTCAM Nova S6, Photron) with a frame rate of 1000 fps. The camera was triggered with the voltage rise signal from the oscilloscope. The workpiece was observed through a glass beaker containing 2.5 L of electrolyte. The images were taken with an exposure time of 1 ms Images taken by the camera consist of 512 × 512 pixels with an area of ~554 mm^2. The total recording duration of each measurement was longer than the PEP process time of 30 s to capture the moment after the process finishes. A halogen cold light source (KL1500, Schott) was employed to visualize the bubbles clearly.

5.3 Results and discussion

5.3.1 Electrical and thermal characterization

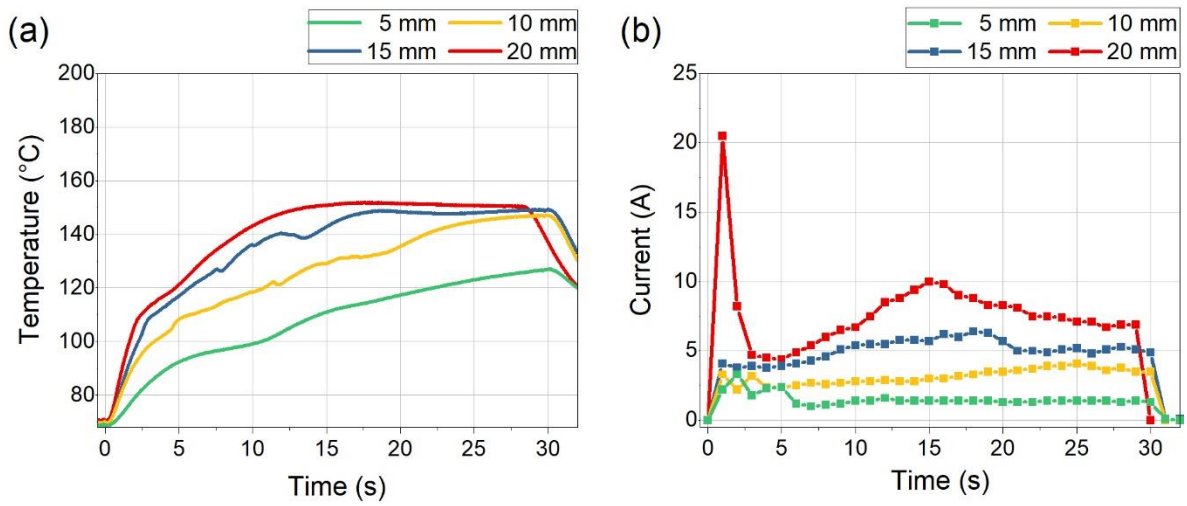

Figure 5.10 (a) Evolution of workpiece temperature and (b) current as a function of the process time at varied immersion depths (adapted from [176]).

Figure 5.10(a) shows the evolution of the workpiece temperature during the PEP process for 30 s at different immersion depths (5 mm–20 mm). A steep increase in the workpiece temperature is observed after the power supply is turned on. However, the temperature increment is impeded at around 110 °C, attributed to the formation of a vapor layer surrounding the anode workpiece surface. As seen in Figure 5.10(b), the electrical current measured synchronously with the temperature rises until 1 s, then drops rapidly during the first few s before stabilizing at 3 s for 20 mm of the immersion depth (*d*). As was observed in the current measurement of *d* = 20 mm, the initial current drop was also observed in other experimental conditions (*d* = 5–15 mm). However, the magnitude and rate of the current drop are less than those of 20 mm. This is because the gaseous layer forms around the anodic workpiece, leading to an increase in electrical resistance. Subsequently, after the current drop, it rises slightly again, accompanying the rise of the workpiece temperature. The current rise, in this case, can be explained by increasing electrolyte conductivity at elevated electrolyte temperatures as a result of enhanced electrolyte dissociation and ionic mobility. Eventually, the workpiece reaches a temperature of ~150 °C, as shown in Figure 5.10(b). As the immersion depth increases, more electrical power is consumed at larger workpiece areas, resulting in a shorter time required to reach its maximum temperature. Then, the temperature gradually falls due to the reduction in current as a stable VGE layer develops. As the immersion depth increases, the temperature and current drop more pronouncedly because a larger exposed area results in more significant current variations. D'yakov et al. reported that the workpiece temperature reaches close to 1000 °C during the anodic plasma electrolytic process with the help of a stable VGE layer [85]. Nevertheless, in our case, the workpiece does not exceed 160 °C since the gaseous layer is unstable, causing recurrent contact between the workpiece and the electrolyte, and the current density is relatively low (0.005 A/mm^2 as compared to 0.015 A/mm^2 in Ref. [85]). The workpiece temperature reaches only 127 °C for the smallest immersion depth (5 mm)

since the power supply is turned off before it can be heated further. When the exposed area decreases, the amount of electrical power dissipated decreases, resulting in a slower heating rate.

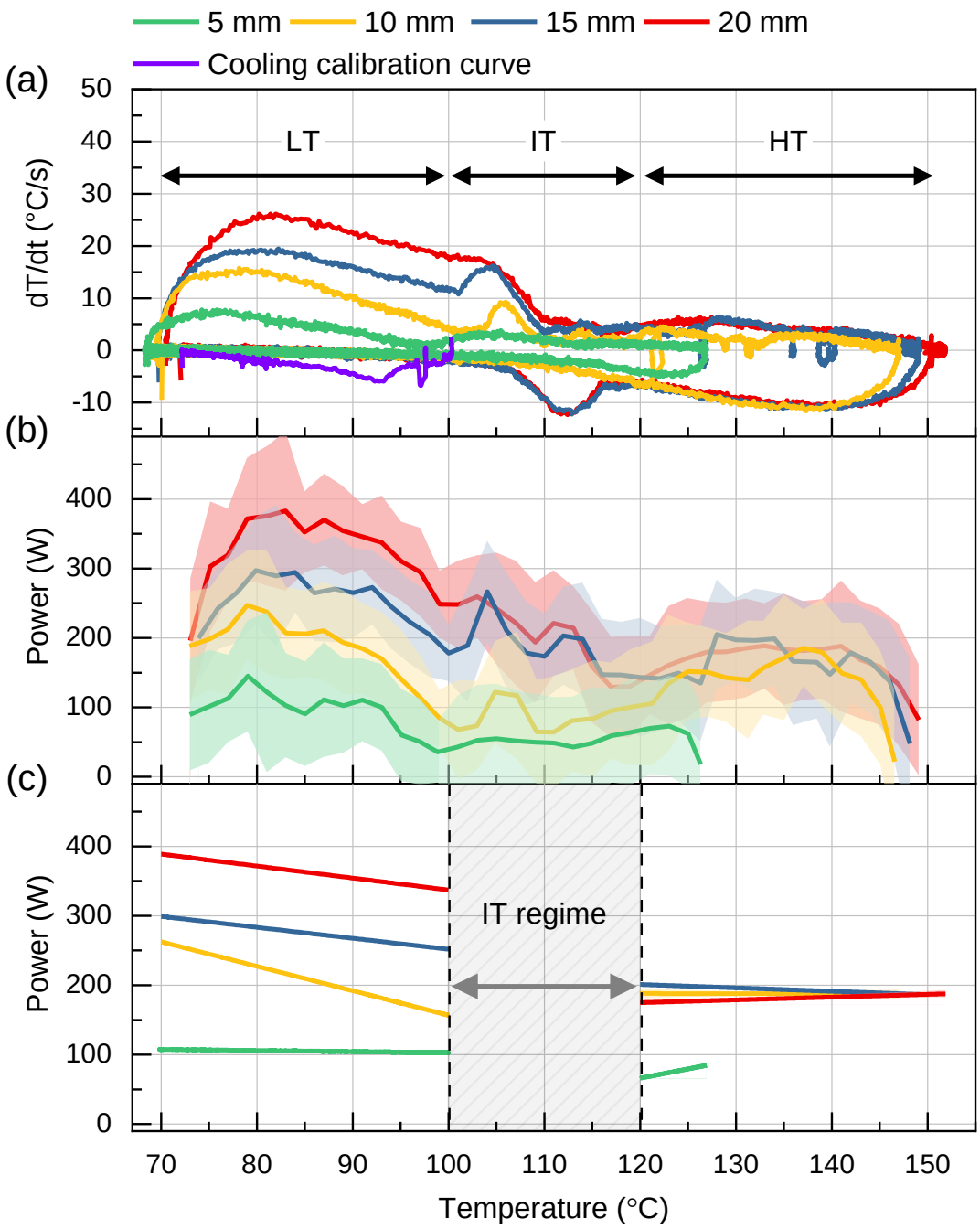

Figure 5.11 (a) Time derivative of temperature as a function of temperature (dT-curve). Estimated power transfer to the workpiece (P_{in}) in relation to temperature at various immersion depths, employing (b) binning and (c) interpolation methods. Shaded regions represent the error band. It should be noted that power values in the LT regime are determined using the cooling calibration curve (purple curve in (a)) (reprinted from [176]).

Using the *dT-depiction*, as illustrated in Figure 5.11(a), the power transferred to the workpiece (P_{in}) for varying immersion depths was evaluated employing the binning method described in Section 5.2.3. Before the results of the evaluated P_{in} are presented, a typical curve path of *dT-depiction* is outlined to shed light on the outcome of the time derivative evaluation method discussed in Section 5.2.3 (see Figure 5.3(a) to (c)). Initially, at the lower temperature (region LT), the *dT-curve* during heating (red curve, left to right in Figure 5.3(b)) experiences a sharp increase when the power supply is activated. After up to 2 s, depending on immersion depth, the curve begins to display a negative slope. The negative slope at ~80 °C emerges as a result of diminished electrical power, which is associated with the development of VGE around the workpiece (see Figure 5.10(b)). Two primary mechanisms contribute to gas layer creation during plasma electrolysis: coalescence of bubbles on the electrode surface by electrochemical reaction and/or local electrolyte vaporization due to Joule heating [*184*]. At this point, the former mechanism is likely to be more prevalent, given that it entails a decrease in electrical current, as the workpiece temperature is below the electrolyte boiling point during this time. Subsequently, in the IT region, the *dT-curve* fluctuates when the temperature reaches the boiling point of the electrolyte.

The deviation of the *dT-curve* can be attributed to the temporally changing VGE, leading to varying load resistance and fluctuating cooling efficiency. As the temperature increases further (≥ 120 °C, region HT), the heating curve again exhibits a negative and approximately linear derivative, although with a reduced slope compared to the LT region until a steady temperature of around 150 °C is reached. The decreased slope can be attributed to less efficient cooling processes due to the existence of VGE. The progression of the cooling curve (Figure 5.3(b), blue curve, right to left) is caused by an initial steep temperature drop (see Figure 5.3(a)) immediately after the power supply is switched off. During further cooling, the slope is comparable to the corresponding heating curve, indicating similar loss terms ($P_{\mathrm{out,h}}$ and $P'_{\mathrm{out,c}}$) at the HT regime. Afterwards, the IT region is passed, where fluctuation around the boiling temperature is observed. Finally, in the LT region, the slope is not comparable to the corresponding heating curve, as described in Section 5.2.3, due to the significantly increased electrolyte temperature (see Section 5.3.2). Therefore, particular attention must be given when evaluating the P_{in} value in this LT regime, necessitating a cooling calibration curve obtained by the procedure described in Section 5.2.3, visible as a purple curve in Figure 5.11(a).

Figure 5.11(b) displays the evaluated P_{in} values obtained through the binning method. Within the LT regime, P_{in} exhibits a gradual decrease as temperatures increase, corresponding to the reduced electrical power following the initial phase (~1 s), see Figure 5.10(b). Also, at the LT regime (below 100 °C) P_{in} is strongly influenced by the workpiece immersion depth (*d*). The P_{in} is over three times higher at *d* = 20 mm than at *d* = 5 mm in this regime. At higher temperatures (above 120 °C, HT), the P_{in} becomes independent of the depth as the curves converge ~180 W except for *d* = 5 mm. This can be explained by the formation of the gaseous layer at high temperatures, which separates the solid anodic workpiece from the liquid electrolyte. As the power supply is turned on, the anodic workpiece heats up due to the joule heating associated with the gas liberation produced by the electrolysis process and the vaporization of the electrolyte. The gaseous layer gradually builds around the workpiece surface when the bubbles coalesce, and the workpiece temperature increases. After the stabilized vapor layer has developed, the system comprises three phases: metallic anode, vapor layer, and liquid electrolyte. In this system, most electrical power is dissipated in the

vapor layer, where the resistance is the highest. A stable interface between the electrolyte and VGE can be maintained as the dissipated power is partially transferred to the bulk electrolyte [68]. Therefore, the P_{in}, which is power transferred to the workpiece, is less effective at higher temperatures (longer process time) since the electrical input power is mainly dissipated within the gaseous layer.

As shown in Figure 5.11(a), the slope of the cooling curve in region HT is approximately the same as that of the heating curve. The parallel linear heating and cooling curves can be obtained during a stable measurement environment when the constant cooling efficiency and heat capacity are assigned [143, 180]. As shown in Figure 5.11(a), during the PEP process, relatively parallel curves can be obtained under the HT regime compared to the LT regime since the formation of a stable gaseous layer is attributed to reducing crucial temperature fluctuations around the workpiece. In Figure 5.11(b), at a temperature above 140 °C, the power of the P_{in} appears to be reduced from ~200 W to even lower than 100 W. The reduction in power at temperatures above 140 °C can be attributed to the transition in temperature resulting from thermal inertia occurring immediately after the power supply is off. Therefore, the difference between $\dot{T}_{\mathrm{h}}$ and $\dot{T}_{\mathrm{c}}$ during this transition period (right after the power supply is turned off) is small, leading to a low P_{in} value, according to Equation 5.3. For the same reason, this undesirable effect is also observed in the P_{in} value during the LT regime (between 70 °C and 80 °C). However, as described in Section 5.2.3, this systematic error can be reduced using an interpolated fitting curve within a selected temperature range. Figure 5.11(c) illustrates the P_{in} values in the low and high-temperature regimes derived by the interpolation curves. The interpolation method yields P_{in} values comparable to those obtained using the binning method: at LT, power values also change according to the immersion depth, and at HT, power values tend to converge, with the exception of a *d* = 5 mm depth, albeit without the occurrence of the aforementioned erroneous values at the beginning and end of the measurement. When the immersion depth (*d*) expands from 5 mm to 20 mm, there is an increase in the mean power within the LT regime. For 5 mm, it commences at 108 W and diminishes to 103 W, while for 20 mm, it begins at 389 W and declines to 337 W. The disparate slopes in power change for the various immersion depths can be attributed to differing decreases in electrical power. Conversely, the mean power values in the HT regime for immersion depths ranging from 10 mm to 20 mm are relatively stable at around 188 W. For an immersion depth of 5 mm the mean power value in the HT regime is underestimated since the workpiece temperature reaches only ~127 °C over the entire process time (30 s), as illustrated in Figure 5.11(a). When the PEP process time is extended enough to reach elevated workpiece temperatures, increased power values similar to those at greater immersion depths (*d*) are expected. It should be noted that the power values in the HT regime have a greater significance in view of PEP than the LT regime since the surface modification effect occurs predominantly at higher temperatures when the VGE accompanying plasma is developed. As illustrated in Figure 5.12, the fraction of power transferred to the anodic workpiece is calculated by dividing the evaluated P_{in} by the electrical input power within LT and HT regimes. The efficiency of power transfer exhibits distinct characteristics in the LT and HT regimes. For the LT regime, the proportion of power transmitted to the anodic workpiece is approximately consistent for immersion depths ranging from 10 mm to 20 mm. The reduced efficiency for 5 mm remains uncertain. Future investigations will be necessary to ascertain whether this is a statistical or physical phenomenon. In the HT regime, the power efficiency for 5 mm is only 13.9% due to using an

underestimated power value in the calculation. When the immersion depth is increased from 10 mm to 20 mm, an efficiency reduction has been observed from 25.7% to 16.7%, as the electrical power is consumed elsewhere.

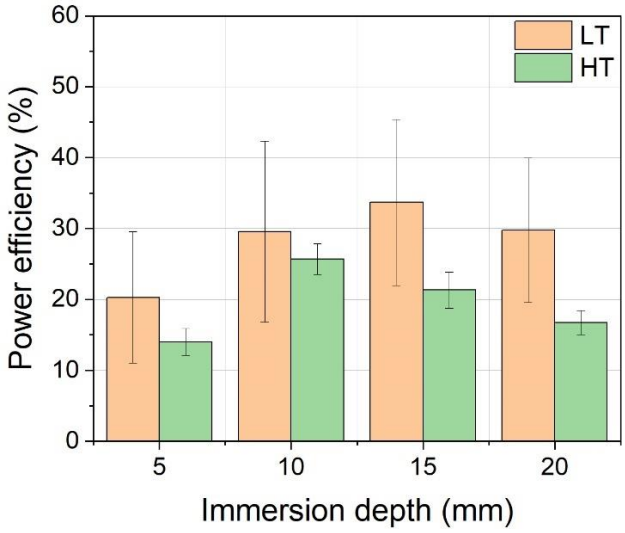

Figure 5.12 Dependencies of efficiency of power transferred to the workpiece (fraction of P_{in} from electrical power) in the LT and HT regimes in different immersion depths, d (reprinted from [176]).

As a stable VGE forms, the majority of heat generation during the PEP process occurs within the VGE, given that it is the location of the highest electrical resistance. The generated heat mostly transfers from VGE to the anode, electrolyte, and air. According to Belkin et al. [68], nearly 90% of the input power is consumed to heat the surrounding electrolyte during the anodic plasma electrolysis. With a deeper immersion depth of the workpiece, the current increases, causing a thicker VGE layer, requiring more power to maintain a stable interface between the VGE and electrolyte phases. This increases the electrolyte temperature. The VGE layer's thickness can be observed using a high-speed camera, as shown in Figure 5.13(a)-(d). Submerged workpieces at depths of 5 mm and 20 mm in the electrolyte are illustrated in Figure 5.13(a) and (c), respectively, prior to the power supply being turned on. Figure 5.13(b) and (d) were captured in both 10 mm and 20 mm at a PEP process time of 29 s and 7.5 s, respectively. As the workpiece temperatures were approximately 150 °C at this time, the gaseous layers of different immersion depths could be directly compared. A yellow dashed line is used to outline the shape of the workpiece to identify the gaseous layer surrounding the workpiece. As illustrated in Figure 5.13(b) and (d), the workpiece surface is observed to be covered with a gaseous layer accompanying discharges. The thickness of the gaseous layer is approximately 1 mm. As the surrounding electrolyte moves, blurring the thin gaseous layer, it is difficult to determine the exact boundary of the gaseous layer, particularly in the immersion depth of *d* = 10 mm. In comparison, at 20 mm, a larger gaseous layer is observed outside the outline of the workpiece than at 10 mm, as displayed in Figure 5.13(c). Based on this observation, it can be concluded that at deeper immersion depths, a thicker VGE layer is formed owing to the rise of the surrounding electrolyte temperature. The temperatures of the electrolyte at different immersion depths (*d*) are simultaneously recorded with the high-speed camera, and the workpiece temperature measurements will be shown below.

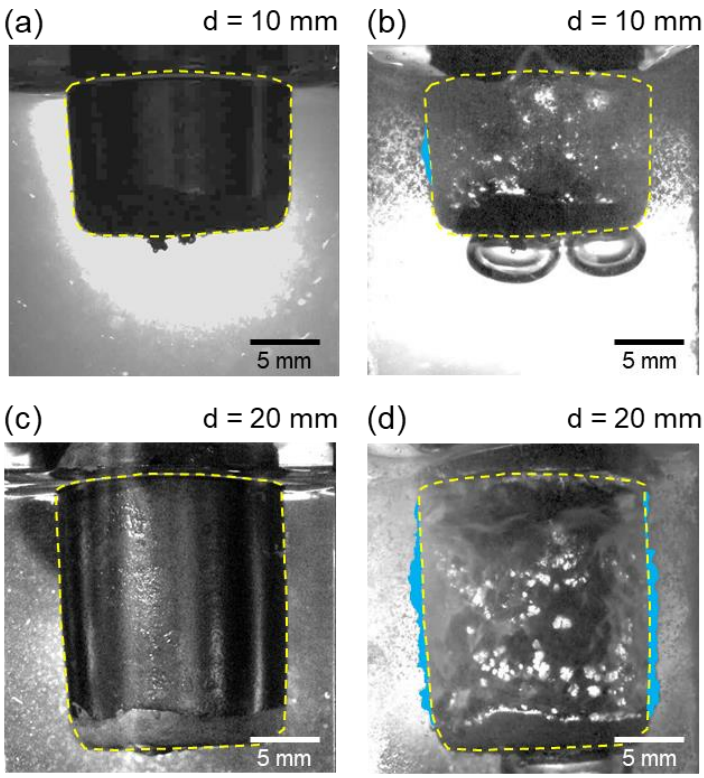

Figure 5.13 Snapshots from high-speed camera of the workpiece: (a) 0 s and (b) 29.2 s in d = 10 mm and (c) 0 s and (d) 7.5 s in d = 20 mm. The yellow dashed line indicates the outline of the workpiece immersed in the electrolyte. The gaseous layer around the workpiece surface is marked in blue in (b) and (d) (reprinted from [176]).

Bubbles lying underneath a workpiece are not considered because they adhere to the epoxy part, which is not the area of interest. The local electrolyte temperature was measured as a function of time to examine the dependence of the electrolyte temperature rise depending on the workpiece immersion depth as illustrated in Figure 5.14. During the PEP process, the electrolyte temperature increases steadily up to 81.5 °C from the starting temperature of ~70 °C at immersion depth, *d* = 20 mm, at a radial distance of 15 mm away from the anodic workpiece and at the bottom of the workpiece in radial direction. The temperature increment is higher when the immersion depth is deeper since more electrical power is consumed with a larger exposed workpiece area. In addition, as the immersion depth decreases from 20 mm to 10 mm, the rise of the electrolyte temperature is delayed, as shown in the inset of Figure 5.14. However, in the case of 5 mm, the temperature rises faster than the other deeper immersion depths. This rise is presumably influenced by the position of the thermocouple, which is fixed to the bottom of the workpiece and therefore varies with the immersion depth. Thus, the movement of the heated electrolytic fluid from the near workpiece surface to the thermocouple needs to be considered. The hydrodynamic model is used in the next section to support the experimental data.

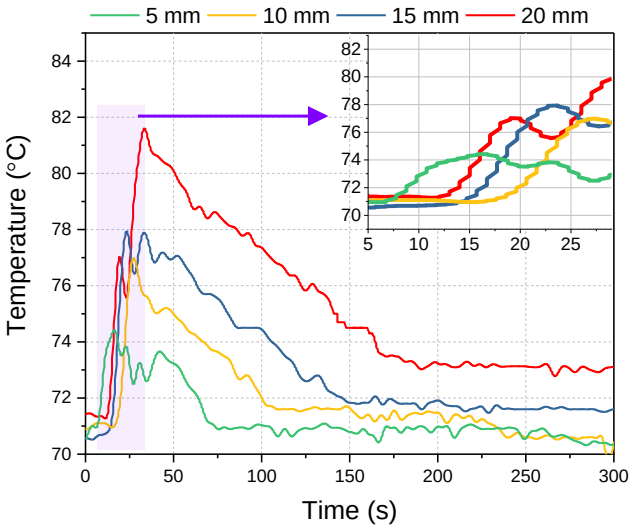

Figure 5.14 Dependencies of the temporal development of electrolyte temperature at different immersion depths (see section 5.2.2 for position of the thermocouple). The inset is an enlargement of the marked area (purple color).

5.3.2 Modeling of electrolyte temperature

The temporal evolution of the electrolyte during the PEP process has been modeled for *d* = 20 mm workpiece immersion depth, which is fully submerged in the electrolyte. This immersion depth was specifically selected since it is deep enough to reduce the influence of the moving electrolyte surface during boiling; therefore, it is the most appropriate for the model to describe. The temporal evolution of the electrolyte during the PEP process has been modeled for *d* = 20 mm workpiece immersion depth, which is fully submerged in the electrolyte. This immersion depth was specifically selected since it is deep enough to reduce the influence of the moving electrolyte surface during boiling; therefore, it is the most appropriate for the model to describe. As shown in Figure 5.15, the local electrolyte temperature measured by the thermocouple is compared to the temperature values from the modeling. The modeling was conducted using k-ε turbulent and laminar models. The turbulent model (marked as a red dashed line) fits the measured values closely until t = 65 s. Afterwards, the laminar model (marked as a blue dashed line) fits the measurement better than the turbulent model since the flow velocity had decreased, and the flow no longer behaved turbulently. When the PEP process is complete at time t = 30 s, the wall temperature reaches its maximum, and the fluid exhibits an intense turbulent character with a Reynolds number of order of 10^5.

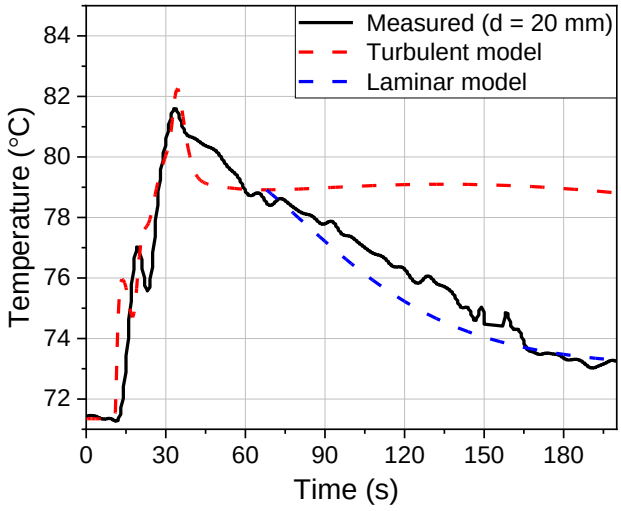

Figure 5.15 Temporal development of electrolyte temperature for d = 20 mm: measured data (solid black line), turbulent model (red dashed line), and laminar model (blue dashed line) (reprinted from [176]).

Figure 5.16(a) illustrates the volume-averaged velocity and streamlines of the fluid mixture. As can be seen, fluid flows from the workpiece to the cathode directly within the topmost fluid sheath and following the electrolyte-air boundary. Near the cathode interface, the fluid “dives” and is transported in a backstreaming flow towards the workpiece. Part of the fluid flows alongside the beaker wall to the bottom, where it is transported to the center and upwards to the workpiece. As depicted in Figure 5.16(b), the volume fraction of the gas is the highest in the vicinity of the workpiece surface, which is 25% due to its high-temperature.

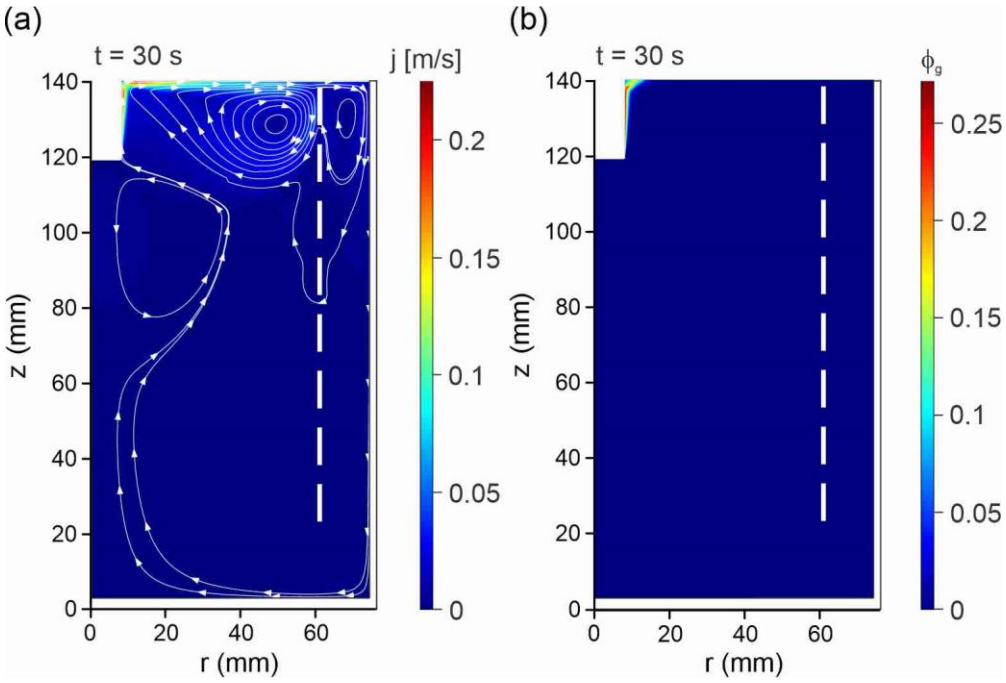

Figure 5.16 (a) Volume average velocity of the fluid mixture along with the streamlines and (b) gas phase volume fraction obtained by modeling for t = 30 s (reprinted from [176]).

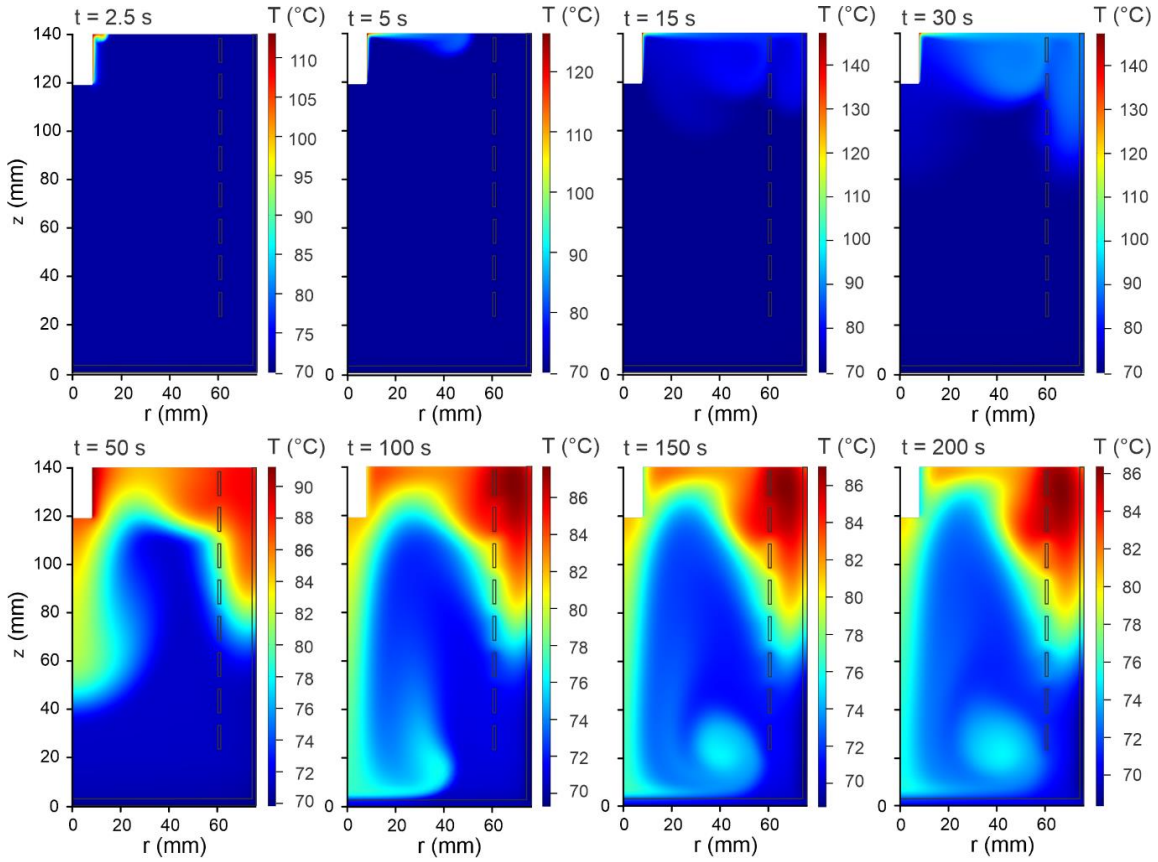

Figure 5.17 Spatio-temporal evolution of fluid mixture temperature obtained by the modeling. Please note the different color scales for each times (reprinted from [176]).

Figure 5.17 represents the modeled spatio-temporal evolution of electrolyte temperature up to simulation time (*t*) of 200 s. Based on the modeling results, the area surrounding the workpiece experiences heating, maintaining a temperature of around 90 °C at *t* = 50 s, which is 20 s after the power supply has been deactivated. These findings underscore the importance of utilizing a calibration curve for the cooling phase within the LT region to properly estimate P_{in} and the choice of the electrolyte container dimension. As already shown in Figure 5.16(a), in the first 30 s of the PEP processing duration, the heated electrolyte is guided by the fluid flow, which means that the heated electrolyte flows from the workpiece towards the cathode surface and back into the direction of the workpiece. When the power supply is turned off, the electrolyte temperature begins to decrease since the workpiece is no longer heated. During this period (*t* = 50–200 s), the temperature near the cathode and beaker wall is the highest since the area near the workpiece is cooled by the upward flow from the bottom of the beaker. It can be speculated that the electrolyte near the workpiece cools down relatively quickly due to a faster flow velocity than in the region near the cathode. Moreover, it is noticed that the electrolyte temperature does not vary significantly near the bottom of the beaker since the heated fluid is transported slowly from the workpiece to the bottom side.

5.3.3 Analysis of longitudinal surface composition via XPS line scans

During the PEP process, a uniformly distributed VGE layer along the workpiece is of immense importance. Otherwise it may lead to a compositional gradient or varied polishing rate in longitudinal direction [16, 85]. The cemented carbide employed here as an anode is a typical tool material used for precision machining. Therefore, the homogeneity of the material surface must be maintained to ensure reliable mechanical stability. Line-scan XPS was implemented to characterize the surface composition of the workpiece in longitudinal direction. One line-scan was performed on the workpiece surface at 1 mm intervals. The intervals are labeled as position 0 (lower part) to position 18 (upper part).

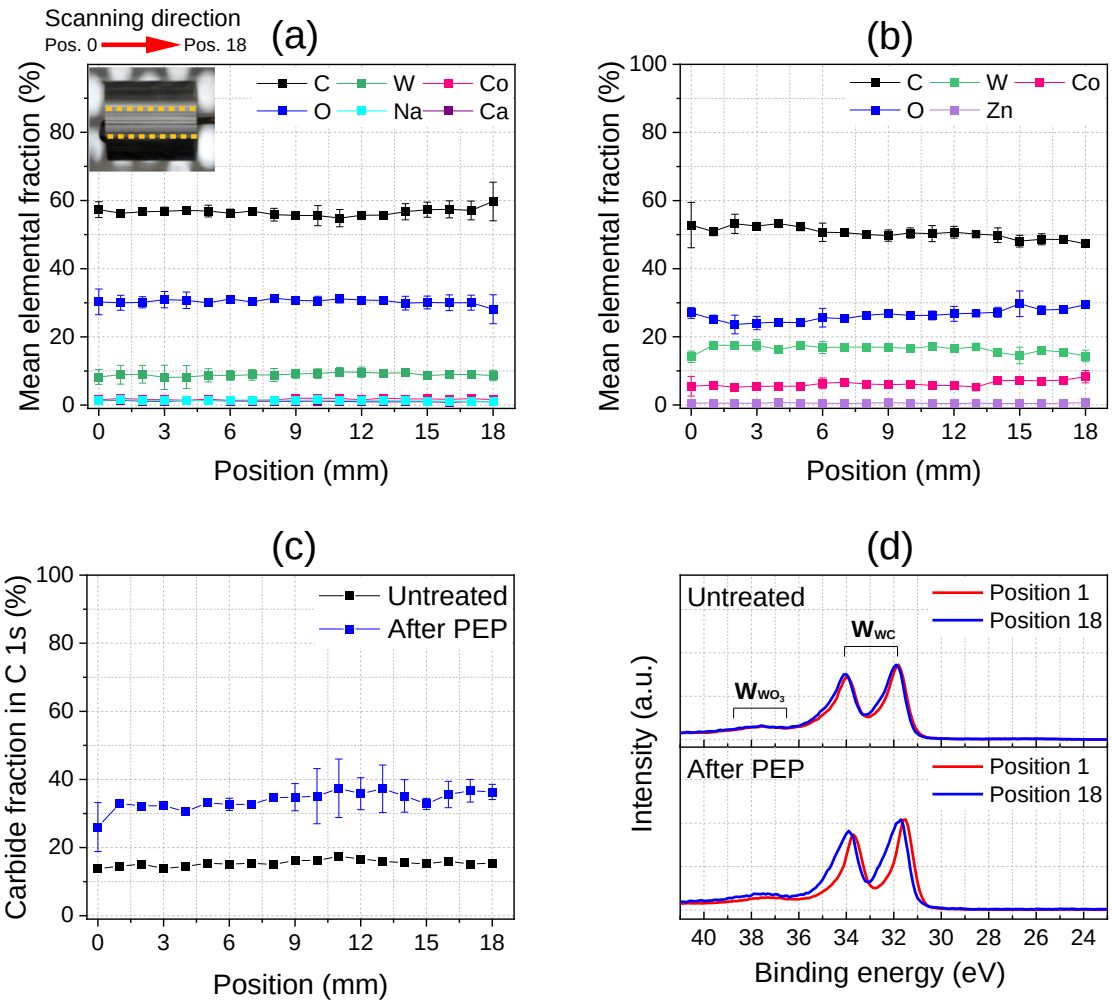

Figure 5.18 XPS line-scan profile data of (a) untreated and (b) 30 s PEP-treated workpieces (complete immersion). The inset shows a photograph of the workpiece indicating the line scanning direction. The line-scanned sections are marked with dotted lines. (c) Binding fraction of carbide in C 1s peak. (d) W 4f spectra of untreated (upper) and 30 s PEP-treated (below) workpieces (reprinted from [176]).

The line scans were performed twice on different sides of the workpiece surface, as depicted in the inset of Figure 5.18(a), and the mean values are plotted in Figure 5.18(a) and (b). The

surface of the untreated workpiece exhibits uniform elemental compositions in longitudinal direction, including C (~55 at%), O (~30 at%), W (~10 at%), Co (~2 at%), as well as small traces of contamination, such as Ca and Na, as shown in Figure 5.18(a). In Figure 5.18(b), after 30 s of the PEP process, the elemental fractions of W and Co noticeably increased to 16 at% and 6 at%, respectively. Meanwhile, the elemental fractions of C and O were reduced to 50% and 26%, respectively. Figure 5.18(c) illustrates the binding fraction of carbide, which consists primarily of metal carbide and adventitious carbon, typically C–C, C–O–C, and O–C=O bondings. Owing to the reduction of the aliphatic carbon after the PEP process, the overall carbide fraction in the scanned lines rises to 34% from 15% after the process, while more W and Co remain on the surface, as was also observed in the XPS results of Section 4.3.1.3. As illustrated in Figure 5.18(b), a slight spatial compositional gradient was observed in case of the C and O elements after the 30 s PEP process. The elemental gradients on the treated surface can be attributed to variations in current density along the vertical direction. A gradient of current density along the length of the workpiece can result from a non-uniformly distributed VGE thickness in which a thicker VGE layer compared to the lower part formed owing to the rise of gas bubbles by buoyant force. As a result, the upper part of the cylindrical workpiece could exhibit a relatively lower current density due to a creation of the thicker VGE layer compared to the lower part, leading to a predominant presence of oxidized WC on its surface. To determine how the chemical state of W is altered, the W 4f spectrum at position 1 (lower part) and position 18 (upper part) is compared, as shown in Figure 5.18(d). The surfaces of the untreated workpiece exhibit peaks at 31.9 and 34 eV on both measuring points, mainly attributed to the existence of carbide bindings from WC without the apparent presence of oxidized phases, denoted by W_{WO3} at 35.5 and 37.6 eV [98]. The W 4f peaks of the PEP-treated workpiece on both the measuring points are quite similar to those of the untreated workpiece. However, after the PEP process, the W_{WC} peaks at position 18 are slightly shifted to a higher binding energy (~0.2 eV), which is attributed to the presence of the oxidized WC phase.

5.3.4 Investigation of gaseous layer development via synchronized high-speed camera and electrical signal measurement

This section provides a comprehensive understanding of the PEP process, focusing on VGE movement and discharge behavior through synchronized high-speed camera and electrical signal measurements.

5.3.4.1 Temporal analysis of the PEP process via high-speed camera synchronized with electrical current measurements

Figure 5.19(a) illustrates a series of images taken using a high-speed camera during the entire 30 s of PEP process. A detailed description of the experiment is provided in Section 5.2.5. At the onset of the experiment, bubbles begin forming around the workpiece surface, as seen in the image at 0.04 s in Figure 5.19(a). In plasma electrolytic processes, bubbles originate from gaseous byproducts resulting from electrochemical redox reactions. Also they can be produced from Joule heating caused by the thermal effects of electrical current flowing through a resistive medium, which in turn heats and vaporizes the electrolyte solution [184]. In this particular case, the rapid emergence of bubbles at this stage (0.04 s) is primarily attributed to

the electrochemical reaction rather than Joule heating, as the brief duration does not allow for the workpiece to heat up appreciably. To confirm this hypothesis, conducting an additional experiment to analyze the gas composition would be required, since vapor bubbles generated through Joule heating could have a different composition compared to those produced by electrochemical reactions. Vapor bubbles typically consist of the vaporized electrolyte solution or solvent (e.g., water vapor), as opposed to the gaseous byproducts of redox reactions. As the process continues, electrical discharges become visible at 0.5 s shown in Figure 5.19(a) (marked in yellow dotted lines).

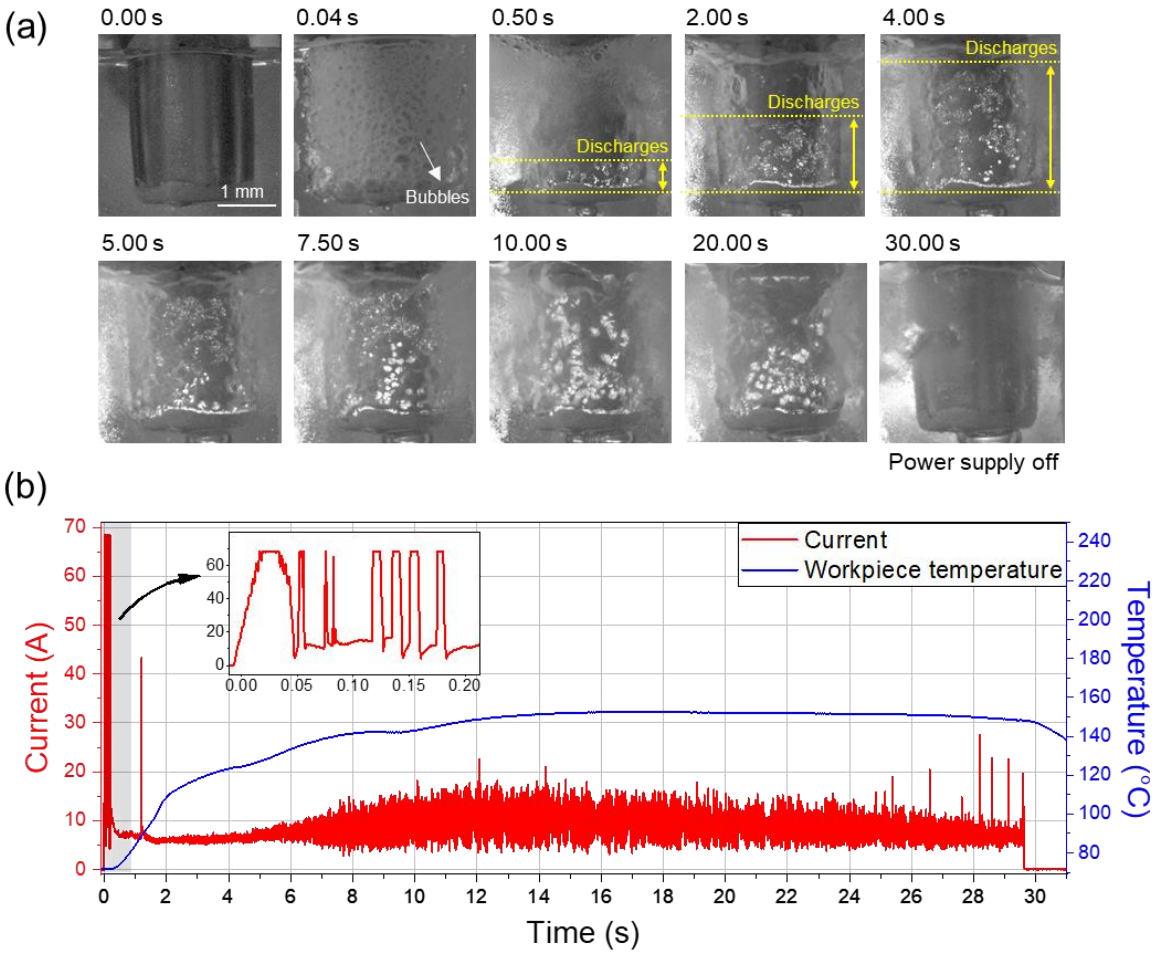

Figure 5.19 (a) Visualization of gas layer development throughout the 30 s PEP process on a fully submerged workpiece (d = 20 mm), captured using a high-speed camera at a frame rate of 1000 fps; (b) the corresponding electrical current waveform and workpiece temperature measurements taken simultaneously with the high-speed camera, including an inset that accentuates the enlarged segment of the current (displayed in grey).

Initially these discharges start at narrow region at the bottom part of the workpiece but gradually expand over time, eventually encompassing the entire workpiece surface area after 4 s. This can be attributed to the development of stabilized gaseous layer associated with the discharges across the entire workpiece. The buoyancy forces acting on the gas bubbles causes them to rise upwards in the electrolyte solution. Accumulation of bubbles at the bottom

part of the electrode lead to the formation of a gas layer, which can act as a medium for the discharge to propagate upwards as the gas continues to rise. The development of the gaseous layer also affects the electrical current during the process. Figure 5.19(b) illustrates that the corresponding electrical current (red curve) exhibits a rapid increase up to 70 A at the onset of the process, but drops below 10 A after around 0.2 s as the gaseous layer develops. In this current surge phase (from 0 to 0.2 s), the workpiece temperature (blue curve) significantly elevates as high electrical power dissipates into heat, causing the workpiece to warm up. Then, the temperature increase rate diminishes with a decrease in current. The inset in the Figure 5.19(b) reveals that the intense current rise occurs intermittently until around 0.2 s which can be hardly repeated due to hydrodynamic instability caused by the intensive bubble formation during this initial phase of the process. In the subsequent phase, the incidence of this sharp current escalation is substantially diminished, ascribed to the development of a stabilized gaseous layer. The current appears to be cut off at 70 A because of the limitations of the current measuring system. Hence, the transient high current exceeds 70 A In further experiments, it was confirmed that the current pulse reaches over 100 A within 1 s. Despite the fact that, during the entire PEP process, the instances exceeding 70 A account for a negligible part; the current remains below 20 A for most of the process duration. Thus, the present current measurement system is still viable to assess the current during the majority of the PEP duration. Since the discharges are observed over the whole area of the workpiece (~4 s), the optical brightness of the discharges intensifies, becoming more prominent after 10 s of the process. This intensification coincides with the temperature increase in the workpiece and the nearby electrolyte. The interdependence between discharge intensity and temperature can be elucidated through the increased number of charged particles involving the discharge activity at elevated temperature. Moreover, changes in liquid viscosity may play a role in the variations in discharge intensity. With increasing temperature, the viscosity of electrolyte solution decreases, which leads to an increase of the mobility of charged particles and facilitates intensifying the discharge emission. In conjunction with the observed changes in discharge behavior, simultaneously monitored current waveform provides additional insight into the process. After approximately 6 s. fluctuations in the current waveform notably begin to appear, as depicted in Figure 5.19(b). These fluctuations offer further evidence of the dynamic nature of the gaseous layer development during the PEP process and serve to corroborate the findings derived from the examination of the discharges and their progression over time.

5.3.4.2 Analysis of Current Waveforms and Frequency Components in the PEP Process

To identify the frequency components within the fluctuating current waveform as it evolves over time, Fast Fourier Transformation (FFT) was performed on the recorded current waveform from the PEP process at a 20 mm immersion depth, analyzing every 6 s interval as indicated in Figure 5.20(a). Figure 5.20(b) presents the power spectrum, depicting the frequency distribution of a current signal's power as the mean squared amplitude (MSA) at 6 s intervals.

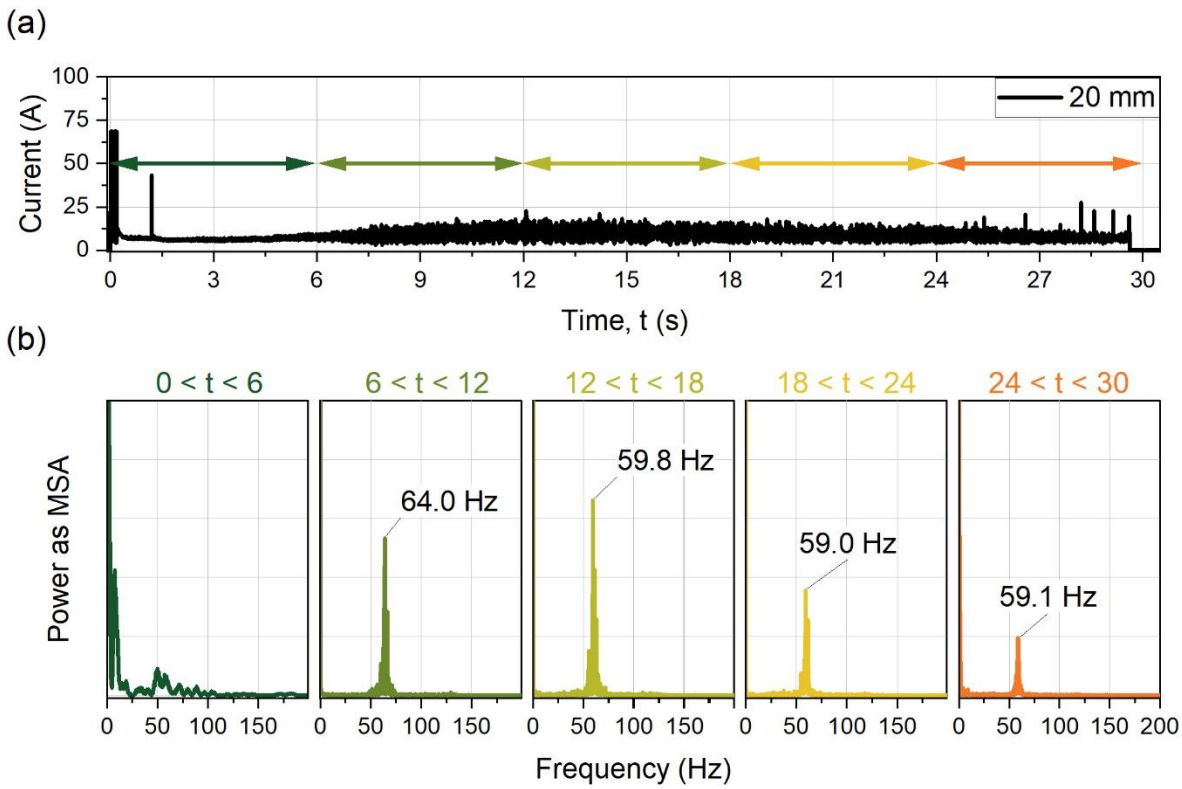

Figure 5.20 (a) Electrical current waveform throughout the PEP process, with arrows denoting the range for FFT analysis. (b) Power spectra as mean square amplitude (MSA) of the current waveform at 6 s intervals throughout the 30 s of the PEP process.

The power spectrum indicates no significant frequency components are discernible within the initial 0 to 6 s. However, in the time span of 6 to 12 s, a noticeable frequency component of roughly 64 Hz appears. After 6 s of the PEP process, each of the power spectrum displays a dominant frequency, which transitions from 64 Hz to 59.1 Hz as the process continues as shown in Figure 5.20(b). The presence of periodic features is not restricted to the PEP process for WC-Co material; they have been observed by other research groups during different plasma electrolytic processes [15, 78]. The pulsed nature of the current in plasma electrolytic processes exhibits two distinct frequency regimes. The low frequency regime, ranging from several tens to hundreds of Hz, originates from the gaseous layer's behavior, while the high frequency regime, which is three orders of magnitude higher, is associated with discharges [185]. For the PEP process investigated in this study, the frequency range around 60 Hz falls within the scope of the low frequency regime. This implies that the pulsed nature of the current originates from the behavior of gaseous layer. Consequently, the frequency shift observed as the PEP process progresses can be related to the velocity of the gaseous layer movement. This subject will be discussed in more detail later. In the power spectrum obtained by FFT, the intensity of power value indicates the magnitude of a distinct frequency component in the signal. As depicted in Figure 5.20(b), the intensity of the power value reduces after 18 s, which may be linked to the formation of a stable gaseous layer as the electrolyte temperature elevates, resulting in the stabilization of the current variation.

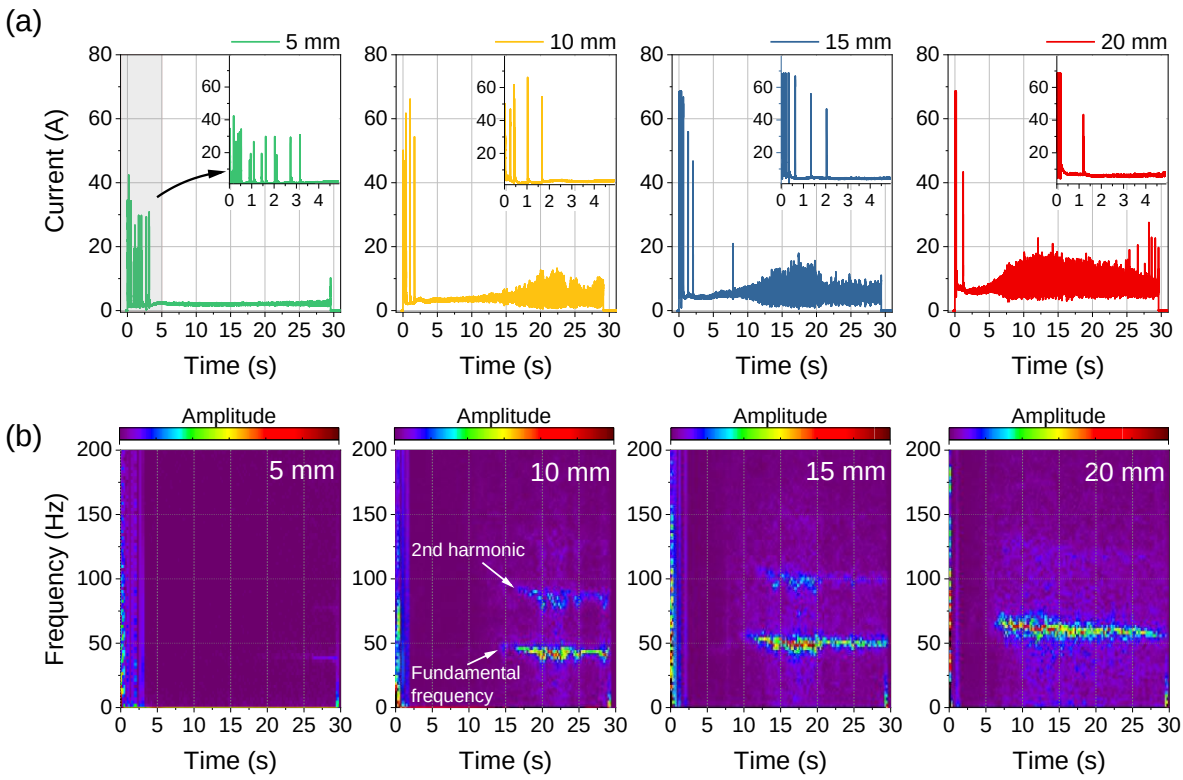

Figure 5.21 (a) Current waveforms captured during the PEP process at different immersion depths (d = 5 – 20 mm). (b) Spectrograms derived from the respective current waveforms.

Additionally, the current was compared at varying immersion depths (*d = 5 – 20 mm*) to observe the fluctuation behavior in response to different exposed areas, as depicted in Figure 5.21(a). With increasing immersion depth, the current value also increases. The insets featured in Figure 5.21(a) for each immersion depth highlight the expanded range of the initial 5 s, offering a more detailed view of the initial current surge as previously described. This current surge is noticeable at all immersion depths, but ceases earlier at deeper immersion depths due to the faster development of a stable gaseous layer. Short-Time Fourier Transform (STFT) analysis was conducted to investigate the temporal behavior of frequency components within the current waveforms, allowing for the monitoring of changes in spectral composition of signals as they evolve in time by converting them from a 1D time array to a 2D time-frequency space. Figure 5.21(b) presents the spectrograms derived from the STFT analysis of the current waveforms with an FFT length of 512. The spectrograms clearly show the presence of the fundamental frequency, which corresponds to the significant magnitude fluctuations in the current signal. However, the fundamental frequency cannot be observed in the case of a 5 mm immersion depth. At the immersion depth of 20 mm, the fundamental frequency appears around 6.5 s into the PEP process time, whereas it is delayed to 10.3 s and 16.5 s for immersion depths of 15 mm and 10 mm, respectively. Furthermore, for the 10 mm and 15 mm cases, the 2nd harmonic is clearly visible at double the fundamental frequency (it is weakly visible in 20 mm too), along with the fundamental frequency. The emergence of harmonic components is a typical feature of non-linear load incorporation within electrical systems. Despite utilizing a DC power source for this PEP process, the current exhibits pulsed

characteristics with a specific frequency due to the dynamic movement and changes in the gaseous layer, which can result in impedance variations and current fluctuations. The results from the spectrogram analysis also represent the substantial amplitude of the current fluctuation at the onset of the process (before 5 s) originating from the current surge, and at the end of the process (~30 s) due to the power supply being switched off. To more accurately pinpoint the onset of the current oscillation, frequency at the maximum amplitude from the spectrogram is depicted in Figure 5.22(a). As immersion depth increases from 10 mm to 20 mm, the initiation of current oscillation and its characteristic frequency shifts to an earlier time, from 16.6 s to 7.1 s. The workpiece temperature, measured synchronously, is illustrated in Figure 5.22(b). From the graphs in Figure 5.22(a) and (b), the commencement of current oscillation with a significant magnitude coincides with a distinct temperature of approximately 140 °C, as indicated by the dashed lines. In the case of 5 mm, the current oscillation is not observed probably since the temperature does not reach to around 140 °C.

This sudden appearance of current oscillation at a distinct temperature can be associated with changes in the gas layer development mechanism due to the transition in boiling regime from nucleate boiling to film boiling. As the temperature difference between the workpiece surface and the surrounding liquid (ΔT) increases, the boiling regime typically transitions through four principal stages presented in Nukiyama's boiling curve [186]: natural convection boiling (ΔT_e < 5 °C), nucleate boiling, transition boiling (30 °C < ΔT < 100 °C), and film boiling (ΔT > 120 °C). In the current situation during the PEP process, ΔT is less than 60 °C, which could place it within the range of transition boiling. This stage, also referred to as unstable or partial film boiling, is an intermediate phase that takes place between nucleate and film boiling. It occurs when the temperature of a heated surface exceeds the maximum heat flux (also known as the critical heat flux) during nucleate boiling but has not yet reached a level sufficient to sustain stable film boiling. As the workpiece surface temperature increases, vapor bubbles form and begin to coalesce, creating a thin and unstable vapor film on the heated surface. This can lead to dynamic changes in electrical impedance, as the vapor film insulates the electrode surface from the electrolyte, potentially causing the non-linear electrical behavior. As demonstrated in Figure 5.22(b), the fundamental frequency declines as the immersion depth decreases. The primary reason for this temperature-related frequency alteration is not yet clear; however, plausible explanations may include changes in the speed of the gaseous layer movement, influenced by variations in physical properties of surrounding electrolyte such as viscosity and surface tension, and increasing vapor pressure as fluid temperature rises. The investigation of gaseous bubble hydrodynamics holds significant importance in a variety of fields, including chemical, petrochemical, wastewater treatment, and nuclear engineering, as it allows for the enhancement of reactor design and operation based on bubble hydrodynamics [187-189]. A number of research groups have confirmed an increase in bubble rise velocity with elevated liquid temperature by meticulously tracking trajectories of gas bubbles using high-speed cameras [190, 191]. Furthermore, several models have been proposed to parameterize the bubble rising velocity under different conditions, considering temperature, liquid, and pressure variations [192-194].

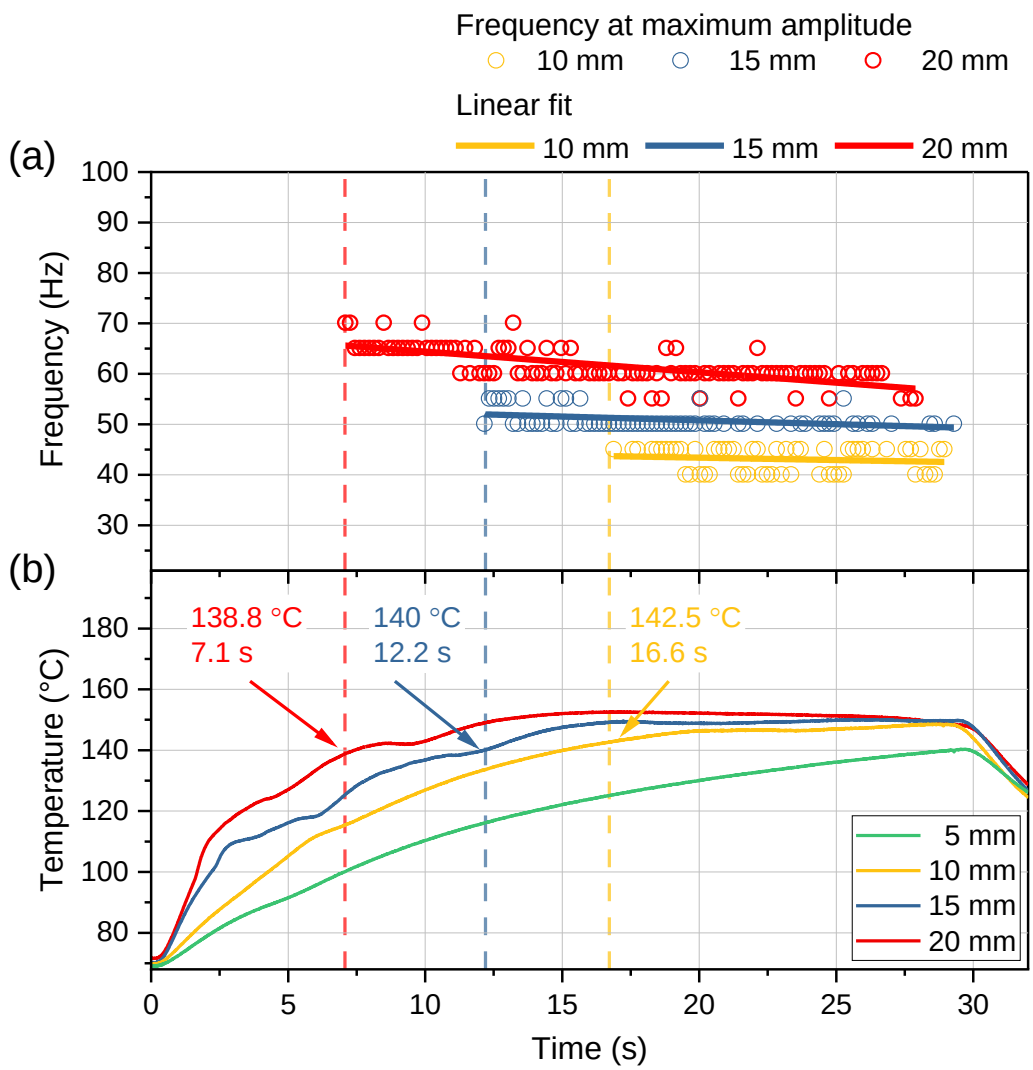

Figure 5.22 Representation of (a) the frequency of the spectrogram at peak current amplitude and (b) workpiece temperature, using a consistent time scale. Dotted lines indicate the moment when the current amplitude begins in order to identify their respective workpiece temperature.

In particular, calculating bubble rise velocity requires determining the drag coefficient based on accurate measurements of bubble size, shape, and aspect ratio. However, as noted in section 5.3.2 (modeling of electrolyte temperature), the PEP process involves turbulent flow with a Reynolds number of the order of 10^5. Furthermore, the PEP process involves the dynamic movement of numerous bubbles accompanied by discharges, as observed using a high-speed camera. This complicates the establishment of a direct mathematical correlation between bubble rise velocity and liquid temperature under the specific conditions of the PEP process, which is beyond the scope of this research. Despite the complexities, it is still viable to discuss the effect of liquid temperature on bubble rise velocity by associating its impact on fluid properties, including density, viscosity, and surface tension. As already shown in Figure 5.14, the surrounding electrolyte temperature increases during the PEP process, as measured 15 mm away from the workpiece. With increasing liquid temperature, fluid density, dynamic viscosity, and surface tension typically decrease, as displayed in Table 5-1.

Table 5-1 Physical properties of water at varied temperature taken from NIST database [195].

Temperature (°C)	Density (kg/m³)	Surface tension (mN/m)	Dynamic viscosity (mPa·s)
70	977.76	64.48	0.40
80	971.79	62.67	0.35
90	965.31	60.82	0.31
100	958.35	58.91	0.28

The changes in fluid properties can affect the bubble rise velocity in several ways. Firstly, a decrease in fluid density results in a reduced buoyancy force acting on the bubble, while also diminishing the fluid's inertia, which in turn leads to a lower drag force on the bubble. The overall effect on bubble rise velocity depends on the balance between buoyancy and drag forces. Secondly, a decrease in surface tension can alter the shape and size of bubbles, which subsequently affects the drag force acting on them, leading to changes in the bubble rise velocity. Lastly, a decrease in fluid viscosity influences the Reynolds number (Re):

$$Re = \frac{\rho_l v_b d_b}{\mu_l} \qquad 5.10$$

where ρ_l is liquid density, v_b is velocity of liquid, and d_b is diameter of bubble, and μ is the dynamic viscosity of the liquid. The drag force (F_d) can be expressed as:

$$F_d = C_d A_b \frac{\rho_l {v_b}^2}{2} \qquad 5.11$$

where C_d is drag coefficient and A_b is cross-sectional area of the bubble. The drag coefficient (C_d) is a dimensionless number used to quantify the drag force which can be determined experimentally or calculated using theoretical models. A change in the Re influences the C_d and eventually the drag force (F_d) on the bubble. Consequently, a reduction in fluid viscosity leads to a decrease in drag force acting on the bubble, which in turn results in an increased bubble rise velocity. The correlation between the bubble rise velocity and the temperature of the liquid has been validated experimentally by Zhen et al. [190]. In their experiment, bubble rise velocity increased by 15% when the temperature changed from 100 °C to 150 °C. They have attempted to explain by relating it to changes in liquid viscosity, gas density, and bubble surface properties. Even though the experiments of Zhen et al. differ from the ones in this study, the relationship between temperature and bubble rise velocity due to changes of liquid and gas properties is experimentally substantiated. Thus, the complex interplay between fluid properties and flow conditions depending on the temperature of the liquid in turbulent flow regimes influences the bubble rise velocity, possibly explaining the noticeable decreasing trend in the current oscillation frequencies at decreasing immersion depths from 20 mm to 10 mm during the PEP process. With a 20 mm immersion depth, the fundamental frequency experiences a 16% change throughout the PEP process, starting from when the frequency becomes observable. This can be associated with changes in fluid properties caused by varied electrolyte temperature during the PEP process. As a stable gas layer envelops the

workpiece, the rise in workpiece temperature experiences a slight reduction due to the lowered electrical power dissipation, as previously explained. Even though the electrolyte temperature consistently rises as shown in Figure 5.14, measurements taken 15 mm from the workpiece may not accurately reflect the electrolyte temperature closer to the workpiece. A reduction in power transfer to the workpiece is caused by the emergence of the gaseous layer. This leads to a decrease in the temperature of both the workpiece and the adjacent electrolyte, which subsequently influences the bubble rise velocity. This change, in turn, has an effect on the bubble rise velocity and, eventually, the current oscillation frequency, until the completion of the PEP process. When the immersion depth is reduced to 10 mm, the frequency decrease over time is less pronounced since the temperature decrease is reduced.

5.3.4.3 Correlation between camera signal intensity and electrical current waveform

To examine the correlation between signals originating from the discharges incorporated with gas layer dynamics and the electrical current waveform, the integrated camera signal intensity is plotted alongside the electrical current waveform, as shown in the Figure 5.23.

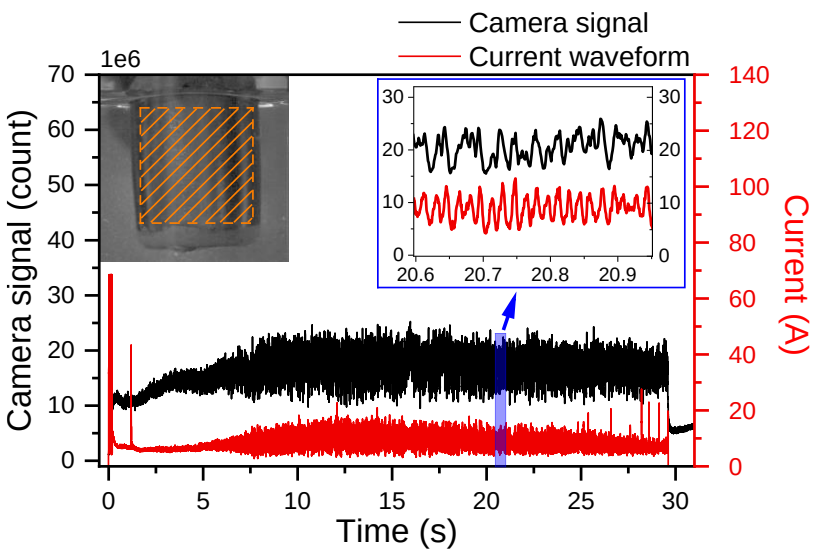

Figure 5.23 Combined plot of the integrated camera signal (black curve) from the selected area (indicated by the shaded region in the inset photo, top-left) over time and the current waveform (red curve) for a 20 mm immersion depth. The inset in the upper right displays an expanded view of the area within the blue box.

The camera signal is restricted to the shaded area in the inset image (top-left), focusing solely on the occurrences within the workpiece area. Despite the black and white image causes both discharges and the gaseous layer to appear bright and challenging to distinguish, discharges are distinctly brighter and occur where the gaseous layer is not excessively thick. As depicted in Figure 5.23, oscillations in the camera signal are found to be analogous to the current waveform. High camera signals are indicative of an enhanced presence of discharges on the workpiece surface, while low camera signals suggest the presence of an excessively thick gaseous layer that hinders sustaining the discharges. The inset in top-right corner of Figure 5.23 reveals an enlarged segment of the graph, outlined in blue, where a correlation between

the camera signal and current waveform is noticeable. From this inset, the correlation between the two graphs originating from separate electrical and optical (but temporally synchronized) measurements can be more clearly discerned. To identify temporal variations in the frequency components of the camera signal over time, spectrogram analysis was executed on the camera signal data at immersion depths ranging from 5 mm to 20 mm as previously conducted on the current waveform. The outcomes were then directly compared with spectrograms of the current waveforms, as presented in Figure 5.24.

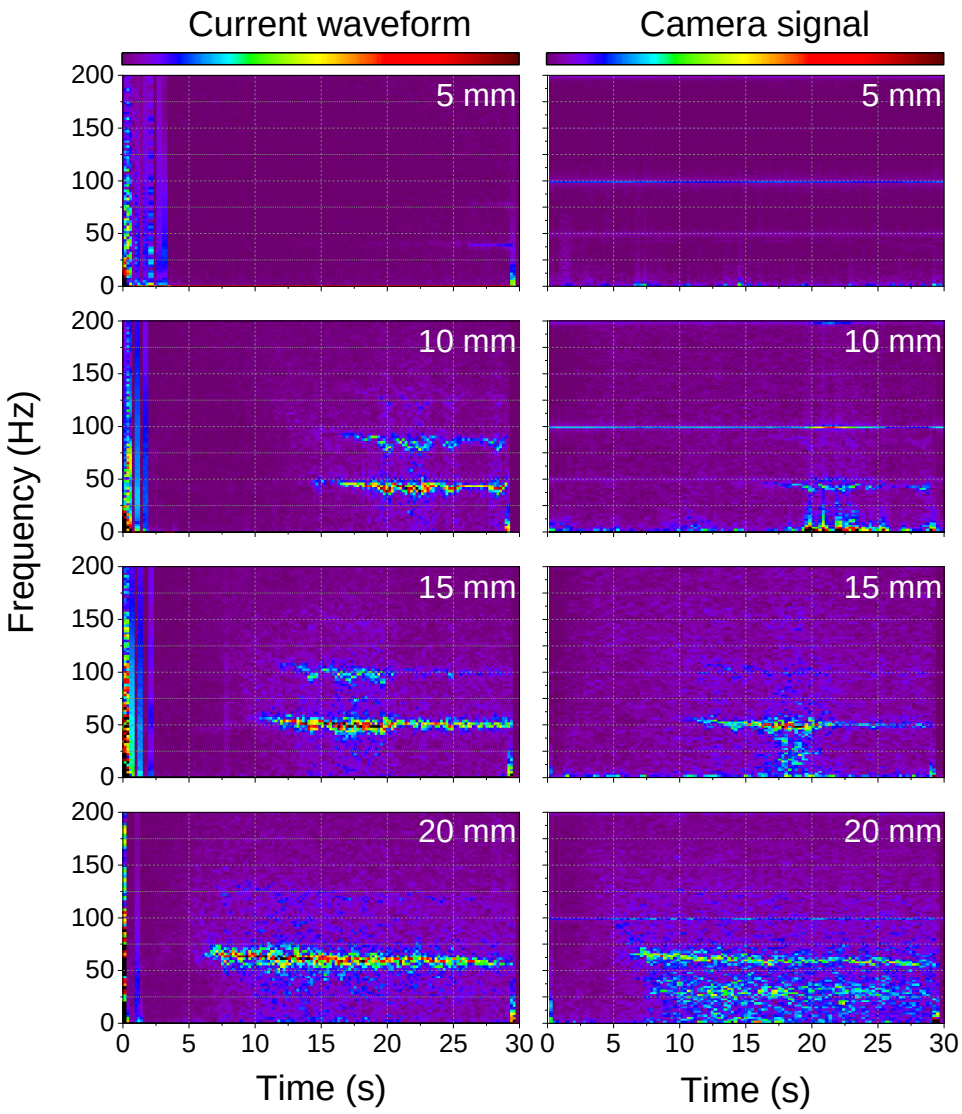

Figure 5.24 Comparative spectrograms for current waveform (left column) and camera signal (right column) at immersion depths of 5 mm to 20 mm.

The spectrograms reveal a noticeable correspondence between the fundamental frequency of the camera signal and the frequency of the electrical current waveform. At the 20 mm immersion depth, the camera signal spectrogram reveals additional frequency components appearing below the fundamental frequency (approximately 65 Hz). Numerous factors could be responsible for the emergence of these extra components, including noise and interference or harmonics and subharmonics. However, attributing these components to noise is difficult, as

their amplitude is as significant as the fundamental frequency, and they appear exclusively below the fundamental frequency, not above it. Furthermore, as they are not integer multiples of the fundamental frequency, they cannot be considered as harmonics or subharmonics. The emergence of extra frequency components could be ascribed to the formation and disintegration of other bubble layers with different periodicity during high-speed camera recording, which can still influence the overall spectral content of the signal. Nonetheless, these additional frequency components are not particularly discernible in the current waveform spectrogram, because the electrical signal, reflecting the overall gaseous layer behavior contributing to the non-linear load effect, does not account for spatial information. Furthermore, the camera signal spectrograms reveal a constant 100 Hz frequency component during the entire PEP process, especially noticeable in the 5 mm and 10 mm cases, which is absent in the electrical signal spectrograms. The use of an oscillating light source in the experimental setup, operating at a 50 Hz alternating current frequency, could explain the observation. The consistency of 100 Hz throughout the process duration suggests it's an artifact originating from this light source. The 100 Hz component is especially prominent in the 5 mm case, as there are fewer discharges within the gaseous layer, allowing the light source's relatively intense component to be observed. Taking into account the fundamental frequency, the electrical and optical signals are interrelated, indicating the time-dependent changes in the gaseous layer that governs the electrical impedance and discharge appearance.

5.3.4.4 Spatially-resolved camera signal analysis during PEP process

Spatially-resolved analysis was conducted using the camera signal data from the high-speed camera measurement to investigate if there is vertical variance of the camera signal during the PEP process, supporting the compositional variance observed by the XPS line-scan analysis shown in section 5.3.2. To perform this analysis, it was crucial to differentiate the discharge emission from the background light originating from the light source. Therefore, the camera signal between 30 s and 40 s was used as the background since the PEP process was already finished, while the time between 15 s and 25 s was selected as the PEP process was actively ongoing, as shown in Figure 5.25(a). To obtain a justifiable comparison of the signals in both time regions the time interval for signal integration was selected as 10 s, corresponding to 10^4 frames for each region. In Figure 5.25(b), the contour plot presents the combined images from 10^4 frames captured during the PEP process between 15 s and 25 s. Figure 5.25(c) presents the vertically resolved camera signal during the PEP process and background at the X-axis position of 13 mm (marked green dotted line in Figure 5.25(b)). In Figure 5.25(c), there is a noticeable vertical gradient in camera count during the PEP process. At the lower part of the workpiece, the difference in camera signal values between the background and PEP phases is nearly three times higher compared to the upper part. This can be attributed to the upwardly directed movement of the gaseous layer, causing the lower part of the workpiece to develop a relatively thinner gaseous layer facilitating discharge generation and resulting in higher camera count. Meanwhile, at the upper part of the workpiece, a thicker gaseous layer is formed, and a weaker discharge intensity is observed from the high-speed camera measurement. The background signal exhibits a subtle vertical camera signal gradient, which can be attributed to the light source illuminating the workpiece. However, as evident in Figure 5.25(c), the vertical gradient significantly intensifies during the PEP process, suggesting that the gradient is mainly associated to the vertically diverse discharges produced during the PEP process.

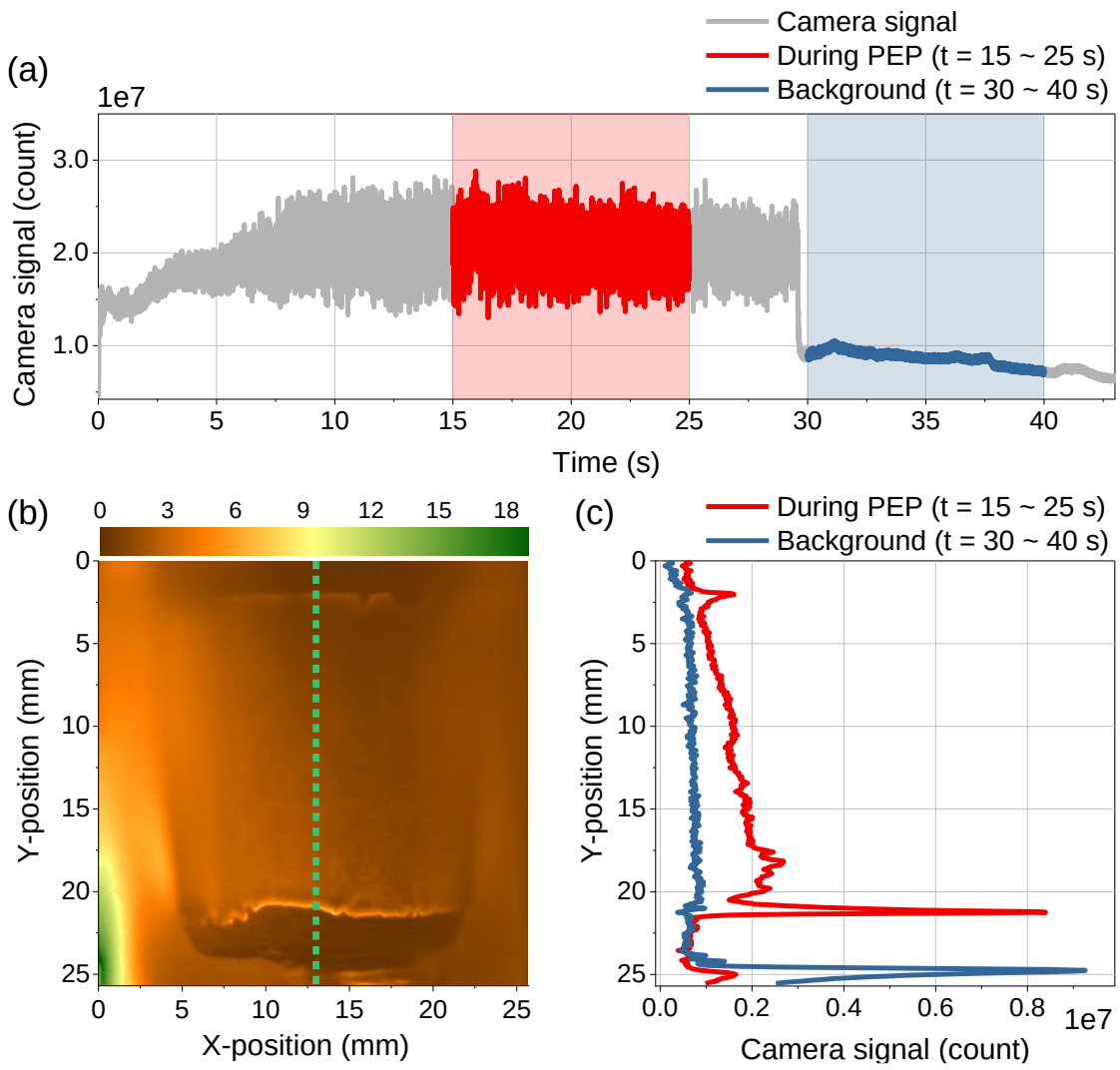

Figure 5.25 (a) Time-dependent camera count, with red markings indicating the PEP process duration (t = 15 s – 25 s) and blue markings representing the background (t = 30 s – 40 s) after the PEP process. (b) Contour plot of merged images (10^4 frames) captured during the PEP process, within the 15 s to 25 s time interval. (c) Temporally integrated camera signal values across the Y-position, as denoted by the green dashed line in (b).

This can be attributed to the upward movement of the gaseous layer, which results in variations in the gaseous layer thickness. Consequently, the impact of light illumination on the observed gradient is minimal compared to the effect of these differentiated discharges. As depicted in Figure 5.25(c), the background camera signal (blue curve) reveals a peak at the Y-position of 25 mm, and the signal from the PEP phase (red curve) similarly presents a peak at the Y-position of 21 mm. The emergence of peaks in the lower part of the workpiece during and after the PEP process can be attributed to different underlying factors. During the PEP process, a peak is noticeable at the lower edge of the cylindrical workpiece, along with a smaller peak at the upper corner (position of 2.5 mm). These specific positions correlate with the points of epoxy glue application for the sealing of thermocouples. The appearance of these peaks during the PEP process can be explained by two primary reasons. The first reason is

associated with the difference in electrical conductivity between the workpiece and the epoxy glue. The epoxy is an insulating material with notably lower conductivity than the metallic electrode. During the PEP process charge accumulation occurs at the interface between the metallic workpiece and epoxy, thereby amplifying the local discharge intensity, as seen in the brighter region around 21 mm in Figure 5.25(b). Another contributing factor is the charge buildup at the sharp edge of the cylindrical workpiece. Despite the epoxy glue covering the top and bottom of the workpiece, it is not guaranteed that the edge is entirely sealed, which may expose the sharp edge during the PEP process. Nevertheless, the first reason is more plausible, given that the epoxy glue is applied irregularly, which protrudes particularly at the X-position between 10 mm to 15 mm as seen in Figure 5.25(b), and the intensified discharge corresponds to this protrusion. Therefore, the peaks observed in the camera signal during the PEP process may arise from the conductivity difference between the two materials. However, the peak observed in the background signal (blue curve in Figure 5.25(c)) at the Y-axis position of 25 mm is already outside the workpiece area. As already depicted in the high-speed camera image in Figure 5.13, a slow-moving bubble adheres beneath the workpiece due to comparatively low fluid velocity underneath the workpiece, as illustrated by modeling in Figure 5.16(a). The electrolyte flow may differ at the side of the workpiece compared to the epoxy-covered area underneath. A more turbulent flow at the side of the workpiece can aid in bubble movement and release, whereas a laminar flow beneath the epoxy can result in stagnating bubbles. Consequently, the peak may arise from the reflected light from this bubble. The camera signal during the PEP process (red curve in Figure 5.25(c)) also exhibits a slight peak at the same peak position as the peak of background signal indicating that the bubble is present not just during the ongoing process but also at the completion of the PEP process.

5.4 Conclusions

In this chapter, diverse diagnostic approaches were implemented to reveal the fundamental processes taking place during the PEP process, focusing on the formation and development of the gaseous layer alongside discharge behavior.

In the first instance, electrical and thermal measurements are employed to characterize the temporal behavior of gaseous layer formation during the PEP process on a cylindrical WC-Co workpiece. The power transferred to the workpiece (P_{in}) at varied effective surface area of workpiece was determined by employing a calorimetric probe method. During the PEP process, distinctive heating features were observed in relation to the temperature of the anode. At the LT regime (T > 100 ºC), the P_{in} varies from 105 W to 363 W as the immersion depth increases from 5 mm to 20 mm, respectively. Meanwhile, in the HT regime (T > 120 ºC), the P_{in} converges to 192 W regardless of the anode immersion depth due to a gaseous layer around the workpiece surface. When the immersion depth, d, is increased from 10 mm to 20 mm, the fraction of power transferred to the anodic workpiece proportionally decreases from 25.7% to 16.7% since more power is consumed to heat the surrounding electrolyte at a deeper immersion depth. During the PEP process, the electrolyte temperature was simultaneously measured by the thermocouple situated 15 mm from the anodic workpiece. The temperature increased to 81.5 °C at 20 mm of immersion depth (d) from the starting temperature of ~70 °C. As the immersion depth (d) is lowered, the electrolyte temperature increment declines, and the

temperature rise gets delayed since less electrical power is consumed with a less exposed workpiece area. The mixture model of liquid and gas phases is employed to model a spatio-temporally resolved temperature evolution of electrolyte in two dimensions. According to the model, the electrolyte flow is turbulent for the first 65 s of the measurement time, then laminar with a decrease in flow velocity. Furthermore, models of the volume-averaged velocity of the fluid mixture and the spatio-temporal evolution of electrolyte temperature indicated that electrolyte fluid flows toward the cathode at the beginning of the PEP process. Then, at ~5 s, it begins to flow reversely toward the anodic workpiece, and the backstream of the fluid flow becomes more powerful, contributing to an increment of the surrounding electrolyte temperature. The spatio-temporally resolved temperature simulation data indicates that the spatial temperature gradient is created around the workpiece's region during the PEP process. The insights gained from spatio-temporal modeling provide crucial information for determining the size of the electrolyte bath. Furthermore, XPS line-scan analysis was carried out to characterize the surface composition of the workpiece surface in a longitudinal direction. According to the XPS results, aliphatic carbon was preferentially removed from the surface of the anodic workpiece after 30 s of the PEP process. After 30 s of the PEP process, a slight compositional gradient was observed in the longitudinal direction for d = 20 mm, possibly due to the non-uniform distribution of current density, which influences the amount of material removed. W 4f peaks also represent the spatial discrepancy in WC binding between the top and bottom of the cylindrical workpiece based on their chemical state. Thus, after the PEP process, there is a slightly different oxidative state of W between the bottom and upper parts of the workpiece at the length of 20 mm.

In the last section of this chapter, synchronized electrical and high-speed camera measurements were used to establish the correlation between the temporal behavior of the non-linear load character of the current waveform and gas layer dynamics. Additionally, the noticeable current oscillation was characterized using spectrogram analysis, which revealed the dependency of the fundamental frequency on the workpiece immersion depth, potentially related to changes in liquid properties based on temperature. Spectrogram analysis was also utilized on high-speed images, validating the correlation between the dominant frequency component seen in the camera signal and the electrical current waveform, roughly 65 Hz when d = 20 mm. Moreover, spatial analysis of the high-speed camera signal confirmed a vertical gradient in the camera signal on the workpiece surface during the PEP process. This increased gradient is ascribed to variations in electrical discharges generated at different vertical positions during the PEP process. These discharges interact with the workpiece, causing material removal and surface refinement. The uneven distribution of discharges across the vertical axis contributes to the pronounced vertical material gradient observed in the XPS analysis. Understanding this gradient is crucial for optimizing the PEP process, as it offers insights into the distribution of discharges and their impact on surface quality, particularly for elongated workpieces.

The insights obtained from this chapter offer a foundation for future research focused on the continued improvement and enhancement of the PEP process. By utilizing the diagnostic techniques discussed in this study, a deeper understanding of the thermal, electrical, and optical properties of the PEP process in conjunction with gaseous layer formation and discharge behavior, has been achieved.

6 Application of PEP in surface finishing of 3D-printed metallic parts

6.1 Introduction

This chapter explores the practical application of plasma electrolytic polishing (PEP) as a surface finishing technique for parts made by additive manufacturing. The surface of a 3D-printed stainless steel (SS) mist chamber is treated by the PEP process to enhance its misting capability, optimizing aerosol production for the creation of plasma-polymerized (pp) films.

6.1.1 Surface-finishing of additive manufactured (AM) parts

3D-printing or additive manufacturing (AM), presents numerous advantages across different industries, primarily because it enables the fabrication of complex and detailed structures that could be challenging or impossible to achieve via conventional manufacturing methods. This versatility paves the way for product customization and the creation of highly detailed models from a variety of materials, including metals and plastics. Among the diverse techniques of 3D-printing, selective laser melting (SLM) has been receiving substantial attention. The growing interest in SLM can be attributed to its unique technological benefits, which enable the fabrication of complex metallic components with high precision and efficiency [7, 196, 197]. Nevertheless, the rough native surface of the SLM-printed part is not suitable for many applications and, thus, requires post-treatment for smoothening the surface [198]. Given its ability to effectively polish complex-shaped workpieces, the PEP process has been identified as a promising technique for improving the surface quality of 3D-printed metallic components.

6.1.2 The use of mist chambers for producing plasma-polymerized thin film

Thin films produced by plasma enhanced chemical vapor deposition (PECVD) techniques are widely used in numerous applications ranging from material to life sciences, as they can improve surface properties without affecting properties of the bulk material [137, 199]. One of the notable advantages of the PECVD process is its comparatively lower material and energy requirements. Additionally, it can produce distinctive films, such as highly branched and cross-linked polymer films, that are unattainable with conventional methods [200-202]. Among traditional vacuum-based PE-CVD techniques, atmospheric-pressure PE-CVD has gained popularity due to its advantages such as simplified processing, no need for vacuum equipment, and area-independent deposition [203, 204]. The process utilized here can be distinguished from conventional PE-CVD; it entails depositing a precursor followed by atmospheric-pressure plasma treatment. An advantage of this method is that it also allows the use of film precursors with low vapor pressure. Instead of vaporizing the precursor, it can be nebulized or sprayed as an aerosol over the substrate, with a subsequent local atmospheric plasma promoting the

cross-linking of the compound [205]. Otherwise, precursors can be deposited using spin coating, dip coating, or single droplet coating [206, 207]. However, these methods present drawbacks, such as limited substrate geometry or difficulty in creating specific microstructures or cavities. In contrast, spray deposition methods using a spray chamber enable easy deposition of non-evaporative and nearly insoluble liquids while achieving homogeneous coatings. Spray chambers, typically utilized in applications such as inductively coupled plasma mass spectrometry (ICP-MS) or inductively coupled plasma atomic emission spectrometry (ICP-AES) [208], demand low liquid flow rates and can be readily combined with the plasma polymerization process. Effective spray applications require careful consideration of factors such as droplet size, distribution, and liquid transport efficiency, all of which depend on the design of the chamber and material [209]. In this regard, mist chambers are preferred for generating small droplets (< 10 µm), making them ideal for synthesizing thin plasma-polymerized (pp) films [210]. The pp-films consist of an irregularly cross-linked network originating from organic molecules and their fragments. In this sense, the plasma-polymerization is largely different from the conventional chemical polymerization, where unsaturated monomer molecules are linked to chains forming polymers-molecules with repeating chemical structure to which structural formula can be assigned. Thus, 3D-printing is chosen as the preferred fabrication method for mist chambers due to its capability to create customized, laboratory-sized objects with various configurations and high reproducibility. Stereolithography (SLA) 3D-printing using methacrylate photopolymer resins has been already investigated [211], but its hydrophobic nature leads to decreased aerosol transport efficiency. Meanwhile, metallic mist chambers fabricated using 3D-printers can provide chemical inertness, compatibility with a broader range of monomers, and longer lifetimes, making them more suitable for specific misting applications. However, the surface properties of the mist chamber play a crucial role in optimizing its misting performance.

Therefore, in this study, the PEP process was incorporated as a surface finishing step on stainless steel (SS) mist chambers produced by SLM type 3D-printers, emphasizing its contribution to enhanced misting performance and functional thin film fabrication through the pp process, ensuring efficient and reproducible thin film deposition. In order to evaluate the impact of the PEP process on the 3D-printed workpiece surfaces and enhance the process parameters, a comprehensive surface characterization was carried out, comprising measurements of surface elemental composition, roughness, morphology, and surface wettability. To determine the effectiveness of the PEP process in enhancing the misting performance of the mist chamber, the mist-out time was measured and directly benchmarked with the untreated mist chamber. Finally, the pp process was performed using the mist produced by PEP-treated metallic chamber, demonstrating that functional thin films can be fabricated in a reproducible and controlled manner.

6.2 Experimental details

6.2.1 Design and manufacturing of the mist chambers

The design of the mist chamber is shown in Figure 6.1(a). Citation [210] contains additional information regarding the design of chamber design and the post-processing method for 3D printing (e.g., slicing). In accordance with the design, the metallic mist chamber was manufactured with 316L SS powder using a SLM type metallic 3D-printer (SLM 280, SLM Solutions Group AG), as depicted in Figure 6.1(b). The 316L SS powder (SLM Solutions Group AG) has a particle size distribution between 10 and 45 µm, and the details of its chemical composition can be found in Table 6-1.

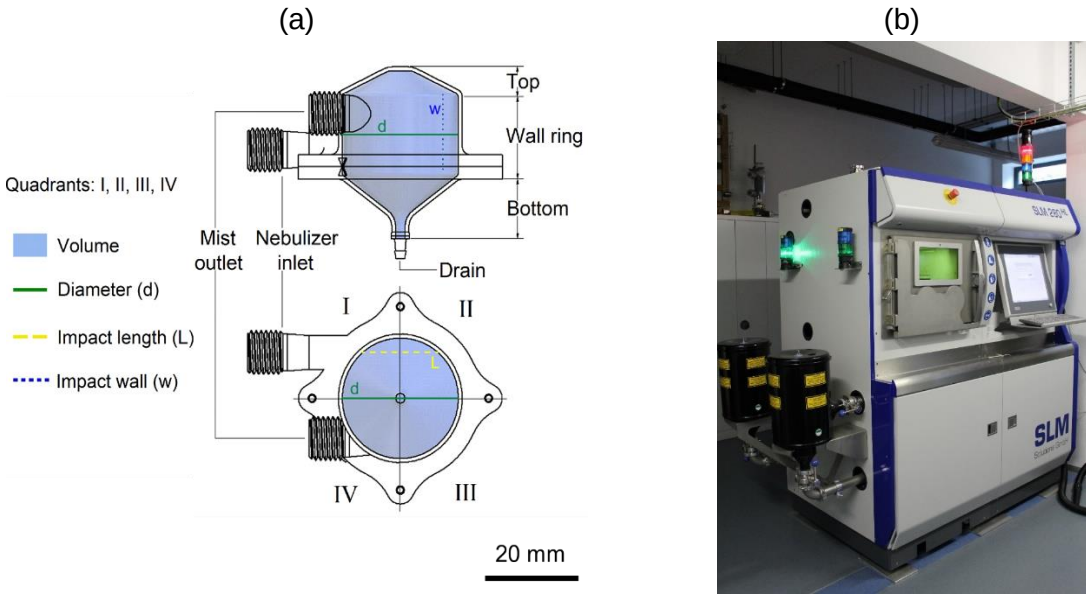

Figure 6.1(a) Depictions of the mist chamber from a side and top perspective along with its design details (adapted from [210]). (b) Photograph of SLM type metallic 3D-printer.

The layer thickness was set to 30 µm for the printing. Support structures were created on the chamber's outer surface to ensure the internal surface's smoothness, facilitating better misting. The chamber was designed to disassemble into two parts, allowing the internal part of the chamber to be polished readily during PEP. The post-process, after the 3D-printing, was followed by removing outer supports and grit-blasting (inner and outer surfaces) with glass beads to eliminate residual powder and debris. To facilitate surface testing, probes with dimensions of 33 mm × 10 mm × 2 mm are produced using the same 3D-printing procedure, simplifying surface investigation. Photographs of the 3D-printed mist chamber and the test probe are displayed in the Figure 6.3.

Table 6-1 Chemical composition of 316L powder used in SLM (wt.%) [212]

Fe	Cr	Ni	Mo	Mn	Si	P	S	C	N
Balance	16 - 18	10 – 14	2 – 3	2	1	0.05	0.03	0.03	0.1

6.2.2 Plasma electrolytic polishing process for 3D-printed parts

A PEP-process was established for the 3D-printed parts. The surface finishing was achieved with an industrial prototype apparatus developed in-house, equipped with a 125 L electrolyte bath (bath #1), as depicted in Figure 6.2. The capability of this apparatus includes delivering a maximum current of 180 A and a voltage of 500 V, ensuring sufficient treatment for large specimens. Control and data sampling of the PEP system, including electrical measurements, were facilitated using a software tool, designed in-house, based on LabVIEW® (National Instruments).

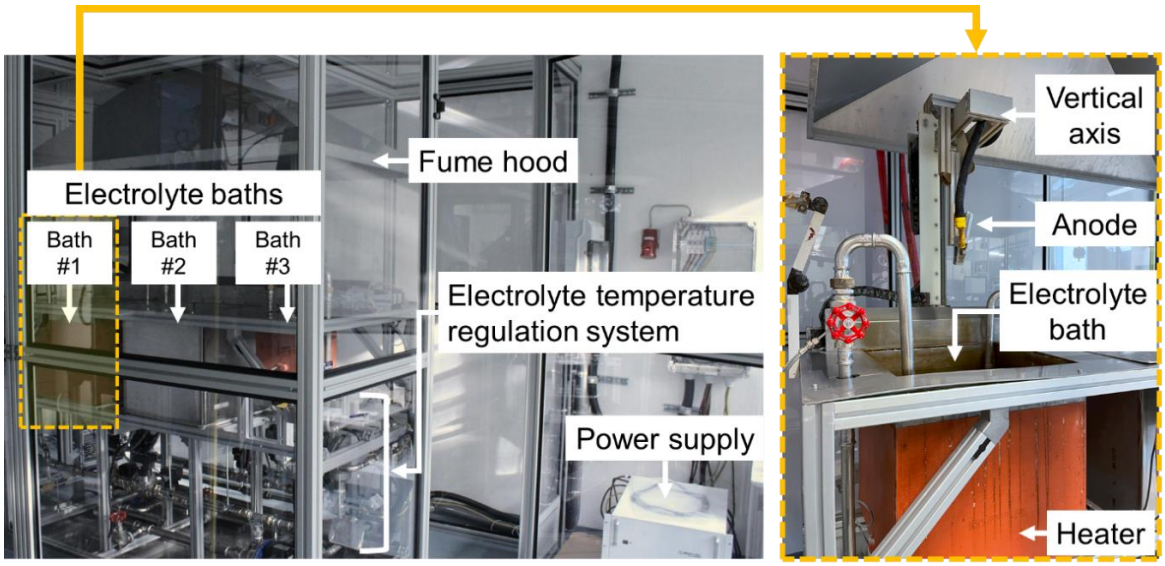

Figure 6.2 A representation of the in-house industrial-scale PEP apparatus at INP Greifswald (left) paired with a zoomed-in image of bath #1 (right).

Previous studies on stainless steel treatment are available [9, 15, 64, 74, 94], and methodologies have been extensively studied and It has been suggested that the $(NH_4)_2SO_4$ electrolyte concentration lies between 2 – 6 wt.%, with a temperature of 40 - 95 °C and a voltage setting of 240 - 400 V. Within this study framework, using the electrolyte of $(NH_4)_2SO_4$, the optimal voltage parameter was identified as 320 V, with the temperature and concentration established at 80 °C and 5 wt%, respectively. The chamber was rotated 90° sequentially three times to compensate for geometrical inhomogeneity and treated for 7.5 min per orientation, as described in Figure 6.3(a). Thus the total treatment time for the chamber part was 22.5 min.

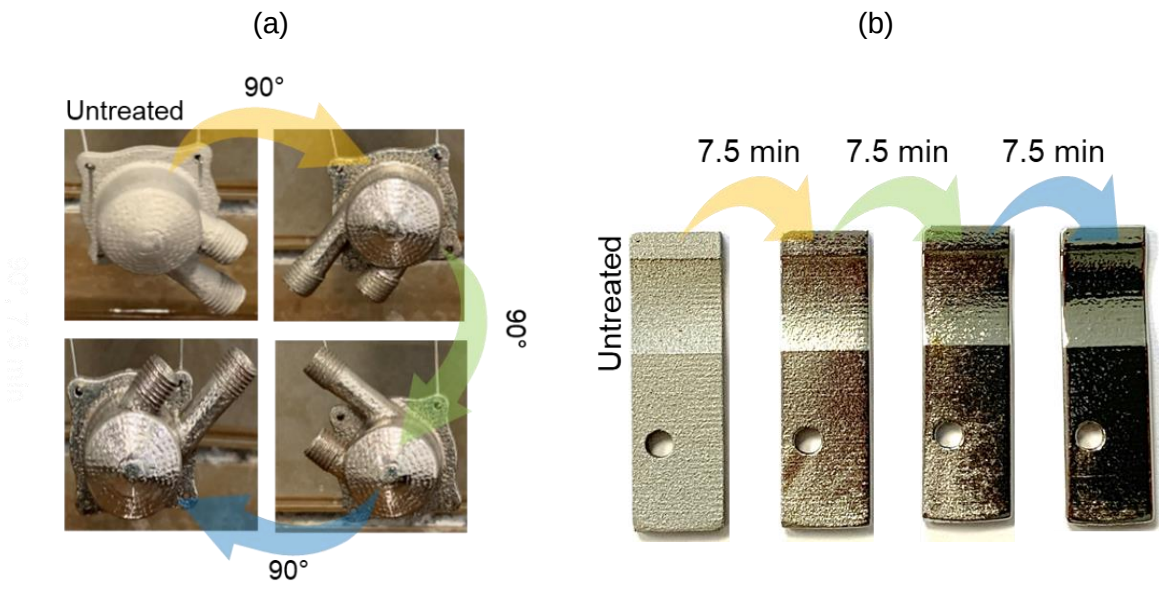

Figure 6.3 (a) Photographs of 3D-printed metallic mist chambers showing the PEP immersion sequence (adapted from [210]) and (b) test specimens for surface characterization.

Figure 6.4 provides a depiction of the typical current-voltage pattern during the PEP process. As the PEP operation progresses, there is a noticeable reduction in current. This current reduction can be attributable to the thickening of the VGE layer around the workpiece, a result of the elevated temperature of the surrounding electrolyte, as highlighted in chapter 5.3.

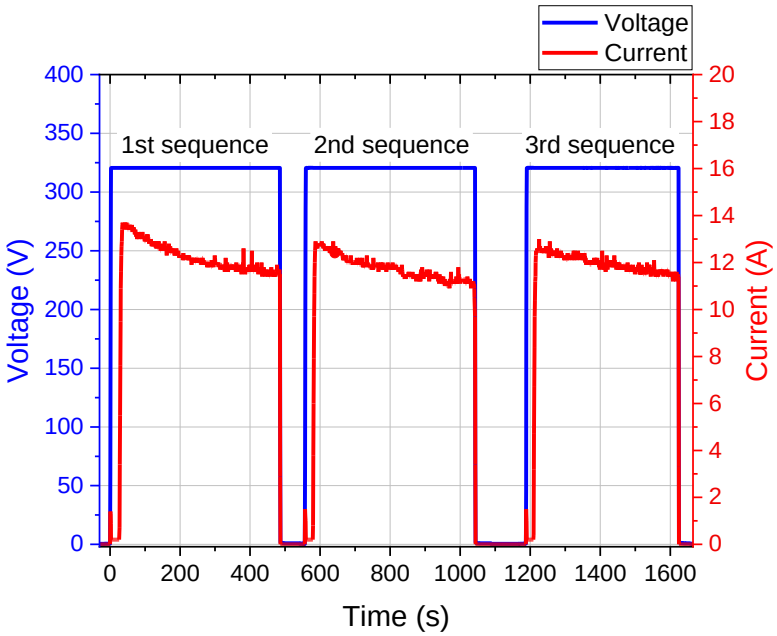

Figure 6.4 Typical voltage-current waveform during the PEP process on the 3D-printed metallic mist chamber. The process consists of three sequences, each lasting 7.5 min per orientation.

Meanwhile, the test specimens for the surface characterization were treated from 7.5 min to 30 min without the rotation procedure, as shown in Figure 6.3(b). After the PEP process, a cleaning procedure using distilled water followed to remove residual electrolytes on the surfaces of 3D-printed parts.

6.2.3 Fabrication of plasma polymerized thin films

The initial step for pp film deposition involves generating mist through a two-step process: nebulization and misting. First, a peristaltic pump (LP-BQ50-1J, Longer) transports liquid monomers into a quartz concentric nebulizer (TQ-30-A1, Meinhard Glass Products) to form an aerosol. Then, aerosols are filtered in the mist chamber connected to the nebulizer, allowing only the small droplets (< 10 µm) to emerge, and a fine and uniform mist is produced at the outlet of the chamber. In this process, larger droplets are drained away. The monomer used here is a mixture of tetrahydrofurfurylmethacrylate (THFMA, $C_9H_{14}O_3$, Sigma-Aldrich) and 1,2,4-trivinylcyclohexane (TVC, $C_6H_9(CH{=}CH_2)_3$, Sigma-Aldrich) with the volume ratio of 1:2 (THFMA:TVC). Afterwards, a non-thermal RF atmospheric-pressure plasma jet (APPJ) is employed for plasma-induced polymerization. A detailed description of the APPJ and the 2-step polymerization process can be found in Ref. [213]. The APPJ was operated at 5 W of input power with an Ar flow rate of 1 slm. The distance between the nozzle outlet and the substrate was 5 mm. The pp film can be obtained by following three steps, as shown in Figure 6.5:

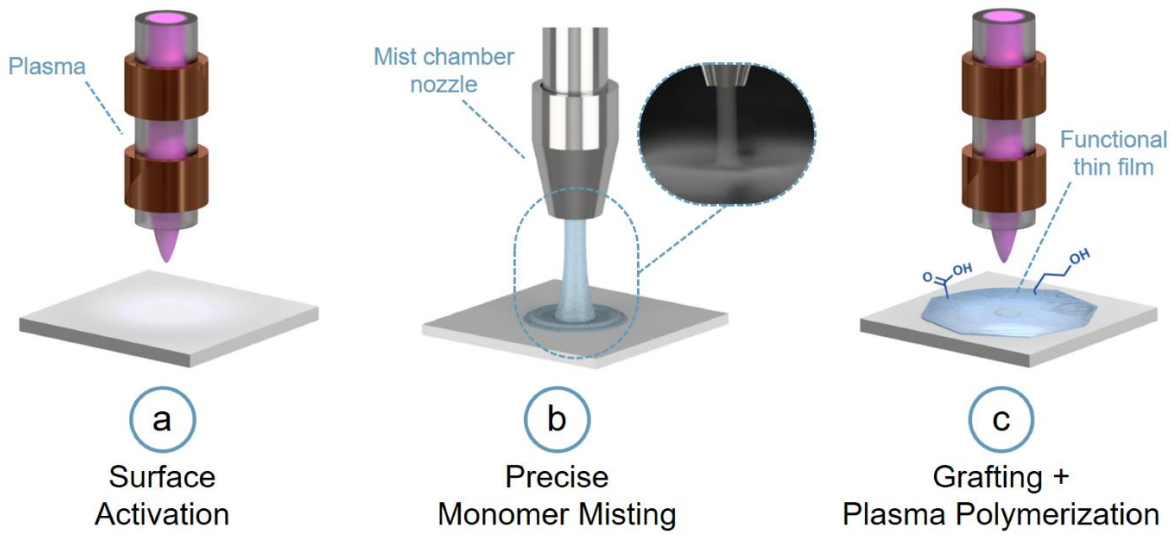

Figure 6.5 Process steps for the plasma-based synthesis of pp-films obtained from liquid monomers (reprinted from [210]).

(1) The substrate is treated by the APPJ for plasma- induced surface activation.

(2) A thin liquid layer is deposited by misting the monomer on the surface-activated substrate using a mist chamber (mist chamber outlet with focusing nozzle, orifice of Ø2 mm, and distance to substrate 2 mm).

(3) For cross-linking process such as plasma-polymerization, the deposited monomer droplet is treated by the APPJ for 16 s.

6.2.4 Analysis of surface properties and misting effectiveness

This section provides a description of the methods used to characterize the surface properties of 3D-printed workpieces and to evaluate the performance of the mist chamber.

6.2.4.1 Optical microscopy

Digital optical microscopy (VHX-1000E, Keyence) was used to observe the effect of PEP on the surface and edges of the 3D-printed parts.

6.2.4.2 Water contact angle

Water contact angle (WCA) measurements were performed on the surface of 3D-printed metallic specimens before and after PEP treatment to evaluate the surface wettability. The measurements were carried out on the surface of the test specimens instead of the mist chamber due to the limited instrumental setup of the WCA apparatus for the complex geometry of the chamber. The measurements were conducted at room temperature under ambient air by the sessile drop method using a WCA 30 optical contact angle analyzer (DataPhysics Instruments GmbH). A drop of 0.5 µL-distilled water was placed on the specimen's surface, and the resting drop's contact angle was evaluated employing a software (SCA 20, DataPhysics Instruments GmbH).

Contact angle measurements were performed four times at different spots on the surface of the each 3D-printed specimen, and the average of these values was used for comparison of the wettability.

6.2.4.3 Ellipsometry

An ellipsometer (M-2000V, J.A. Woollam Co.) was used to determine the thickness of the pp-films at incidence angles of 55°, 65°, and 75°. Optical data obtained for the films were fitted using the Cauchy model, including non-uniformity and roughness, using CompleteEASE software (version 5.01, 2013, J.A. Woollam Co.). Each pp-film was measured three times to obtain the average thickness value.

6.2.4.4 Quartz crystal microbalance

To quantitatively evaluate the mist chamber's performance, a customized quartz crystal microbalance (QCM, OpenQCM, Novaetech S.r.l) was employed to measure the mass of the misted liquid monomer mixture. The QCM measurement was performed as follows. First, the nebulizer was prepared with the monomer, and then, the QCM was initiated. To stabilize the signal, the QCM was allowed to run for a certain period of time until it reached the crystal's fundamental resonant frequency (f_0). Then, the nebulizer pump was operated, producing the aerosol into the mist chamber, and the misting started on the surface of the QCM crystal. The QCM was run up to the resonance peak, where it plateaus. The resonance peak was maintained for 3 s and then began to decline. In the final step, the nebulizer pump was turned off, and the chamber ran dry while a new QCM crystal was installed to start a new measurement. Although the QCM measurement was acquired over a longer period of time, a

selected portion of the data was considered for the analysis, with an offset of 2 s before nebulization (0 to 2 s at f_0), to the peak oscillation, as well as the 3 s of the resonance peak. The acquired oscillations in quartz crystal's frequency (Δf) from the QCM measurement are then converted to the mass difference (Δm) based on Sauerbrey's formula [214], as expressed in Equation 6.1, to obtain a mist chamber performance indicator defined as mist-out time (T_{mist}). T_{mist} is considered as a way to measure and compare the transport efficiency of the mist, in which the shorter the time, the faster the misted particles leave the chamber, meaning better efficiency.

$$\Delta f = -\frac{2f_0^2 \Delta m}{A\sqrt{\rho_q \mu_q}} \qquad 6.1$$

The T_{mist} was obtained by determining the time (X-axis) when the mass peak (Y-axis) fell 1% and subsequently subtracting the time interval before nebulization starts ($T_{\Delta m_0}$ = 2 s) as described below:

$$T_{mist} = \left(T_{\Delta m_{peak}} - \frac{1 \times T_{\Delta m_{peak}}}{100}\right) - T_{\Delta m_0} \qquad 6.2$$

More detailed description of the T_{mist} determination is available in Ref. [210].

6.3 Results and discussion

The capability of the PEP process extends beyond modifying surface roughness, influencing surface crystalline structure and elemental concentration, possibly linked to surface wettability. The section commences by outlining various surface characterization techniques used to examine the impact of PEP on the surface of 3D-printed parts. Following this, the performance evaluation of the mist chamber, influenced by the PEP process, is elaborated upon.

6.3.1 Influence of plasma electrolytic polishing on surface of 3D-printed part

For the initial part of the surface characterization, the PEP effect on the surface crystal structure of the 3D-printed test specimen was investigated using GIXRD shown in Figure 6.6(a). The XRD diffraction patterns present that the peaks at (43.5°, 50.5°, 74.5°) are noticeable on the surface of 3D-printed parts before and after the PEP process. These peaks have been designated as the face-centered cubic (fcc) austenite phase (PDF 00-047-1417 (Fe, Ni) Taenite), representing a typical pattern observed in SS [215, 216]. After the PEP processes, no significant changes in phase composition were detected. However, as shown in Figure 6.6(b), the crystallite size, determined by Scherrer's equation at the dominant peak appearing at 43.5°, increases from ~16 nm in the untreated specimen up to ~34 nm after the PEP process. The grain size increase could be ascribed to the preferential dissolution of the smaller grains, which leads to relatively larger grains remaining post-PEP processing.

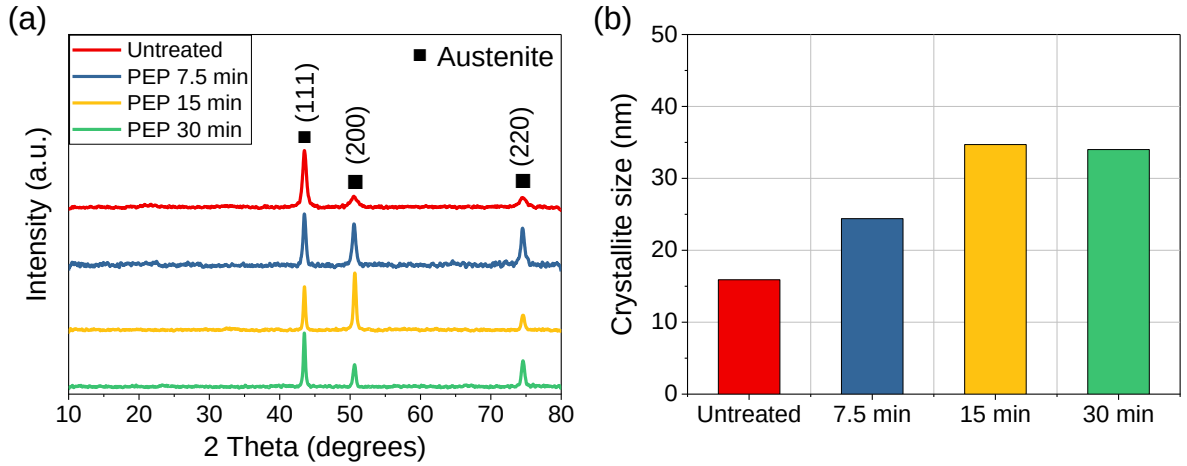

Figure 6.6 (a) Comparison of XRD diffraction patterns on the surface of 316L SS fabricated via SLM, pre- and post-PEP for durations of 7.5, 15, and 30 min. (b) Crystallite sizes estimated by Scherrer's equation.

While the elevated workpiece temperature during the PEP process could potentially influence the growth of the austenitic phase grain size, this notion is not entirely convincing. Salarvand et al. [216] observed an increase in the crystallite size of the 3D-printed 316L SS by SLM from 19.4 nm to 29.9 nm after the furnace heat treatment at 1100 °C. However, as demonstrated in the prior section 5.3.1, the workpiece temperature during the PEP process could be maintained below 200 °C. Conversely, during SLM, the laser-affected part's temperature can surpass 1500 °C [217], making the heat effect more significant before the PEP process. Therefore, the observed increase in crystallite size following the PEP process in these conditions can be explained by the preferential dissolution of the smaller grains. The crystallite size shows no increase from 15 min to 30 min, possibly because the surface of 3D-printed SS specimen achieves an equilibrium state after a certain length of PEP. In this equilibrium state, the rate of surface material dissolution decelerates, thereby maintaining a constant crystallite size. This can be further substantiated by the later shown changes in surface roughness measured by WLI.

The performance of the mist chamber can be dependent on the chemical composition of its surface, as it contributes to the surface's wettability, which in turn governs the formation of droplets and their size distribution in the misting chamber. In order to investigate how the PEP process influences the surface's chemical composition of 3D-printed parts, XPS analysis was conducted. Prior to XPS analysis the surface of the 3D-printed test specimens were etched with an Ar cluster ions beam for 300 s to remove contamination. As depicted in Figure 6.7, there is a substantial change in the elemental fractions on the surface of 3D-printed specimen after the PEP process compared to the untreated specimen. However, this change becomes less apparent as the polishing duration progresses from 7.5 to 30 min. Prior to PEP treatment, the surface of 3D-printed part, contains 25 at% C, which could be due to residual surface contamination that persists even after the ion etching.

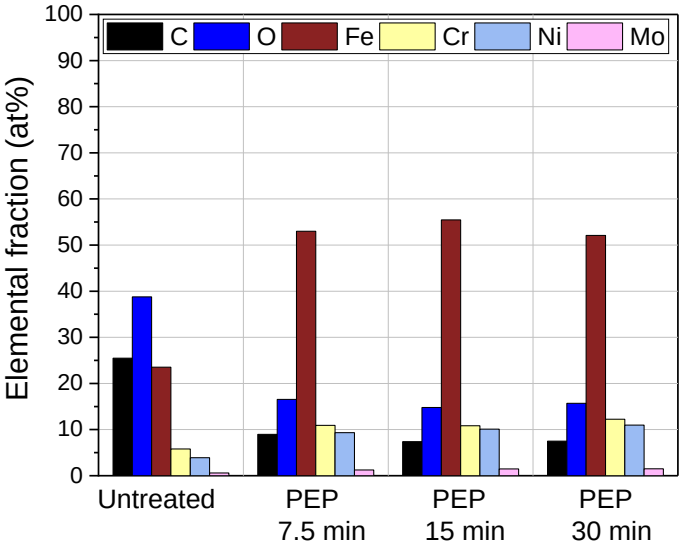

Figure 6.7 Comparison of surface elemental composition of 3D-printed specimens, before and after PEP treatment, over a range of durations from 7.5 min to 30 min.

After the implementation of the PEP process, the C content notably drops to 7 at%, which is a result of the elimination of C-containing impurities during the process. The elemental fraction of O experiences a significant drop from 39 at% to 16 at% after the PEP process, possibly because of the removal of oxidized compounds, particularly iron and chromium This was further investigated by carrying out peak fitting to determine the chemical state of Fe and Cr on the untreated and PEP-treated (30 min) parts, with the results presented in Table 6-2.

Table 6-2 Relative fractions of metallic and oxidized components of Fe and Cr, determined via peak fitting of Fe $2p_{3/2}$ and Cr $2p_{3/2}$, respectively.

	Fe $2p_{3/2}$		**Cr $2p_{3/2}$**	
	Metallic Fe	Oxidized Fe	Metallic Cr	Oxidized Cr
Untreated	60%	40%	50%	50%
PEP 30 min	80%	20%	65%	35%

The result indicates an increase in metallic Fe and Cr content after the PEP process, which ascribe to the exposure of the underneath metal surface after oxidized Fe and Cr removal. In stainless steel (SS), Cr is a crucial element that contributes to its anti-corrosion properties. Therefore, it is important to prevent significant changes in the Fe and Cr ratio (Fe/Cr) during the PEP process. Based on the data presented in Figure 6.7, the Fe/Cr ratio remains consistently within the range of 4-5 both before and after the PEP treatment, regardless of the PEP process duration. This suggests that the corrosion resistance property provided by Cr can be effectively preserved after the PEP process. As a result, the chemical inertness required for practical use of the mist chamber can be maintained.

The morphological features of the untreated and PEP-treated (30 min) specimens were compared by OM and SEM, as demonstrated in Figure 6.8.

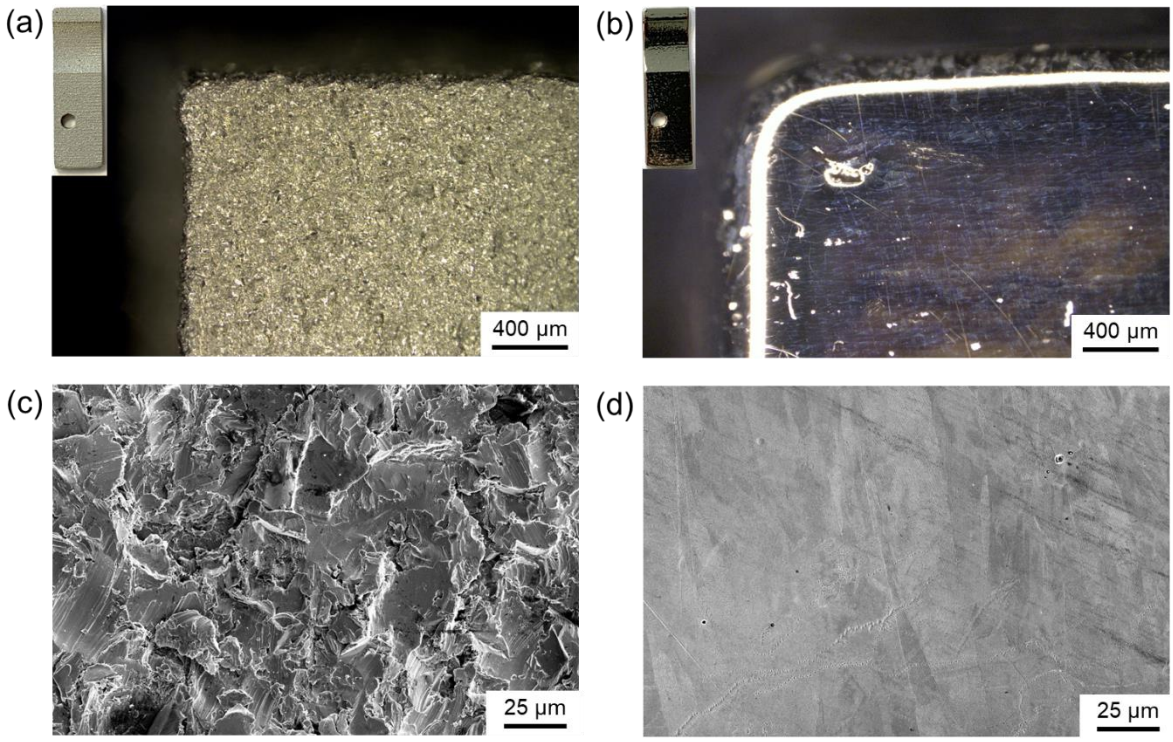

Figure 6.8 Comparative representation of the corner part of 3D-printed specimens, observed via OM: (a) untreated, (b) PEP treated (30 min), and the surface of the specimens as inspected by SEM: (c) untreated, (d) PEP treated (30 min).

As illustrated in Figure 6.8 (a) and (c), the surface of the untreated specimen is characterized by a distinctively rough and irregular morphology. Such texture is mainly due to the partial melting of metallic powder, a common occurrence in the SLM process. This necessitates meticulous selection of the SLM parameters or the implementation of a post-processing treatment to mitigate this issue [218-220]. Contrastingly, after undergoing a 30-min PEP process, the specimen surface showcases a markedly improved, glossy and even surface, as displayed in Figure 6.8(b) and (d). Additionally, the PEP process yields a specimen with more uniformly structured and significantly blunter edges than those found on the untreated specimen.

In order to quantitatively assess the surface roughness, WLI analysis was employed, and 3D surface topologies of untreated and PEP-treated specimens are depicted in Figure 6.9 (a)–(d). Figure 6.9(e) displays areal surface roughness values (S_a) as a function of the PEP process time from 7.5 min to 30 min and the untreated specimen. As the longer PEP treatment was applied, the areal roughness decreased to 3.1 µm. Notably, as the treatment time is prolonged, the roughness value decays exponentially, which can be speculated from two possibilities. First, the polishing rate is higher at surface protrusions; therefore, these are rapidly removed at the beginning of the PEP process. Consequently, the surface becomes progressively flatter, and the polishing rate reduces as the PEP duration is prolonged [13].

Second, as the PEP process takes longer, the thickness of the gaseous layer around the workpiece expands as the surrounding electrolyte temperature rises. Thus, it reduces current density causing a diminished polishing rate [11]. The dominant influencing factor is yet to be determined, requiring more comprehensive systematic exploration. This could entail examining the roughness at more precise time intervals to assess the first factor and executing process diagnostics such as measuring the temperature of both the workpiece and surroundings, as well as observing the VGE layer size to evaluate the second factor.

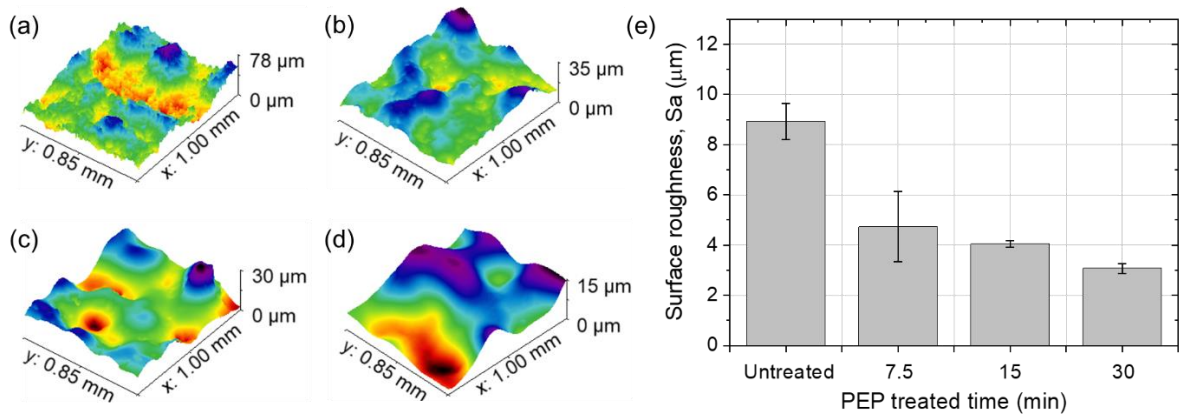

Figure 6.9 WLI-characterized 3D topographical profiles of SLM-built specimens before and after PEP treatment at various durations: (a) untreated, (b) 7.5 min, (c) 15 min, and (d) 30 min. Surface roughness values (S_a) are illustrated in (e) (reprinted from [210]).

Figure 6.10 exhibits WCA measurements of untreated and PEP-treated specimens' surfaces. The untreated specimen attains a contact angle of 59.25° while it increases to 76.70° after the PEP treatment for 7.5 min. The slight rise in the WCA can be ascribed to the modification of surface chemistry caused by the PEP process as evidenced by the XPS analysis, which indicates a relative increase in the fraction of metallic components compared to oxidized elements. This could influence the surface wettability, leading to a higher WCA. Additionally, the PEP process refines the surface, reducing the contact area for water, which might also contribute to subsequent increase in the WCA. However, the contact angle was not considerably changed as the PEP time extended from 7.5 min to 30 min since the surface elemental chemistry and roughness was not substantially altered during this period. Then, the 3D-printed mist chamber was treated with the PEP for 30 min. Even though the WCA does not significantly vary from 7.5 min to 30 min of PEP duration, the PEP treatment was conducted for 30 min with three rotations to ensure a homogeneous polishing effect throughout the mist chamber area, as described in Section 6.2.2.

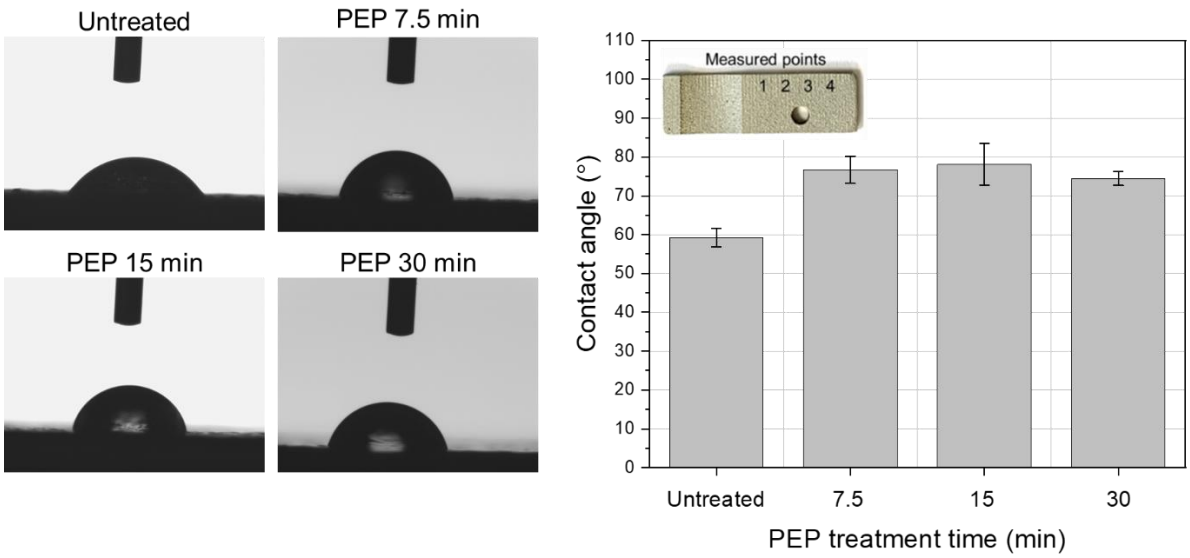

Figure 6.10 WCA measurements on 3D-printed SS specimens before and after the PEP process (reprinted from [210]).

Since the chamber is divided into two parts (top and bottom), the parts were treated separately by the PEP process. Table 6-3 summarizes the weight of 3D-printed chamber parts before and after the PEP process. As a result of the PEP process, the mass is reduced around 5 - 6%. In the following section, the misting performance test results will be discussed.

Table 6-3 Weight changes of 3D-printed mist chambers before and after PEP

Parts	Initial mass (g)	Mass after PEP (g)	Mass change (%)
Top	43.0	40.8	-5.1
Bottom	17.1	16.1	-5.8

6.3.2 Performance of the mist chamber

Figure 6.11(a) depicts the mass difference of the measured mist, Δm, converted by Sauerbrey's formula from Δf acquired by the QCM measurement to compare the 3D-printed mist chamber performance before and after the PEP process. Based on these results, the mist-out time (T_{mist}) was determined as described in Section 6.2.4.4 and is plotted in Figure 6.11(b). With a PEP-treated chamber, T_{mist} is approximately 60% faster than with untreated mist chambers. The reduced T_{mist} is attributed to diminished pore size and roughness of the surface after the PEP process, which contributes to a faster exit of smaller droplets towards the mist chamber's outlet by the argon stream, yielding better transport efficiency by preventing large droplets from accumulating on walls. Moreover, the large droplets that remain are easily drained away through the drainage of the chamber at the bottom owing to the smoothened surface, avoiding undesired recirculation and reduction of the inner volume of the chamber due to excess monomer inflow. In this sense, the improvement can be accredited to the surface's morphology after the PEP process rather than the wettability, as the contact angle increased compared to untreated surfaces.

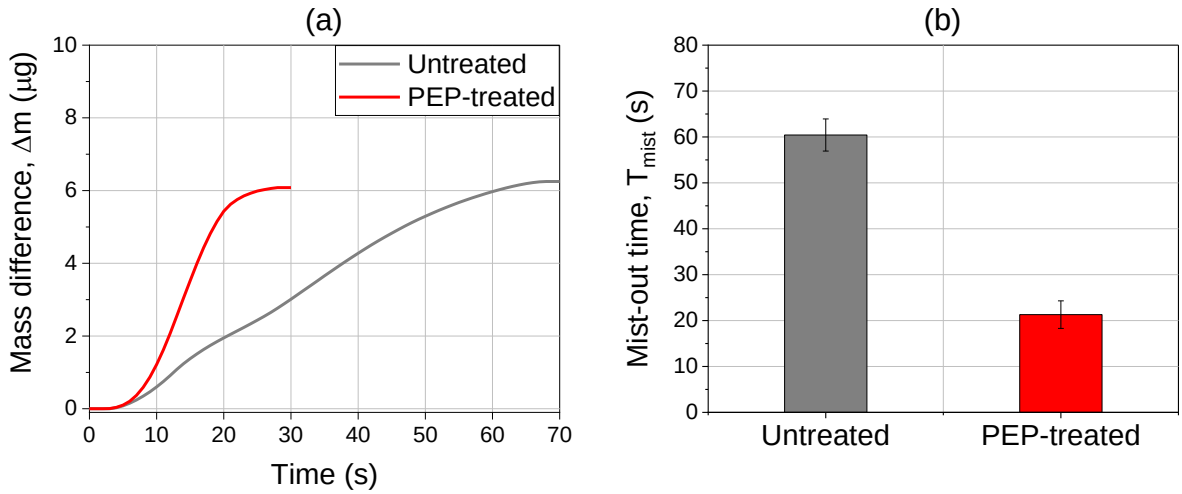

Figure 6.11 Results of the QCM measurements for a 3D-printed mist chamber before and after the PEP process: (a) mass difference, Δm, and (b) mist-out time, T_{mist} (reproduced from [210]).

As a further step, the pp process was performed using APPJ for 16 s on the mist obtained by the mist chambers with variable misting times to determine whether the deposited mist generated by the 3D-printed mist chamber could be transformed into uniform pp-films of controllable thickness and how the surface characteristics of the mist chamber affects it. Depending on the amount of deposited liquid monomer, the thickness and morphology of the films can be varied, and their functionalities are eventually influenced. Thus, after the APPJ treatment, ellipsometry was carried out to determine the thickness of the pp-films deposited on Si wafers. As illustrated in Figure 6.12, the thickness of the pp-films varies from 19.1 nm to 153.5 nm as the misting time is prolonged from 3 min to 15 min, respectively. The PEP-treated chamber produced pp-films were considerably thicker than films obtained from untreated chambers, up to 10 times thicker in the case of 3 s of misting time. This result is consistent with those presented in the previous section regarding T_{mist}. As seen in Figure 6.12, no thickness data were obtained for misting times of 15 s from the mist chamber since the 16 s of the APPJ treatment was insufficient to achieve a polymerized thin film for the considerable amount of mist emitted. Ref. [210] contains more details regarding pp-films, including their stability, morphology, and monomer conversion degree. Therefore, it can be concluded that it is feasible to fabricate homogeneous thin pp-films by employing the metallic 3D-printed mist chamber. Furthermore, the pp-films thickness can be obtained in a controlled manner by adequately selecting the surface status determined by the post-treatment, the chamber configuration, and the misting conditions.

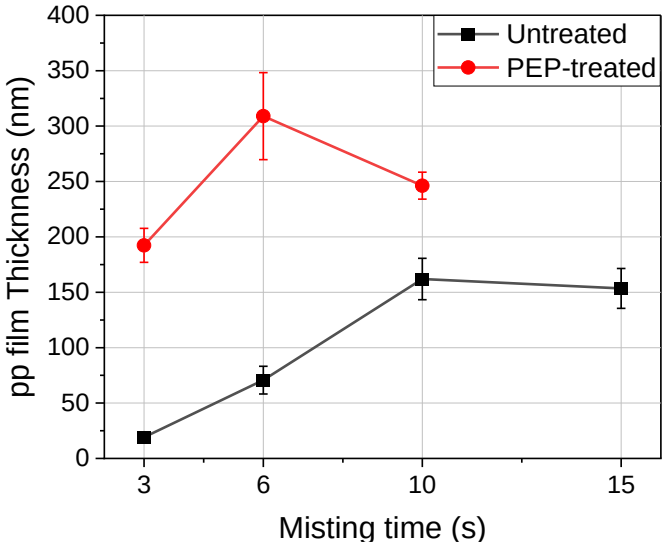

Figure 6.12 Comparison of the average pp-film thickness at various misting times obtained by 3D-printed mist with untreated and after PEP (reprinted from [210])

6.4 Conclusions

The objective of this chapter was to illustrate the practicality of integrating the PEP process with metallic 3D-printing technology, specifically targeting the surface finishing of SLM-fabricated SS mist chambers, thereby optimizing the misting performance for the creation of reproducible and uniform pp-films. A comprehensive study has been conducted, considering 3D-printing, surface-finishing, characterization, and fabrication of pp-films to assess misting performance.

From the GIXRD analysis, there was no major phase changes after the PEP process but did show an increase in crystallite size after PEP due to the preferential dissolution of smaller grains. The XPS analysis revealed that after the PEP process the C-containing contamination was significantly removed and the metallic Fe and Cr are more exposed as its oxides are removed during the PEP process. However, there was not notable change in Fe/Co ratio after the PEP process, suggesting that the chemical inertness of mist chamber can be maintained after the PEP process. Furthermore, post-PEP treatment, the surface morphology of 3D-printed specimens is substantially enhanced, as shown by OM, with a marked reduction in pores and edge irregularities. As the duration of the PEP process extends to 30 min, the surface roughness value (S_a) decreases from 8.9 µm to 3.1 µm, as characterized by WLI. The change in surface wettability following the PEP treatment was verified by WCA measurements. However, as the duration of the PEP process is extended to 30 min from 7.5 min, the surface wettability does not exhibit substantial changes.

The QCM analysis was carried out to measure the mist-out time to determine the mist chamber's performance. With the PEP-treated mist chamber, the misting time was reduced by ~65% compared to the as-3D-printed part owing to the smooth inner surface of the chamber which facilitated the faster exit of the desired droplets (through the mist chamber's outlet), appropriate drainage of the larger droplets and avoided undesired recirculation effects. The

APPJ treatment was implemented on the deposited mist generated by 3D-printed mist chambers to fabricate the pp-films. The results showed that the thickness of the pp-films could be manipulated with a 3D-printed mist chamber in a range of ~20 nm to 350 nm, depending on the misting time. As a result of the surface-finishing of the mist chamber by the PEP process, pp-films can be produced in a highly reproducible, homogeneous and time-efficient way, making them suitable for mass production.

As demonstrated in this study, the PEP process was successfully adapted for its intended purpose: finishing the surface of complex geometrical AM parts in an environment-friendly manner. Apart from this application, producing metallic AM parts combined with the PEP process comprises an innovative and highly effective surface-finishing process for an ever-growing sustainable AM production chain.

7 Summary and outlook

The main aim of the thesis was to investigate the PEP process involving surface characterization techniques and process diagnostics to elucidate the fundamental mechanisms occurring on the different metallic surfaces as a result of the PEP process. In addition, a feasibility study with actual applications for PEP surface treatment has also been elucidated to prove its potential for expanding PEP's range of applications. The main conclusions from this study are summarized below.

An early part of this thesis describes the use of PEP as a surface pretreatment method before deposition of the hard coating process on WC-Co-based cutting tools. Different types of electrolytes have been attempted for the surface polishing of the WC-Co workpiece. The results indicate that W on the tool surface can readily dissolve in Na_2CO_3 due to the alkaline environment facilitating WO_3 dissolution. Therefore, an appropriate voltage regime must be selected to effectively dissolve WC on a workpiece's surface. The results of the voltage variation experiment indicated that the process voltage at 110 V resulted in WC dissolution, while surface oxidation dominantly occurred at 30 V and 200 V. Furthermore, an increase in the Co atomic content on the workpiece surface after the PEP process at 110 V was identified by the XPS analysis, resulting from the selective dissolution of WC. However, there was a problem with excessive material dissolution on the corners, resulting in a blunt-cutting edge, which can be suppressed by increasing the process voltage. It can be speculated that a higher applied voltage leads to thicker VGE layers being generated, and a reduction of current density. Thus, excessive dissolution at corners can be reduced. In addition, by varying the orientation of the workpiece during treatment, it was possible to significantly improve the uniformity of the tool edge radius.

The effect of PEP on surface decontamination was explored by applying defined contamination to tool surfaces. The PEP process was optimized by varying voltage and process duration. Additionally, to achieve geometrical homogeneity in the cutting tool, the direction of sample immersion was also taken into account. This was complemented with analysis of cutting edge radius employing WLI. Analyses of ATR-FTIR and XPS revealed that, after the PEP process, the contaminants had been successfully removed, as less contamination remained on its surface than even on the as-received workpiece, which was treated by the commercial precleaning technique. Afterwards, the PEP-treated tools were subjected to hard coating (TiN) deposition using R-HiPIMS in combination with the plasma fine-cleaning process. A machining test was conducted to assess the performance of the coated tools with the PEP treatment, and the results were benchmarked with the coated tool with a conventional cleaning process. This procedure was also performed with the AlTiSiN hard coating, which was deposited by an industrial-standardized equipment and process to prove its industrial applicability. As a result of the machining tests, both coated tools (TiN and AlTiSiN) with PEP pretreatment showed improved cutting performance with extended tool lifetimes and enhanced adhesion strength over conventionally cleaned coated tools because the PEP process eliminated contamination from the tool surface properly. Based on this result, besides providing superior machining performance, the PEP can be a viable alternative to conventional cleaning procedures due to its eco-friendly and cost-effective aspects. However, this study is limited to a specific carbide

insert of SNMA120604, which has specific geometrical dimensions and fixed material composition. Therefore, further research is required to determine how the PEP process impacts more complex-shaped cemented carbide tools such as drills and endmills, as well as diverse material compositions, to obtain the process versatility.

As the vapor gaseous envelope (VGE) during the PEP process strongly influences the material removal rate and longitudinal uniformity, electrical and thermal measurements were used to characterize the temporal behavior of gaseous layer formation on a cylindrical WC-Co workpiece. Through the use of the calorimetric probe method, the incoming power to the workpiece surface was determined. The immersion depth, *d*, of the workpiece was adjusted to study its influence on the effective workpiece area. Within 30 s of the PEP process, the workpiece temperature reached ~150 °C involving the development of the gaseous layer. However, the temperature did not increase further since it is prevented by recurrent contact with the surrounding electrolyte. Based on the time-derivative of the temperature curve, the power transferred to the workpiece (P_{in}) was determined, and the distinctive heating characteristics were revealed depending on the workpiece temperature. In the LT regime (T < 100 ºC), the P_{in} was strongly influenced by the workpiece immersion depth (*d*), whereas in the HT regime (T > 120 ºC), the P_{in} converged regardless of the anode immersion depth due to the generation of the VGE layer. In the HT regime, when the immersion depth increases, more power is consumed to heat the surrounding electrolyte, resulting in relatively less power being transferred to the workpiece. The surrounding electrolyte temperature was measured simultaneously, and it was revealed that as immersion depth (*d*) is lowered, electrolyte temperature increment declines. Furthermore, the rate of temperature increase is slowed as less power is consumed with a smaller workpiece surface area. At larger effective area of the workpiece, there was a reduction in the efficiency of power consumption at the anodic workpiece from 25.7% to 16.7%. This relates to changes in the surrounding electrolyte temperature and has been corroborated by 2D-hydrodynamic modeling of the spatio-temporal evolution of an electrolyte. The model revealed that the electrolyte flows turbulently during the PEP process, whereas laminar flow dominates as the flow velocity reduces after the PEP process is completed. Furthermore, the model showed the reversed fluid stream from the cathodic wall to the anodic workpiece, contributing to the increase in the electrolyte temperature around the workpiece. In the region near the workpiece, it is evident that the spatial temperature gradient of the electrolyte is prominent; however, as the workpiece is distanced, the gradient becomes smaller. The spatio-temporal model further demonstrates pivotal insights in determining the optimal size of the electrolyte bath. An XPS line-scan analysis was performed to characterize the surface composition of the workpiece surface longitudinally. Notably, there was a slight compositional elemental gradient of C and O along the longitudinal direction of immersion depth of ~20 mm, possibly resulting from the non-uniform density distribution of the current, contributing to a variation in material removal rates along the vertical direction. Furthermore, W 4f peaks reflect the spatial discrepancy in WC binding between the top and bottom of the cylindrical workpiece. As a result of the PEP process for 30 s, the oxidative state of W differs slightly between the bottom and upper portions of the workpiece within 20 mm of the workpiece length. Therefore, when the cylindrical workpieces are more extended, a spatial gradient can be expected to be more pronounced. Thus, it is imperative to investigate further to generate a longitudinally homogenized VGE layer to

produce a uniformly distributed surface composition and a uniform material removal rate of the workpiece.

Furthermore, through synchronized electrical and high-speed camera measurements, it was found that as the non-linear load character of the current waveform fluctuates, there are corresponding changes in the gas layer dynamics, with a notable consistency in their patterns. Spectrogram analysis was employed to characterize the noticeable current oscillation, revealing the dependency of the fundamental frequency on the workpiece immersion depth, potentially associated with changes in liquid properties based on temperature. Spectrogram analysis was also utilized on high-speed images, verifying the match between the main frequency component and the electrical current waveform. This frequency correspondence suggests a relation between current oscillation and bubble layer movement, yielding a more profound understanding of the mechanisms controlling material surface treatment processes. In addition, spatial analysis of the high-speed camera signal confirmed a vertical gradient in the camera signal on the workpiece surface during the PEP process. This increased gradient is likely attributable to variations in discharges generated at different vertical positions during the PEP process. Comprehending this gradient is critical for optimizing the PEP process, as it provides insights into the distribution of discharges and their influence on surface quality, particularly for elongated workpieces.

The final part of this thesis presents another application of the PEP process combined with the 3D-printing technology to demonstrate its practical applicability as a surface finishing method. The PEP process was applied to 3D-printed SS mist chambers created by SLM to improve the misting performance by modifying their surfaces, ultimately fabricating pp film efficiently in a controlled manner. The optimal conditions for the PEP process were established, incorporating a workpiece rotating sequence, which led to smooth finishes on the surfaces of the 3D-printed metallic parts. Furthermore, by extending the duration of the PEP process, the areal roughness value of the surface (S_a) was further reduced. Additionally, the PEP-treated surface exhibited slightly more hydrophobic features than the as-3D-printed workpiece, possibly due to the removal of oxidized Fe and Cr on the SS surface, along with an increase in the metallic Fe and Cr present on the newly exposed surface matrix following the PEP process. A subsequent QCM analysis revealed that the PEP-treated mist chamber had a 65% faster misting time than the as-3D-printed part. This was due to the smooth inner surface of the chamber produced by the PEP process, which made it easier for smaller droplets to drain quickly. Though the PEP process enhances the drainage rate considerably, the underlying mechanism is still elusive, necessitating further study. After PEP treatment, it was observed that the surface becomes slightly hydrophobic from the contact angle measurement but is still measured for static mode contact angle measurements using water droplets. A more detailed examination of how the monomer mist interacts with the chamber walls would help determine why the drainage becomes faster. By treating the mist generated by 3D-printed mist chambers with APPJ, it has been found that the fabrication of the pp-film is feasible. Additionally, the thickness of the pp-films could be adjusted depending on the misting time. From the surface-finished mist chamber by the PEP process, pp-films can be produced up to 10 times thicker than those from an untreated chamber within the same misting period with high reproducibility. Hence, this study showed that PEP could be successfully applied to a mist chamber to produce pp-films. Finally, it is suggested that PEP can be an effective and ecological means for post-processing complex-shaped AM components to improve their surface smoothness.

Above, limitations and potential suggestions concerning the PEP process were detailed, specific to the topic of each chapter. Nonetheless, beyond these specifics, additional considerations are essential for the further advancement of the PEP process, especially in terms of its industrial application. First, despite the environmental benefits of PEP owing to the use of low-concentrated electrolytes, it still requires substantial amounts of energy, especially in case of large-scale applications. Therefore, it is important to optimize the electrical energy efficiency. Furthermore, a significant amount of material from the anodic workpiece surface precipitates in the electrolyte during the PEP process. It is therefore suggested to investigate the possibility of recycling the powder generated by the PEP process for better ecological results. While this thesis focused mainly on stainless-steel and WC-Co based cemented carbide, there is immense demand for many other materials that need to be polished. The importance of finding an electrolyte suitable for various materials cannot be overstated, but it is equally essential to expand the already developed technique; for example, the pretreatment of WC-Co can also be used to remove coatings (also known as "decoating"). However, this cannot be achieved without an in-depth knowledge of the fundamental processes occurring during the PEP process involving a variety of influencing factors. Hence, further research should be conducted to investigate the plasma properties within the discharge and how they interact with the workpiece surface through spectral analysis of the emission during the PEP process.

8 References

[1] D.K. Dwivedi, "Surface Engineering", *Springer India, New Delhi*, (2018).

[2] B. Tuck, "The chemical polishing of semiconductors", *Journal of Materials Science* **10** (1975) 321-339.

[3] S. Marimuthu, A. Triantaphyllou, M. Antar, D. Wimpenny, H. Morton, M. Beard, "Laser polishing of selective laser melted components", *International Journal of Machine Tools and Manufacture* **95** (2015) 97-104.

[4] W.-L. Zhu, A. Beaucamp, "Compliant grinding and polishing: A review", *International Journal of Machine Tools and Manufacture* **158** (2020) 103634.

[5] G. Yang, B. Wang, K. Tawfiq, H. Wei, S. Zhou, G. Chen, "Electropolishing of surfaces: theory and applications", *Surface Engineering* **33** (2017) 149-166.

[6] A. Vafadar, F. Guzzomi, A. Rassau, K. Hayward, "Advances in metal additive manufacturing: A review of common processes, industrial applications, and current challenges", *Applied Sciences* **11** (2021) 1213.

[7] S.A.M. Tofail, E.P. Koumoulos, A. Bandyopadhyay, S. Bose, L. O'Donoghue, C. Charitidis, "Additive manufacturing: scientific and technological challenges, market uptake and opportunities", *Materials Today* **21** (2018) 22-37.

[8] K. Nestler, F. Böttger-Hiller, W. Adamitzki, G. Glowa, H. Zeidler, A. Schubert, "Plasma Electrolytic Polishing – An Overview of Applied Technologies and Current Challenges to Extend the Polishable Material Range", *Procedia CIRP* **42** (2016) 503-507.

[9] Y. Huang, C. Wang, F. Ding, Y. Yang, T. Zhang, X. He, L. Zheng, N. Li, "Principle, process, and application of metal plasma electrolytic polishing: a review", *International Journal of Advanced Manufacturing Technology* **114** (2021) 1893-1912.

[10] J. Wang, L.C. Suo, L.L. Guan, Y.L. Fu, "Optimization of Processing Parameters for Electrolysis and Plasma Polishing", *Applied Mechanics and Materials* **217-219** (2012) 1368-1371.

[11] I. Danilov, M. Hackert-Oschätzchen, M. Zinecker, G. Meichsner, J. Edelmann, A. Schubert, "Process Understanding of Plasma Electrolytic Polishing through Multiphysics Simulation and Inline Metrology", *Micromachines* **10** (2019) 214.

[12] A. Yerokhin, V.R. Mukaeva, E.V. Parfenov, N. Laugel, A. Matthews, "Charge transfer mechanisms underlying Contact Glow Discharge Electrolysis", *Electrochimica Acta* **312** (2019) 441-456.

[13] M. Cornelsen, C. Deutsch, H. Seitz, "Electrolytic Plasma Polishing of Pipe Inner Surfaces", *Metals* **8** (2018) 12.

[14] C. Zhou, H. Su, N. Qian, Z. Zhang, J. Xu, "Characteristics and function of vapour gaseous envelope fluctuation in plasma electrolytic polishing", *The International Journal of Advanced Manufacturing Technology* **119** (2022) 7815-7825.

[15] P.N. Belkin, S.A. Kusmanov, E.V. Parfenov, "Mechanism and technological opportunity of plasma electrolytic polishing of metals and alloys surfaces", *Applied Surface Science Advances* **1** (2020) 100016.

[16] E.V. Parfenov, R.G. Farrakhov, V.R. Mukaeva, A.V. Gusarov, R.R. Nevyantseva, A. Yerokhin, "Electric field effect on surface layer removal during electrolytic plasma polishing", *Surface and Coatings Technology* **307** (2016) 1329-1340.

[17] C.J. Evans, E. Paul, D. Dornfeld, D.A. Lucca, G. Byrne, M. Tricard, F. Klocke, O. Dambon, B.A. Mullany, "Material Removal Mechanisms in Lapping and Polishing", *CIRP Annals* **52** (2003) 611-633.

[18] Z.W. Zhong, "Recent Advances in Polishing of Advanced Materials", *Materials and Manufacturing Processes* **23** (2008) 449-456.

[19] C.A. Cooper, L.D. Cooley, "Mirror-smooth surfaces and repair of defects in superconducting RF cavities by mechanical polishing", *Superconductor Science and Technology* **26** (2012) 015011.

[20] Y. Huang, G. Xiao, H. Zhao, L. Zou, L. Zhao, Y. Liu, W. Dai, "Residual stress of belt polishing for the micro-stiffener surface on the titanium alloys", *Procedia CIRP* **71** (2018) 11-15.

[21] W. Han, F. Fang, "Eco-friendly NaCl-based electrolyte for electropolishing 316L stainless steel", *Journal of Manufacturing Processes* **58** (2020) 1257-1269.

[22] W. Simka, M. Kaczmarek, A. Baron-Wiecheć, G. Nawrat, J. Marciniak, J. Zak, "Electropolishing and passivation of NiTi shape memory alloy", *Electrochimica Acta* **55** (2010) 2437-2441.

[23] A. Boschetto, L. Bottini, L. Macera, F. Veniali, "Post-processing of complex SLM parts by barrel finishing", *Applied Sciences* **10** (2020) 1382.

[24] R. Chaghi, C. Cervera, H. Aït-Kaci, P. Grech, J.B. Rodriguez, P. Christol, "Wet etching and chemical polishing of InAs/GaSb superlattice photodiodes", *Semiconductor Science and Technology* **24** (2009) 065010.

[25] P. Tyagi, T. Goulet, C. Riso, F. Garcia-Moreno, "Reducing surface roughness by chemical polishing of additively manufactured 3D printed 316 stainless steel components", *International Journal of Advanced Manufacturing Technology* **100** (2019) 2895-2900.

[26] B.L.T. Aman Nigam, "Effects of In-Situ Mechanical and Chemical Polishing on Surface Topography of Additively Manufactured Fiber-Reinforced Polymers", *Solid Freeform Fabrication 2021: Proceedings of the 32nd Annual International Solid Freeform Fabrication Symposium* (2018) 376-387.

[27] W. Han, F. Fang, "Fundamental aspects and recent developments in electropolishing", *International Journal of Machine Tools and Manufacture* **139** (2019) 1-23.

[28] S. Ichimura, K. Kokubun, M. Hirata, S. Tsukahara, K. Saito, Y. Ikeda, "Measurement of outgassing characteristics from a vacuum chamber fabricated for pressure calibration in UHV/XHV region", *Vacuum* **53** (1999) 291-294.

[29] E.S. Lee, "Machining Characteristics of the Electropolishing of Stainless Steel (STS316L)", *The International Journal of Advanced Manufacturing Technology* **16** (2000) 591-599.

[30] T.E. Norgate, S. Jahanshahi, W.J. Rankin, "Assessing the environmental impact of metal production processes", *Journal of Cleaner Production* **15** (2007) 838-848.

[31] F. Chen, X. Miao, Y. Tang, S. Yin, "A review on recent advances in machining methods based on abrasive jet polishing (AJP)", *International Journal of Advanced Manufacturing Technology* **90** (2017) 785-799.

[32] F.C. Tsai, B.H. Yan, C.Y. Kuan, F.Y. Huang, "A Taguchi and experimental investigation into the optimal processing conditions for the abrasive jet polishing of SKD61 mold steel", *International Journal of Machine Tools and Manufacture* **48** (2008) 932-945.

[33] P.V. Rao, S.G. Young, D.H. Buckley, "Morphology of an aluminum alloy eroded by a normally incident jet of angular erodent particles", *Wear* **92** (1983) 31-49.

[34] M. Barletta, S. Guarino, G. Rubino, V. Tagliaferri, "Progress in fluidized bed assisted abrasive jet machining (FB-AJM): Internal polishing of aluminium tubes", *International Journal of Machine Tools and Manufacture* **47** (2007) 483-495.

[35] S. Ally, J.K. Spelt, M. Papini, "Prediction of machined surface evolution in the abrasive jet micro-machining of metals", *Wear* **292-293** (2012) 89-99.

[36] B. Rosa, P. Mognol, J.-y. Hascoët, "Laser polishing of additive laser manufacturing surfaces", *Journal of Laser Applications* **27** (2015) S29102-S29102.

[37] G. Annamaria, B. Massimiliano, V. Francesco, "Laser polishing: a review of a constantly growing technology in the surface finishing of components made by additive manufacturing", *Springer London*, (2022).

[38] A. Krishnan, F. Fang, "Review on mechanism and process of surface polishing using lasers", *Frontiers of Mechanical Engineering* **14** (2019) 299-319.

[39] J.E. Foster, "Plasma-based water purification: Challenges and prospects for the future", *Physics of Plasmas* **24** (2017) 055501.

[40] A.L. Yerokhin, X. Nie, A. Leyland, A. Matthews, S.J. Dowey, "Plasma electrolysis for surface engineering", *Surface and Coatings Technology* **122** (1999) 73-93.

[41] K.D. Weltmann, T. von Woedtke, "Plasma medicine—current state of research and medical application", *Plasma Physics and Controlled Fusion* **59** (2017) 014031.

[42] P. Bruggeman, C. Leys, "Non-thermal plasmas in and in contact with liquids", *Journal of Physics D: Applied Physics* **42** (2009) 053001.

[43] P. Lukes, M. Clupek, V. Babicky, P. Sunka, "Pulsed electrical discharge in water generated using porous-ceramic-coated electrodes", *IEEE Transactions on Plasma Science* **36** (2008) 1146-1147.

[44] S. Horikoshi, N. Serpone, "In-liquid plasma: A novel tool in the fabrication of nanomaterials and in the treatment of wastewaters", *RSC Adv.* **7** (2017) 47196-47218.

[45] S.M. Korobeinikov, A.V. Melekhov, A.S. Besov, "Breakdown Initiation in Water with the Aid of Bubbles", *High Temperature* **40** (2002) 652-659.

[46] M. Muhammad Arif, G. Abdul, M. Salman Akbar, "Water purification by electrical discharges", *Plasma Sources Science and Technology* **10** (2001) 82.

[47] P. Bruggeman, E. Ribežl, A. Maslani, J. Degroote, A. Malesevic, R. Rego, J. Vierendeels, C. Leys, "Characteristics of atmospheric pressure air discharges with a liquid cathode and a metal anode", *Plasma Sources Science and Technology* **17** (2008) 025012.

[48] E.S. Bobkova, S.A. Smirnov, Y.V. Zalipaeva, V.V. Rybkin, "Modeling Chemical Composition for an Atmospheric Pressure DC Discharge in Air with Water Cathode by 0-D model", *Plasma Chemistry and Plasma Processing* **34** (2014) 721-743.

[49] Q. Xiong, Z. Yang, P.J. Bruggeman, "Absolute OH density measurements in an atmospheric pressure dc glow discharge in air with water electrode by broadband UV absorption spectroscopy", *Journal of Physics D: Applied Physics* **48** (2015) 424008.

[50] S. Reuter, T. von Woedtke, K.-D. Weltmann, "The kINPen—a review on physics and chemistry of the atmospheric pressure plasma jet and its applications", *Journal of Physics D: Applied Physics* **51** (2018) 233001.

[51] J. Winter, R. Brandenburg, K.D. Weltmann, "Atmospheric pressure plasma jets: an overview of devices and new directions", *Plasma Sources Science and Technology* **24** (2015) 064001.

[52] R. Foest, E. Kindel, A. Ohl, M. Stieber, K.D. Weltmann, "Non-thermal atmospheric pressure discharges for surface modification", *Plasma Physics and Controlled Fusion* **47** (2005) B525.

[53] T.P. Kasih, A. Kharisma, M.K. Perdana, R.D.J. Murphiyanto, "Development of non-thermal plasma jet and its potential application for color degradation of organic pollutant in wastewater treatment", *IOP Conference Series: Earth and Environmental Science* **109** (2017) 012004.

[54] J. Friedrich, "Chapter 11. Plasma Polymerization - The Plasma Chemistry of Polymer Surfaces: Advanced Techniques for Surface Design", *Wiley-VCH*, (2012), 337-375.

[55] P.J. Bruggeman, M.J. Kushner, B.R. Locke, J.G.E. Gardeniers, W.G. Graham, D.B. Graves, R.C.H.M. Hofman-Caris, D. Maric, J.P. Reid, E. Ceriani, D. Fernandez Rivas, J.E. Foster, S.C. Garrick, Y. Gorbanev, S. Hamaguchi, F. Iza, H. Jablonowski, E. Klimova, J. Kolb, F. Krcma, P. Lukes, Z. Machala, I. Marinov, D. Mariotti, S. Mededovic Thagard, D. Minakata, E.C. Neyts, J. Pawlat, Z.L. Petrovic, R. Pflieger, S. Reuter, D.C. Schram, S. Schröter, M. Shiraiwa, B. Tarabová, P.A. Tsai, J.R.R. Verlet, T. von Woedtke, K.R. Wilson, K. Yasui, G. Zvereva, "Plasma–liquid interactions: a review and roadmap", *Plasma Sources Science and Technology* **25** (2016) 053002.

[56] K. Tachibana, Y. Takekata, Y. Mizumoto, H. Motomura, M. Jinno, "Analysis of a pulsed discharge within single bubbles in water under synchronized conditions", *Plasma Sources Science and Technology* **20** (2011) 034005.

[57] H. Aoki, K. Kitano, S. Hamaguchi, "Plasma generation inside externally supplied Ar bubbles in water", *Plasma Sources Science and Technology* **17** (2008) 025006.

[58] J. Pawłat, S. Ihara, C. Yamabe, I. Pollo, "Oxidant Formation and the Decomposition of Organic Compounds in Foaming Systems", *Plasma Processes and Polymers* **2** (2005) 218-221.

[59] S. Wang, L. Wen, Y. Wang, Y. Cheng, Y. Cheng, Y. Zou, Y. Zhu, G. Chen, J. Ouyang, D. Jia, Y. Zhou, "One-step fabrication of double-layer nanocomposite coating by plasma electrolytic oxidation with particle addition", *Applied Surface Science* **592** (2022) 153043.

[60] S.K. Sen Gupta, R. Singh, "Cathodic contact glow discharge electrolysis: its origin and non-faradaic chemical effects", *Plasma Sources Science and Technology* **26** (2017) 015005.

[61] A. Wehnelt, "Ein elektrolytischer Stromunterbrecher", *Annalen der Physik* **304** (1899) 233-272.

[62] V.S. Rudnev, M.S. Vasilyeva, N.B. Kondrikov, L.M. Tyrina, "Plasma-electrolytic formation, composition and catalytic activity of manganese oxide containing structures on titanium", *Applied Surface Science* **252** (2005) 1211-1220.

[63] L. Zhu, W. Zhang, H. Liu, L. Liu, F. Wang, Z. Qiao, "Single Dense Layer of PEO Coating on Aluminum Fabricated by “Chain-like” Discharges", **15** (2022) 4635.

[64] H. Duan, H. Sun, G. Ji, D. Yang, S. Li, J. Wang, Y. Xiang, "Biological Corrosion Resistance and Osteoblast Response of 316LVM Polished Using Electrolytic Plasma", *Coatings* **12** (2022) 1672.

[65] D.-S. Tsai, C.-C. Chou, "Review of the Soft Sparking Issues in Plasma Electrolytic Oxidation", *Metals* **8** (2018) 105.

[66] Y. Guo, A. Rogov, A. Hird, B. Mingo, A. Matthews, A. Yerokhin, "Plasma electrolytic oxidation of magnesium by sawtooth pulse current", *Surface and Coatings Technology* **429** (2022) 127938.

[67] H. Zeidler, F. Boettger-Hiller, J. Edelmann, A. Schubert, "Surface Finish Machining of Medical Parts Using Plasma Electrolytic Polishing", *Procedia CIRP* **49** (2016) 83-87.

[68] P.N. Belkin, A. Yerokhin, S.A. Kusmanov, "Plasma electrolytic saturation of steels with nitrogen and carbon", *Surface and Coatings Technology* **307** (2016) 1194-1218.

[69] E.V. Parfenov, A. Yerokhin, R.R. Nevyantseva, M.V. Gorbatkov, C.-J. Liang, A. Matthews, "Towards Smart Electrolytic Plasma Technologies: An Overview of Methodological Approaches to Process Modelling", *Surface and Coatings Technology* **269** (2015) 2-22.

[70] H.-P. Schulze, H. Zeidler, O. Kröning, F. Böttger-Hiller, M. Herzig, "Process analysis of plasma-electrolytic polishing (PeP) of forming tools", *International Journal of Material Forming* **15** (2022) 6.

[71] V. Duradzhi, I. Bryantsev, A.J.E.O.M. Tokarov, "Investigation of erosion of the anode under the action of an electrolytic plasma on it", *Elektronnaya Obrabotka Materialov* **5** (1979) 15-19.

[72] C. Zhou, H. Su, N. Qian, Z. Zhang, J. Xu, "Characteristics and function of vapour gaseous envelope fluctuation in plasma electrolytic polishing", *The International Journal of Advanced Manufacturing Technology* (2022).

[73] V.N. Duradji, D.E. Kaputkin, A.Y. Duradji, "Aluminum treatment in the electrolytic plasma during the anodic process", *Journal of Engineering Science & Technology Review* **10** (2017) 81-84.

[74] I. Danilov, S. Quitzke, A. Martin, P. Steinert, M. Zinecker, A. Schubert, "Influence of Plasma Electrolytic Polishing on Surface Roughness of Steel, Aluminum and Cemented Carbide", Proceedings of the 11th Congress of the German Academic Association for Production Technology (WGP) in Dresden, *Springer International Publishing*, (2022), 265-273.

[75] B. Seo, H.-K. Park, H.G. Kim, W.R. Kim, K. Park, "Corrosion behavior of additive manufactured CoCr parts polished with plasma electrolytic polishing", *Surface and Coatings Technology* **406** (2021) 126640.

[76] M. Polak, K.-D. Weltmann, R. Ihrke, M. Fröhlich, A. Quade, "Method for Polishing Conductive Metal Surfaces", (2018), Patent No. *PCT/EP2017/066768*, International Patent.

[77] D.E.K. Valentin Nikolaevich Duradzhi, Andrey Yuryevich Duradzhi, "Method of electrolyte-plasma processing of metal surface", (2015), Patent No. *RU2013129493/02A*, Russia Patent.

[78] S. Quitzke, O. Kroning, D. Safranchik, H. Zeidler, I. Danilov, A. Martin, F. Bottger-Hiller, S. Essel, A. Schubert, "Design and setup of a jet-based technology for localized small scale Plasma electrolytic Polishing", *Journal of Manufacturing Processes* **75** (2022) 1123-1133.

[79] S. Kißling, "Chemische und elektrochemische Methoden zur Oberflächenbearbeitung von galvanogeformten Nickel-Mikrostrukturen", PhD Dissertation (2014), Karlsruher Institut für Technologie (KIT).

[80] R. Syah Putra, M. Sarkawi, F. Faikha, L. Fitmoko, "Analysis of Bubbles Size Produced in Electroflotation Using Graphite and Stainless Steel Electrode With DinoCapture 2.0", 2021 IEEE International Conference on Health, Instrumentation & Measurement, and Natural Sciences (InHeNce) in Medan, Indonesia, (2021), 1-5.

[81] S. Quitzke, O. Kröning, D. Safranchik, H. Zeidler, I. Danilov, A. Martin, F. Böttger-Hiller, S. Essel, A. Schubert, "Design and setup of a jet-based technology for localized small scale Plasma electrolytic Polishing", *Journal of Manufacturing Processes* **75** (2022) 1123-1133.

[82] R.R. Nevyantseva, S.A. Gorbatkov, E.V. Parfenov, A.A. Bybin, "The influence of vapor–gaseous envelope behavior on plasma electrolytic coating removal", *Surface and Coatings Technology* **148** (2001) 30-37.

[83] A. Piel, "Plasma Physics: An Introduction to Laboratory, Space, and Fusion Plasmas", *Springer Berlin, Heidelberg*, (2010).

[84] A. Fridman, "Plasma Chemistry", *Cambridge University Press, Cambridge*, (2008).

[85] I.G. D'yakov, V.S. Belkin, S.Y. Shadrin, P.N. Belkin, "Peculiarities of heat transfer at anodic plasma electrolytic treatment of cylindrical pieces", *Surface Engineering and Applied Electrochemistry* **50** (2014) 346-355.

[86] H. Fizeau, L. Foucault, "Recherches sur l'intensite´ de la lumie`re e´mise par le charbon dans l'expe´rience de Davy (EN: Study of the intensity of the light emitted by the carbon in the experiment of Davy)", *Annales de chimie et de physique* (1844) 370-384.

[87] H.H. Kellogg, "Anode Effect in Aqueous Electrolysis", *Journal of The Electrochemical Society* **97** (1950) 133.

[88] C. Zhou, N. Qian, H. Su, Z. Zhang, W. Ding, J. Xu, "Effect of energy distribution on the machining efficiency and surface morphology of Inconel 718 nickel-based superalloy using plasma electrolytic polishing", *Surface and Coatings Technology* **441** (2022) 128506.

[89] S. An, R. Foest, K. Fricke, H. Riemer, M. Fröhlich, A. Quade, J. Schäfer, K.-D. Weltmann, H. Kersten, "Pretreatment of cutting tools by plasma electrolytic polishing (PEP) for enhanced adhesion of hard coatings", *Surface and Coatings Technology* **405** (2021) 126504.

[90] A. Hickling, G.R. Newns, "Glow-discharge electrolysis. Part V. The contact glow-discharge electrolysis of liquid ammonia", *Journal of Chemical Society* (1961) 5186-5191.

[91] A. Hickling, M.D. Ingram, "Contact glow-discharge electrolysis", *Transactions of the Faraday Society* **60** (1964) 783-793.

[92] R. Wüthrich, J.D. Abou Ziki, "Chapter 2. Historical Overview of Electrochemical Discharges - Micromachining Using Electrochemical Discharge Phenomenon (Second Edition)", *William Andrew Publishing, Boston*, (2015), 13-33.

[93] A. Piel, "Chapter 11. Plasma Generation - Plasma Physics: An Introduction to Laboratory, Space, and Fusion Plasmas", *Springer Berlin, Heidelberg*, (2010), 323-350.

[94] M. Cornelsen, C. Deutsch, H. Seitz, "Influence of the Velocity and the Number of Polishing Passages on the Roughness of Electrolytic Plasma Polished Pipe Inner Surfaces", *Metals* **8** (2018) 330.

[95] P.D. Vaňa, Š. Podhorský, M. Hurajt, V. Hanzen, "Surface Properties of the Stainless Steel X 10 CrNi 18 / 10 after Aplication of Plasma Polishing in Electrolyte", *International Journal of Modern Engineering Research (IJMER)* **3** (2013) 788-792.

[96] J. Wang, L.C. Suo, L.L. Guan, Y.L. Fu, "Analytical Study on Mechanism of Electrolysis and Plasma Polishing", *Advanced Materials Research* **472-475** (2012) 350-353.

[97] O.V. Kalenchukova, P.K. Nagula, D.L. Tretinnikov, "About changes in the chemical composition of the electrolyte in the process of electrolytic-plasma treatment of materials", *Materials, Methods & Technologies* **9** (2015) 404-413.

[98] J.F. Moulder, J. Chastain, "Handbook of X-ray Photoelectron Spectroscopy: A Reference Book of Standard Spectra for Identification and Interpretation of XPS Data", *Physical Electronics Division, Perkin-Elmer Corporation*, (1992).

[99] K. Siegbahn, "ESCA. Atomic, Molecular and Solid State Structure Studied by Means of Electron Spectroscopy", *Nova acta Regiae Societatis Scientiarum Upsaliensis*, (1967).

[100] B.S. Lee, T.C. Strand, "Profilometry with a coherence scanning microscope", *Applied Optics* **29** (1990) 3784-3788.

[101] P.J.J.A.o. Caber, "Interferometric profiler for rough surfaces", *Applied Optics* **32** (1993) 3438-3441.

[102] P. Pavliček, E. Mikeska, "White-light interferometer without mechanical scanning", *Optics and Lasers in Engineering* **124** (2020) 105800.

[103] ISO, "Geometrical Product Specifications (GPS) — Surface texture: Profile method — Rules and procedures for the assessment of surface texture - 4288:1996", (1996).

[104] M. Seah, L. Chiffre, "Surface and Interface Characterization - Springer Handbook of Materials Measurement Methods", *Springer Berlin Heidelberg, Berlin, Heidelberg*, (2006).

[105] EVIDENT, "Surface Roughness Measurement—Parameters", Access year: *https://www.olympus-ims.com/en/metrology/surface-roughness-measurement-portal/parameters/*

[106] C.F. Wyen, K. Wegener, "Influence of cutting edge radius on cutting forces in machining titanium", *CIRP Annals* **59** (2010) 93-96.

[107] N. Yao, Z.L. Wang, "Handbook of Microscopy for Nanotechnology", *Springer US*, (2006).

[108] K. Akhtar, S.A. Khan, S.B. Khan, A.M. Asiri, "Scanning Electron Microscopy: Principle and Applications in Nanomaterials Characterization - Handbook of Materials Characterization", *Springer International Publishing, Cham*, (2018), 113-145.

[109] B.C. Smith, "Fundamentals of Fourier transform infrared spectroscopy", *CRC press, Boca Raton*, (2011).

[110] Y. Chen, C. Zou, M. Mastalerz, S. Hu, C. Gasaway, X. Tao, "Applications of Micro-Fourier Transform Infrared Spectroscopy (FTIR) in the Geological Sciences—A Review", *International Journal of Molecular Sciences* **16** (2015) 30223-30250.

[111] PerkinElmer, "FT-IR Spectroscopy Attenuated Total Reflectance (ATR)", (2005).

[112] D. Baizar, H. Ledbetter, "Accurate Modeling of Size and Strain Broadening in the Rietveld Refinement: The “Double-Voigt” Approach", *Advances in X-ray Analysis* **38** (1994) 397-404.

[113] D. Balzar, "Voigt-Function Model in Diffraction Line-Broadening Analysis", *International Union of Crystallography Monographs on Crystallography* **10** (2000).

[114] S. Sinha Ray, "Chapter 4. Techniques for characterizing the structure and properties of polymer nanocomposites - Environmentally Friendly Polymer Nanocomposites", *Woodhead Publishing*, (2013), 74-88.

[115] S. Sinha Ray, "Chapter 3. Structure and Morphology Characterization Techniques - Clay-Containing Polymer Nanocomposites", *Elsevier, Amsterdam*, (2013), 39-66.

[116] M. Veerapandian, K. Yun, "Study of Atomic Force Microscopy in Pharmaceutical and Biopharmaceutical Interactions - A Mini Review", *Current Pharmaceutical Analysis* **5** (2009) 256-268.

[117] "Ökologische und funktionsoptimierte Vorbehandlungs-kette für die Plasmabeschichtung komplex geformter Schneidwerkzeuge (ÖkoClean)", *Deutsche Bundesstiftung Umwelt*, 33033/01 (2020).

[118] "VDW Market Report 2022", *Verein Deutscher Werkzeugmaschinenfabriken e. V. (VDW)*, ISSN 2567-1316 (2022).

[119] K. Bobzin, "High-performance coatings for cutting tools", *CIRP Journal of Manufacturing Science and Technology* **18** (2017) 1-9.

[120] R.A. Mahdavinejad, A. Mahdavinejad, "ED machining of WC–Co", *Journal of Materials Processing Technology* **162-163** (2005) 637-643.

[121] Y. Isik, "Tool life and performance comparison of coated tools in metal cutting", *International Journal of Materials and Product Technology* **39** (2010) 240-250.

[122] Z.-J. Liu, Z.-K. Liu, C. McNerny, P. Mehrotra, A. Inspektor, "Investigations of the bonding layer in commercial CVD coated cemented carbide inserts", *Surface and Coatings Technology* **198** (2005) 161-164.

[123] R. Haubner, M. Lessiak, R. Pitonak, A. Köpf, R. Weissenbacher, "Evolution of conventional hard coatings for its use on cutting tools", *International Journal of Refractory Metals and Hard Materials* **62** (2017) 210-218.

[124] F. Klocke, B. Döbbeler, M. Binder, N. Kramer, R. Grüter, D. Lung, "12.3 Ecological evaluation of PVD and CVD coating systems in metal cutting processes", 11th Global Conference on Sustainable Manufacturing in Berlin, Germany, (2013), 381 - 386.

[125] S. Carvalho, L. Rebouta, A. Cavaleiro, L.A. Rocha, J. Gomes, E. Alves, "Microstructure and mechanical properties of nanocomposite (Ti,Si,Al)N coatings", *Thin Solid Films* **398-399** (2001) 391-396.

[126] N. He, H. Li, L. Ji, X. Liu, H. Zhou, J. Chen, "High temperature tribological properties of TiAlSiN coatings produced by hybrid PVD technology", *Tribology International* **98** (2016) 133-143.

[127] L. Wang, L. Li, G. Li, Q. Ma, "Improved Adhesion of TiAlSiN Nanocomposite Coatings on Cemented Carbide Substrate by Pre-Implantation", *Coatings* **9** (2019) 209.

[128] C.-L. Chang, S.-G. Shih, P.-H. Chen, W.-C. Chen, C.-T. Ho, W.-Y. Wu, "Effect of duty cycles on the deposition and characteristics of high power impulse magnetron sputtering deposited TiN thin films", *Surface and Coatings Technology* **259** (2014) 232-237.

[129] Q. Ma, L. Li, Y. Xu, J. Gu, L. Wang, Y. Xu, "Effect of bias voltage on TiAlSiN nanocomposite coatings deposited by HiPIMS", *Applied Surface Science* **392** (2017) 826-833.

[130] G. Li, J. Sun, Y. Xu, Y. Xu, J. Gu, L. Wang, K. Huang, K. Liu, L. Li, "Microstructure, mechanical properties, and cutting performance of TiAlSiN multilayer coatings prepared by HiPIMS", *Surface and Coatings Technology* **353** (2018) 274-281.

[131] F. Deuerler, H. van den Berg, R. Tabersky, A. Freundlieb, M. Pies, V. Buck, "Pretreatment of substrate surface for improved adhesion of diamond films on hard metal cutting tools", *Diamond and Related Materials* **5** (1996) 1478-1489.

[132] H.K. Tönshoff, A. Mohlfeld, C. Gey, J. Winkler, "Surface modification of cemented carbide cutting tools for improved adhesion of diamond coatings", *Surface and Coatings Technology* **108-109** (1998) 543-550.

[133] A. Obrosov, R. Gulyaev, M. Ratzke, A.A. Volinsky, S. Bolz, M. Naveed, S. Weiß, "XPS and AFM Investigations of Ti-Al-N Coatings Fabricated Using DC Magnetron Sputtering at Various Nitrogen Flow Rates and Deposition Temperatures", *Metals* **7** (2017) 52.

[134] Y.-x. Cui, W.-s. Wang, B. Shen, F.-h. Sun, "A study of CVD diamond deposition on cemented carbide ball-end milling tools with high cobalt content using amorphous ceramic interlayers", *Diamond and Related Materials* **59** (2015) 21-29.

[135] F. Cai, Y. Gao, W. Fang, T. Mao, S. Zhang, Q. Wang, "Improved adhesion and cutting performance of AlTiSiN coatings by tuning substrate bias voltage combined with Ar ion cleaning pre-treatment", *Ceramics International* **44** (2018) 18894-18902.

[136] H. Caliskan, P. Panjan, C. Kurbanoglu, "Chapter 3.16. Hard Coatings on Cutting Tools and Surface Finish - Comprehensive Materials Finishing", *Elsevier, Oxford*, (2017), 230-242.

[137] P.M. Martin, "Chapter 1. Deposition Technologies: An Overview - Handbook of Deposition Technologies for Films and Coatings (Third Edition)", *William Andrew Publishing, Boston*, (2010), 1-31.

[138] J.T. Gudmundsson, "Physics and technology of magnetron sputtering discharges", *Plasma Sources Science and Technology* **29** (2020) 113001.

[139] D. Lundin, K. Sarakinos, "An introduction to thin film processing using high-power impulse magnetron sputtering", *Journal of Materials Research* **27** (2012) 780-792.

[140] Q. Luo, S. Yang, K.E. Cooke, "Hybrid HIPIMS and DC magnetron sputtering deposition of TiN coatings: Deposition rate, structure and tribological properties", *Surface and Coatings Technology* **236** (2013) 13-21.

[141] J.E. Greene, J.E. Sundgren, L. Hultman, I. Petrov, D.B. Bergstrom, "Development of preferred orientation in polycrystalline TiN layers grown by ultrahigh vacuum reactive magnetron sputtering", *Applied Physics Letters* **67** (1995) 2928-2930.

[142] J.R. Conrad, J.L. Radtke, R.A. Dodd, F.J. Worzala, N.C. Tran, "Plasma source ion-implantation technique for surface modification of materials", *Journal of Applied Physics* **62** (1987) 4591-4596.

[143] S. Gauter, M. Fröhlich, H. Kersten, "Direct calorimetric measurements in a PBII and deposition (PBII&D) experiment with a HiPIMS plasma source", *Surface and Coatings Technology* **352** (2018) 663-670.

[144] E. Uhlmann, H. Riemer, S. An, M. Fröhlich, H. Paschke, M. Petersen, "Ecological and functional optimization of the pretreatment process for plasma based coatings of cutting tools", *Procedia Manufacturing* **33** (2019) 618-624.

[145] K.M. Andersson, L. Bergström, "Oxidation and dissolution of tungsten carbide powder in water", *International Journal of Refractory Metals and Hard Materials* **18** (2000) 121-129.

[146] M. Anik, K. Osseo-Asare, "Effect of pH on the Anodic Behavior of Tungsten", *Journal of The Electrochemical Society* **149** (2002) B224.

[147] D. Tamboli, S. Seal, V. Desai, A. Maury, "Studies on passivation behavior of tungsten in application to chemical mechanical polishing", *Journal of Vacuum Science & Technology A* **17** (1999) 1168-1173.

[148] E.A. Kneer, C. Raghunath, S. Raghavan, J.S. Jeon, "Electrochemistry of Chemical Vapor Deposited Tungsten Films with Relevance to Chemical Mechanical Polishing", *Journal of The Electrochemical Society* **143** (1996) 4095-4100.

[149] M. Zhibin, W. Jianhua, W. Qingchong, W. Chuanxin, "Adhesion improvement of diamond films on cemented carbides with copper implant layer", *Thin Solid Films* **390** (2001) 104-106.

[150] Y. Huang, H. Xiao, Z. Ma, J. Wang, P. Gao, "Effects of Cu and Cu/Ti interlayer on adhesion of diamond film", *Surface and Coatings Technology* **202** (2007) 180-184.

[151] K. Vandierendonck, M. Nesládek, S. Kadlec, C. Quaeyhaegens, M. Van Stappen, L.M.M. Stals, "W/WC diffusion barrier layers for CVD diamond coatings deposited on WC-Co: microstructure and properties", *Surface and Coatings Technology* **98** (1998) 1060-1065.

[152] M. Nesládek, K. Vandierendonck, C. Quaeyhaegens, M. Kerkhofs, L.M. Stals, "Adhesion of diamond coatings on cemented carbides", *Thin Solid Films* **270** (1995) 184-188.

[153] S.Y. Shadrin, P.N. Belkin, "Analysis of models for calculation of temperature of anode plasma electrolytic heating", *International Journal of Heat and Mass Transfer* **55** (2012) 179-186.

[154] T.W. Clyne, S.C. Troughton, "A review of recent work on discharge characteristics during plasma electrolytic oxidation of various metals", *International Materials Reviews* **64** (2019) 127-162.

[155] J. Martin, A.V. Nominé, J. Stef, A. Nominé, J.X. Zou, G. Henrion, T. Grosdidier, "The influence of metallurgical state of substrate on the efficiency of plasma electrolytic oxidation (PEO) process on magnesium alloy", *Materials & Design* **178** (2019) 107859.

[156] T. Mizuno, T. Ohmori, T. Akimoto, A. Takahashi, "Production of Heat during Plasma Electrolysis in Liquid", *Japanese Journal of Applied Physics* **39** (2000) 6055-6061.

[157] S.Y. Shadrin, A.V. Zhirov, P.N. Belkin, "Formation regularities of gaseous vapour plasma envelope in electrolyzer", *Surface Engineering and Applied Electrochemistry* **52** (2016) 110-116.

[158] H. Zeidler, T. Böttger, S. Schröder, M. Schneider, C. Lämmel, F. Sahr, J. Tardelli, L. Exbrayat, "Analysis of Plasma-Electrolytic Polishing Process Initiation", *Procedia CIRP* **108** (2022) 782-786.

[159] A.B. Rogov, A. Matthews, A. Yerokhin, "Role of cathodic current in plasma electrolytic oxidation of Al: A quantitative approach to in-situ evaluation of cathodically induced effects", *Electrochimica Acta* **317** (2019) 221-231.

[160] J. Flores-Mena, J. Diaz-Reyes, J.A.J.R.m.d.f. Balderas-Lopez, "Structural properties of WO3 dependent of the annealing temperature deposited by hot-filament metal oxide deposition", *Revista Mexicana de Fisica* **58** (2012) 504-509.

[161] P.V. Krasovskii, O.S. Malinovskaya, A.V. Samokhin, Y.V. Blagoveshchenskiy, V.A. Kazakov, A.A. Ashmarin, "XPS study of surface chemistry of tungsten carbides nanopowders

produced through DC thermal plasma/hydrogen annealing process", *Applied Surface Science* **339** (2015) 46-54.

[162] D. Cabrera-German, G. Gomez-Sosa, A. Herrera-Gomez, "Accurate peak fitting and subsequent quantitative composition analysis of the spectrum of Co 2p obtained with Al Kα radiation: I: cobalt spinel", *Surface and Interface Analysis* **48** (2016) 252-256.

[163] S. Hochstrasser-Kurz, D. Reiss, T. Suter, C. Latkoczy, D. Günther, S. Virtanen, P. Uggowitzer, P. Schmutz, "ICP-MS, SKPFM, XPS, and microcapillary investigation of the local corrosion mechanisms of WC-Co hardmetal", *Journal of The Electrochemical Society* **155** (2008) C415-C426.

[164] B.S. Linke, "Sustainability concerns in the life cycle of bonded grinding tools", *CIRP Journal of Manufacturing Science and Technology* **7** (2014) 258-263.

[165] J.B.J.W. Hegeman, J.T.M. De Hosson, G. de With, "Grinding of WC–Co hardmetals", *Wear* **248** (2001) 187-196.

[166] O. Jovic, T. Smolic, Z. Jurisic, Z. Meic, T. Hrenar, "Chemometric Analysis of Croatian Extra Virgin Olive Oils from Central Dalmatia Region", *Croatica Chemica Acta* **86** (2013) 335-344.

[167] N. Vlachos, Y. Skopelitis, M. Psaroudaki, V. Konstantinidou, A. Chatzilazarou, E. Tegou, "Applications of Fourier transform-infrared spectroscopy to edible oils", *Analytica Chimica Acta* **573-574** (2006) 459-465.

[168] M.A. Moharam, L.M. Abbas, "A study on the effect of microwave heating on the properties of edible oils using FTIR spectroscopy", *African Journal of Microbiology Research* **4** (2010) 1921-1927.

[169] J. Coates, "Interpretation of Infrared Spectra, A Practical Approach - Encyclopedia of Analytical Chemistry: Applications, Theory, and Instrumentation", (2006).

[170] J. Dorado, G. Almendros, J.A. Field, R. Sierra-Alvarez, "Infrared spectroscopy analysis of hemp (Cannabis sativa) after selective delignification by Bjerkandera sp at different nitrogen levels", *Enzyme and Microbial Technology* **28** (2001) 550-559.

[171] T. Zhao, J.M. Zhou, V. Bushlya, J.E. Ståhl, "Effect of cutting edge radius on surface roughness and tool wear in hard turning of AISI 52100 steel", *The International Journal of Advanced Manufacturing Technology* **91** (2017) 3611-3618.

[172] T. Vopat, Š. Podhorský, M. Sahul, M. Haršáni, "Cutting edge preparation of cutting tools using plasma discharges in electrolyte", *Journal of Manufacturing Processes* **46** (2019) 234-240.

[173] M. Goud, A.K. Sharma, C. Jawalkar, "A review on material removal mechanism in electrochemical discharge machining (ECDM) and possibilities to enhance the material removal rate", *Precision Engineering* **45** (2016) 1-17.

[174] P. Gupta, G. Tenhundfeld, E.O. Daigle, D. Ryabkov, "Electrolytic plasma technology: Science and engineering—An overview", *Surface and Coatings Technology* **201** (2007) 8746-8760.

[175] P.N. Belkin, "Anode electrochemical thermal modification of metals and alloys", *Surface Engineering and Applied Electrochemistry* **46** (2010) 558-569.

[176] S. An, L. Hansen, T. Wolff, R. Foest, M. Fröhlich, A. Quade, M. Stankov, H. Kersten, "Energetic characterization during plasma electrolytic polishing of cemented tungsten carbide", *Journal of Applied Physics* **134** (2023) 033305.

[177] L. Hansen, L. Rosenfeldt, K.A. Reck, H. Kersten, "Understanding the energy balance of a surface barrier discharge for various molecular gases by a multi-diagnostic approach", *Journal of Applied Physics* **129** (2021) 053308.

[178] J.A. Thornton, "Substrate heating in cylindrical magnetron sputtering sources", *Thin Solid Films* **54** (1978) 23-31.

[179] H. Kersten, H. Deutsch, H. Steffen, G.M.W. Kroesen, R. Hippler, "The energy balance at substrate surfaces during plasma processing", *Vacuum* **63** (2001) 385-431.

[180] T. Kewitz, M. Fröhlich, H. Kersten, "Analysis of passive calorimetric probe measurements at high energy influxes", *EPJ Techniques and Instrumentation* **4** (2017) 1.

[181] L. Rosenfeldt, L. Hansen, H. Kersten, "The Use of Passive Thermal Probes for the Determination of Energy Fluxes in Atmospheric Pressure Plasmas", *IEEE Transactions on Plasma Science* **49** (2021) 3325-3335.

[182] T. Bo, "CFD Homogeneous Mixing Flow Modelling to Simulate Subcooled Nucleate Boiling Flow", *SAE International*, Paper No. 2004-01-1512 (2004).

[183] J. Yao, P. Zhu, L. Guo, F. Yang, Z. Zhang, J. Ren, Z. Wu, "Study of a metal hydride based thermal energy storage system using multi-phase heat exchange for the application of concentrated solar power system", *International Journal of Hydrogen Energy* **46** (2021) 29332-29347.

[184] R. Wüthrich, J.D.A. Ziki, "Chapter 4. The Gas Film—A Key Element - Micromachining Using Electrochemical Discharge Phenomenon (Second Edition)", *William Andrew Publishing*, (2015), 63 - 94.

[185] E.V. Parfenov, R.R. Nevyantseva, S.A. Gorbatkov, "Process control for plasma electrolytic removal of TiN coatings. Part 1: Duration control", *Surface and Coatings Technology* **199** (2005) 189-197.

[186] S. Nukiyama, "The maximum and minimum values of the heat Q transmitted from metal to boiling water under atmospheric pressure", *International Journal of Heat and Mass Transfer* **9** (1966) 1419-1433.

[187] L. Yu, M. Han, F. He, "A review of treating oily wastewater", *Arabian Journal of Chemistry* **10** (2017) S1913-S1922.

[188] A.A. Kulkarni, J.B. Joshi, "Bubble Formation and Bubble Rise Velocity in Gas−Liquid Systems: A Review", *Industrial & Engineering Chemistry Research* **44** (2005) 5873-5931.

[189] R.T. Lahey, "The analysis of phase separation and phase distribution phenomena using two-fluid models", *Nuclear Engineering and Design* **122** (1990) 17-40.

[190] Z. Tian, Y. Cheng, X. Li, L. Wang, "Bubble shape and rising velocity in viscous liquids at high temperature and pressure", *Experimental Thermal and Fluid Science* **102** (2019) 528-538.

[191] T. Okawa, T. Tanaka, I. Kataoka, M. Mori, "Temperature effect on single bubble rise characteristics in stagnant distilled water", *International Journal of Heat and Mass Transfer* **46** (2003) 903-913.

[192] X. Luo, J. Zhang, K. Tsuchiya, L.-S. Fan, "On the rise velocity of bubbles in liquid-solid suspensions at elevated pressure and temperature", *Chemical Engineering Science* **52** (1997) 3693-3699.

[193] D. Rodrigue, "A General Correlation for the Rise Velocity of Single Gas Bubbles", **82** (2004) 382-386.

[194] I.K. Kure, H.A. Jakobsen, N.L. Forgia, J. Solsvik, "Experimental investigation of single bubbles rising in stagnant liquid: Statistical analysis and image processing", **33** (2021) 103611.

[195] I.H.B. Eric W. Lemmon, Marcia L. Huber, and Mark O. McLinden, "NIST Standard Reference Database Number 69, Eds. P.J. Linstrom and W.G. Mallard", *National Institute of Standards and Technology*, (retrieved April 15, 2023).

[196] S.C. Altıparmak, B. Xiao, "A market assessment of additive manufacturing potential for the aerospace industry", *Journal of Manufacturing Processes* **68** (2021) 728-738.

[197] A.K. Singla, M. Banerjee, A. Sharma, J. Singh, A. Bansal, M.K. Gupta, N. Khanna, A.S. Shahi, D.K. Goyal, "Selective laser melting of Ti6Al4V alloy: Process parameters, defects and post-treatments", *Journal of Manufacturing Processes* **64** (2021) 161-187.

[198] D. Zhang, J. Yu, H. Li, X. Zhou, C. Song, C. Zhang, S. Shen, L. Liu, C. Dai, "Investigation of Laser Polishing of Four Selective Laser Melting Alloy Samples", *Applied Sciences* **10** (2020) 760.

[199] J. Asim, A.-w. Mohamed Shaaban, H. Ahmed Hosny, "Chapter 8. Advance Deposition Techniques for Thin Film and Coating - Modern Technologies for Creating the Thin-film Systems and Coatings", *IntechOpen, Rijeka*, (2017).

[200] M. Joshi, B.S. Butola, "Chapter 14. Application technologies for coating, lamination and finishing of technical textiles - Advances in the Dyeing and Finishing of Technical Textiles", *Woodhead Publishing*, (2013), 355-411.

[201] M. Montazer, T. Harifi, "Chapter 7. Nanocoating and lamination - Nanofinishing of Textile Materials", *Woodhead Publishing*, (2018), 95-107.

[202] M.K. Purkait, M.K. Sinha, P. Mondal, R. Singh, "Chapter 3. Temperature-Responsive Membranes - Interface Science and Technology", *Elsevier*, (2018), 67-113.

[203] F. Massines, C. Sarra-Bournet, F. Fanelli, N. Naudé, N. Gherardi, "Atmospheric Pressure Low Temperature Direct Plasma Technology: Status and Challenges for Thin Film Deposition", *Plasma Processes and Polymers* **9** (2012) 1041-1073.

[204] D. Merche, N. Vandencasteele, F. Reniers, "Atmospheric plasmas for thin film deposition: A critical review", *Thin Solid Films* **520** (2012) 4219-4236.

[205] J. Schäfer, K. Fricke, F. Mika, Z. Pokorná, L. Zajíčková, R. Foest, "Liquid assisted plasma enhanced chemical vapour deposition with a non-thermal plasma jet at atmospheric pressure", *Thin Solid Films* **630** (2017) 71-78.

[206] A.S.H. Makhlouf, "Chapter 1. Current and advanced coating technologies for industrial applications - Nanocoatings and Ultra-Thin Films", *Woodhead Publishing*, (2011), 3-23.

[207] Y. Shi, M. Osada, Y. Ebina, T. Sasaki, "Single Droplet Assembly for Two-Dimensional Nanosheet Tiling", *ACS Nano* **14** (2020) 15216-15226.

[208] J.L. Todolí, S. Maestre, J. Mora, A. Canals, V. Hernandis, "Comparison of several spray chambers operating at very low liquid flow rates in inductively coupled plasma atomic emission spectrometry", *Fresenius' Journal of Analytical Chemistry* **368** (2000) 773-779.

[209] C. Rivas, L. Ebdon, S.J. Hill, "Effect of different spray chambers on the determination of organotin compounds by high-performance liquid chromatography–inductively coupled plasma mass spectrometry", *Journal of Analytical Atomic Spectrometry* **11** (1996) 1147-1150.

[210] L. Barillas, E. Makhneva, S. An, K. Fricke, "Functional Thin Films Synthesized from Liquid Precursors by Combining Mist Chambers and Atmospheric-Pressure Plasma Polymerization", *Coatings* **11** (2021) 1336.

[211] S. Hidalgo, L. Barillas, K.-D. Weltmann, K. Fricke, "Influencia del diseño de una cámara de niebla en la deposición de nano-películas delgadas líquidas – prueba de concepto", *Revista Tecnología en Marcha* **33** (2020) 130-142.

[212] SLM SOLUTIONS - Material Data Sheet (Fe-Alloy 316L (1.4404))

[213] J. Schäfer, R. Foest, A. Quade, A. Ohl, K.D. Weltmann, "Local deposition of SiOx plasma polymer films by a miniaturized atmospheric pressure plasma jet (APPJ)", *Journal of Physics D: Applied Physics* **41** (2008) 194010.

[214] G. Sauerbrey, "Verwendung von Schwingquarzen zur Wägung dünner Schichten und zur Mikrowägung", *Zeitschrift für Physik* **155** (1959) 206-222.

[215] W.-S. Shin, B. Son, W. Song, H. Sohn, H. Jang, Y.-J. Kim, C. Park, "Heat treatment effect on the microstructure, mechanical properties, and wear behaviors of stainless steel 316L prepared via selective laser melting", *Materials Science and Engineering: A* **806** (2021) 140805.

[216] V. Salarvand, H. Sohrabpoor, M.A. Mohammadi, M. Nazari, R. Raghavendra, A. Mostafaei, D. Brabazon, "Microstructure and corrosion evaluation of as-built and heat-treated 316L stainless steel manufactured by laser powder bed fusion", *Journal of Materials Research and Technology* **18** (2022) 4104-4113.

[217] M.J. Ansari, D.-S. Nguyen, H.S. Park, "Investigation of SLM Process in Terms of Temperature Distribution and Melting Pool Size: Modeling and Experimental Approaches", *Materials* **12** (2019) 1272-1272.

[218] E. Yasa, J.P. Kruth, "Microstructural investigation of Selective Laser Melting 316L stainless steel parts exposed to laser re-melting", *Procedia Engineering* **19** (2011) 389-395.

[219] M.-H. Hong, B.K. Min, T.-Y. Kwon, "The Influence of Process Parameters on the Surface Roughness of a 3D-Printed Co–Cr Dental Alloy Produced via Selective Laser Melting", **6** (2016) 401.

[220] A. Matras, "Research and Optimization of Surface Roughness in Milling of SLM Semi-Finished Parts Manufactured by Using the Different Laser Scanning Speed", **13** (2020) 9.

List of Figures

Figure 2.1 Photograph of 3D-printed metallic parts (316L stainless steel): untreated (left) and polished (right) 5

Figure 2.2 Visualization of direct water-based multichannel pulsed electrical discharges (source: [43]) 7

Figure 2.3 Application of liquid treatment using an argon plasma jet (kINPen) (adapted from [50]) 8

Figure 2.4 Visualization of discharges during the plasma electrolytic oxidation (PEO) process (taken from [66]) 9

Figure 2.5 Schematic illustration of plasma electrolytic polishing apparatus (reprinted from [70]). 10

Figure 2.6 Voltage-current characteristics of the PEP process, accompanied by images representing each voltage regime (U_a to U_d), ranging from bubble formation to plasma development on the workpiece surface (taken from [9]). 12

Figure 2.7 Schematic illustration of the electron avalanche effect (reproduced from [83]). ... 14

Figure 2.8 Paschen curve for water vapor. The calculation was performed according to Equation 2.14 using the constants A = 0.1 (Pa·cm)$^{-1}$, B = 2.2 V·(Pa·cm)$^{-1}$, and γ = 0.1. 15

Figure 2.9 Photographs of the anode workpiece under the PEP process for varied materials including: (a) AISI 316 stainless steel [14]) , (b) Inconel 718 Ni-based superalloy [88], and (c) WC-Co-based cemented carbide [89]. 16

Figure 2.10 Gas discharge circuit (left) and its corresponding I-V characteristics (right) (reprinted from [92]). 16

Figure 2.11 Surface roughness values of stainless-steel (AISI 304) workpieces before and after the PEP process measured by AFM (reprinted from [11]). 18

Figure 2.12 Schematic diagram of the PEP process by Vaňa et al. (adapted from [95]) 19

Figure 2.13 Schematic illustration of the formation of a streamer discharge. (1) Electrolyte, (2) photoionization, (3) ions, (4) electrons, (5) workpiece surface, (6) secondary electrons, (7) avalanche head, (8) the streamer, (9) plasma channel, and (10) a gas explosion (reprinted from [13]) 20

Figure 3.1 A schematic diagram of an undisturbed (left) and the shell electron energy of an atom subjected to XPS (right). The core electrons, bound to the atom, occupy the lowest energy states 1s, 2s, and 2p. Incident X-rays excite to an unbound state above the surface workfunction, ϕ (adapted from [98]) 24

Figure 3.2 Schematic diagram of white light interferometer (adapted from [102]). 25

Figure 3.3 Visual depiction of the arithmetic mean height of a line, Ra. 26

Figure 3.4 Visual representation of areal arithmetical mean height, Sa (reprinted from [105]. 27

Figure 3.5 (a) photograph of WLI equipment for the tool cutting edge measurement. (b) 3D profiles of cutting edge on as-received (upper) and PEP-treated inserts (bottom) measured by WLI. 28

Figure 3.6 Gaussian fitted circle process to define a cutting-edge radius (Reprinted from Wyen et al. [106]). 28

Figure 3.7 Schematic diagram of attenuated total reflectance Fourier transform infrared spectroscopy (ATR-FTIR) (adapted from [111]). 30

Figure 3.8 Schematic representation of the atomic force microscope (AFM) apparatus (adapted from [116]). 32

Figure 4.1 Trend in global machine tool production over the last 20 years sourced from the VDW Market Report 2022 ([118]). 33

Figure 4.2 Photographic illustration of the variety of scale, surface coatings, and geometric complexity of precision tools (Source: GÜHRING KG). 34

Figure 4.3(a) Photograph and (b) schematic illustration of PEP equipment. 35

Figure 4.4 A schematic diagram of a magnetron sputtering system (reprinted from [138]). .. 36

Figure 4.5 (a) HiPIMS/PBII apparatus. (b) Schematic diagram of HiPIMS/PBII system. 37

Figure 4.6 Voltage and current waveforms of synchronized HiPIMS (bottom) and PBII (upper) process with delay of 35 µs. 38

Figure 4.7 Magnetron sputtering system from a company, A+S. 39

Figure 4.8 Universal lathe DMG MORI CTX gamma 1250 TC. 40

Figure 4.9 Photographs of WC-Co-based tools: (a) untreated and PEP-treated with (b) $(NH_4)_2SO_4$ and (c) Na_2CO_3 41

Figure 4.10 XPS analysis of untreated and PEP-treated sample: (a) elemental composition and (b) W 4f spectra of the tool surface. 42

Figure 4.11 (a) Electrical conductivity of Na_2CO_3 electrolytes and (b) current-voltage characteristics at varying electrolyte concentrations (ranging from 2 wt% to 12 wt%) at consistent temperature of 70 °C (adapted from [89]). 43

Figure 4.12 (a) Electrical conductivity of Na_2CO_3 electrolyte and (b) current-voltage characteristics at varying electrolyte temperatures (ranging from 40 °C to 80 °C) at fixed concentration of 10 wt%. (adapted from [89]). 44

Figure 4.13 (a) A series of photographs illustrating stages of the PEP process at distinct voltages. (b) Evolution of current density over the process voltage from 0 V to 400 V. The segment highlighted in red is detailed further in the inset. 45

Figure 4.14 Photographs of tool workpiece (a) before and after the PEP process at varied voltages: (b) 30 V (V_1-V_2), (c) 110 V (V_2-V_3), and (d) 200 V (V_3-V_4). 46

Figure 4.15 (a) XPS survey spectra of untreated and PEP-treated workpieces. XPS depth profile data of (b) untreated and (b–d) PEP-treated inserts at different voltages (30, 110, and 200 V). 47

Figure 4.16 XPS spectra of highly-resolved W 4f (left side) and Co 2p (right side) peaks of (a), (e)untreated, and PEP-treated at (b), (f) 30 V, (c), (g)110 V, and (d), (h)200 V insert surfaces. 48

Figure 4.17 XRD patterns of untreated and PEP-treated inserts at different process voltages of 30 V, 110 V, and 200 V (adapted from [89]). 50

Figure 4.18 SEM images of the (a) untreated and PEP-treated inserts at different process voltages: (b) 30 V, (c) 110 V, and (d) 200 V. EDX mapping images of the (e) untreated and PEP-treated inserts at different process voltages: (f) 30 V, (g) 110 V, and (h) 200 V. 51

Figure 4.19 (a) 3D surface profile on the untreated tool surface measured by WLI. (upper) and line profile corresponding to the specified line (below). (b) Comparative average roughness (Ra) values for untreated and PEP-treated tool surfaces across voltages ranging from 30 V to 200 V. 52

Figure 4.20 Photographs of contaminated insert tools. 53

Figure 4.21 (a) ATR-FTIR spectra of as-received, contaminated, and cleaned inserts' surfaces. 54

Figure 4.22 (a) XPS survey spectra of as-received and PEP-treated inserts. (b) High-resolution XPS spectra of carbon (C 1s) (Adapted from Ref. [89]). 55

Figure 4.23 (a) Comparative cutting-edge radius for as-received inserts and PEP-treated inserts under Processes 1-5 (voltage variations between 90 V and 110 V). (b) Comparison of cutting-edge radius on all four orientations of the tools before and after the PEP Process 6.56

Figure 4.24 SEM images of the insert tools; (a) Process 1, (b) Process 2, and (c) Process 3. 58

Figure 4.25 Scratch test results for coated turning tools with each Process - Process 1: (a), Process 2: (b), and Process 3: (c). Green lines in the graphs represent $LC2$. Images of the scratched areas corresponding to each process - Process 1: (d), Process 2: (e), and Process 3: (f). Green circles in the images mark the $LC2$ point. 59

Figure 4.26 Comparison of tool life time ($tVB0.3$) and critical load. 60

Figure 4.27 SEM images of the insert tools; (a) Process 1, (b) Process 2, and (c) Process 3 60

Figure 4.28 Comparison of (a) cutting-edge radius and (b) tool life $t_{VB0.3}$ and critical load..... 61

Figure 5.1 (a) Schematic illustration of the experimental setup. (b) Photograph of PEP apparatus (left) and enlarged photographs of the workpiece in the electrolyte without PEP and during PEP (right) with indicated immersion depth, d (reprinted from [176]). 65

Figure 5.2 (a) A schematic representation of the modeling domain for the workpiece, including the computational mesh. (b) A comparison is presented between the wall temperature and the temperature simulated by the model at the measurement location. 66

Figure 5.3 An example of assessing the power transfer to a workpiece: (a) measured workpiece temperature over time. The time-derivative of the temperature curve over time (dT-curve) for two methods: (b) binning and (c) linear interpolation (reprinted from [176]). 67

Figure 5.4 A schematic representation of the calibration process for acquiring the cooling calibration curve in the LT regime. 69

Figure 5.5 Representative curve of the calibration procedure: (a) Recorded temperature as a function of time during the calibration procedure (b) comparison of the dT-depiction between the original cooling curve (blue) and the calibrated cooling curve (red). 70

Figure 5.6 Schematic representation of the method used to determine the heat capacity of the workpiece. 70

Figure 5.7 Change in the temperature of water in the isothermal container after the heated workpiece has been transferred. 71

Figure 5.8 (a) Schematic description of the modeling domain and (b) illustration of the computational mesh. 73

Figure 5.9 Schematic illustration of a synchronized high-speed camera and electrical measurement. 74

Figure 5.10 (a) Evolution of workpiece temperature and (b) current as a function of the process time at varied immersion depths (adapted from [176]). 75

Figure 5.11 (a) Time derivative of temperature as a function of temperature (dT-curve). Estimated power transfer to the workpiece (Pin) in relation to temperature at various immersion depths, employing (b) binning and (c) interpolation methods. Shaded regions represent the error band. It should be noted that power values in the LT regime are determined using the cooling calibration curve (purple curve in (a)) (reprinted from [176]). 76

Figure 5.12 Dependencies of efficiency of power transferred to the workpiece (fraction of Pin from electrical power) in the LT and HT regimes in different immersion depths, d (reprinted from [176]). 79

Figure 5.13 Snapshots from high-speed camera of the workpiece: (a) 0 s and (b) 29.2 s in d = 10 mm and (c) 0 s and (d) 7.5 s in d = 20 mm. The yellow dashed line indicates the outline of the workpiece immersed in the electrolyte. The gaseous layer around the workpiece surface is marked in blue in (b) and (d) (reprinted from [176]). 80

Figure 5.14 Dependencies of the temporal development of electrolyte temperature at different immersion depths (see section 5.2.2 for position of the thermocouple). The inset is an enlargement of the marked area (purple color). 81

Figure 5.15 Temporal development of electrolyte temperature for d = 20 mm: measured data (solid black line), turbulent model (red dashed line), and laminar model (blue dashed line) (reprinted from [176]). 82

Figure 5.16 (a) Volume average velocity of the fluid mixture along with the streamlines and (b) gas phase volume fraction obtained by modeling for t = 30 s (reprinted from [176]). 82

Figure 5.17 Spatio-temporal evolution of fluid mixture temperature obtained by the modeling. Please note the different color scales for each times (reprinted from [176]). 83

Figure 5.18 XPS line-scan profile data of (a) untreated and (b) 30 s PEP-treated workpieces (complete immersion). The inset shows a photograph of the workpiece indicating the line scanning direction. The line-scanned sections are marked with dotted lines. (c) Binding fraction of carbide in C 1s peak. (d) W 4f spectra of untreated (upper) and 30 s PEP-treated (below) workpieces (reprinted from [176]). 84

Figure 5.19 (a) Visualization of gas layer development throughout the 30 s PEP process on a fully submerged workpiece (d = 20 mm), captured using a high-speed camera at a frame rate of 1000 fps; (b) the corresponding electrical current waveform and workpiece temperature measurements taken simultaneously with the high-speed camera, including an inset that accentuates the enlarged segment of the current (displayed in grey). 86

Figure 5.20 (a) Electrical current waveform throughout the PEP process, with arrows denoting the range for FFT analysis. (b) Power spectra as mean square amplitude (MSA) of the current waveform at 6 s intervals throughout the 30 s of the PEP process. 88

Figure 5.21 (a) Current waveforms captured during the PEP process at different immersion depths (d = 5 – 20 mm). (b) Spectrograms derived from the respective current waveforms. 89

Figure 5.22 Representation of (a) the frequency of the spectrogram at peak current amplitude and (b) workpiece temperature, using a consistent time scale. Dotted lines indicate the moment when the current amplitude begins in order to identify their respective workpiece temperature. 91

Figure 5.23 Combined plot of the integrated camera signal (black curve) from the selected area (indicated by the shaded region in the inset photo, top-left) over time and the current waveform (red curve) for a 20 mm immersion depth. The inset in the upper right displays an expanded view of the area within the blue box. 93

Figure 5.24 Comparative spectrograms for current waveform (left column) and camera signal (right column) at immersion depths of 5 mm to 20 mm. 94

Figure 5.25 (a) Time-dependent camera count, with red markings indicating the PEP process duration (t = 15 s – 25 s) and blue markings representing the background (t = 30 s – 40 s) after the PEP process. (b) Contour plot of merged images (10^4 frames) captured during the PEP process, within the 15 s to 25 s time interval. (c) Temporally integrated camera signal values across the Y-position, as denoted by the green dashed line in (b). 96

Figure 6.1(a) Depictions of the mist chamber from a side and top perspective along with its design details (adapted from [210]). (b) Photograph of SLM type metallic 3D-printer. 101

Figure 6.2 A representation of the in-house industrial-scale PEP apparatus at INP Greifswald (left) paired with a zoomed-in image of bath #1 (right). 102

Figure 6.3 (a) Photographs of 3D-printed metallic mist chambers showing the PEP immersion sequence (adapted from [210]) and (b) test specimens for surface characterization. 103

Figure 6.4 Typical voltage-current waveform during the PEP process on the 3D-printed metallic mist chamber. The process consists of three sequences, each lasting 7.5 min per orientation. 103

Figure 6.5 Process steps for the plasma-based synthesis of pp-films obtained from liquid monomers (reprinted from [210]). 104

Figure 6.6 (a) Comparison of XRD diffraction patterns on the surface of 316L SS fabricated via SLM, pre- and post-PEP for durations of 7.5, 15, and 30 min. (b) Crystallite sizes estimated by Scherrer's equation. 107

Figure 6.7 Comparison of surface elemental composition of 3D-printed specimens, before and after PEP treatment, over a range of durations from 7.5 min to 30 min. 108

Figure 6.8 Comparative representation of the corner part of 3D-printed specimens, observed via OM: (a) untreated, (b) PEP treated (30 min), and the surface of the specimens as inspected by SEM: (c) untreated, (d) PEP treated (30 min). 109

Figure 6.9 WLI-characterized 3D topographical profiles of SLM-built specimens before and after PEP treatment at various durations: (a) untreated, (b) 7.5 min, (c) 15 min, and (d) 30 min. Surface roughness values (S_a) are illustrated in (e) (reprinted from [210]). 110

Figure 6.10 WCA measurements on 3D-printed SS specimens before and after the PEP process (reprinted from [210]). 111

Figure 6.11 Results of the QCM measurements for a 3D-printed mist chamber before and after the PEP process: (a) mass difference, Δm, and (b) mist-out time, $Tmist$ (reproduced from [210]). 112

Figure 6.12 Comparison of the average pp-film thickness at various misting times obtained by 3D-printed mist with untreated and after PEP (reprinted from [210]) 113

List of Tables

Table 2-1 Comparison of various polishing techniques by their mechanisms and application concerns (adapted from [9]) 6

Table 2-2 Parameters of the PEP process for various materials 11

Table 4-1 Process parameters for plasma fine-cleaning and TiN deposition 38

Table 4-2. Process parameters for PEP pretreatment 41

Table 4-3. Process parameters for PEP pretreatment 46

Table 4-4 Binding fraction of the W 4f and Co $2p_{3/2}$ peaks 49

Table 4-5 Elemental fractions of tool surfaces measured by EDX 51

Table 4-6 Overview of pretreatment methods for cleaning tools 53

Table 4-7 FTIR band assignment of insert surface 54

Table 4-8 PEP process parameters 56

Table 4-9 Overview of cleaning and coating processes on the tools 58

Table 4-10 Overview of cleaning and coating processes on the tools 60

Table 5-1 Physical properties of water at varied temperature taken from NIST database [195]. 92

Table 6-1 Chemical composition of 316L powder used in SLM (wt.%) [212] 101

Table 6-2 Relative fractions of metallic and oxidized components of Fe and Cr, determined via peak fitting of Fe $2p_{3/2}$ and Cr $2p_{3/2}$, respectively 108

Table 6-3 Weight changes of 3D-printed mist chambers before and after PEP 111

List of Abbreviation

A

Abrasive Jet Polishing: AJP, 6
Additive Manufacturing: AM, 6
Atmospheric Pressure Plasma Jets: APPJ, 8
Atomic Force Microscope: AFM, 31
Attenuated Total Reflection Fourier Transform Intrared Spectroscopy: ATR-FTIR, 30

C

Charged Coupled Device: CCD, 25
Contact Glow Discharge Electrolysis: CDGE, 16

D

DC Magnetron Sputtering: DCMS, 34
Direct Current: DC, 16

E

Electron Spectroscopy for Chemical Analysis: ESCA, 23
Energy Dispersive X-ray: EDX, 29

F

Fast Fourier Transformation: FFT, 87
Flank wear land: VB, 40
Fourier Transform Infrared spectroscopy: FTIR, 29

G

Grazing Incidence X-ray Diffraction: GIXRD, 31

H

High Power Impulse Magnetron Sputtering: HiPIMS, 34

I

Inductively Coupled Plasma Atomic Emission Spectrometry: ICP-AES, 100
Inductively Coupled Plasma Mass Spectrometry: ICP-MS, 100

L

Low-Angle Backscattered Electron: LABE, 29

M

Mean Squared Amplitude: MSA, 87

P

Physical Vapor Deposition: PVD, 34
Plasma Based Ion Implantation: PBII, 37
Plasma Electrolytic Oxidation: PEO, 44
Plasma Electrolytic Polishing: PEP, 9
Plasma Enhanced Chemical Vapor Deposition: PECVD, 99
plasma-polymerized: pp, 100

Q

Quartz Crystal Microbalance: QCM, 105

R

Radio Frequency: RF, 104

S

Scanning Electron Microscopy: SEM, 29
Selective Laser Melting: SLM, 99
Short-Time Fourier Transform: STFT, 89
Stainless Steel: SS, 99
Stereolithography: SLA, 100

U

Ultraviolet: UV, 7

V

Vapor Gaseous Envelope: VGE, 13
Vertical Scanning Interferometry: VSI, 25

W

Water Contact Angle: WCA, 105
White Light Interferometry: WLI, 25

X

X-ray Diffraction: XRD, 31
X-ray Photoelectron Spectroscopy: XPS, 23

List of Publications & Conference Contributions

Publications in Peer-Reviewed Journals

1. **S. An**, L. Hansen, T. Wolff, R. Foest, M. Fröhlich, A. Quade, M. Stankov, H. Kersten; "Energetic characterization during plasma electrolytic polishing of cemented tungsten carbide", *Journal of Applied Physics*, 134 (2023) p. 033305.
2. L. Barillas, E. Makhneva, **S. An**, K. Fricke; "Functional Thin Films Synthesized from Liquid Precursors by Combining Mist Chambers and Atmospheric-Pressure Plasma Polymerization", *Coatings*, *11* (2021) 1336
3. **S. An**, R. Foest, K. Fricke, H. Riemer, M. Fröhlich, A. Quade, J. Schäfer, K.-D. Weltmann, H. Kersten; "Pretreatment of cutting tools by plasma electrolytic polishing (PEP) for enhanced adhesion of hard coatings", *Surface and Coatings Technology***,** *405* (2021) 126504
4. E. Uhlmann, H. Riemer, **S. An**, M. Fröhlich, H. Paschke, M. Petersen; "Ecological and functional optimization of the pretreatment process for plasma based coatings of cutting tools", *Procedia Manufacturing*, *33* (2019), 618-624

Contributions to Workshops and Conferences

(Presenter underlined)

1. **S. An**, L. Hansen, T. Kewitz, G. Gött, S. Kwak, M. Fröhlich, R. Foest, K. Fricke, A. Quade, K.-D. Weltmann, H. Kersten; "Diagnostic of temporal behavior of a plasma electrolytic polishing process", *DPG Meeting "SMuK 2021*, August, 2021 (Poster)
2. **S. An**, H. Riemer, R. Ihrke, A. Quade, R. Foest, K. Fricke, M. Fröhlich, Holger Kersten; "Pretreatment of cutting tools by plasma electrolytic polishing (PEP) for enhanced adhesion of hard coatings", *12th Asian-European International Conference on Plasma Surface Engineering (AEPSE 2019)*, September 2019 (Oral)
3. **S. An**, R. Ihrke, A. Quade, H. Riemer, M. Petersen, H. Paschke, M. Fröhlich; "Investigation of surface pretreatment on cemented carbide cutting tools by plasma electrolytic polishing (PEP) for enhanced hard coating adhesion", *16th International Conference on Plasma Surface Engineering (PSE 2018)*, September 2018 (Poster)
4. M. Fröhlich, R. Ihrke, **S. An**, H. Testrich; "Plasma based surface finishing of 3D printed metallic parts", *16th International Conference on Plasma Surface Engineering (PSE 2018)*, September 2018 (Oral)
5. **S. An**, R. Ihrke, A. Quade, M. Fröhlich; "Plasma electrolytic polishing technology for surface cleaning of cemented-carbide cutting tools", *20th International Summer School on Vacuum, Electron and Ion Technologies*, September 2017 (Poster)
6. **S. An**, R. Ihrke, M. Fröhlich; "A method of plasma electrolytic polishing process for cemented-carbide cutting tools", *The 5th International Workshop on Solution Plasma and Molecular Technologies (SPM-5)*, June 2017 (Oral)

Sworn declaration

I, Sehoon An, hereby declare that

i. Apart from the supervisor's guidance, the content and design of the thesis is all my own work;
ii. This thesis has not been submitted either partially or wholly as part of a doctoral degree to another examining body. No materials has been published or submitted for publication other than indicated in this thesis;
iii. This thesis has been prepared subject to the Rules of Good Scientific Practice of the German Research Foundation;
iv. No academic degree has ever been withdrawn.

Greifswald, August 2023

Sehoon An

Acknowledgement

Drawing closer to the conclusion of my PhD, it is abundantly clear that this milestone is not solely my own. It is the culmination of collective efforts, encouragement, and invaluable support from many. This note is a heartfelt acknowledgment to everyone who has been a part of my academic journey.

Foremost, I express my profound appreciation to Prof. Dr. Holger Kersten for granting me the unparalleled opportunity to pursue my doctorate at the University of Kiel. His unwavering interest, guidance, and faith in my potential have been pivotal throughout this journey. Though words may fall short, I owe him immensely for this accomplishment.

The role of Prof. Dr. Maik Fröhlich in setting the stage for my academic adventure in Germany is noteworthy. From introducing me to Plasma Electrolytic Polishing (PEP) to ensuring my smooth integration into the German work environment and culture, his contributions have been foundational. Even after relocation to Zwickau, his continued oversight of my PhD work has been greatly appreciated.

I extend special gratitude to Dr. Rüdiger Foest. He has been more than just a mentor, acting as a guiding light during challenging academic terrains and personal trials. His welcoming attitude, allowing me to approach and seek counsel, has often been the sanctuary I needed, and his wisdom has often provided clarity.

Over the almost last seven years, the Plasma Oberflächen Technologie (POT) group has become like a second home to me. Jens Zöllner-Krummer stands out, not only as a reliable colleague but as a dear friend. Whenever I needed technical support on the intricacies of PEP equipment or diagnostic tools, Jens was always there to assist. Beyond our professional interactions, he has guided me through the bureaucracy, introduced me to the beautiful local scenic spots, and took the time to teach me German, enhancing my interaction with colleagues and focus at work. Also, I am deeply appreciative of Dr. Holger Testrich, who reviewed my thesis and ensured smooth administrative processes regarding visa issues. Guiding me academically and brightening days with deadpan humor, my office-mate, Dr. Frank Hempel frequently surprised me with Monty Python quotes (which I had no prior knowledge) and stressed the significance of the 5 (or is it 7?) P rules essential for a proficient scientist. I am grateful for the other office-mate Mandy Holländer, not only for our enlightening discussions on PEP but also for her invaluable assistance in translating parts of my thesis into German. Also thanks to Dr. Antje Quade for not only XPS measurement and hosting annual summer garden event, making good memories. Every member of the team, from Daniel Köpp, Urte Kellner, Tony Krüger, and Dr. Jan Schäfer, to Dr. Andre Naumann, and our former POT colleagues like Roland Ihrke, Uwe Lindemann, Dr. Thorben Wolff, and Dr. Katja Fricke, has offered invaluable insights and forged a strong sense of camaraderie.

My time here has also been shaped by the unsung heroes across various departments and administrative divisions of INP Greifswald. Special acknowledgments go to Gregor Gött for high-speed camera operations and my gratitude extends to Camila Andrea Rojas Nunez and Dr. Marcel Wetegrove for their assistance and training in SEM-EDX operations. I am also grateful for the collaborative efforts of Dr. Marjan Stankov, who took charge of the modeling

part of our work. I would also like to express my gratitude to “mi amiga”, Laura Barillas-Mora for collaboration in the development of the 3D-printed mist chamber with Dr. Ekaterina Makhneva. In addition, I am grateful to Dr. Ralf-Peter Methling for his review of my thesis and for inspiring me to engage in running activities. Furthermore, I appreciate the director of the institute, Prof. Dr. Klaus-Dieter Weltmann, for continuously providing me the opportunity to advance my research.

Gratitude is also due to collaborators from various departments and the project partners. Also, the Plasma Technology Group at Kiel University has been invaluable, with special acknowledgment to Dr. Luka Hansen for his continuous academic support in calorimetric measurement and for fostering a welcoming environment every time I visited Kiel.

My peers have played an instrumental role, especially Dr. Sehyun Kwak, with his invaluable insights into spectrogram and image analysis. Additionally, I thank Dr. Alexander Puth for reviewing my thesis. I'm also grateful to my friends in Greifswald, including Simon, Thalita, Fabian, Jonas, Laura (VS), Alex, Jan, Sandra, George, Miguel, Jasmin, Christina, Sarah, Alex, Marco, Primoz, Monique, Jaroslav, Hyeonyoung, Robert, Yeonhwa, Jaeyoung, Hanna, Chanwoo, Gaeun and many others, for the delightful memories created during my staying here in Greifswald.

Lastly, and most importantly, at the heart of my journey lies my family. My wife, Hyunjin, who traveled all the way to Germany to be by my side, has truly been the wind beneath my wings, providing unwavering support and showering me with boundless love and patience. To my parents, whose unconditional sacrifices and teachings have shaped me, and to my sisters and in-laws, who consistently believed in me even during the toughest times, I dedicate this achievement.

In conclusion, this PhD is not only a reflection of my academic pursuits but also a testament to the contributions from each one of you. From the depths of my heart, thank you.

Sehoon An

Greifswald, August 2023